

**ENVIRONMENTAL CONDITIONS OF THE
EXTREMES OF STAR FORMATION:
FROM QUIESCENT CLOUDS TO SUPER STAR
CLUSTERS**

Molly Katherine Finn
Sunnyvale, California

B.S. Physics & Astronomy, University of Rochester, 2017

M.S. Astronomy, University of Virginia, 2019

A Dissertation Presented to the Graduate
Faculty of the University of Virginia
in Candidacy for the Degree of
Doctor of Philosophy

Department of Astronomy

University of Virginia
April 2023

Committee Members:

Kelsey E. Johnson
Remy Indebetouw
Nitya Kallivayalil
Karen McGlathery

© Copyright by

Molly Katherine Finn

All rights reserved

April 14, 2023

Abstract

Galaxies form stars in a wide variety of cluster configurations, from loose open clusters that are prevalent in the Milky Way and quickly dissociate, to compact globular clusters that have survived as bound systems for billions of years. To understand the full range of star formation throughout cosmic time, we need to observe extreme environments with a wide variety of star-forming abilities and we need to observe the cold, star-forming molecular gas directly. This dissertation presents work focused on understanding the physical conditions of the molecular gas in a variety of environments and developing new methods for analyzing molecular tracers.

In Chapter 2, I present observations of a molecular cloud identified in the merging Antennae galaxies with the potential to form a globular cluster, nicknamed the “Firecracker.” Since star formation has not yet begun at an appreciable level in this region, this cloud provides an example of what the birth environment of a globular cluster may have looked like before stars form and disrupt the natal physical conditions. I demonstrate that the Firecracker would require an extremely high external pressure to remain bound, which is remarkably consistent with theoretical expectations.

In Chapter 3, I present a comparative study of two galaxies from the LEGUS sample: barred spiral NGC 1313 and flocculent spiral NGC 7793. These two galaxies have similar masses, metallicities, and star formation rates, but NGC 1313 is forming significantly more massive star clusters than NGC 7793. I find surprisingly small differences between the molecular cloud populations in the two galaxies, but there are much larger variations in cloud properties between different regions within each galaxy, especially for NGC 1313. The massive cluster formation of NGC 1313 may be driven by its greater variation in environments, allowing more clouds with the

necessary conditions to arise.

In Chapter 4, I present a comparison of four different regions in the LMC: The regions 30 Dor, N159, and N113 are actively forming massive stars, while the quiescent Molecular Ridge is forming almost no massive stars, despite its large reservoir of molecular gas. I find that the Ridge has significantly lower kinetic energy at a given size scale and also lower surface densities than the other regions, resulting in higher virial parameters. This suggests that the Ridge is not forming massive stars as actively as the other regions because it has less dense gas and not because collapse is suppressed by excess kinetic energy.

In Chapter 5, I present a multi-line non-LTE fitting tool to create pixel-by-pixel maps of kinetic temperature, volume density, and column density in the LMC's Molecular Ridge. The fitted volume density is strongly correlated with the YSOs while no other easily observed metric could match this correlation. This indicates that the fitted volume density is uniquely able to capture the relevant star-forming ability of the cloud.

Finally, in Chapter 6 I depart from star formation to discuss Dark Skies, Bright Kids, an astronomy outreach program that focuses on enriching science education in under-served elementary schools. I find that over the course of our programs, students become more confident in their science abilities, especially female students. I also find that on days that students report being creative and asking questions, they were more likely to say they felt like a scientist and were interested in the day's topic, suggesting that creativity can be just as important as doing experiments for generating interest in and a sense of participating in science.

Acknowledgements

Being here at this point, both in terms of completing a thesis and in life in general, is due almost entirely to the many people who have supported me, cheered me on, and been a friend to me at every step of the way. I feel incredibly lucky to have been surrounded by such wonderful people. I couldn't possibly list everyone who has had a positive impact on me, but below are some highlights from throughout my life.

Thank you to...

My mom—Thank you for your endless warmth and joy and love. I can't imagine life without you there in my corner. Anytime I'm down I know that you'll pick me back up and believe in me.

My dad—You have been one of the best sources of advice and support my whole life, and I owe so much of who I am today to you. Many of my opinions, interests, and tastes come from you because I always thought you were so cool and wanted to be like you when I grew up.

My brother, Sean—You are one of my favorite people in the whole world and I am so lucky that I got to grow up with you as the biggest constant in my life.

Erik, Rose, Judy, Melissa, Amy, Mark, and Lila—Growing up with you all around was so much fun and I learned a lot from each of you along the way.

Nolan, Joe, Austin, Eva, Hayley, and Ava—Adding you to my family has been a joy, I only wish I got to see you all more often.

My family-in-law, Denny, Angela, Bridget, Conor, Ruby, Sarah, Robbie, Elizabeth, Emma, and Grampie—You all have been so welcoming and made me feel like family right from the start. You are so much fun to be around and I look forward to many more beach trips and family gatherings for years to come.

Kelsey and Remy—I am so glad that I had you both as advisors in graduate school, I have learned so much from each of you. I deeply appreciate that you cared not just about my research, but also about me as a person, and that you were so supportive of everything I did.

Nitya—Thank you for being on my committee, but also for being such a positive part of the astronomy department. We are lucky to have you.

Karen—I don't know you well, which is all the more reason to be grateful that you agreed to take on the work of being on my committee.

Allie—I am so thankful that Kelsey hired you because having another Iowan around made grad school much more fun. I wouldn't have accomplished nearly as much without being able to get on zoom with you at a moment's notice to bounce ideas off of each other and then accidentally end up chatting for hours.

Theo and Grace—Working with you both was an absolute joy and I can't wait to see all the wonderful things you both will do.

Eric Mamajek—Thank you for getting me started in astronomy research and for all of your support throughout my undergrad career. My love of star formation can

easily be traced back to you.

Luke Maud and Magnus Persson—My summer in Leiden was my favorite of undergrad, and a big part of that was having such wonderful advisors.

Shami Chatterjee and Jim Cordes—I learned how cool interferometry was from you, and even though I chose to study star formation, I still think pulsars are the coolest astronomical objects.

All of my research collaborators, near and far—thank you for making my research better, and for being so kind and supportive.

My Iowa friends—We had so many fun times in band, Envirothon, debate, Science Olympiad, playing Battlestar Galactica, and hanging out at El Portal. You all are clearly where I developed my sense of humor and I wish I was in Iowa more often to see you.

Mrs. Fritzell—You were so supportive of me in high school and constantly pushed me to be my best. I developed my love for science in your classroom, and I most certainly would not be where I am today if not for you.

Miss Kimi—You taught me so much about tenacity and discipline and the importance of doing what you love. It is amazing how much the skills I learned in dance class are exactly the ones I needed most to get a PhD in astronomy.

All of my Rochester friends that I met through my classes, Φ KT, Weldon St, capoeira, and random, lucky happenstance—What a joy it was to spend my Rochester years with all of you. I look back on those times with so much fondness, and it's because of each and every one of you.

Louvre—Dance has always been and will always be a big part of my life and a big part of my heart, and I am so fortunate that I got to share that with all of you. Louvre Love <3

The POA and all its inhabitants, especially Ananya and Jon—Thank you for making physics classes bearable. The POA was my real home while in Rochester and no other library can ever compare. I hope that I never think about a fly-ball governor again, but at least I had you all to think about it with.

My Rochester mentors, such as Janet Fogg, Eleanor Oi, Belinda Redden, and my many unforgettable professors—Your guidance and support meant the world to me and I wouldn't have gotten where I am without your invaluable advice, care, and advocacy.

Ruka—You have been an endless fountain of wisdom all the years I've known you. I am so lucky that I had you around to offer advice and wiggle your ears at me.

Steven—You were my first friend in college and I'm so happy that we have stayed close for years after. I love catching up and reminiscing with you about our college shenanigans, and I invariably come away from conversations with you with interesting new ideas and perspectives on life.

Emma—Between physics, dance, and living together, I think I spent about 99.9% of my time in college in your presence, and it was truly lovely. You are probably the person I've been the goofiest around, although part of that was probably the lack of

sleep. Either way, I feel deeply comfortable being myself around you, and that's a rare, wonderful thing.

UVA graduate students, past and present—Thank you to everyone who has ever gone to Nelly's, Escafé, restaurant club, wineries, Astronomy on Tap, Fry's Spring Station trivia, grilled and chilled, played D&D, or hiked with me. Despite everything people say about grad school being hard and not a good time at all, I can honestly say that I have deeply enjoyed my time in Charlottesville because I had you all around, keeping it fun.

Dark Skies, Bright Kids—DSBK has been one of my favorite parts of grad school. Thank you to everyone who made it possible, including everyone who helped out with planning and running clubs (especially during COVID), past graduate students who built it into what it is, assessment team members, all the teachers who have helped us, and most importantly, the students who participated. I really think astronomy is the most exciting when I'm telling a kid about it.

Whitney—There is so much to thank you for, but my biggest thanks is for how caring and supportive you are of everyone you meet.

Xiaoshan, Abby, Jordan, Allison, Robby, David, Hannah, Sean, Trey, Thankful, Riley, Paul, and Katrina—Your friendship has been a critical part of me getting through grad school with most of my mental health intact. You are all wonderful people and it's a joy to know you.

Tom and Harvey—With only a few exceptions that happen several times a day, you two are perfect in every way and the best cats in the world. You have unequivocally made my life better.

Matt—I can't possibly put into words how much you mean to me. You are easily the best thing to have happened to me in grad school and the future looks much brighter with you by my side. Thank you for every time that you've cheered me up, listened to a rant, danced in the kitchen with me, and crouched down to give me a hug. I love you very much.

And lastly, to you, the reader—I was promised that no one would read my thesis. If you're here, that probably means that you either have an actual interest in my research or in me as a person. Either way, I genuinely appreciate your interest and I thank you for reading this much at least.

With much love,
Molly

Table of contents

List of Figures	xiii
List of Tables	xv
1 Introduction	1
1.1 Star Formation	2
1.2 Star Formation in Galaxies	4
1.2.1 Scaling Relations	5
1.2.2 Starburst Galaxies	9
1.2.3 Quiescent Environments	10
1.3 Globular Cluster Formation and Super Star Clusters	11
1.4 Molecular Gas Observations	14
1.4.1 Carbon Monoxide	14
1.4.2 Other Molecular Emission Lines	16
1.5 Calculating Molecular Gas Properties	18
1.5.1 Velocity Dispersion	18
1.5.2 CO-to-H ₂ Conversion	18
1.5.3 Local Thermal Equilibrium	20
1.5.4 Non-LTE Emission Modelling with RADEX	21
1.6 Molecular Gas Relations	22
1.6.1 Size-Linewidth Relation	22
1.6.2 Virial Equilibrium	23
1.7 The Atacama Large Millimeter/submillimeter Array	27
2 The Physical Conditions of a Proto-Globular Cluster	28
2.1 Introduction	28
2.2 Observations	32
2.3 Analysis	35
2.3.1 CO Line Profiles and Cloud Extraction	35
2.3.2 Cloud Mass	37
2.3.3 Expected Continuum Emission	42
2.3.4 X_{CO} Conversion Factor	43

2.3.5	Column Density Radial Profile	45
2.3.6	Cloud Pressure	48
2.3.7	Kinematics of the Local Environment	52
2.3.8	HCN and HCO ⁺	53
2.4	Discussion	59
2.4.1	Internal Structure	59
2.4.2	High Pressure Environment	61
2.4.3	Comparisons to Other Molecular Clouds	63
2.4.4	Tracing Cluster Evolution	64
2.4.5	CO-to-H ₂ Conversion Factor	66
2.4.6	Star Formation Efficiency	66
2.5	Conclusions	68
3	A Comparative Study of Spiral Galaxy Environments	71
3.1	Introduction	71
3.1.1	NGC 1313	77
3.1.2	NGC 7793	78
3.2	Observations	80
3.2.1	NGC 1313 CO(2-1)	80
3.2.2	NGC 7793 CO(2-1)	82
3.2.3	Region Selection	83
3.3	Cluster Catalogs	83
3.3.1	Cluster Counts	86
3.3.2	Cluster Property Distributions	87
3.4	Molecular Gas Structure Decomposition	92
3.4.1	Dendrogram Segmentation	92
3.4.2	Clump Segmentation	93
3.5	Calculating Cloud Properties	93
3.5.1	Mass	93
3.5.2	Velocity Dispersion	96
3.5.3	Radii	96
3.5.4	Derived Quantities	97
3.6	Size-Linewidth Relations	98
3.6.1	Regional Size-Linewidth Relations	103
3.7	Virialization	105
3.7.1	Regional Virialization	107
3.8	Property Distribution Comparisons	109
3.8.1	Global Comparison	109
3.8.2	NGC 1313 Region Comparison	116
3.8.3	NGC 7793 Region Comparisons	122
3.8.4	Inter-Galaxy Region Comparisons	122
3.9	Discussion	126

3.10	Conclusions	129
4	Structure Analysis of the Quiescent Molecular Ridge	133
4.1	Introduction	133
4.2	Observations	137
4.2.1	Molecular Ridge	138
4.2.2	30 Doradus	139
4.2.3	N159	139
4.2.4	N113	141
4.3	Structure Decomposition	141
4.3.1	Dendrogram Segmentation	143
4.3.2	Clump Segmentation	144
4.3.3	Fractal Dimension	145
4.4	Derived Properties	147
4.5	Size-Linewidth Relations	150
4.5.1	Size-Linewidth with CS	153
4.6	Virialization	153
4.7	Variation within the Ridge	160
4.8	Spatial Dependence	164
4.9	Discussion	168
4.10	Conclusions	172
5	Fitting Non-LTE Models to Map Physical Conditions	175
5.1	Introduction	175
5.2	Observations	180
5.2.1	ALMA Data	181
5.2.2	APEX Data	186
5.3	RADEX Fitting	187
5.3.1	Fitting Method	187
5.3.2	Generating Maps of Physical Parameters	195
5.4	Clump Definitions and Properties	198
5.4.1	Clump Definitions	198
5.4.2	Derived Clump Properties	200
5.5	Associated YSOs	202
5.5.1	YSO Selection	202
5.5.2	YSO Fitting	205
5.5.3	YSO Matching	207
5.6	Comparing RADEX Fitting to Other Methods	207
5.6.1	LTE Method	207
5.6.2	X_{CO} Method	209
5.6.3	Diagnostic Line Ratios	212
5.7	Trends with Star Formation	219

5.7.1	Trend with Fitted Density	219
5.7.2	Other Common Star Formation Tracers	220
5.7.3	Discussion of Density Correlation	226
5.8	Conclusions	228
6	Elementary Student Perceptions Of Science	232
6.1	Introduction	232
6.2	Program Background	236
6.2.1	Organization Overview	236
6.2.2	Program Structure	236
6.3	Methods	238
6.3.1	Participants	238
6.3.2	Data Sources	239
6.4	Data Analysis and Results	244
6.4.1	Research Question 1	244
6.4.2	Research Question 2	248
6.4.3	Research Question 3	250
6.5	Discussion	253
6.5.1	Actionable Suggestions	257
6.6	Limitations	258
6.7	Conclusions	259
7	Conclusions	262
8	Appendices	268
A1	Beam Filling Factor in RADEX Fitting	269
A2	Evaluating RADEX Fitting Performance	275
A2.1	Dependence on $^{12}\text{CO}(1-0)$	280
A3	RADEX Fitting Method	282
A4	Data for Chapter 3: LEGUS Galaxy Comparison	284
A5	Data for Chapter 4: Molecular Ridge Structure Analysis	289
A6	Data for Chapter 5: RADEX Fitting and YSO Comparison	297

List of Figures

1.1	Series of star cluster HST images	2
1.2	Star formation schematic from Christensen (2019)	3
1.3	Schmidt-Kennicutt Law from Kennicutt & Evans (2012)	6
1.4	Dense gas - star formation rate relation from Gao & Solomon (2004)	7
1.5	Schmidt-Kennicutt Law measured on sub-kpc scales from Bigiel et al. (2008)	8
1.6	HST image of the Antennae galaxies	9
1.7	HST image of R136	12
1.8	Schematic of super star cluster formation from Johnson (2002)	13
1.9	X_{CO} relation from Bolatto et al. (2013)	20
1.10	Size-linewidth relation from Larson (1981) and Solomon et al. (1987)	24
1.11	Virial balance of molecular clouds from Heyer et al. (2009)	26
1.12	Photo of the Atacama Large Millimeter/submillimeter Array	27
2.1	Image of the Antennae galaxies and panel showing the Firecracker.	32
2.2	Continuum image of non-detection in the Firecracker.	34
2.3	Line profiles of $^{12}\text{CO}(2-1)$, $^{12}\text{CO}(3-2)$, and $^{13}\text{CO}(2-1)$	36
2.4	3-D visualization of the Firecracker.	38
2.5	Integrated intensity and peak intensity of $^{12}\text{CO}(2-1)$ and $^{13}\text{CO}(1-0)$ in the Firecracker.	39
2.6	Surface density map measured in the Firecracker.	41
2.7	Mass estimates based on assumed abundance ratios.	44
2.8	Map and distribution of X_{CO} values.	46
2.9	Radial profiles of the column density in the Firecracker.	49
2.10	Surface density vs. velocity metric, showing virialization and external pressure of the Firecracker as a function of aperture.	51
2.11	Position-velocity diagram showing a bridge feature.	54
2.12	HCN(4-3) and $\text{HCO}^+(4-3)$ in the Firecracker.	55
2.13	Ratios of HCN/HCO^+ and HCO^+/CO in super star clusters.	57
2.14	Schematic showing the evolutionary trend of HCN and HCO^+ emission.	65
3.1	HST images and star cluster maps of NGC 1313 and NGC 7793	72
3.2	$\text{CO}(2-1)$ observations of the two galaxies	81

3.3	Sub-galactic region selection in the two galaxies	84
3.4	Global cluster properties in the two galaxies	89
3.5	Cluster propeties in NGC 1313	90
3.6	Cluster properties in NGC 7793	91
3.7	Size-linewidth fitted slope for both galaxies	101
3.8	Size-linewidth fitted intercept for both galaxies	102
3.9	Size-linewidth fitted slope and intercept for sub-galactic regions . . .	104
3.10	Virialization of clouds in both galaxies	106
3.11	Virialization of clouds in sub-galactic regions	108
3.12	Global distributions of observed properties	110
3.13	Global distributions and derived properties	112
3.14	Corner plot of derived quantities	114
3.15	Bootstrapped KS tests for all regions and properties	117
3.16	Bootstrapped AD tests for all regions and properties	118
3.17	Regional distributions of observed properties in NGC 1313	119
3.18	Regional distributions of derived properties in NGC 1313	121
3.19	Regional distributions of observed properties in NGC 7793	123
3.20	Regional distributions of derived properties in NGC 7793	124
4.1	Map of the LMC with regions of interest highlighted.	136
4.2	Integrated intensity of $^{13}\text{CO}(1-0)$ and $\text{CS}(2-1)$ in the Molecular Ridge.	138
4.3	Integrated intensity of $^{13}\text{CO}(2-1)$ and $\text{CS}(2-1)$ in 30 Dor.	140
4.4	Integrated intensity of $^{13}\text{CO}(1-0)$ in N159.	142
4.5	Integrated intensity of $^{13}\text{CO}(1-0)$ in N113.	142
4.6	Dendrogram of the Molecular Ridge.	144
4.7	Perimeter-area fractal dimension in LMC regions.	146
4.8	Size-linewidth relation in LMC regions with fitted power laws.	152
4.9	Size-linewidth relation in LMC regions with only the intercept of the power law fitted.	154
4.10	Size-linewidth relation for $\text{CS}(2-1)$ structures.	155
4.11	Surface density vs. velocity metric to examine the virialization of clouds in LMC regions.	157
4.12	Distribution of α_{vir} values in the Ridge and 30 Dor.	158
4.13	Distribution of surface densities in the Ridge and 30 Dor.	159
4.14	Map of the Molecular Ridge colored by each structure's α_{vir} parameter.	162
4.15	Histograms of the α_{vir} parameter by region in the Ridge.	163
4.16	Size-linewidth relation of different regions of the Molecular Ridge.	165
4.17	Values of α_{vir} in the Ridge plotted against distance to potential influences.	167
5.1	Map of the LMC and the Molecular Ridge.	179
5.2	Emission line maps in the Molecular Ridge.	182
5.3	Low-resolution map of $^{13}\text{CO}(1-0)$ used in model-fitting.	188

5.4	Example line profiles of $^{12}\text{CO}(1-0)$, $^{12}\text{CO}(2-1)$, $^{13}\text{CO}(1-0)$, and $^{13}\text{CO}(2-1)$.	189
5.5	Example of a RADEX model-fitting probability distribution from representative data.	193
5.6	RADEX-fitted maps of N_{CO} , T_{kin} , and n_{H_2} in the Molecular Ridge.	196
5.7	Diagram of clumps identified in the Molecular Ridge.	199
5.8	Positions of embedded YSOs in the Molecular Ridge.	203
5.9	Derived X_{CO} values from RADEX-fitted N_{CO}	210
5.10	Volume density fitted by RADEX plotted against ratios of ^{13}CO to ^{12}CO .	213
5.11	Temperature and density against ratios of upper and lower transitions of ^{12}CO and ^{13}CO	215
5.12	Density fitted by RADEX plotted against dense gas ratios.	218
5.13	Trends between YSOs and the RADEX-fitted volume density.	221
5.14	Trends of YSOs and n_{H_2} with other observational metrics.	225
6.1	Likert scale question example	241
6.2	Before- and after-club Likert scale responses	245
6.3	Likert scale responses by demographic	247
6.4	Fraction of “true” responses to NOS statements	249
8.1	Example of a probability distribution with beam filling factor fitted.	270
8.2	Example of a probability distribution from poorly-detected data.	271
8.3	Example of a probability distribution from fitting the ratios of the line intensities rather than absolute intensities.	273
8.4	Line-of-sight path length of the fitting results with varying beam filling factors.	274
8.5	Example of how well we recover n_{H_2} as a function of T_{kin}	276
8.6	An example of how precise our fitting of n_{H_2} is as a function of T_{kin}	277
8.7	The accuracy and precision of N_{CO} as a function of N_{CO}	278
8.8	Offsets from the true value of N_{CO}	279
8.9	A comparison of how N_{CO} is fit when three lines are included instead of four.	281
8.10	Offsets from the true value of N_{CO} when three lines are included instead of four.	281

List of Tables

2.1	ALMA Band 6 and Band 7 Observations of the Antennae	34
2.2	Data cube parameters for detected transitions in the Firecracker region	35
2.3	Molecular Cloud Measured Properties	38
2.4	Possible values for the mass ($10^6 M_{\odot}$)	42
2.5	Molecular Cloud Derived Properties	52
2.6	Integrated Fluxes of Emission Lines	56
3.1	Properties of NGC 1313 and NGC 7793	75
3.2	ALMA $^{12}\text{CO}(2-1)$ Observations	82
3.3	Number of cloud structures and clusters in each galaxy and region . .	94
3.4	Fitted slopes and intercepts for size-linewidth relations	106
3.5	Boostrapped two-sample KS and AD test results between NGC 1313 and NGC 7793 global properties	114
3.6	Comparison of observed properties between environments	127
4.1	Observations used in this analysis	137
4.2	Results of dendrogram and clump segmentation, and fractal dimension, D_2 , for each region	145
4.3	K-S test p-values of α_{vir} distributions in pairings of regions within the Ridge, derived from $^{13}\text{CO}(1-0)$	161
5.1	Observations used in this analysis	181
5.2	Comparison of different methods of determining mass and temperature.	207
6.1	Data source summary	238
6.2	Before- and after-club survey questions	242
6.3	Daily survey questions	243
6.4	Mann-Whitney U test results for demographic differences in science confidence	248
6.5	Fraction of “correct” responses to NOS statements	250
6.6	Odds of daily activities being correlated with stronger science identity	252
8.1	Comparison of RADEX fitting methods	282

8.2	Catalog of NGC 1313 dendrogram properties	285
8.3	Catalog of NGC 1313 clump properties	286
8.4	Catalog of NGC 7793 dendrogram properties	287
8.5	Catalog of NGC 7793 clump properties	288
8.6	Catalog of Molecular Ridge dendrogram properties	290
8.7	Catalog of Molecular Ridge clump properties	291
8.8	Catalog of 30 Dor dendrogram properties	292
8.9	Catalog of 30 Dor clump properties	293
8.10	Catalog of N159 dendrogram properties	294
8.11	Catalog of N113 dendrogram properties	295
8.12	Catalog of Molecular Ridge CS(2-1) dendrogram properties	296
8.13	Integrated Line Fluxes of Clumps	298
8.14	Derived Clump Properties	299
8.15	Fitted YSO Properties	300

Chapter 1

Introduction

In a galaxy in our universe, there lived a star. Not a massive, irregular, merging galaxy, filled with violent cloud collisions and supernovae feedback, nor yet a red, dead, elliptical galaxy with no gas left to form stars from: it was a spiral galaxy, and that means comfortable star formation.

Most stars form in clusters, but these clusters range from small, sparse open clusters that disperse soon after formation, to massive, dense globular clusters that survive for billions of years (examples shown in Figure 1.1). A lot of work has gone into understanding how individual stars form, but we still do not have a clear picture of what conditions determine the cluster environment in which stars form. We know that different galactic environments are home to different types of clusters. In this work, I focus on understanding how the physical conditions of the gas in those galactic environments affect what kinds of star clusters form.



Fig. 1.1.— Series of Hubble Space Telescope (HST) images of star clusters. *Top, left to right:* NGC 290; NGC 3603; NGC 602; Trapezium cluster; *Bottom, left to right:* Westerlund 2; Pleiades; R136; M15.

1.1 Star Formation

Stars form from cold, dense clouds of gas and dust. These clouds are made up primarily of hydrogen that has gotten cold enough that the hydrogen atoms pair up and create a molecule: H_2 . Because the hydrogen is now in a molecular state, we call this gas molecular gas, and we call the clouds molecular clouds¹.

We still do not fully understand how these molecular clouds themselves are formed (Chevance et al. 2020a), but large structures of molecular gas build up in galaxies and we know that they have complex, hierarchical structures. This means that rather than smooth spheres of gas with similar properties throughout, the molecular clouds have structure and regions of higher densities. As we study molecular clouds with greater resolution, we find those structures themselves have structure, and so on.

¹Gas that is primarily made up of single hydrogen atoms is called atomic gas.

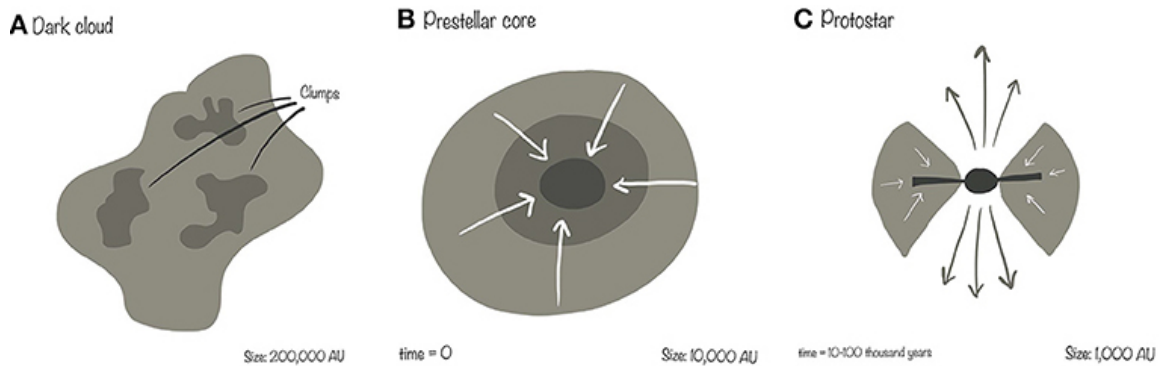


Fig. 1.2.— Schematic showing the initial stages of molecular cloud collapse and star formation. Image adapted from Christensen (2019).

The largest of these structures are referred to as giant or super-giant molecular clouds (GMCs or SGMCs). Astronomers will use terms like “clouds” or “clumps” to refer to substructure within the GMCs, though there is no set definition for these terms. At higher resolution, we see the molecular gas form long, filamentary structures. The term “core” is usually reserved for the smallest, highest-density structures within GMCs that are the sites where individual stars form (see Figure 1.2).

As molecular clouds grow and become more dense, they feel a stronger and stronger gravitational pull of each molecule on all the other molecules that make up the cloud. This gravitational pull is called self-gravity. When this gravitational pull becomes strong enough, the cloud starts to collapse in on itself, with all of the material falling inwards and becoming more and more dense. At the center of this collapse, a protostar is formed. This protostar will continue accreting, growing denser and hotter until it is finally hot enough that is able to begin fusing hydrogen, at which point it is considered a “main sequence” star.

As early as the protostar stage, the molecular material that created the star begins to be dispersed. By the time the star begins fusion, it has usually cleared out all of this material. Since it can be difficult to determine which of the earliest stages of star

formation an object is in, astronomers use the term “young stellar objects” (YSOs) to refer to objects that may be protostars through pre-main sequence stars that are still clearing their natal material.

1.2 Star Formation in Galaxies

The majority of all star formation in the local universe takes place in disk galaxies like the Milky Way (Brinchmann et al. 2004). In these galaxies, stars and gas orbit a central supermassive black hole in a large circular plane. These galaxies usually have spiral arms that act like cosmic traffic jams. As stars and gas orbit the galaxy, they get caught up in these spiral arms, but ultimately move through the arms.

While in the spiral arms, the molecular gas conglomerates into large GMCs that then collapse and form stars (Dobbs & Pringle 2013), meaning that spiral arms are the sites of most of the star formation in spiral galaxies. Previous studies have shown that the molecular clouds in spiral arms have higher surface densities and pressures than the clouds between the spiral arms in the interarm regions (Colombo et al. 2014).

The most detailed studies of star formation focus on stars forming in the Milky Way because of how close they are, allowing us to achieve extremely high resolution. The Milky Way is a fairly typical spiral galaxy in a lot of ways (Bland-Hawthorn & Gerhard 2016), although it is forming stars more slowly than we would expect based on its mass (Mutch et al. 2011).

Most of the young star clusters forming in the Milky Way are forming what we call “open clusters”, meaning that the stars in these clusters are not gravitationally bound to each. These clusters typically have masses between 10 and 1000 M_{\odot} ² (Portegies Zwart et al. 2010). Because they do not have the gravitational energy to hold them-

² M_{\odot} denotes a solar mass - the mass of the Sun. It is the most common unit of mass in astronomy.

selves together, the stars will quickly drift apart. The Pleiades is a famous example of an open star cluster in the Milky Way.

1.2.1 Scaling Relations

To better understand a wider range of star formation than the Milky Way can offer, we turn to other galaxies. The trade-off, however, is a loss of resolution and sensitivity. In galaxies outside of our Local Group³, we cannot resolve individual stars or the smallest star clusters. To characterize the star formation happening in other galaxies, astronomers turn to observed laws called scaling relations that relate galactic-scale properties to one another.

One of the most famous of these scaling relations in the field of star formation is the Schmidt-Kennicutt Law (also referred to as the Kennicutt-Schmidt Law or Schmidt Law; Schmidt 1959; Kennicutt 1998). The law relates the surface density of all the gas in the galaxy (both atomic and molecular) to the surface density of the star formation rate (SFR) in the galaxy over many orders of magnitude (Figure 1.3).

Because these properties are measured for the whole galaxy where the scale height or depth of the galaxy is constant, this indicates a close relation between the density of the molecular gas in the galaxy and the density of star formation. Since stars form from dense molecular gas, it is not surprising that such a relation exists. Kennicutt (1998) found that these two quantities are not linearly related, but rather are related by a power law with a slope of 1.4 ± 0.15 . The exact slope of this power law depends on assumptions about how to measure the mass of the molecular gas (Narayanan et al. 2011).

³The Local Group is the group of gravitationally bound galaxies that includes the Milky Way. Other notable members include the Andromeda Galaxy, the Triangulum Galaxy, the Large and Small Magellanic Clouds, and many other dwarf galaxies.

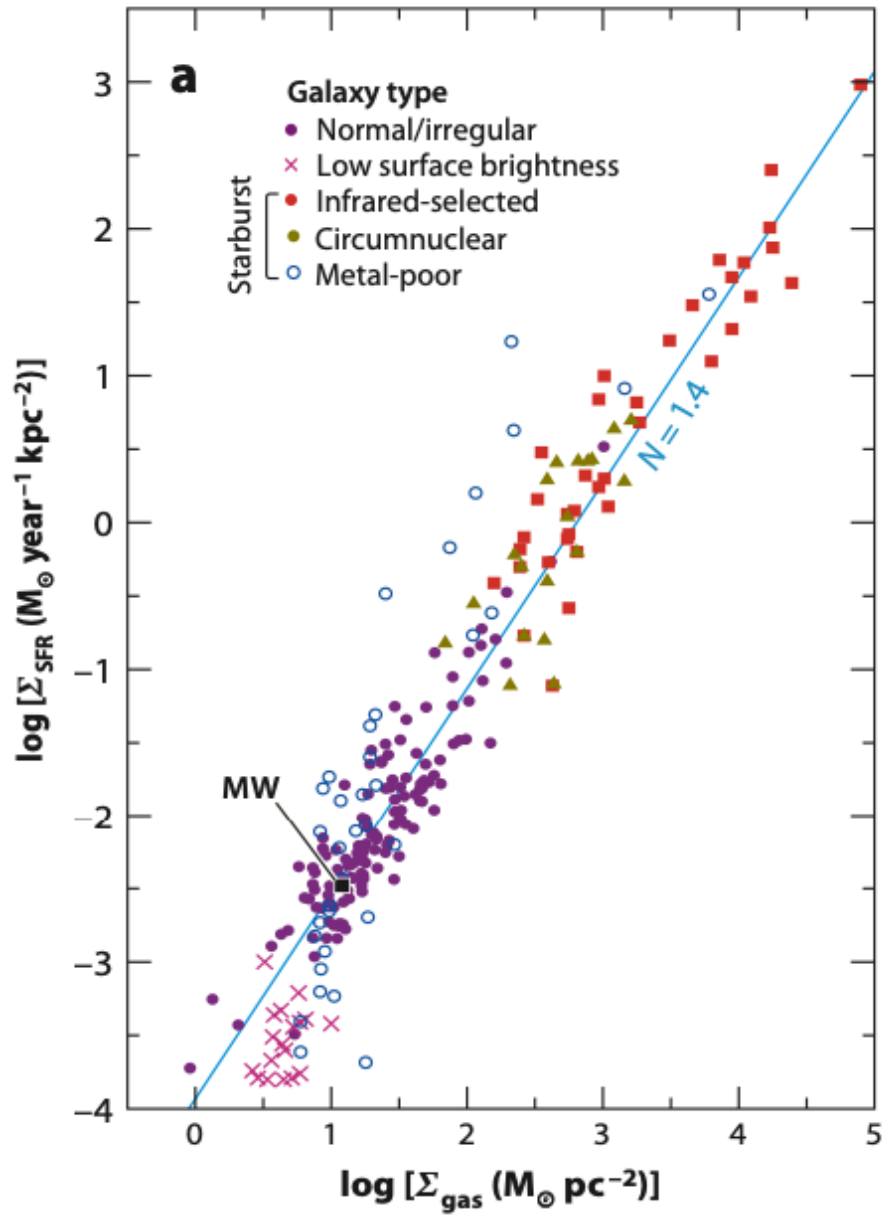


Fig. 1.3.— Relation between the globally-averaged star formation rate surface density and the surface density of the gas in a galaxy, referred to as the Schmidt-Kennicutt Law. Figure from Kennicutt & Evans (2012).

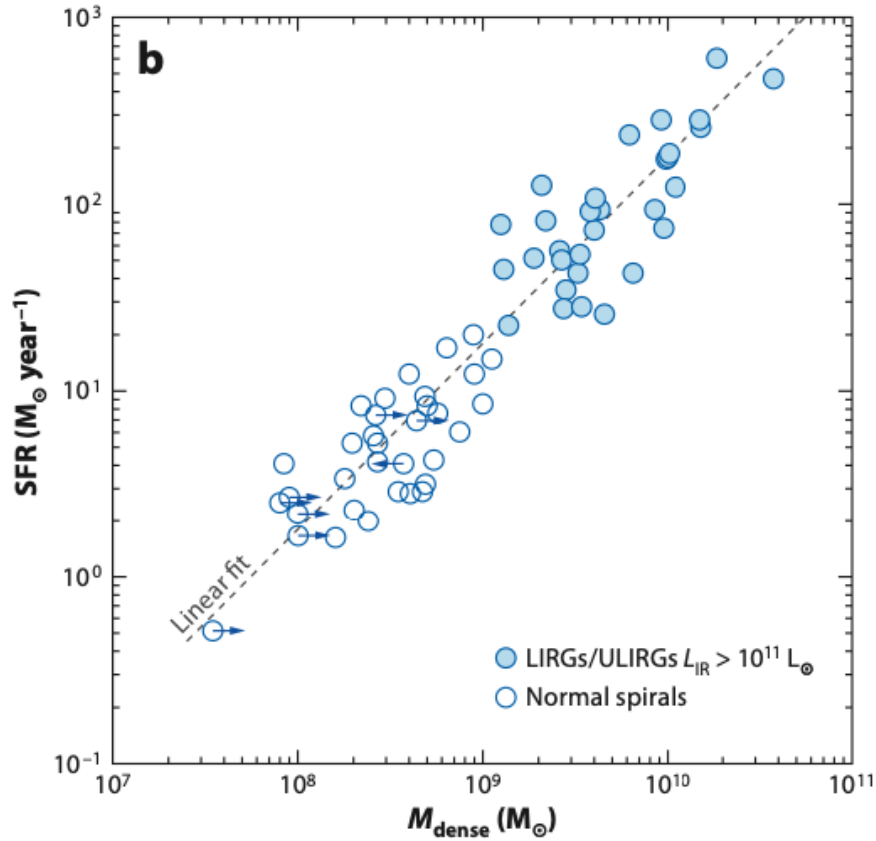


Fig. 1.4.— Relation between the total star formation rate and the total amount of dense gas as traced by HCN in galaxies. Figure from Kennicutt & Evans (2012), which was adapted from Gao & Solomon (2004).

Similarly, Gao & Solomon (2004) found a close correlation between the total star formation in a galaxy and the total mass of the dense gas in the galaxy (Figure 1.4). In this case, Gao & Solomon (2004) use the molecule HCN to trace only the gas that is part of the dense inner structures of the molecular clouds. I will discuss molecular tracers including HCN in more detail in Section 1.4.2. Unlike the Schmidt-Kennicutt Law, this relation follows a linear trend, suggesting a more direct relation between the two properties.

The Schmidt-Kennicutt Law holds less well as we begin resolving the internal

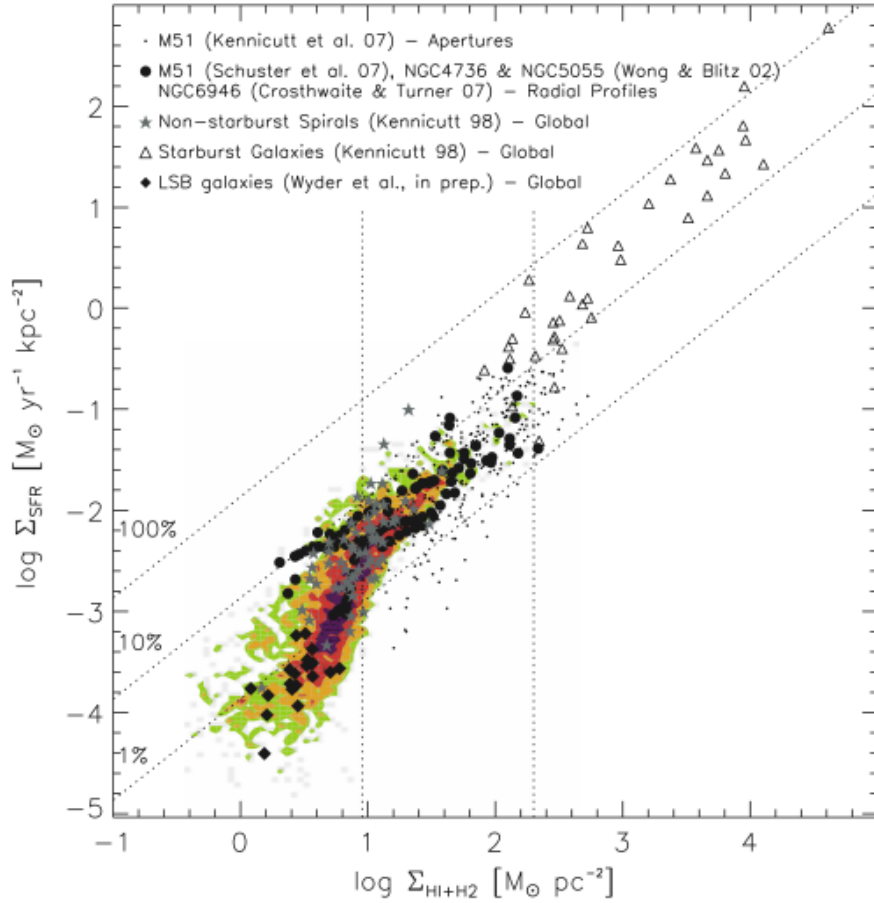


Fig. 1.5.— Relation between the star formation rate surface density and the surface density of the gas measured at sub-kpc scales in nearby galaxies showing a turnover at low density. The diagonal lines show linear relations of constant star formation efficiency. Figure from Bigiel et al. (2008).

structure of galaxies. There appears to be a turnover at lower gas surface densities where the power law becomes much steeper (Figure 1.5), and Bigiel et al. (2008) find that the slope relating these two properties varies significantly between and within galaxies. While this relation has excellent power at understanding global galaxy properties, it is more limited as we begin to achieve higher resolution in extragalactic studies.



Fig. 1.6.— HST image of the merging Antennae galaxies, a proto-typical starburst galaxy undergoing a major interaction. It is currently forming thousands of SSCs, making it an excellent laboratory for studying SSC formation.

1.2.2 Starburst Galaxies

Starburst galaxies are galaxies that are forming stars at extremely high rates. Where the Milky Way is forming stars at a rate of approximately $1 M_{\odot}/\text{yr}$ (Robitaille & Whitney 2010), starburst galaxies are forming stars at rates of hundreds or even thousands of M_{\odot}/yr . The primary reason that galaxies go through a starburst phase is because they are merging or interacting with another galaxy. The Antennae galaxies (Figure 1.6) are a quintessential example of a pair of merging galaxies undergoing a starburst.

The most actively star forming of the starburst galaxies are usually caused by two gas-rich massive galaxies merging with one another. This collision causes the GMCs to collide and compress, making them more likely to collapse into stars. Smaller mergers and interactions between galaxies of any size can still cause starbursts, however.

The frequency of these galactic collisions and subsequent starbursts has not been constant through cosmic history. By studying distant galaxies, we see light that has taken billions of years to reach us. This means that as we look far away, we look back in time. Madau et al. (1998) measured the star formation rate of galaxies throughout time and determined that 10 billion years ago (at a redshift of $z \sim 2$), the universe was forming stars approximately ten times more rapidly than today. This was likely due to a greater frequency of galaxy collisions as smaller galaxies merged to become the massive galaxies we see today (Conselice 2006).

1.2.3 Quiescent Environments

Just as there are starburst environments that are creating more stars than expected, there also environments that are creating fewer stars than expected. This lack of star formation is much less understood than the reasons for a burst of star formation.

One of the most well-known examples of a region with surprisingly little star formation is the center of the Milky Way, known as the Galactic Center. This part of our galaxy has a high density of molecular gas and is forming several massive clusters (Portegies Zwart et al. 2010), but based on scaling relations like the Schmidt-Kennicutt Law, we would expect the region to be forming significantly more stars (Kauffmann et al. 2017).

There is another region in our Local Group that also is surprisingly quiescent—the Molecular Ridge in the Large Magellanic Cloud (LMC). This region contains nearly a third of all the molecular gas in the galaxy, and yet is forming almost no massive stars. In this thesis, I discuss observations of the molecular gas in the Ridge to better understand what gas conditions cause not just starbursts, but also quiescence.

1.3 Globular Cluster Formation and Super Star Clusters

Globular clusters are dense, bound star clusters that are commonly seen in every massive galaxy (Harris et al. 2013). The globular clusters we see in the Milky Way are all ancient - nearly as old as the Galaxy itself. Furthermore, theoretical predictions suggest that they have a high mortality rate, with potentially $\lesssim 1\%$ surviving to 10 billion years old (Fall & Zhang 2001). This suggests then that globular cluster formation was abundant in the early universe when the Milky Way formed, but for some reason the local galaxies have long since stopped forming them. Understanding how globular clusters form can therefore probe the star-forming conditions of the early universe during galaxy formation and evolution.

With out current technology, we cannot directly observe early universe globular cluster formation. Galaxies that far away (and so long ago) are too far for us to resolve any galactic structure, let alone individual star forming regions. Fortunately, we have discovered a similar type of star formation happening nearby in the form of “super star clusters” (SSCs; O’Connell et al. 1994). These young, dense clusters have many of the same properties as globular clusters, implying that SSCs are likely very similar to the progenitors of the ancient globular clusters we are familiar with (McLaughlin & Fall 2008).

All of these SSCs have been discovered in starburst environments. The Antennae galaxies is home to thousands of SSCs (Whitmore et al. 2010), with many more still actively forming. By studying SSC formation in starburst galaxies, we can better understand what conditions are necessary for them to form and how starburst galaxies today are recreating the conditions of the early universe. The closest known SSC is



Fig. 1.7.— HST image of R136, a super star cluster in the 30 Doradus region of the LMC. It is the most massive young star cluster in the Local Group.

R136 in the 30 Doradus (30 Dor) region of the LMC (shown in Figure 1.7), although with a mass of $8.7 \times 10^4 M_{\odot}$, it is on the small side for SSCs, which typically have masses $> 10^5 M_{\odot}$.

So far, SSCs have primarily been observed at optical and ultraviolet wavelengths, which are only visible after stars have formed and at least partially cleared out their surrounding natal material (see Figure 1.8). More recently, these studies have extended to the radio, where we can observe newly formed SSCs that are still deeply embedded in the surrounding gas cloud (e.g. Johnson & Kobulnicky 2003; Johnson


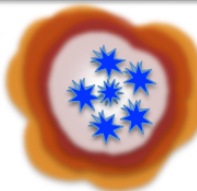
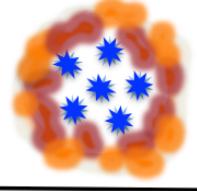

Evolutionary State		Observable Wavelengths
Proto Cluster		Millimeter - Infrared
Natal Cluster		Radio - Infrared
Emerging Cluster		Infrared - Optical
Adolescent Cluster		Ultraviolet - Infrared

Fig. 1.8.— Schematic showing the stages of star cluster formation and emergence and the wavelengths at which each stage can be observed. Figure from Johnson (2002).

et al. 2009; Costa et al. 2021). However, to understand the initial conditions that allow SSCs to form, we need to observe earliest stages of formation by studying the molecular gas itself at millimeter wavelengths, before any stars have formed and begun disrupting the natal environment. This stage of formation is expected to be short-lived, lasting only $\sim 0.5 - 1$ million years (Johnson et al. 2015), making these objects rare and difficult to find.

1.4 Molecular Gas Observations

1.4.1 Carbon Monoxide

Atoms and molecules behave differently from matter at macroscopic scales. They follow the rules of quantum mechanics. The primary idea behind quantum mechanics is that atoms and molecules can become energized, but they can only absorb and emit specific amounts of energy at a time—their energy is quantized. For example, a hydrogen atom can emit exactly 13.6 eV of energy, or 3.4 eV, or 1.5 eV, and so on.

When atoms and molecules emit this specific quanta of energy as light, that amount of energy corresponds to a specific wavelength and frequency of light. This means that if you split light up by wavelength or frequency, you will see bright lines at the wavelengths that correspond to abundant atoms and molecules. Some of the brightest lines that molecules in space emit come from them rotating. This is called rotational spectroscopy.

Molecular gas is primarily made up of molecular hydrogen, but since H_2 is symmetric and made up of two of the same atom, it has no electric dipole moment. It still has rotational emission lines from its quadrupole moment, but those require higher temperature to excite and are relatively faint. This makes it extremely difficult to directly observe the H_2 , even though it is abundant.

Instead we observe the second-most abundant molecule: carbon monoxide, or CO. CO is made up of a carbon atom and an oxygen atom, and so is not symmetric and has bright rotational emission lines. Some of the most common lines that I use in this thesis are transitions between its first and ground excitation states, denoted CO $J = 1 \rightarrow 0$ or shortened to CO(1-0). This line emits at a frequency of 115.271 GHz. I also often observe CO(2-1) at a frequency of 230.538 GHz and CO(3-

2) at 345.796 GHz. These frequencies correspond to wavelengths of 2.6 mm, 1.3 mm, and 0.87 mm.

The brightness of these lines depends on the temperature and density of the gas, as well as on how many CO molecules are along the line-of-sight that we observe, called the column density. The temperature and density determine how often and how hard the molecules bump into each other, including how often CO bumps into H₂ molecules, which is the primary way that CO molecules gain the energy necessary to emit energy. This is called collisional excitation. The temperature and density then determine how often each molecule emits energy. Each individual molecule emits a single photon with energy corresponding to the transition, so the line gets brighter as there are more molecules emitting.

After a photon gets emitted by a molecule, it still needs to travel out of the cloud before we can observe it. However, another CO molecules could absorb that photon if they collide. The likelihood that a photon will get absorbed, or the fraction of light that gets observed per unit length, coefficient, $\alpha - \nu$, where the subscript ν implies that the value depends on the frequency of the light. A photon with a frequency that corresponds to the CO line frequency is much more likely to be absorbed than a photon with a different frequency. We can integrate over this absorption coefficient along a line of sight, and this integral is defined as the optical depth, τ_ν .

If the optical depth is much less than 1, the cloud is considered optically thin, which means that light can easily escape the cloud. This makes it easier to determine how many molecule along the line of sight there are because almost every time a molecule emits, we see the photon from it. If the optical depth is much more than 1, the cloud is considered optically thick, which means that the cloud is opaque and we only see light that comes from the outer layer of the cloud, where photons are

most likely to escape. This makes it impossible to determine the number of molecules along the line of sight. However, when the CO is optically thick we know that the brightness of the line we measure is closely matched instead to how often the CO molecules emit, which is closely matched to the temperature of the gas. Optically thin and thick molecular tracers are therefore both important to understanding cloud properties.

To see CO emission lines, the gas needs to be warm and dense enough that there are sufficient collisions to keep the molecules excited. The necessary temperature for the gas depends on which transition we are interested in. For CO(1-0) the excitation energy corresponds to a temperature of 5.5 K, for CO(2-1) it is 16.6 K, and for CO(3-2) it is 33.2 K. As the gas gets hotter, higher transitions become brighter as the molecules more regularly have the high energies necessary to be in upper excited states.

The necessary density depends on the temperature of the gas, but for a typical molecular gas temperature of 30 K, the critical density of CO(1-0) where the excitation rate is equal to the de-excitation rate is approximately $2.2 \times 10^3 \text{ cm}^{-3}$ (Yang et al. 2010; Bolatto et al. 2013). However, CO is typically so optically thick in molecular clouds that the photons get trapped and the critical density is effectively reduced to $< 10^2 \text{ cm}^{-3}$ (Shirley 2015).

1.4.2 Other Molecular Emission Lines

CO Isotopologues

The CO molecule I have discussed thus far is composed of one carbon atom with 6 protons and 6 neutrons for a total of 12 nucleons, and one oxygen atom with 8 protons and 8 neutrons for a total of 16 nucleons. However, some atoms called isotopes have

additional neutrons in their nucleus that add mass without adding additional electric charge and so the element remains the same. Atoms and isotopes are denoted with the total number of nucleons (^{12}C is how you would explicitly write standard carbon). Molecules can be made with these isotopes, which are themselves called isotopologues, also denoted with the total number of nucleons in each atom of the molecule. If the number of nucleons is not written, it is assumed to be the standard version of the atom with the same number of protons and neutrons.

The most common isotopologue of CO is ^{13}CO , CO made with ^{13}C and ^{16}O . ^{13}CO is 50-100 times less abundant than ^{12}CO (Nikolić et al. 2007). I use $^{13}\text{CO}(1-0)$ and $^{13}\text{CO}(2-1)$ lines throughout this thesis.

Dense gas tracers

Other molecules besides CO and its isotopologues also have rotational emission lines. These molecules have different excitation parameters and so their emission can be used to trace different physical and chemical conditions in the molecular gas, such as tracing where the gas is dense, hot, or experiencing shock waves.

HCO^+ , HCN, and CS are all molecules commonly used as “dense gas tracers” because of their high critical densities relative to CO. At a temperature of 20 K, their critical densities for the (1-0) transition are $4.5 \times 10^4 \text{ cm}^{-3}$, $3.0 \times 10^5 \text{ cm}^{-3}$, and $1.1 \times 10^4 \text{ cm}^{-3}$, respectively (Shirley 2015). Their excitation energies for the first excitation state are 4.3 K, 4.3 K, and 2.4 K, respectively.

1.5 Calculating Molecular Gas Properties

1.5.1 Velocity Dispersion

One of the benefits of using spectroscopy to observe molecular emission is that it provides us with an additional dimension to observe our data. We have two spatial dimensions that are the image we see on the sky, but we also have a frequency dimension. When molecules emit light, they emit a specific frequency. But if the molecules are moving towards us or away from us, that motion will change their frequency slightly. This effect is called a Doppler shift: objects moving towards us are blueshifted and objects moving away are redshifted.

In nearby galaxies where I study molecular gas, the absolute velocity of the gas moving towards or away from us is usually not physically interesting. What *is* interesting is measuring how much the gas in a molecular cloud is moving around with random large-scale motions called turbulence. The gas will have a distribution of different velocities and we can measure the width of this distribution to determine the velocity dispersion or linewidth. This metric tells us about how much kinetic energy the molecular cloud has. We know that most of the turbulence in the molecular gas is supersonic, meaning that the gas is moving around faster than the speed of sound in the gas (Elmegreen & Scalo 2004, and references therein).

1.5.2 CO-to-H₂ Conversion

The brightness of CO lines depends on the kinetic temperature, H₂ volume density, and CO column density of the gas. However, most molecular gas in galaxies has similar temperatures and volume densities, especially when averaged over GMCs. This means that at low resolutions, the brightness of CO depends almost exclusively

on the column density of CO. The abundance of CO is also fairly constant among environments with similar metallicities⁴, which means that the brightness of CO is closely matched to the total molecular gas mass (Figure 1.9). This relation has been carefully calibrated to measure a CO-to-H₂ conversion factor, called X_{CO} or α_{CO} . X_{CO} is defined as

$$N_{\text{H}_2} = X_{\text{CO}} \times W_{\text{CO}}$$

where N_{H_2} is the column density of H₂ in units of cm⁻² and W_{CO} is the total intensity of CO(1-0) measured in units of K km s⁻¹. The factor α_{CO} is defined as

$$M_{\text{gas}} = \alpha_{\text{CO}} \times L_{\text{CO}}$$

where M_{gas} is the total mass of gas in M_{\odot} and L_{CO} is the total luminosity of CO(1-0) in units of K km s⁻¹ pc⁻². The most commonly used value of X_{CO} is $2 \times 10^{20} \text{ cm}^{-2} (\text{K km/s})^{-1}$ and the corresponding value for α_{CO} is $4.3 M_{\odot} (\text{K km s}^{-1} \text{ pc}^{-2})^{-1}$ (Bolatto et al. 2013).

This conversion factor is extensively used to determine the molecular gas mass from extragalactic observations of CO. However, using it requires caution because this relation relies heavily on the assumption that the excitation conditions and abundance of CO are similar to the environments in which it was calibrated, primarily the Milky Way and nearby galaxies. Notably, starburst environments are known to have brighter CO emission relative to their gas masses, and so a factor of $X_{\text{CO}} = 0.5 \times 10^{20} \text{ cm}^{-2} (\text{K km/s})^{-1}$ is used instead. Recent efforts have been made

⁴The amount of metal enrichment in the gas, where by metals astronomers mean any element besides hydrogen and helium. Primordial gas after the Big Bang was made up of only hydrogen and helium, but over time stars have fused heavier elements in their cores and then spread those elements into the surrounding medium through supernovae.

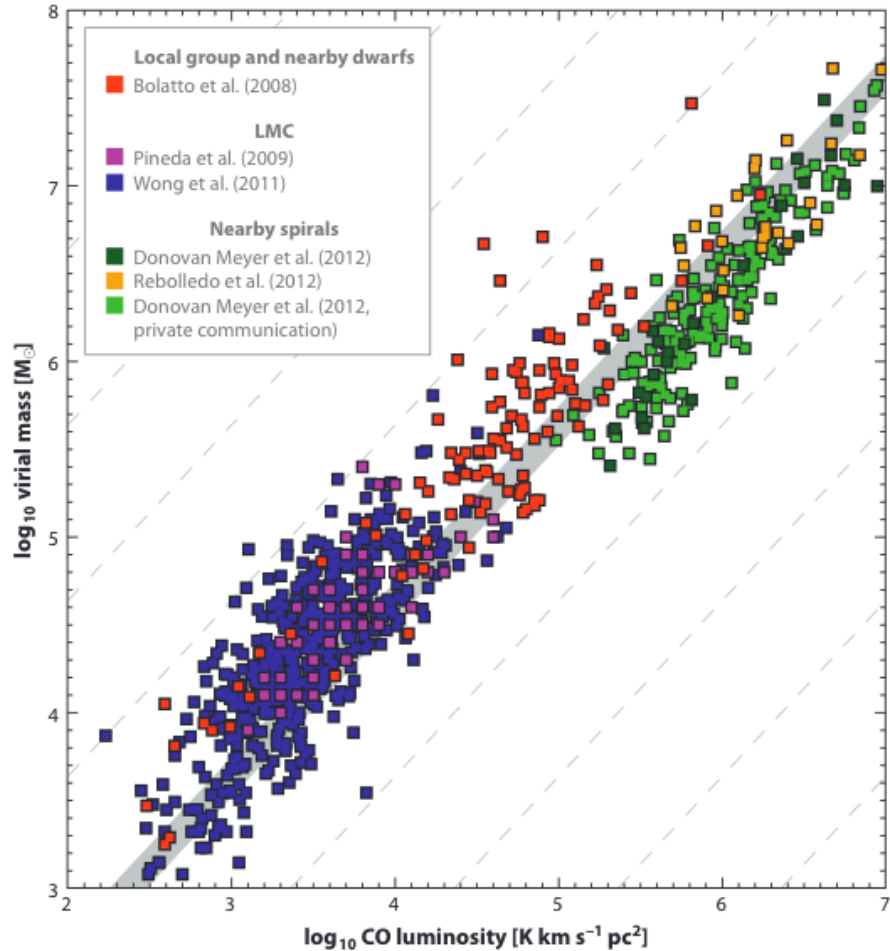


Fig. 1.9.— Relation between a molecular cloud’s CO(1-0) luminosity and virial mass. This relation has been used to calibrate a CO-to- H_2 conversion factor, X_{CO} . Figure from Bolatto et al. (2013).

to make more careful calibrations of X_{CO} that take into account the metallicity of the gas and the brightness of the CO itself as an indication of excitation conditions (Schruba et al. 2012; Bolatto et al. 2013; Hunt et al. 2015; Gong et al. 2020).

1.5.3 Local Thermal Equilibrium

To better account for variations in CO excitation, especially as we move to higher resolutions that observe the clumps within GMCs, it is better to avoid the assumption

of an X_{CO} factor. One way to do this is to assume that the gas is in local thermodynamic equilibrium (LTE). Here we define LTE as when the distribution of molecules in upper and lower energy states can be perfectly described by a Boltzmann distribution with constant excitation temperature, T_{ex} , and that the gas is sufficiently dense that the T_{ex} is equal to the kinetic energy, T_{kin} .

This method requires observations of an optically thick line, most commonly ^{12}CO , an optically thin line, usually an isotopologue such as ^{13}CO , and an assumption about the abundance ratio between the two. The equations used to derive the CO column density and temperature are discussed in detail in Chapter 2, based on equations from Mangum & Shirley (2015). With a further assumption of the CO abundance relative to H_2 , one can then determine the total mass of the cloud, often referred to as M_{LTE} .

This method can conveniently determine the mass and temperature of the molecular gas with observations of only two molecular lines. It also accounts for variations in the excitation temperature along different sightlines and so is an improvement over assuming an X_{CO} factor. However, we know that molecular clouds are often not in LTE. Also, the volume density of the gas drops out of the equations when we assume LTE, so this method does not allow us to calculate the gas density.

1.5.4 Non-LTE Emission Modelling with RADEX

To avoid assumptions that the gas is in LTE, we need account for the radiative transfer of the emitted photons through the molecular gas. This requires sophisticated modeling and is computationally expensive. However, van der Tak et al. (2007) developed a publicly available non-LTE radiative transfer code called RADEX that avoids some of the extensive computations of radiative transfer by instead calculating the escape probability of a photon emitted by a molecule.

RADEX can determine the intensity of any molecular transition line that collisional rates are known for (usually from the Leiden Atomic and Molecular Database; Schöier et al. 2005) based on input background temperature, kinetic temperature, H₂ volume density, and the column density and linewidth of the molecular species in question. With output from these models, we can fit the observed intensity of multiple molecular emission lines to determine the temperature, volume density, and column density of the gas.

Fitting RADEX models allows us to avoid assuming the gas is in LTE and also enables us to determine the volume density of the gas. The drawbacks are that this method of determining the gas's physical conditions requires a lot more observations and computation than other methods. In Chapter 5 I discuss my process of fitting RADEX models in detail.

1.6 Molecular Gas Relations

1.6.1 Size-Linewidth Relation

With observations of a molecular emission line for a cloud (usually CO), we learn the spatial extent of the cloud as well as its velocity dispersion/linewidth. Early studies of molecular clouds in the Milky Way showed that there is a power law relation between the size and linewidth of the cloud of the form

$$\sigma_v = a_0 R^{a_1}$$

where σ_v is the linewidth, R is the radius or size, and a_0 and a_1 are values fit to the relation. The original work on this relation by Larson (1981) fit values of $a_0 = 1.1$ and $a_1 = 0.38$, though later Solomon et al. (1987) performed a broader survey of clouds

in the disk of the Milky Way to measure $a_0 = 1.0 \pm 0.1$ and $a_1 = 0.5 \pm 0.05$ (see Figure 1.10). These latter values are the most commonly cited for the size-linewidth relation.

This relation has been used to study and understand molecular clouds at many size scales and in different environments. The slope of the power law relation (a_1) is related to the energy cascade - how kinetic energy is transferred among the different size scales within a cloud. The intercept of the power law relation (a_0) is related to the total amount of kinetic energy in the cloud. Many different fitted values have been measured in different environments and with different molecular tracers, and there is often a lot of scatter in the relation (e.g. Goodman et al. 1998; Oka et al. 2001; Nayak et al. 2016; Wong et al. 2019; Indebetouw et al. 2020; Wong et al. 2022; Finn et al. 2022)

1.6.2 Virial Equilibrium

In addition to measuring the size and linewidth, we can also determine the mass of a cloud, and these three properties can be combined to further understand the physical conditions of the cloud. One of the most common conditions that we look for in a cloud is if it is in virial equilibrium.

The concept of virial equilibrium comes from the virial theorem, which provides an equation for the balance of a system's kinetic energy with a binding force, usually gravitational potential energy. In the case of self-gravity with no outside forces, the virial theorem states

$$2\langle T \rangle = -\langle U \rangle$$

where T is the kinetic energy and U is the gravitational potential energy. A molecular

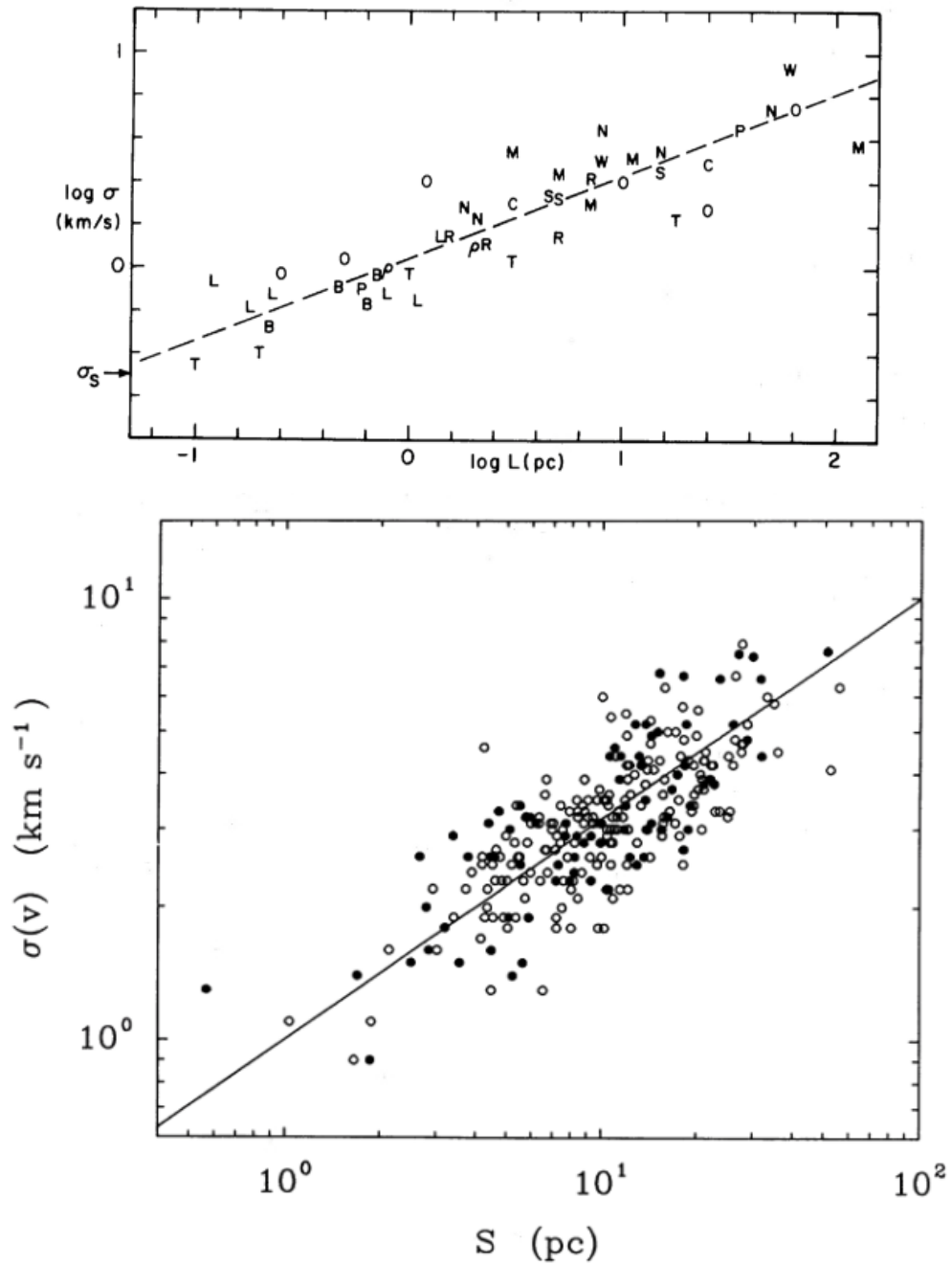


Fig. 1.10.— Relation between the size and velocity dispersion of molecular clouds. *Top*: Figure from Larson (1981) showing the first demonstration of this relation. *Bottom*: Figure from Solomon et al. (1987) measuring this relation for clouds in the disk of the Milky Way, and which is most commonly compared to in further studies.

cloud is in virial equilibrium when this relation is true. To characterize the extent to which a cloud is in virial equilibrium, we use the virial parameter, α_{vir} , which is the ratio between the twice the kinetic energy and the potential energy:

$$\alpha_{\text{vir}} = \frac{5\sigma_v R}{GM}$$

where σ_v is the linewidth, R is the radius, G is the gravitational constant, and M is the mass of the cloud. Clouds in virial equilibrium will have $\alpha_{\text{vir}} = 1$. A virial parameter greater than one means a cloud is dominated by kinetic energy and a virial parameter less than one means it is dominated by gravity and will likely collapse to form stars.

Heyer et al. (2009) determined that some of the scatter in the size-linewidth relation was due to clouds being in or near virial equilibrium. Normalizing the size-linewidth relation as $\sigma_v/R^{0.5}$, sometimes called the velocity metric, shows a relation with the surface density of the cloud (Figure 1.11). A line through this plot shows where clouds in virial equilibrium would fall.

Observational studies such as Heyer et al. (2009) show that molecular clouds are often not in virial equilibrium but rather are gravitationally unbound. However, the interpretation of the virial parameter requires caution because there are other forces, such as external pressures, that could help a cloud remain bound. This could happen, for example, if molecular clouds are colliding, causing them to experience ram pressure (e.g.; Finn et al. 2019; Tsuge et al. 2021). If a cloud is in free-fall collapse, its velocity dispersion will also be enhanced, making it appear unbound by simple virial analysis (Field et al. 2011).

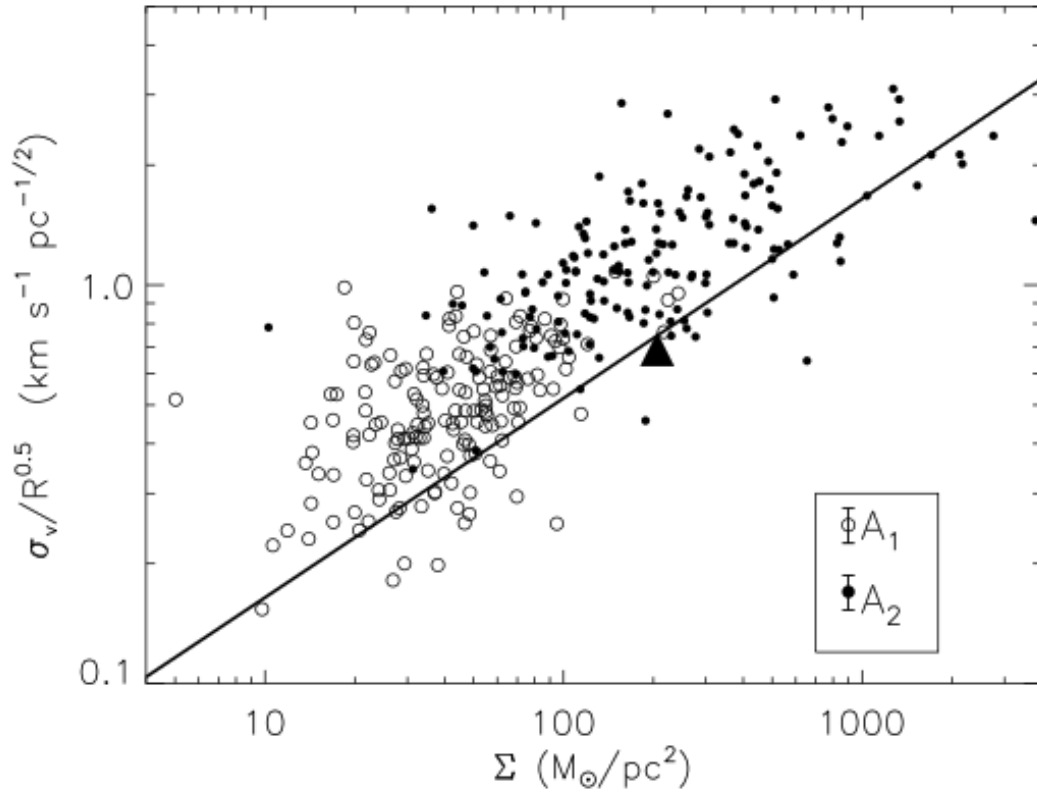


Fig. 1.11.— Figure from Heyer et al. (2009) showing the relation between the velocity dispersion and size, called the velocity metric, and the surface density of Milky Way clouds measured by Solomon et al. (1987). The diagonal line represents virial equilibrium, where the cloud’s gravity is balanced by its kinetic energy. Clouds falling above this line are more dominated by kinetic energy while clouds below this line are dominated by gravity and are expected to collapse. Clouds labeled A_1 use the area of the cloud calculated by Solomon et al. (1987), while cloud labeled A_2 use the area from the half-power isophote calculated by Heyer et al. (2009).



Fig. 1.12.— Photo of ALMA at night, photo credit ESO/Christoph Malin.

1.7 The Atacama Large Millimeter/submillimeter Array

Many recent leaps in the study of molecular gas comes from the advent of the Atacama Large Millimeter/submillimeter Array (ALMA). ALMA is an observatory situated in the Atacama Desert of Chile at an elevation 16,500 ft where there is little water in the air that would otherwise absorb millimeter wavelength light.

Of the 66 antennae that make up ALMA, 54 have diameters of 12 m and 12 have diameters of 7 m. When these antennae all act together using interferometry, they have the sensitivity of a 90 m diameter antenna and resolution as high as a 16 km antenna. The resolution obtained by ALMA depends on the wavelength observed and how spread out its dishes are, ranging from 160 m to 16 km. At the frequency of the CO(1-0) line, this corresponds to resolutions from 3.3'' to 0.033''. The majority of the data presented in this thesis comes from ALMA.

Chapter 2

The Physical Conditions of a Proto-Globular Cluster

The text in Chapter 2 appeared in the *Astrophysical Journal* (Finn et al. 2019) as “New Insights into the Physical Conditions and Internal Structure of a Candidate Proto-globular Cluster.”

2.1 Introduction

As some of the oldest objects in the universe, globular clusters are important probes of the early stages of galaxy formation and evolution. They are abundant in all massive galaxies (Harris et al. 2013), despite theoretical predictions that they have a high mortality rate, with potentially $\lesssim 1\%$ surviving to 10 Gyr (Fall & Zhang 2001). This suggests that the star formation process that created globular clusters was abundant in the early universe.

The discovery of young, dense star clusters in nearby galaxies, dubbed “super star clusters” (SSCs), provided evidence that this star formation process is still occurring

in the present universe (O’Connell et al. 1994). Further studies imply that these SSCs are likely very similar to the progenitors of the ancient globular clusters we are familiar with (McLaughlin & Fall 2008), though most will not survive to >10 Gyr. These clusters are primarily observed at optical and UV wavelengths, so most of our knowledge is confined to stages of evolution that occur after the progenitor cloud has formed stars and the cluster has at least partially emerged from its nascent molecular cloud.

To observe the earliest stages of formation and evolution, we need to look at millimeter wavelengths that can see the structure of the molecular clouds, before stars have formed and while the birth environment is still intact. This stage of formation is expected to be short-lived, lasting only $\sim 0.5 - 1$ Myr (Johnson et al. 2015), and so these objects are expected to be rare and therefore difficult to find.

To form a globular cluster, a molecular cloud must have a sufficiently large mass within a relatively small radius. If we take the typical globular cluster to have a half-light radius of $\lesssim 10$ pc (van den Bergh et al. 1991) and a stellar mass of $\gtrsim 10^5 M_\odot$ (Harris & Pudritz 1994), and assuming a star formation efficiency (SFE) of 20 – 50% (Ashman & Zepf 2001; Kroupa et al. 2001), then if a globular cluster loses approximately half its mass over the course of 10 Gyr, the progenitor molecular cloud must have an initial mass of $\gtrsim 10^6 M_\odot$ and a radius of < 25 pc (Johnson et al. 2015). To constrain the evolutionary stage of the cluster to before the onset of star formation, the cloud must also have no associated thermal radio emission, which would penetrate the surrounding material and indicate that stars have formed and begun ionizing the surrounding gas.

We also expect that a molecular cloud forming a massive star cluster must be subject to a high external pressure. Elmegreen & Efremov (1997) show that globular

clusters with masses of $> 10^5 M_\odot$ and core radii of 1-10 pc would require an external pressure of $P_0/k \sim 10^7 - 10^9 \text{ K cm}^{-3}$ during formation for the resulting object to be bound. This pressure is orders of magnitude larger than typical ISM pressures in the disc of the Milky Way, and is likely to only be achieved in particular scenarios, including interactions between galaxy systems. This makes the merging Antennae galaxies, where high densities and pressures as well as an abundant population of optically-visible SSCs have been observed (Whitmore 2000), a prime location to search for such a molecular cloud. At a distance of 22 Mpc, it is also close enough that with ALMA, we are now able to resolve size scales that are comparable to those of the precursor molecular clouds which could generate globular clusters.

Using data from an ALMA Early Science project, Whitmore et al. (2014) found a candidate pre-SSC cloud in the overlap region of the Antennae using CO(3-2) with a beam size of $0.56'' \times 0.43''$. Follow up analysis by Johnson et al. (2015) characterized it as having an inferred mass of $3.3\text{--}15 \times 10^6 M_\odot$, a deconvolved radius of $< 24 \pm 3 \text{ pc}$, and a pressure of $P_0/k \gtrsim 10^9 \text{ K cm}^{-3}$, all of which are consistent with expectations for a SSC-forming cloud. It also has no detectable associated thermal radio emission, where the upper limit on the peak ionizing flux from Johnson et al. (2015) is $N_{\text{Ly}\alpha} \approx 6 \times 10^{50} \text{ s}^{-1}$, which corresponds to ~ 60 O-type stars, or $M_* \lesssim 10^4 M_\odot$, which is more than two orders of magnitude less than the inferred mass of the cloud. Given that the expected resultant cluster will have a mass of $M_* > 10^5 M_\odot$, this is taken to indicate that the Firecracker is likely to still be in a very early stage of formation. Johnson et al. (2015) also demonstrate that the cloud is most likely supported by turbulence, and so on a timescale of $\sim 1 \text{ Myr}$ this turbulence will dissipate, initiating collapse if the cloud is bound, or dispersal if it is not.

This cloud has been nicknamed the ‘‘Firecracker,’’ and to the best of our knowledge,

is the only example found thus far that has the potential to be in the earliest stages of forming a massive star cluster with the potential to evolve into a globular cluster. Some very young SSCs have been identified with associated molecular gas (e.g. Leroy et al. 2018; Turner et al. 2017; Oey et al. 2017), but all of these also have associated thermal radio emission indicative of stars having formed. With the exception of one source from Leroy et al. (2018), this star formation is above the detection threshold for the Firecracker cloud.

Here we present new, high resolution ALMA observations of $^{12}\text{CO}(2-1)$, $^{12}\text{CO}(3-2)$, and $^{13}\text{CO}(2-1)$ emission that are capable of resolving the structure of the Firecracker cloud and improve upon the previous characterization of the source (Figure 2.1). The combination of the optically thick ^{12}CO and the optically thin ^{13}CO allow us to more directly measure the mass, while the improved resolution permits a more accurate size measurement for the cloud.

We also observe $\text{HCN}(4-3)$ and $\text{HCO}^+(4-3)$ emission, the ratio of which is postulated to be associated with evolutionary stage for massive cluster forming molecular clouds (Johnson et al. 2018). These observations further confirm the Firecracker cloud is still in the early stages of evolution, with little disruption from star formation.

In Section 2.2 we will discuss the ALMA observations that are used in this analysis. In Section 2.3.1, we describe the extraction of the cloud from the surrounding medium, and in Sections 2.3.2–2.3.4 we discuss obtaining the mass of the cloud and constraining the associated parameters. In Section 2.3.5, we compare the column density structure to that predicted for a Bonnor-Ebert sphere. Section 2.3.6 focuses on the pressure environment of the cloud and in Section 2.3.7 we consider cloud-cloud collision as a source of that pressure. In Section 2.3.8 we discuss how HCN and HCO^+ can be used as tracers of the evolutionary state of cluster formation. In Section 2.4, we discuss

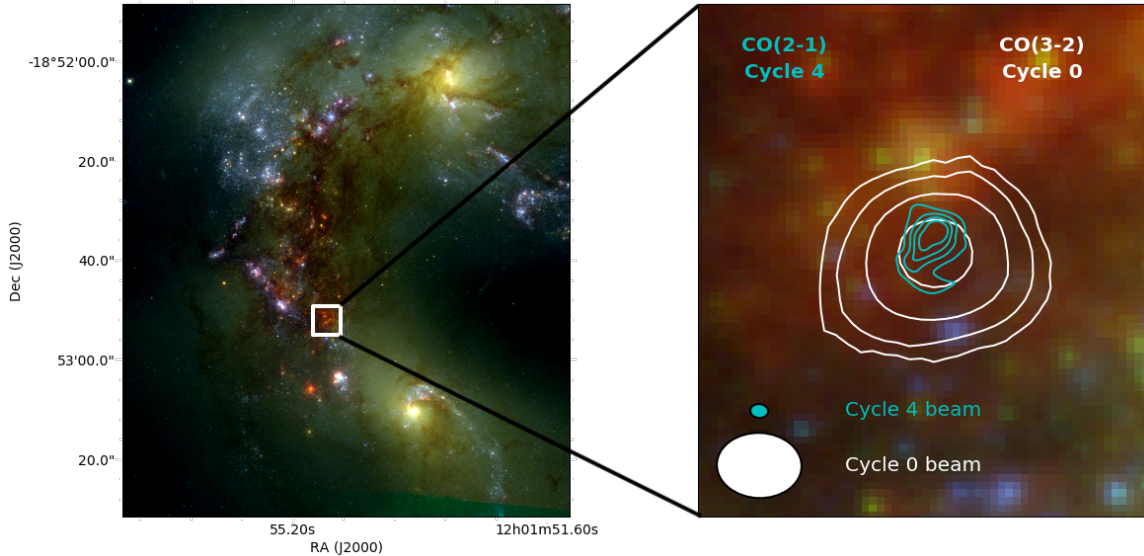


Fig. 2.1.— *Left*: Three-color Hubble Space Telescope image of the Antennae galaxies where red is Pa α , green is F814W, and blue is F435W. *Right*: Proto-SSC in the Overlap region with CO(3-2) moment 0 contours (0.4, 0.8, 1.6, 3.2 Jy beam $^{-1}$ km s $^{-1}$, white) from Johnson et al. (2015) ALMA Cycle 0 data, and CO(2-1) moment 0 contours (10, 15, 20, 25 σ , $\sigma = 0.04$ Jy beam $^{-1}$ km s $^{-1}$, cyan) from ALMA Cycle 4. The improved resolution of the Cycle 4 data allows us to now resolve the cloud and its structure. The synthesized beams for the Cycle 0 and Cycle 4 data are 0.43" \times 0.56" (46 \times 60 pc) and 0.09" \times 0.12" (10 \times 13 pc) respectively.

the various implications of these results for our understanding of cluster formation environments, and in Section 2.5 we summarize the main findings in this work.

2.2 Observations

We observed the overlap region of the Antennae galaxies using ALMA Band 6 and Band 7 in both extended and compact configurations during ALMA Cycles 3 and 4 (program codes 2015.1.00977.S and 2016.1.00924.S). The number of antennae online varied between 37 and 46. These observations are summarized in Table 2.1. The flux calibrators used were J1256-0547 and J1037-2934, and we estimate the flux uncertainty to be 10% based on the variability in these sources. The bandpass was

calibrated with J1256-0547, J1229+0203, and J1037-2934, and phase was calibrated with J1215-1731. These observations included continuum emission at each frequency, as well as emission from $^{12}\text{CO}(2-1)$, $^{12}\text{CO}(3-2)$, $^{13}\text{CO}(2-1)$, $\text{C}^{18}\text{O}(2-1)$, $\text{HCN}(4-3)$, $\text{HCO}^+(4-3)$, $\text{CS}(5-4)$, and $\text{H}30\alpha$. The data from these observations were reduced and calibrated using the CASA 4.7.2 pipeline, and no self-calibration was performed. Images were created using Briggs weighting with robust parameters varying between 0.5 and 2.0, and using a 2646×2646 pixel grid, with pixels of $0.014''$. The Firecracker cloud region is much smaller than the telescope primary beam ($<1''$ compared to $16.9''$ - $26.6''$ for our range of frequencies), so no primary beam correction is required.

In the vicinity of the Firecracker, there is diffuse continuum emission at all three frequencies throughout the area, associated with the SGMCSs in the overlap region. However, there is no peak in emission or any morphology in the continuum associated with the Firecracker itself, based on the well-detected CO emission (see Figure 2.2). We therefore consider this a non-detection of the Firecracker, with 5σ upper limits for the peak emission of $3.0 \times 10^{-4} \text{ Jy beam}^{-1}$ at 349 GHz, $9.5 \times 10^{-5} \text{ Jy beam}^{-1}$ at 237 GHz, and $6.0 \times 10^{-5} \text{ Jy beam}^{-1}$ at 226 GHz. We also did not detect $\text{C}^{18}\text{O}(2-1)$, $\text{CS}(5-4)$, or $\text{H}30\alpha$ in this region. The 5σ upper limits for these transitions are $0.85 \text{ mJy beam}^{-1}$ for $\text{C}^{18}\text{O}(2-1)$, $1.75 \text{ mJy beam}^{-1}$ for $\text{CS}(5-4)$, and $2.25 \text{ mJy beam}^{-1}$ for $\text{H}30\alpha$ at a velocity resolution of 10 km s^{-1} for each.

For the remaining transitions, the Firecracker cloud was detected strongly in $^{12}\text{CO}(2-1)$, $^{12}\text{CO}(3-2)$, and $^{13}\text{CO}(2-1)$, and weakly in $\text{HCN}(4-3)$ and $\text{HCO}^+(4-3)$. The parameters of the data cubes for each detected transition are summarized in Table 2.2. The RMS was determined using line-free channels. Figure 2.3 shows the three CO line profiles in this region, and Figure 2.4 shows the full $^{12}\text{CO}(2-1)$ emission cube's spatial and velocity structure.

Table 2.1: ALMA Band 6 and Band 7 Observations of the Antennae

Date	Central Freq. (GHz)	Time on Source (minutes)	Max. Baseline (m)
Sep 17-22 2016	226	156	3200
Aug 8 2017	226	51	3700
Nov 22 2016	226	10	704
Aug 8 2017	237	30	3700
Nov 19 2016	237	9	704
Jul 23 2017	349	19	3600
Nov 27 2016	349	6	704
Dec 12 2016	349	5	650

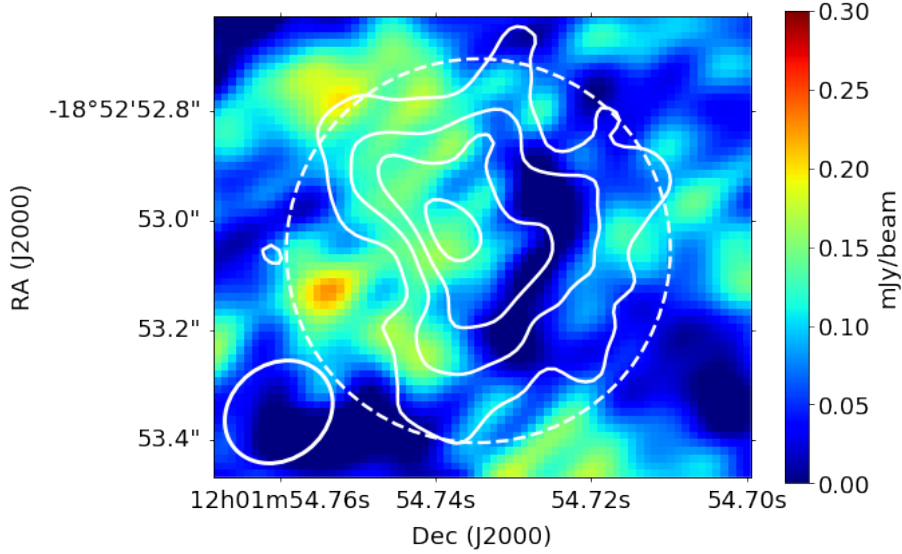


Fig. 2.2.— Band 7 continuum image, overlaid with contours of $^{13}\text{CO}(2-1)$ and the $0.35''$ radius aperture in which the integrated flux was measured. The peak emission is 3.8σ and is not coincident with the peak CO emission, leading to us consider this a non-detection. The image is scaled to 5σ , with $\sigma = 0.06 \text{ mJy beam}^{-1}$. The integrated flux within the white dashed aperture is $S_{880} = 0.78 \pm 0.2 \text{ mJy}$, which is likely due to the diffuse continuum emission in the region, and is used to set an upper limit on the mass of the cloud. The synthesized beam is shown in the lower left corner and has a size of $0.17'' \times 0.21''$.

2.3 Analysis

2.3.1 CO Line Profiles and Cloud Extraction

To obtain and compare line profiles for the $^{12}\text{CO}(2-1)$, $^{12}\text{CO}(3-2)$, and $^{13}\text{CO}(2-1)$ emission, the data cubes were each convolved to the synthesized beam of $^{13}\text{CO}(2-1)$ and are measured within a $0.24''$ radius aperture. The peak brightness temperatures of $^{12}\text{CO}(2-1)$ and $^{12}\text{CO}(3-2)$ are $T_{\text{CO}(2-1)} = 17 \pm 2$ K and $T_{\text{CO}(3-2)} = 16 \pm 2$ K, suggesting that these transition lines are nearly thermalized in this region. These line profiles are shown in Figure 2.3.

From these profiles, we also see that there is a second velocity component along the line of sight that we infer is a separate cloud that should not be included in analysis. Using the 3D visualization tool `shwirl` (Vohl 2017), we show the extraction of the cloud from the surrounding field. This corresponds to a $0.98'' \times 0.84''$ rectangle around the cloud centered on $12:01:54.73 -18:52:53.1$, and velocities in the range $1430\text{--}1555$ km s^{-1} .

From this extraction, we made total intensity maps (moment 0), integrating over the velocity range $1430\text{--}1555$ km s^{-1} , and peak intensity maps (moment 8) for $^{12}\text{CO}(2-1)$, $^{12}\text{CO}(3-2)$, and $^{13}\text{CO}(2-1)$. The total intensity (moment 0) and peak intensity (moment 8) maps for each CO transition are shown in Figure 2.5. The properties of

Table 2.2: Data cube parameters for detected transitions in the Firecracker region

Transition	Robust	Synth. Beam (arcsec ²)	RMS/chan (mJy/beam)	Channel (km/s)
$^{12}\text{CO}(2-1)$	0.5	0.09×0.12	0.6	5
$^{12}\text{CO}(3-2)$	0.5	0.15×0.16	2.0	5
$^{13}\text{CO}(2-1)$	2.0	0.17×0.18	0.25	5
HCN(4-3)	2.0	0.17×0.20	1.2	15
$\text{HCO}^+(4-3)$	2.0	0.17×0.21	1.0	15

Notes. Quoted channel widths reflect values adopted to improve sensitivity.

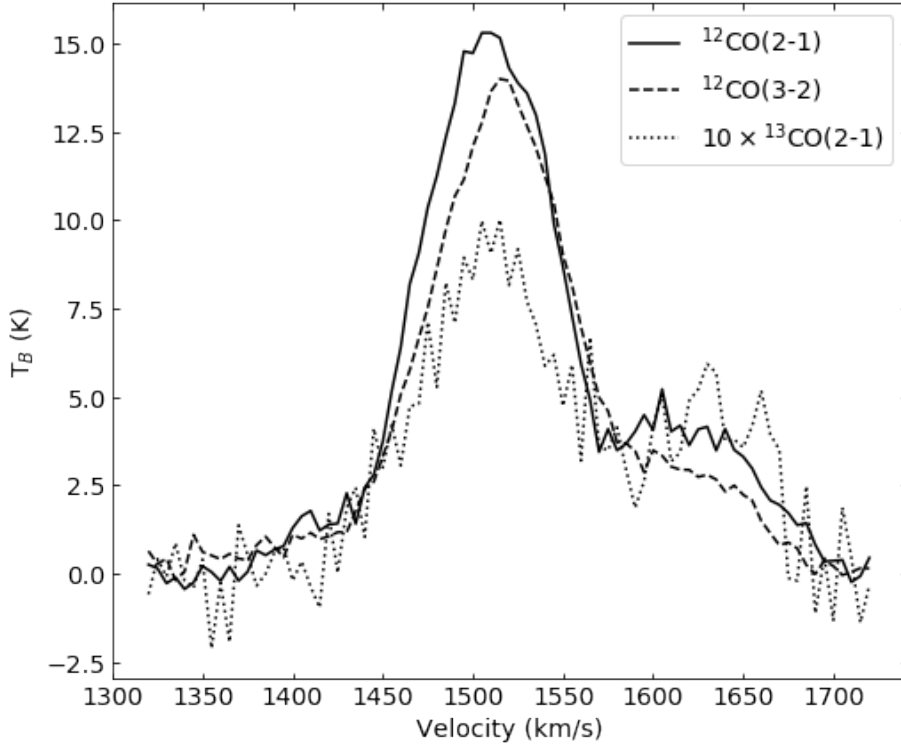


Fig. 2.3.— Line profiles of $^{12}\text{CO}(2-1)$, $^{12}\text{CO}(3-2)$, and $^{13}\text{CO}(2-1)$ as measured in a $0.24''$ radius region centered on the peak $^{13}\text{CO}(2-1)$ emission. The $^{13}\text{CO}(2-1)$ profile has been multiplied by a factor of 10 for easier comparison. Each data set was convolved to the same beam size of $0.17'' \times 0.18''$. The similarity of the peak brightness temperatures of $^{12}\text{CO}(2-1)$ and $^{12}\text{CO}(3-2)$ indicate that these lines are approximately thermalized. Furthermore, these spectra show that there is a second velocity component along the line of sight, as expected from previous observations by Johnson et al. (2015). This component is assumed to be separate from the Firecracker cloud, so we extract only the primary velocity component from the data cube for all further analysis (see Figure 2.4).

the cloud measured from these cubes for the extracted region are given in Table 2.3.

To determine the size of the cloud from these observations, we use the $^{13}\text{CO}(2-1)$ emission, since it is optically thin and gives a better representation of the cloud's structure than the optically thick ^{12}CO . We define a characteristic radius, which is the radius of a circle with the same area as that enclosed by the 5σ contour of the $^{13}\text{CO}(2-1)$ total intensity (moment 0) map. This characteristic radius for the Firecracker is 0.21", which corresponds to a size of 21 pc at a distance of 22 Mpc.

2.3.2 Cloud Mass

Observations of both $^{12}\text{CO}(2-1)$ and $^{13}\text{CO}(2-1)$ allow us to determine the optical depth of the cloud by assuming an abundance ratio for these two molecules and assuming that their excitation temperatures are the same. If the excitation temperature of ^{13}CO is lower than ^{12}CO , this assumption will underestimate the mass. We also assume that $^{12}\text{CO}(2-1)$ is thermalized with respect to $^{12}\text{CO}(1-0)$, as expected from the line profiles (Figure 2.3). If $^{12}\text{CO}(2-1)$ is not thermalized, this assumption will also underestimate the mass.

In the overlap region of the Antennae, the $^{12}\text{CO}/^{13}\text{CO}$ abundance ratio has been measured to be $X_{12}/X_{13} \simeq 70$, though it is poorly constrained in this region and could vary from 40 to 200 (Zhu et al. 2003). We convolved the $^{12}\text{CO}(2-1)$ image to the synthesized beam of $^{13}\text{CO}(2-1)$, then fit Gaussian profiles to the velocity profile for each $^{12}\text{CO}(2-1)$ pixel. We then fit Gaussian profiles to the $^{13}\text{CO}(2-1)$ velocities, fixing the central velocity to be the same as the corresponding $^{12}\text{CO}(2-1)$ pixel, and masking pixels where a solution to the fit could not be found. Taking the ratio of the peak brightness temperatures of these two molecular lines at each unmasked pixel, we created a map of the peak optical depth, τ_{12} , using the equation

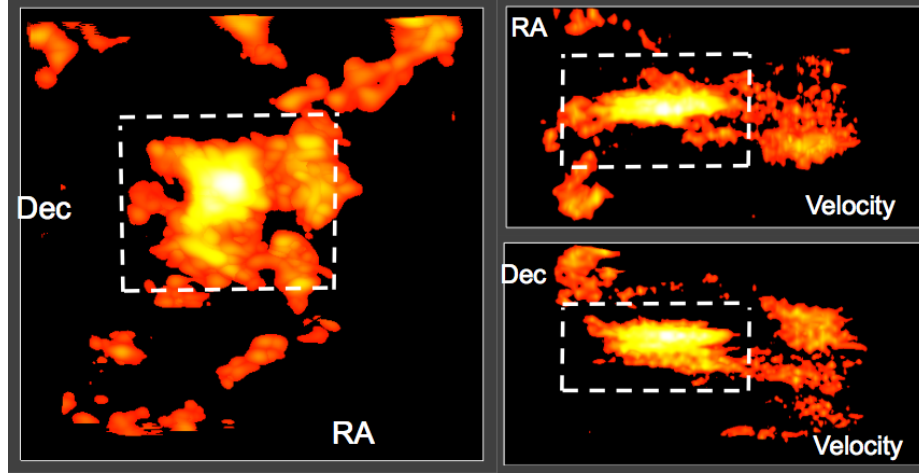


Fig. 2.4.— Three different 2-D projections of the $^{12}\text{CO}(2-1)$ data cube using the 3-D visualization tool `shwirl` to examine the structure of the cloud in velocity space. Each box shows the same range of data. The white dashed line shows the extraction of the cloud from the surrounding field and second velocity component. The extraction is a cube extending $0.98''$ in right ascension, $0.84''$ in declination, centered on $12:01:54.73 - 18:52:53.1$ and with a velocity range of $1430\text{--}1555 \text{ km s}^{-1}$.

Table 2.3: Molecular Cloud Measured Properties

RA (J2000)	12:01:54.73
Dec (J2000)	-18:52:53.0
V_{LSR} (km s^{-1})	1516 ± 5
$S_{^{12}\text{CO}(2-1)}$ (Jy km s^{-1})	14 ± 1
$S_{^{12}\text{CO}(3-2)}$ (Jy km s^{-1})	26 ± 2
$S_{^{13}\text{CO}(2-1)}$ (Jy km s^{-1})	0.87 ± 0.2
$\sigma_{v,^{12}\text{CO}(2-1)}$ (km s^{-1})	36 ± 3
$\sigma_{v,^{12}\text{CO}(3-2)}$ (km s^{-1})	38 ± 3
Radius (arcsec)	0.21

Notes. Measurements of the velocity properties were based on Gaussian fitting of the line profiles for $^{12}\text{CO}(2-1)$ and $^{12}\text{CO}(3-2)$, after the second velocity component was subtracted out with a Gaussian fit. The integrated flux was measured within an aperture with a radius of $0.35''$. The characteristic radius is the radius of a circle with the same area as that enclosed by the 5σ contour of the $^{13}\text{CO}(2-1)$ moment 0 map (see Figure 2.5).

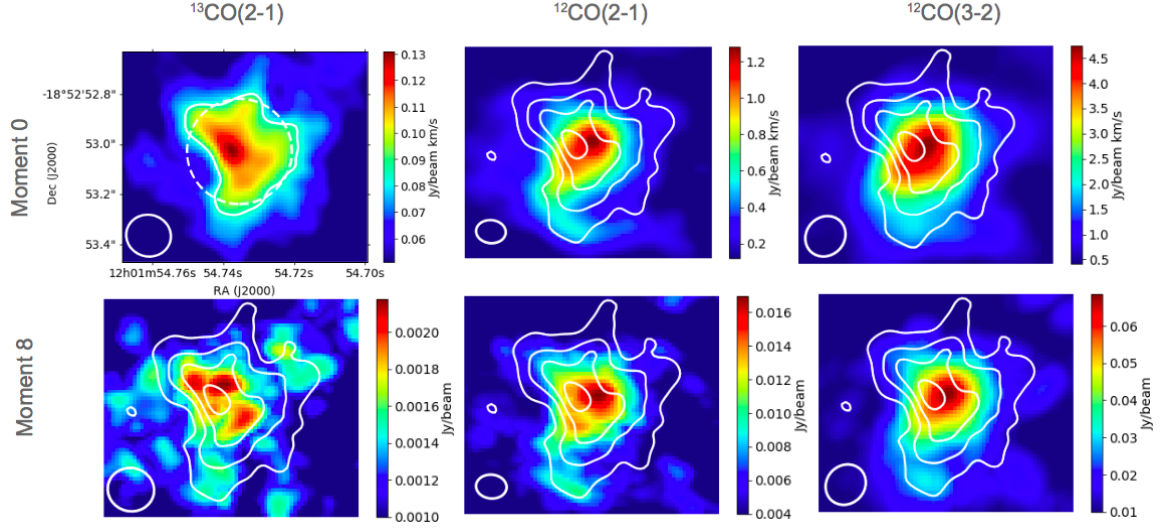


Fig. 2.5.— *Top row*: Total intensity (moment 0) maps. *Bottom row*: Peak intensity (moment 8) maps. *Left column*: $^{13}\text{CO}(2-1)$. *Middle column*: $^{12}\text{CO}(2-1)$. *Right column*: $^{12}\text{CO}(3-2)$. In the $^{13}\text{CO}(2-1)$ moment 0 image (upper left), the solid white line represents the 5σ ($\sigma=0.017$ Jy beam $^{-1}$ km s $^{-1}$) contour, and the dashed white line represents the circle with area equal to that enclosed by the 5σ contour. The radius of this circle is $0.21''$, which is taken to be the characteristic radius of the cloud. In the other images, contours of the $^{13}\text{CO}(2-1)$ are overplotted at $4, 5, 6,$ and 7σ levels. Synthesized beams are shown in the bottom left corners of each image, and are $0.17'' \times 0.18''$ for $^{13}\text{CO}(2-1)$, $0.09'' \times 0.12''$ for $^{12}\text{CO}(2-1)$, and $0.15'' \times 0.16''$ for $^{12}\text{CO}(3-2)$.

$$\frac{T_{12}}{T_{13}} = \frac{T_{x,12}}{T_{x,13}} \frac{1 - e^{-\tau_{12}}}{1 - e^{-\tau_{13}}} = \frac{1 - e^{-\tau_{12}}}{1 - e^{-\tau_{13}}}, \quad (2.1)$$

by taking $\tau_{12}/\tau_{13} = X_{12}/X_{13}$ and assuming that the excitation temperatures for ^{12}CO and ^{13}CO are equal ($T_{x,12} = T_{x,13}$). From these optical depths, we found the peak excitation temperature, T_x , at each pixel given by

$$T_{12} = (1 - e^{-\tau_{12}}) \frac{T_{\text{UL}}}{e^{T_{\text{UL}}/T_x} - 1}, \quad (2.2)$$

where $T_{\text{UL}} = 11.07$ K for ^{12}CO .

We then determined τ_{12} for each velocity in the cube, giving us a profile of the optical depth for each pixel. This was done by using Equation 2.1 with the ratio of the brightness temperature of $^{12}\text{CO}(2-1)$ and $^{13}\text{CO}(2-1)$ wherever $^{13}\text{CO}(2-1)$ was detected ($> 4\sigma$, $\sigma = 0.02$ K). Where $^{13}\text{CO}(2-1)$ was not detected and $^{12}\text{CO}(2-1)$ was detected, we used Equation 2.2 with the brightness temperature of $^{12}\text{CO}(2-1)$ only, and assuming that the excitation temperature does not vary with velocity. The data cubes were masked with thresholds of 3σ ($\sigma = 0.6$ mJy beam $^{-1}$ for $^{12}\text{CO}(2-1)$ and $\sigma = 0.25$ mJy beam $^{-1}$ for $^{13}\text{CO}(2-1)$). With the assumption that the excitation temperature remains constant at all velocities within the cloud, we found the column density at each pixel using the equation from Mangum & Shirley (2015):

$$N_{tot} = \frac{8\pi\nu_0^2 Q}{c^2 A_{ul} g_u} e^{\frac{E_u}{kT_x}} \left(e^{\frac{h\nu_0}{kT_x}} - 1 \right)^{-1} \int_0^\infty \tau_\nu d\nu \quad (2.3)$$

For ^{12}CO , this equation becomes

$$\frac{N_{tot}^{12}}{\text{cm}^{-2}} = 3.3 \times 10^{14} \left(\frac{T_x}{B_0} + \frac{1}{3} \right) \frac{1}{e^{\frac{-5.53}{T_x}} - e^{\frac{-16.6}{T_x}}} \int_0^\infty \tau_\nu d\nu, \quad (2.4)$$

where $B_0 = 2.7674$ K for ^{12}CO .

From these column densities, we take an $\text{H}_2/^{12}\text{CO}$ abundance ratio of $\text{H}_2/^{12}\text{CO} = 10^4 - 10^5$, which is typical of Milky Way IRDCs, before or slightly after protostellar objects have formed, akin to the stage we expect the Firecracker to most likely be in (Gerner et al. 2014). The Antennae has a very nearly solar metallicity, $[Z] = +0.07 \pm 0.03$ (Lardo et al. 2015), so the default expectation is that its chemistry is similar to the Milky Way's. We then assume the total mass is 1.3 times the mass of H_2 to derive the total mass surface density (shown as a map in Figure 2.6). Taking a pixel area of $A = 2.23$ pc 2 , we can add the mass from each pixel to get the total mass of the cloud.

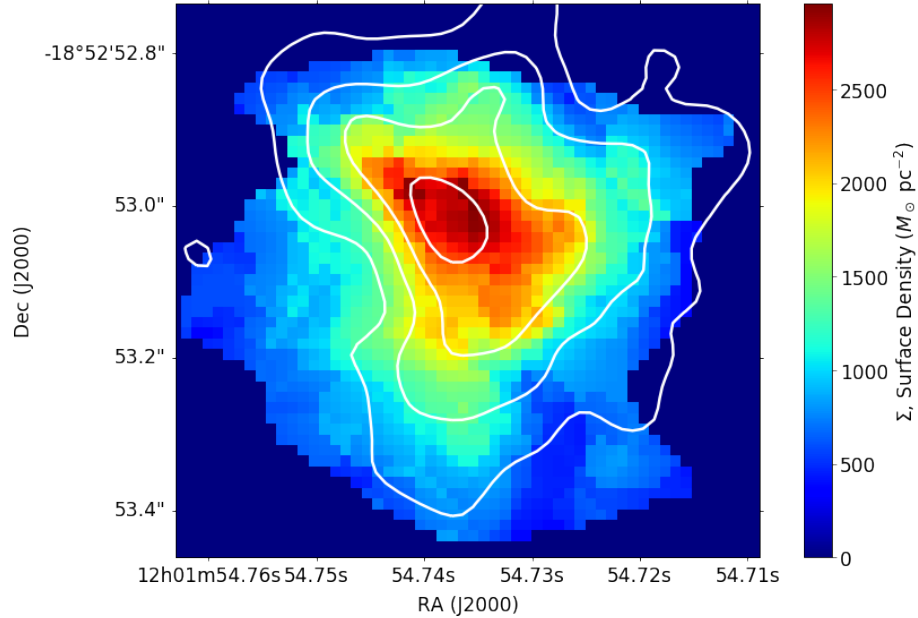


Fig. 2.6.— Map of the mass surface density. This version was created with the assumed parameters $X_{12}/X_{13} = 70$ and $H_2/^{12}\text{CO} = 10^{4.5}$. Summing over all the pixels and assuming a pixel area of 2.23 pc^2 results in a total mass of $4.5 \times 10^6 M_\odot$. Overplotted are contours of $^{13}\text{CO}(2-1)$ moment 0.

Different combinations of values in the expected ranges of X_{12}/X_{13} and $H_2/^{12}\text{CO}$ were used, resulting in masses that varied in the range $1.0\text{--}31 \times 10^6 M_\odot$. In Section 2.3.3, we will put additional constraints on the upper limit of this mass range due to dust emission. Mass estimates for a few selected parameter combinations are given in Table 2.4, and estimates for the full range of parameter combinations are shown in Figure 2.7. The mass directly tracks variations in $H_2/^{12}\text{CO}$, with an order of magnitude change in $H_2/^{12}\text{CO}$ corresponding to an order of magnitude change in mass. The resulting mass is less sensitive to X_{12}/X_{13} , with a factor of five change in this value only resulting in a factor of ~ 3 change in mass.

The range in masses that results from varying these parameters is in good agreement with measurements made by Johnson et al. (2015), which had lower spatial resolution ($0.56'' \times 0.43''$) and did not have optical depth information.

2.3.3 Expected Continuum Emission

The lack of detected continuum emission associated with the Firecracker sets further constraints on the mass of the cloud. At all three frequencies, there is diffuse continuum emission associated with the larger region, but no morphology or peak emission associated with Firecracker above 3.8σ (Figure 2.2). We consider this a non-detection of the Firecracker, and use the integrated flux from the diffuse emission to set an upper limit on the Firecracker’s dust mass.

Using the Band 7 observations (in which the dust emission from the Firecracker should be brightest), we flagged the emission lines to create a continuum image with a beam FWHM of $0.17'' \times 0.21''$ and an RMS of $0.06 \text{ mJy beam}^{-1}$. The integrated flux in a $0.35''$ radius circular region around the Firecracker is $S_{880} = 0.78 \pm 0.2 \text{ mJy}$.

From Wilson et al. (2008),

$$M_{dust} = 74,220 S_{880} D^2 \frac{(e^{17/T} - 1)}{\kappa} (M_{\odot}), \quad (2.5)$$

where S_{880} is measured in Janskys at $880\mu\text{m}$ (Band 7), D is measured in Mpc, κ is the dust emissivity measured in $\text{cm}^2 \text{ g}^{-1}$, and T is measured in K. For the Antennae system, $D = 22 \text{ Mpc}$. Taking $T_{Kin} \simeq T_{ex}$, the temperature measured in this region is 25–35 K. Typical values adopted for the dust emissivity and gas-to-dust ratio in these

Table 2.4: Possible values for the mass ($10^6 M_{\odot}$)

		$X_{12}/X_{13} =$			
		40	70	120	200
$\text{H}_2/^{12}\text{CO} =$	10^4	1.0	1.4	2.1	3.1
	$10^{4.5}$	3.3	4.5	6.5	9.7
	10^5	11	14	21	31

Notes. Masses for given combinations of X_{12}/X_{13} and $\text{H}_2/^{12}\text{CO}$ assumptions are given in the body of the table with units of $10^6 M_{\odot}$.

types of environments are $\kappa = 0.9 \pm 0.13 \text{ cm}^2 \text{ g}^{-1}$ and a ratio of 120 ± 28 (Wilson et al. 2008).

If we take the most extreme values to maximize M_{dust} within the expected range for each parameter (so $S_{880} \leq 1.34 \text{ mJy}$, $T \geq 25 \text{ K}$, $\kappa \geq 0.77 \text{ cm}^2 \text{ g}^{-1}$), the upper limit on the dust mass would be $M_{dust} \leq 6 \times 10^4 M_{\odot}$. Taking the maximum gas-to-dust ratio ≤ 148 , the largest total mass that would be consistent with the continuum non-detection would be $9 \times 10^6 M_{\odot}$. This is then taken as the upper limit on the mass of the Firecracker.

We also note that this continuum non-detection at $880 \mu\text{m}$ would suggest that the previous unresolved continuum detection at this frequency in Johnson et al. (2015) was likely instead picking up the diffuse emission of the larger region rather than the Firecracker itself.

We can compare this limit to the mass estimates from different combinations of X_{12}/X_{13} and $\text{H}_2/^{12}\text{CO}$ values. Mass estimates for the full range of parameter combinations are shown in Figure 2.7, with a line representing the upper limit derived from the lack of continuum emission. Parameter combinations above this line are ruled out for the Firecracker region. For example, if the assumed X_{12}/X_{13} ratio is taken to be 200, the value of $\text{H}_2/^{12}\text{CO}$ must be less than $10^{4.5}$.

2.3.4 X_{CO} Conversion Factor

We use the masses and column densities that we derive to calculate the CO-to- H_2 conversion factor, X_{CO} , in the Firecracker. In starburst regions, this conversion factor is typically taken to be $X_{CO} = 0.5 \times 10^{20} \text{ cm}^{-2} (\text{K km s}^{-1})^{-1}$, but is expected to vary by up to a factor of four (Bolatto et al. 2013). In non-starbursting regions, the typical value taken is $X_{CO} = 2.0 \times 10^{20} \text{ cm}^{-2} (\text{K km s}^{-1})^{-1}$.

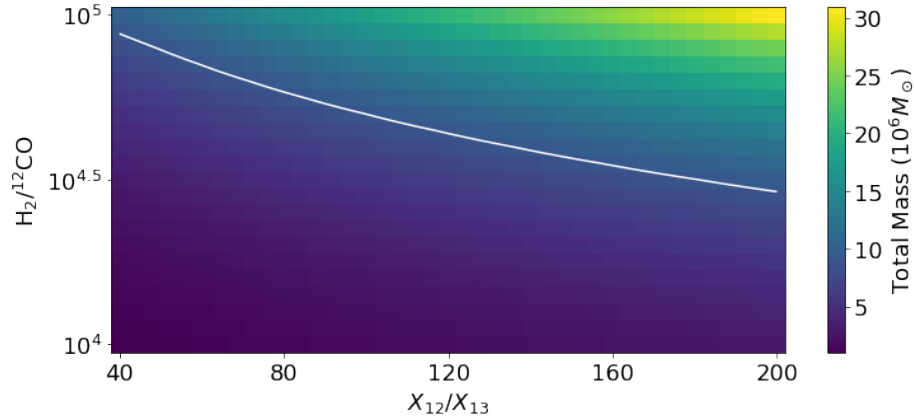


Fig. 2.7.— Mass estimates derived from the full ranges of expected X_{12}/X_{13} and $H_2/^{12}\text{CO}$ values. The white line represents the upper limit on the mass derived from the continuum non-detections ($9 \times 10^6 M_\odot$), and so parameter combinations falling above this line on the plot can be ruled out for the Firecracker region. The lower limit on the mass ($1 \times 10^6 M_\odot$) is set by the lower limits of the adopted X_{12}/X_{13} and $H_2/^{12}\text{CO}$ values in the bottom left of the plot.

Considering the range of expected masses up to the upper mass limit from the continuum non-detections, we create maps of X_{CO} in the Firecracker cloud for each set of abundance parameter assumptions. Fitting a Gaussian to the distribution of values within each map, the average values vary in the range $X_{CO} = (0.12 - 1.1) \times 10^{20} \text{ cm}^{-2} (\text{K km s}^{-1})^{-1}$ for the Firecracker region. This is consistent with the typically assumed value for starbursts.

We also see that this conversion factor appears to vary spatially over the Firecracker region. Figure 2.8 shows a map of the derived X_{CO} factor within the Firecracker region based on a map of the column density, and the map of the integrated line intensity of $^{12}\text{CO}(2-1)$, which we assume is thermalized with respect to $^{12}\text{CO}(1-0)$ ($^{12}\text{CO}(2-1)/^{12}\text{CO}(1-0) = 1$), and convert to K km s^{-1} (Figure 2.5). Within such a map for a single set of X_{12}/X_{13} and $H_2/^{12}\text{CO}$ assumptions, the value of X_{CO} varies by up to $\sim 80\%$ of the average across the Firecracker region.

Furthermore, a histogram of the values for each map show that the distribution

has a component of Gaussian noise, but the distribution at the higher and lower ends cannot be entirely explained by Gaussian noise in the measurements. These values are likely tracing physical variations in the conversion factor. When taking into account these spatial variations, as well as the range of mass estimates, we find that the conversion factor in the Firecracker can take on values in the range $X_{CO} = (0.08 - 2.0) \times 10^{20} \text{ cm}^{-2}$.

2.3.5 Column Density Radial Profile

We examine the radial profile of the column density derived in Section 2.3.2 as a component of the mass estimate by calculating the azimuthal average of 1-pixel-wide (0.014") annuli around the center of the cloud as determined by the peak N_{H_2} estimate. These annuli extend from a radius of 0.042" (4.5 pc) to the outer radius as determined by the 5σ contour of the $^{13}\text{CO}(2-1)$ (0.24", 26 pc). We measure this radial profile for column density estimates that assumed $X_{12}/X_{13} = 40, 70, 120,$ and 200. Since we only consider the column density normalized to the central peak when fitting the profile, assumptions of $\text{H}_2/^{12}\text{CO}$ do not affect the fit.

To determine the physical nature of this internal structure, we compare it to the density profile of an isothermal, self-gravitating, pressure-confined sphere as described by Bonnor (1956) and Ebert (1955) and referred to as a Bonnor-Ebert profile. Starting with equations for hydrostatic equilibrium, an isothermal equation of state, and Poisson's equation, they arrive at a form of the Lane-Emden equation (Chandrasekhar 1967):

$$\frac{1}{\xi^2} \frac{d}{d\xi} \left(\xi^2 \frac{d\psi}{d\xi} \right) = \exp(-\psi) \quad (2.6)$$

In this equation, they have defined $\xi \equiv \left(\frac{4\pi G \rho_C}{a^2} \right)^{1/2} r$ as the dimensionless radial pa-

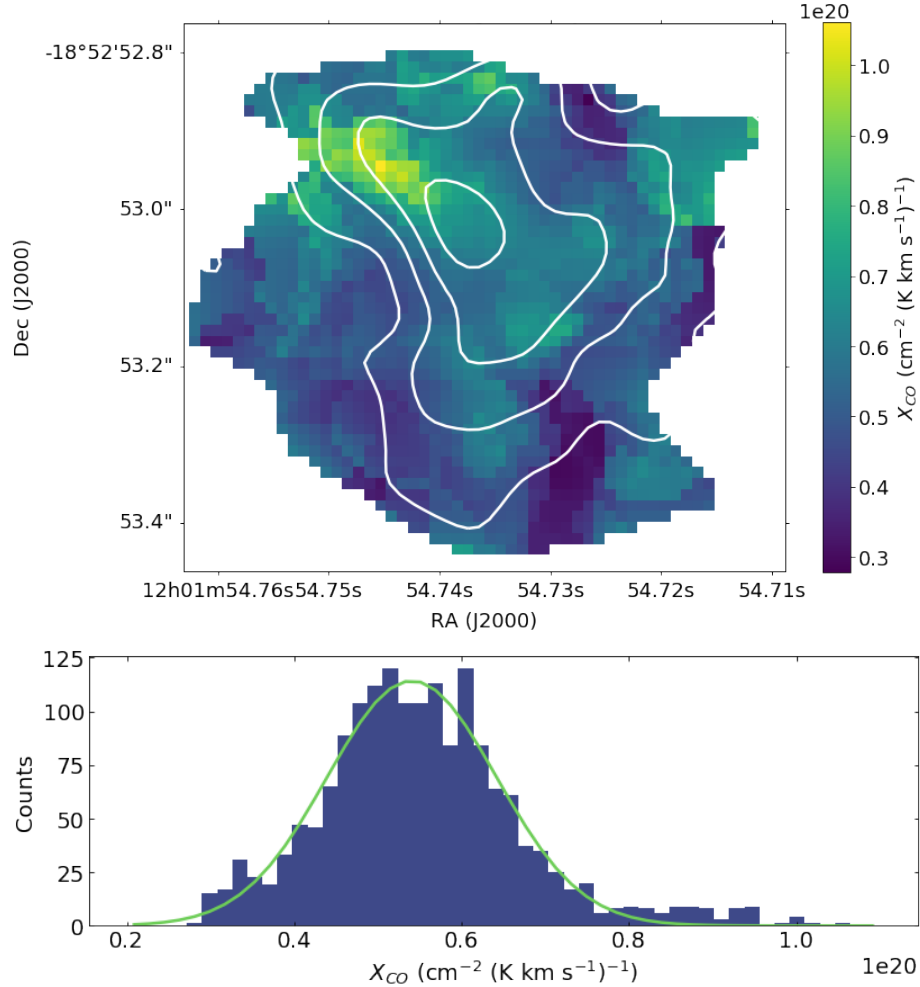


Fig. 2.8.— *Top*: Spatial variation of the X_{CO} factor with contours of $^{13}\text{CO}(2-1)$ moment 0 overplotted. The values here are based on mass calculation assumptions of $X_{12}/X_{13} = 70$ and $\text{H}_2/^{12}\text{CO} = 10^{4.5}$, resulting in a total mass of $4.5 \times 10^6 M_{\odot}$. Under these assumptions, X_{CO} varies in the range $(0.3-1.1) \times 10^{20} \text{ cm}^{-2} (\text{K km s}^{-1})^{-1}$ within this region. The values in this map will scale with different X_{12}/X_{13} and $\text{H}_2/^{12}\text{CO}$ assumptions, which results in a full range of $X_{CO} = (0.08-2.0) \times 10^{20} \text{ cm}^{-2}$. *Bottom*: Histogram of values in the plot above, with the fitted Gaussian overplotted. The distribution shows that there is a component of Gaussian noise with a mean value of $X_{CO} = 0.54 \times 10^{20} \text{ cm}^{-2}$ and a width of $X_{CO} = 0.1 \times 10^{20} \text{ cm}^{-2}$. However, the values on the upper and lower ends are higher than expected for only Gaussian noise, suggesting that these variations in measured X_{CO} are due to physical variations, not just error in the measurements.

parameter, where ρ_C is the central density and $a = \sqrt{\frac{k_B T}{\mu m_p}}$ is the isothermal sound speed. We have defined $\psi(\xi) \equiv \frac{\Phi_g}{a^2} = -\ln(\rho/\rho_C)$ as the dimensionless gravitational potential.

The Bonnor-Ebert profile is derived by numerically integrating this equation with the boundary conditions $\psi(0) = 0$ and $\frac{d\psi(0)}{d\xi} = 0$ to obtain a relation between ρ/ρ_C and ξ . This density ratio can then be converted to a column density ratio with the assumption that the cloud is spherical. This profile is then fit to the observed structure profile by determining the best-fit values of ξ_{max} , the value of ξ at the outer radius of the cloud. The resulting best fit for the derived set of column densities is characterized by $\xi_{max} = 3.4 \pm 0.4$. This fit has a χ^2 value of 7.15, although when only the profiles with $X_{12}/X_{13} = 70, 120,$ and 200 are used, this fit changes to $\xi_{max} = 3.2 \pm 0.2$ with a χ^2 value of 1.66.

We note that in this fit, the cloud is resolved, but the points used in the fit are separated by less than the beam size, and so are correlated with each other. We also fit a circular Gaussian to the column density map, and plot the profile of this Gaussian in Figure 2.9 as well. The cloud is consistent with both the Bonnor-Ebert profile and this Gaussian profile.

The $X_{12}/X_{13} = 40$ profile may appear separate from the other three profiles due to the slightly different morphology the mass map takes on when the ^{12}CO is less optically thick, as is the case with this assumed lower abundance ratio. The other three profiles agree very well with each other. At the edge of the cloud, each profile begins to hit a noise threshold and so would be expected not to drop off as quickly as predicted, which agrees well with the observed profile.

The Bonnor-Ebert fit of the cloud's structure implies that it may be well-characterized as an isothermal, self-gravitating, pressure-confined sphere. We also note, however, that simulations of evolving star forming cores by Ballesteros-Paredes et al. (2003)

suggest that a Bonnor-Ebert profile can be mimicked by clouds that are not in hydrostatic equilibrium. This could be the case here for the Firecracker cloud, and so we are cautious in drawing conclusions about the cloud's physical state from this profile fit. The implications of this fit and concerns associated with it are addressed further in Section 2.4.1.

2.3.6 Cloud Pressure

We examine the effect of the cloud's environment on the parameters derived thus far by comparing the surface density, Σ , to a size-linewidth coefficient, σ_V^2/R . The velocity dispersions were determined by fitting two Gaussian profiles to the $^{12}\text{CO}(3-2)$ emission line, one of which accounts for the second velocity component along the line of sight. The radius is taken to be the size of the aperture being measured, and the surface density is taken as the average within that aperture, based on the range of mass maps derived in Section 2.3.2.

We determine these parameters for four different apertures, shown in the right panel of Figure 2.10. The largest, Aperture 4, is selected to include all $^{13}\text{CO}(2-1)$ emission above $\approx 4\sigma$, with a radius of 0.35" (37 pc). The next, Aperture 3, is selected to approximately match the size of the 5σ contour of the $^{13}\text{CO}(2-1)$, with a radius of 0.24" (26 pc). The next, Aperture 2, is selected to approximately follow the contour of 6σ emission, with a radius of 0.14" (15 pc). Aperture 1 is approximately the $^{12}\text{CO}(2-1)$ beam size, with a radius of 0.06" (6.4 pc).

From the left panel of Figure 2.10, these parameters indicate that the cloud is neither in virial equilibrium nor in free fall, implying that to be bound (as circumstantially suggested by its morphology), the cloud must be subject to a high external pressure with $P_e/k \gtrsim 10^8 \text{ K cm}^{-3}$. This would agree with previous analysis by John-

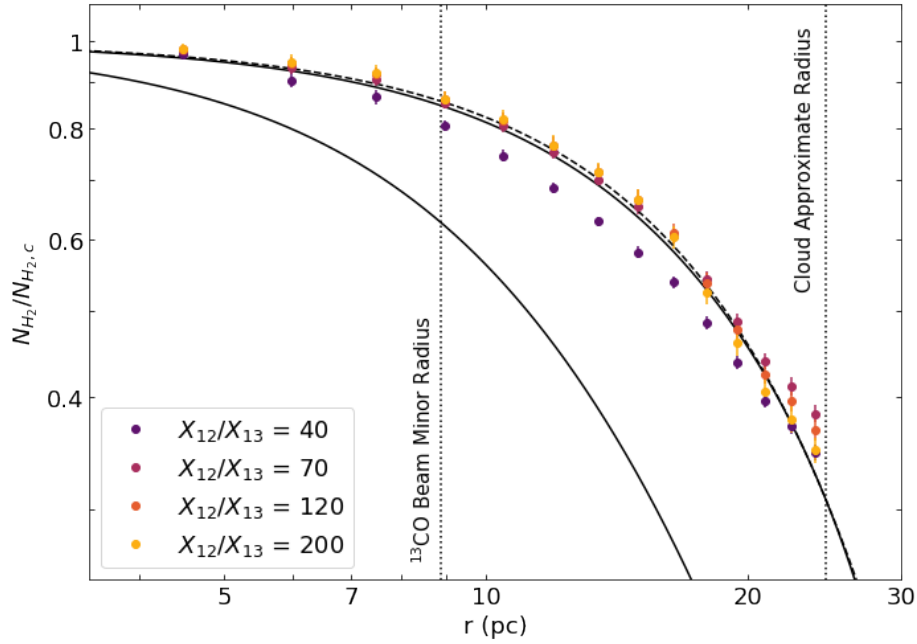


Fig. 2.9.— Radial profiles of the column density, N_{H_2} , normalized to the central column density, $N_{H_{2,c}}$, for different assumptions of X_{12}/X_{13} . Overplotted is the Bonnor-Ebert profile describing an isothermal, self-gravitating, pressure-confined sphere, with a fit characterized by $\xi_{max} = 3.4 \pm 0.4$ (upper solid line), as well as the profile of the fitted gaussian (dashed line). The lower solid line is the Bonnor-Ebert profile with $\xi_{max} = 6.5$, indicating the profile below which the cloud would be gravitationally unstable. Since our best fit falls above this profile, the cloud is consistent with being gravitationally stable. The error in the column density is taken to be the standard deviation in the azimuthal averaging. The dotted lines represent the radius of the $^{13}\text{CO}(2-1)$ synthesized beam and the radius of the cloud. This Bonnor-Ebert fit has a χ^2 value of 7.15.

son et al. (2015), the fit of the Bonnor-Ebert profile in Section 2.3.5, and theoretical expectations for cluster formation (Elmegreen & Efremov 1997).

Furthermore, we see that the inferred pressure increases as the aperture radius decreases, zooming in on the central region of the cloud. This may be an indication that we are tracing an internal pressure structure. It also may, however, be a measurement effect, since the radius of the selected aperture may not be a good indicator of the bound radius in the given region.

Also compared in the leftmost panel of Figure 2.10 young massive clusters discovered by Leroy et al. (2018) in NGC 253, for which star formation has been detected. These clusters include both a gas and stellar mass component (with gas masses in the range $10^{3.6} - 10^{5.7} M_{\odot}$, and stellar masses in the range $10^{4.1} - 10^{6.0} M_{\odot}$), and we also compare the ratio M_{gas}/M_* to their position in this plot. Most of the clusters fall along either the free fall or virial equilibrium lines, but one notable cluster with a significantly higher M_{gas}/M_* than all of the other clusters is above these lines, suggesting a high external pressure ($P_e/k \gtrsim 10^9 \text{ K cm}^{-3}$) would be required to keep it bound. Another cluster with a more modestly enhanced M_{gas}/M_* is also above virial and free fall lines. This may be an indication that the pressure environment of massive clusters is correlated with the evolutionary stage of the cluster. This would support a scenario in which clusters form in high pressure environments, then the pressure dissipates or is dispelled as stars form and the cluster emerges.

Assuming the cloud is bound, we can also directly calculate what the expected external pressure would be from the cloud's mass M , its radius R , and its velocity dispersion σ_V with the equation from Elmegreen (1989):

$$P_e = \frac{3\Pi M \sigma_V^2}{4\pi R^3} \quad (2.7)$$

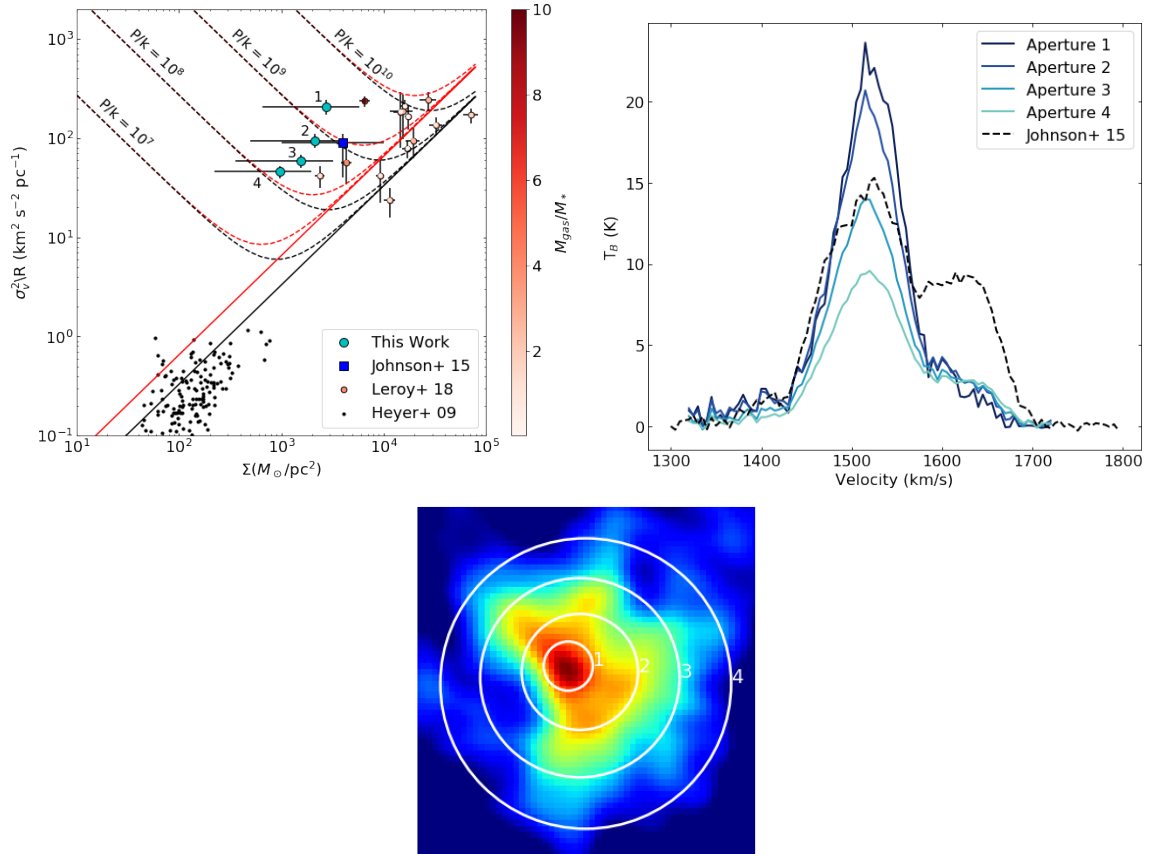


Fig. 2.10.— *Top left*: The size-linewidth coefficient (σ_v^2/R) and surface density (Σ) for the Firecracker cloud as measured in different apertures (cyan circles) and in previous analysis by Johnson et al. (2015) (blue square). Also shown are young massive clusters from Leroy et al. (2018) in NGC 253, colored based on the ratio of M_{gas}/M_* , and typical molecular clouds observed in the Milky Way by Heyer et al. (2009) for comparison (black circles). The black line corresponds to virial equilibrium, while the red lines correspond to free fall conditions (Field et al. 2011). *Top right*: The $^{12}\text{CO}(3-2)$ line profiles in each of the four regions as well as from previous analysis by Johnson et al. (2015) (dashed line). The linewidth remains approximately the same in each region, despite the large changes in peak brightness temperature. The larger contribution from the second velocity component in the Johnson et al. (2015) line profile is likely due to their larger synthesized beam ($0.56'' \times 0.43''$) as compared to $0.16'' \times 0.15''$). *Bottom*: The four chosen apertures plotted on the $^{13}\text{CO}(2-1)$ moment 0 map. These have radii of $0.06''$, $0.14''$, $0.24''$, and $0.35''$ for Apertures 1, 2, 3, and 4, which correspond to sizes of 6.4, 15, 26 and 37 pc respectively.

where $n_e = \Pi \langle n_e \rangle$, and we take $\Pi = 0.5$ (Johnson et al. 2015). If we calculate this pressure for Aperture 2 and a mid-range mass estimate, the mass within the aperture is $M = 1.5 \times 10^6 M_\odot$, $R = 15$ pc, and $\sigma_V = 38$ km s⁻¹, so the external pressure for this aperture would be $P_e/k = 4 \times 10^8$ K cm⁻³. This measurement varies greatly with aperture selection and the mass estimate, and the full range of possible values is given in Table 2.5. This pressure range agrees with the values expected from Figure 2.10.

2.3.7 Kinematics of the Local Environment

To examine the larger local environment that may be causing the high external pressure derived above, we look at the kinematics of the surrounding region. If the source of pressure is ram pressure from the collision of molecular clouds, we might expect to see a “broad bridge” feature connecting the two clouds in the position-velocity diagram, as described by Haworth et al. (2015).

Using ¹²CO(2-1) emission of the Firecracker and the surrounding giant molecular cloud, we created a total intensity (moment 0) map by integrating over the velocity range 1430–1555 km s⁻¹, and a mean velocity (moment 1) map using a 0.6 mJy threshold. These maps were used to choose an angle and cut for a position-velocity diagram that would capture the proposed collision axis where the velocity gradient is greatest. These cuts and the resulting position-velocity diagram are shown in

Table 2.5: Molecular Cloud Derived Properties

Radius (pc)	M (10 ⁶ M _⊙)	T _{Kin} (K)	n _{H₂} (cm ⁻³)	P/k (K cm ⁻³)
22	1–9	25–40	360–3150	0.5–22 × 10 ⁸

Notes. The characteristic radius is the radius of a circle with the same area as that enclosed by the 5σ contour of the ¹³CO(2-1) moment 0 map, with the assumption that the distance to the Antennae system is 22 Mpc. We also assume that

$$T_x \simeq T_{Kin}.$$

Figure 2.11.

The Firecracker does appear as a bridge between the two adjacent clouds, although it appears somewhat spatially separated from each. Its morphology is different from that of the broad bridge feature from Haworth et al. (2015), but this may be due to a difference in viewing angle, as the line-of-sight of the simulated position-velocity diagrams from Haworth et al. (2015) were made directly along the collision axis. This would seem to suggest that cloud-cloud collision is likely occurring, and may be the source of pressure that we observe.

2.3.8 HCN and HCO⁺

HCN and HCO⁺ are both tracers of dense gas. HCN has an optically thin critical density of $n_{crit} = 1.7 \times 10^5 \text{ cm}^{-3}$ at 50 K, and an upper state energy of $T = 4.3 \text{ K}$ (Shirley 2015). HCO⁺ has $n_{crit} = 2.9 \times 10^4 \text{ cm}^{-3}$ at 50 K for optically thin gas and a very similar upper state energy of $T = 4.3 \text{ K}$. Despite this similarity, these molecules do not appear to always be spatially correlated (Johnson et al. 2018). This trend is continued in the Firecracker region.

Both of these species are weakly detected, with HCN(4-3) at the 4.1σ level and HCO⁺(4-3) at the 5.5σ level in the total intensity (moment 0) map. The parameters of the data cube are given in Table 2.2. We created total intensity maps for each transition by integrating over the velocity range 1430–1565 km s⁻¹, and these are shown in Figure 2.12. In these images, it is apparent that the morphologies of the emission from these two molecules are quite different from each other (Figure 2.12).

Integrated fluxes from HCN(4-3) and HCO⁺(4-3), as well as the ¹²CO(2-1), ¹²CO(3-2), and ¹³CO(2-1) lines, for each aperture described in Figure 2.10 are given in Table 2.6.

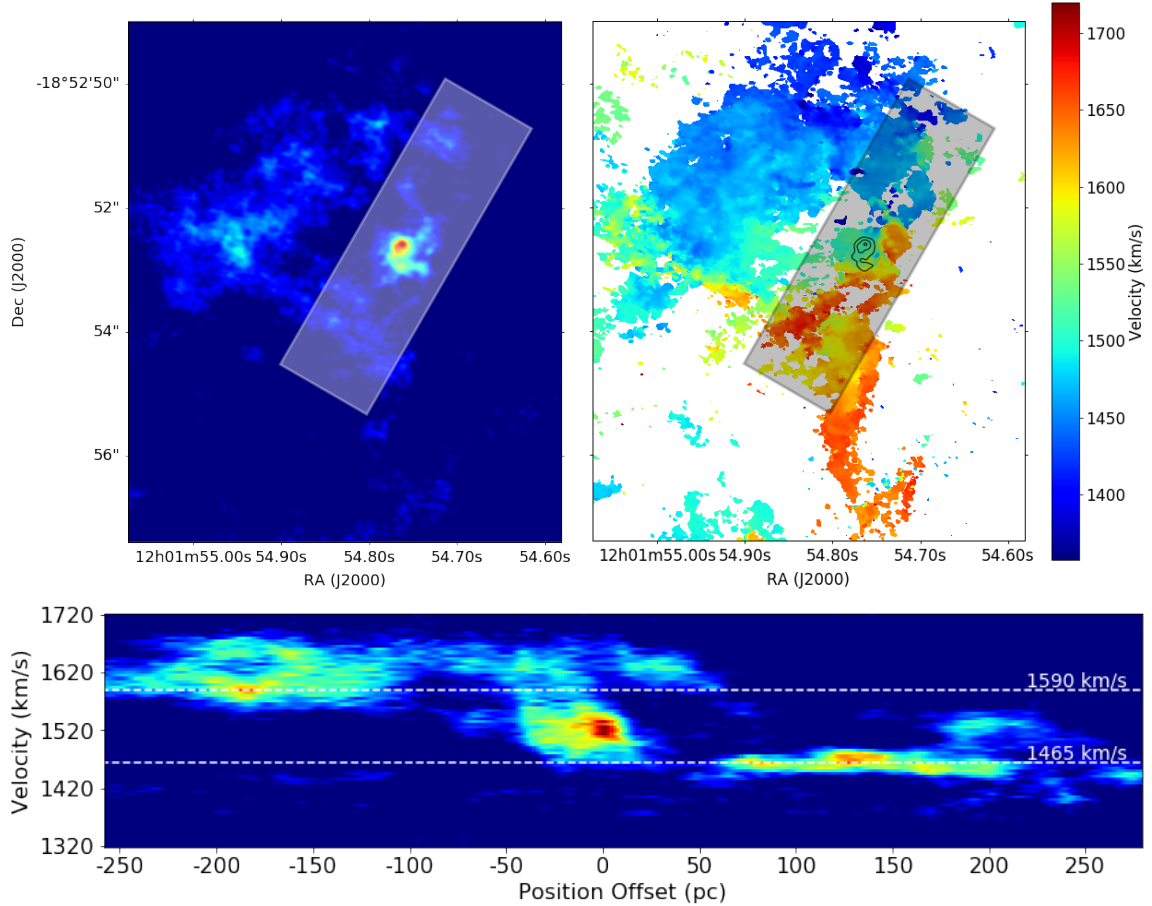


Fig. 2.11.— *Top Left*: Moment 0 map of the Firecracker and the surrounding region, with the cut for the position-velocity diagram over plotted as a white rectangle. *Top Right*: Moment 1 map of the same region, with the same cut shown as a gray rectangle. The cut was taken to roughly align with the greatest velocity gradient, which we expect would be the collision axis. Contours of the moment 0 of the Firecracker cloud are shown in black. *Bottom*: Position-velocity diagram of the Firecracker from the cut shown above. The Firecracker cloud is seen in the center, and appears to be a ‘bridge’ between the clouds on either side, from the top left of the plot to the bottom right. This bridge feature may be indicative of cloud-cloud collision, providing the high external pressure inferred in the Firecracker. The velocities of the colliding clouds are shown with the dotted lines, suggesting a relative collision velocity of $\sim 125 \text{ km s}^{-1}$.

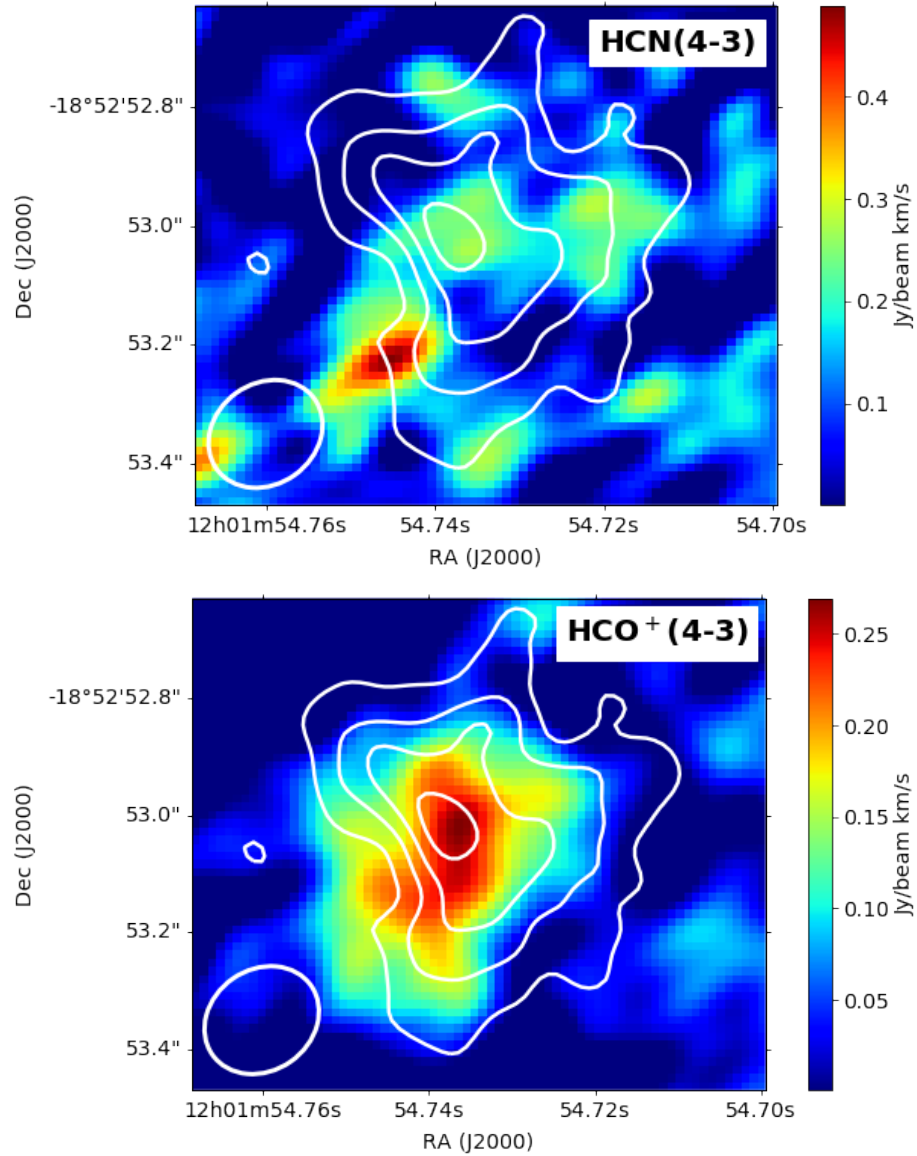


Fig. 2.12.— *Top*: Total intensity (moment 0) map of HCN(4-3). *Bottom*: Total intensity (moment 0) map of HCO⁺(4-3). These total intensity maps were created by integrating across the velocity range 1430–1565 km s⁻¹. Both have contours of ¹³CO(2-1) moment 0 overplotted. Synthesized beams are 0.17" × 0.20" and 0.17" × 0.21" for HCN and HCO⁺ respectively.

From these moment 0 maps, we determine the average surface brightness of these two molecular lines in a 0.35" region around the Firecracker cloud (Aperture 4 in Figure 2.10), is 33 K km s⁻¹ for HCN(4-3), and 22 K km s⁻¹ for HCO⁺(4-3). These are much lower than the values measured in this region by Schirm et al. (2016), which are 46 K km s⁻¹ for HCN(1-0) and 73 K km s⁻¹ for HCO⁺(1-0). These values from Schirm et al. (2016) have been updated to account for a beam filling factor of 0.02 that we determine based on the cloud's now-resolved size of 0.21" and the Schirm et al. (2016) beam of 1.52"×1.86" for HCN(1-0) and 1.51"×1.85" for HCO⁺(1-0). This is expected, since Schirm et al. (2016) present their measurements as upper limits due to the low resolution likely causing contamination from the surrounding region. We also expect that HCN(4-3) and HCO⁺(4-3) are not thermalized with respect to HCN(1-0) and HCO⁺(1-0), which further accounts for our lower surface brightness.

We can next compare the relative line strengths in the Firecracker region to follow up on the analysis of Johnson et al. (2018), which suggested that HCN and HCO⁺ strengths are associated with the evolution of proto-clusters. To do this, we convolve these images, as well as the ¹²CO(2-1) emission, to the same beam size (0.17"×0.21") and look at the ratios of HCN(1-0)/HCO⁺(4-3) and HCO⁺(1-0)/¹²CO(2-1), using

Table 2.6: Integrated Fluxes of Emission Lines

	Ap. 1	Ap. 2	Ap. 3	Ap. 4
S _{¹²CO(2-1)}	0.96	4.5	9.3	14
S _{¹²CO(3-2)}	1.7	8.3	18	26
S _{¹³CO(2-1)}	0.04	0.19	0.50	0.90
S _{H₂CO(4-3)}	0.07	0.26	0.63	1.1
S _{HCO⁺(4-3)}	0.07	0.30	0.64	0.78

Notes. All integrated fluxes are measured in Jy km s⁻¹. Selected apertures are described in Section 2.3.6, shown in Figure 2.10, and have radii of 0.06", 0.14", 0.24", and 0.35" for Apertures 1, 2, 3, and 4, which correspond to sizes of 6.4, 15, 26 and 37 pc respectively.

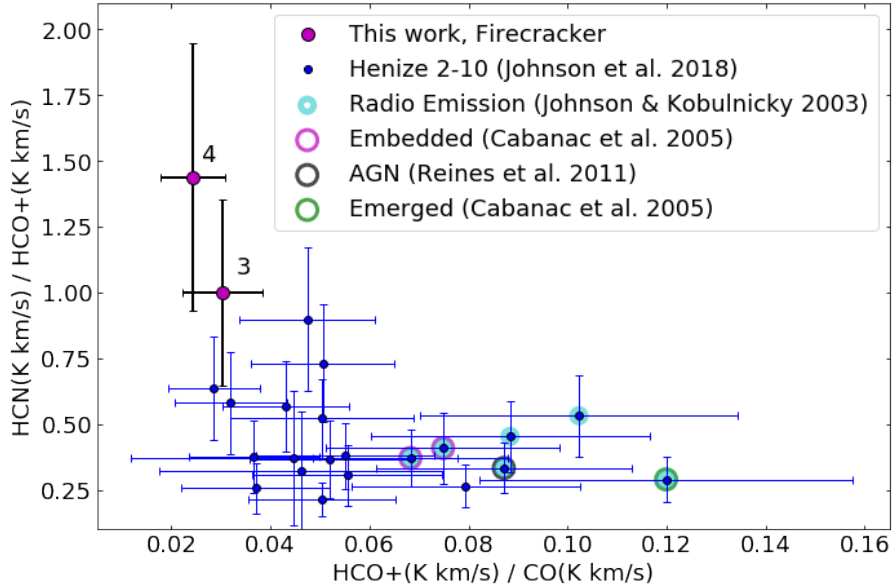


Fig. 2.13.— Ratios of HCN/HCO⁺ and HCO⁺/CO for natal SSCs in Henize2-10 from Johnson et al. (2018) (blue) and the Firecracker (magenta). For the Firecracker, the HCO⁺/CO ratio is a lower limit. Apertures for the Firecracker are defined as in Figure 2.10, where Apertures 1 and 2 are not included since the synthesized beam is now larger than those regions. The trend in these regions from the pre-SSC Firecracker in the upper left to the older, star forming clusters in the bottom right suggests that HCN, HCO⁺, and CO may be tracing cluster evolution.

the average surface brightness in K km s⁻¹ (Figure 2.13). We look at these ratios in Apertures 3 and 4 as defined in the right panel of Figure 2.10. Apertures 1 and 2 are not included since their radii are smaller than the synthesized beam for the new images.

We compare these ratios to those measured for HCN(1-0), HCO⁺(1-0), and CO(2-1) in potential natal-SSCs found in the Henize 2-10 dwarf galaxy by Johnson et al. (2018). These natal-SSCs were selected via peaks in ¹²CO(2-1) emission, and 6 of the 21 regions had associated thermal radio emission (Johnson & Kobulnicky 2003), indicative of stars having already formed. Two of these regions with associated radio emission are also shown to have high optical extinction, $A_V > 10$ (Cabanac

et al. 2005), implying that the clusters are still heavily embedded and have only recently formed stars. Another region exhibits nonthermal emission, suggesting a low-luminosity AGN (Reines et al. 2011) or an older evolutionary state, while another region includes several supernova remnants, has emerged from its surrounding gas, and has a cluster age of > 6 Myr (Cabanac et al. 2005).

In Figure 2.13, we compare the two Firecracker apertures to those in Henize 2-10 and see that our new data supports the trend found by Johnson et al. (2018). As clusters evolve, these two line ratios appear to change, with regions that have already formed stars showing a higher ratio of HCO^+/CO and a lower HCN/HCO^+ ratio than regions at an earlier stage of evolution.

Note that in this work we measure $\text{HCN}(4-3)$ and $\text{HCO}^+(4-3)$ rather than $\text{HCN}(1-0)$ and $\text{HCO}^+(1-0)$ as was used by Johnson et al. (2018). Due to the same upper state energies for HCN and HCO^+ , we expect that the ratio of HCN/HCO^+ is not much affected by this difference, but the measured values of the ratio HCO^+/CO are lower limits for the Firecracker cloud.

We also note that the ratios seen in Figure 2.13 differ for the two regions within the Firecracker, with values measured in Aperture 4 indicating a younger evolutionary stage than in Aperture 3. This seems to once again confirm the trend, as we would expect using a smaller aperture focused on the central region would include the gas most likely to begin star formation first, while the larger aperture includes more surrounding gas that has not yet begun evolving towards star formation. Thus the gas within Aperture 3 is expected to be at a more evolved state than the gas averaged within Aperture 4.

For comparison, measurements in Henize 2-10 by Johnson et al. (2018) used an aperture of $0.8''$, which at a distance of 9 Mpc corresponds to a physical size of 35

pc. This is approximately the same size as Aperture 4 in the Firecracker analysis.

2.4 Discussion

2.4.1 Internal Structure

In Figure 2.9, we show that the radial profile of the derived column density can be fit to a Bonnor-Ebert profile with $\xi_{max} = 3.4 \pm 0.4$, implying that the cloud might be described by an isothermal, self-gravitating, pressure-confined sphere.

If the fit is taken to be a true indication of the physics governing the cloud, then the value of ξ_{max} that characterizes the best fit has further implications for the structure and state of the Firecracker cloud. It was shown by Bonnor (1956) that values of $\xi_{max} > 6.5$ are gravitationally unstable and will collapse. This would imply that our cloud, which is fit by $\xi_{max} = 3.4 \pm 0.4$, is still stable. This agrees with the results found in the left panel of Figure 2.10, which show that the cloud is not experiencing free-fall collapse. This also further supports the belief that this cloud has not begun star formation and is an example of an undisturbed precursor cloud.

Using the parameter $\xi_{max} = 3.4$, we can also determine from the numerical solution of the Lane-Emden equation that the density contrast from the center to the boundary of the cloud would be $\rho_C/\rho_R = 3.2$. We can define a dimensionless mass,

$$m \equiv \frac{P_e^{1/2} G^{3/2} M}{a^4} = \left(4\pi \frac{\rho_C}{\rho_R} \right)^{-1/2} \xi_{max}^2 \left. \frac{d\psi}{d\xi} \right|_{\xi_{max}} \quad (2.8)$$

where P_e is the bounding pressure, M is the total mass, a is the isothermal sound speed, and all of the values on the right side of the equation are known via the numeric solution to the Lane-Emden equation and the boundary condition of $\xi_{max} = 3.4$. We find that the dimensionless mass for the Firecracker cloud is $m = 0.84$. This is less

than the critical dimensionless mass derived by Bonnor (1956), $m = 1.18$, which is expected since we already demonstrated the cloud is stable.

We can then derive from our definitions of ξ , m , and the isothermal pressure equation of state that

$$a^2 = \frac{\xi_{max}}{m} \frac{GM}{R} \left(\frac{\rho_R}{\rho_C} \right)^{1/2} \left(\frac{1}{4\pi} \right)^{1/2} \quad (2.9)$$

which allows us to determine a , the characteristic velocity of the equation of state in the Firecracker cloud. This velocity would be the isothermal sound speed, but in the Firecracker, we are likely dominated by microturbulence rather than thermal velocities. Depending on the value taken for the total mass, this velocity falls in the range $a = 10 - 30 \text{ km s}^{-1}$. This is within a factor ~ 2 to the velocity dispersion we measure in the cloud ($\sigma_V \sim 37 \text{ km s}^{-1}$).

From this value for a^2 , we can also derive another estimate of the external pressure confining the cloud, using an equation derived from the definition of m :

$$P_e = \frac{m^2 a^8}{M^2 G^3} \quad (2.10)$$

Taking the range of mass estimates, the external pressure in the Bonnor-Ebert profile would be $P_e/k = 0.05 - 4 \times 10^8 \text{ K cm}^{-3}$, which agrees with the lower end of the pressure range determined in Section 2.3.6.

While these results do agree with expectations from the rest of our analysis, we also note that the profile is also consistent with a Gaussian profile, and also that it is possible for cores to be fit with a Bonnor-Ebert profile despite not actually obeying the physics of a stable, isothermal, pressure-confined sphere. Ballesteros-Paredes et al. (2003) show that 65% of the dynamic cores in their hydrodynamic models can be fit by Bonnor-Ebert profiles, and nearly half of these fits would suggest the dynamically

evolving clouds are in hydrostatic equilibrium. Furthermore, their work shows that the parameters determined from the fits often varied from the actual values and depended on which projection of the core was used. We therefore are cautious in drawing firm conclusions from this fitted Bonnor-Ebert profile.

2.4.2 High Pressure Environment

To determine the source of the high external pressure implied by Figure 2.10 and the Bonnor-Ebert fit, we look to the encompassing cloud and its kinematics. Johnson et al. (2015) estimate that the weight of the surrounding super giant molecular cloud would only reach $P/k \sim 10^7 \text{ K cm}^{-3}$. This falls short of the expected external pressure by one or two orders magnitude.

One mechanism that may be able to increase the pressure in the region to the values we observe is ram pressure from colliding filaments. The Firecracker cloud is located at the confluence of two CO filaments identified by Whitmore et al. (2014), the region has a large velocity gradient across it, and is associated with strong H₂ emission (Herrera et al. 2011, 2012). Work by Wei et al. (2012) also shows that the overlap region may be dominated by compressive shocks. All of these would be consistent with collisions causing the high external pressure observed for the Firecracker cloud. Furthermore, the now-resolved irregular structure of the cloud is consistent with the source of pressure being non-isotropic, as we would expect in the case of colliding gas filaments. This type of cloud-cloud collision has also been invoked as a trigger for massive star formation in several young clusters within the Milky Way and LMC, such as the Orion Nebula Cluster (Fukui et al. 2018, and references therein). Oey et al. (2017) also see two kinematic components in a young SSC, which they suggest could be infall from cloud-cloud collision, or outflow due to feedback from the newly

formed stars.

Examination of the position-velocity diagram (Figure 2.11) shows a hint of a “broad bridge” feature, described by Haworth et al. (2015) to be a signature of cloud-cloud collision. If this is indeed a case of cloud-cloud collision, we can use the X_{CO} factor derived in Section 2.3.4 to determine the density of the clouds on either side of the Firecracker. Taking the average value of $X_{CO} = 0.61 \times 10^{20} \text{ cm}^{-2} (\text{K km s}^{-1})^{-1}$, and assuming that the cross sections along the line of sight of the colliding clouds are twice the Firecracker’s diameter, so have a depth of 88 pc, we find that the density of the colliding clouds is approximately $\rho \sim 10^{-21} \text{ g cm}^{-3}$ ($n_{H_2} \sim 220 \text{ cm}^{-3}$).

From Figure 2.11, the velocities of the two colliding clouds are approximately 1465 km s^{-1} and 1590 km s^{-1} , suggesting that the projected velocity difference at which they would be colliding is $v \sim 125 \text{ km s}^{-1}$. Taking the ram pressure to be $P = \rho v^2$, this would imply that the pressure caused by such a cloud-cloud collision would be $P/k \sim 1.1 \times 10^9 \text{ K cm}^{-3}$. While this is a fairly rough estimate of the ram pressure, it demonstrates that such a scenario would be capable of providing the high external pressures required for the Firecracker cloud to be bound.

Furthermore, this cloud-cloud collision scenario would imply that there will be a continued inflow of gas as the cloud begins to form a cluster of stars. Such an inflow would allow for accretion along filaments during the formation process, an important feature of the simulated cluster formation by Howard et al. (2018). This would support their suggestion that massive clusters can be formed by the same mechanisms that form smaller, less massive clusters.

2.4.3 Comparisons to Other Molecular Clouds

To the best of our knowledge, the Firecracker is the only object that has been identified as having the properties necessary for SSC formation, while also having no detected thermal radio emission above a level of $N_{\text{Lyc}} \approx 6 \times 10^{50} \text{ s}^{-1}$, which corresponds to ~ 60 O-type stars, or $M_* \lesssim 10^4 M_\odot$. Given the cloud's mass of $M_{\text{gas}} = 1 - 9 \times 10^6 M_\odot$, this upper limit for stars formed is still at least two orders of magnitude less than the cloud's mass and so the Firecracker is likely to still be at a very early stage of cluster formation. Comparisons for this cloud must then come from SSCs that have detected star formation or galactic clouds that are forming less massive clusters that do not have the potential to form SSCs (where SSCs are expected to need $\gtrsim 10^5 M_\odot$ to survive to be globular clusters).

Leroy et al. (2018) identified a population of young massive clusters that have begun forming stars at detectable levels in NGC 253 ($N_{\text{Lyc}} > 5 \times 10^{50} \text{ s}^{-1}$), but most of which are still embedded in their natal material. They have gas masses in the range $10^{3.6} - 10^{5.7} M_\odot$, stellar masses in the range $10^{4.1} - 10^{6.0} M_\odot$, and FWHM sizes in the range 1.2-4.3 pc. Most of the clusters fall along the line for either virial equilibrium or free fall in the left panel of Figure 2.10, but a couple with a notably higher M_{gas}/M_* ratio are above these lines, suggesting that they would require a high external pressure to remain bound, similar to the Firecracker cloud. This may indicate a trend with evolution, since clusters at an early stage of formation will have turned less of their gas into stars. This would then support a scenario in which massive clusters are formed in high pressure environments, and then as stars form and the cluster evolves, the high pressure dissipates or is dispelled.

We also note that the Firecracker shares several properties with the molecular cloud Sgr B2 in the CMZ of the galaxy. Sgr B2 has a mass of $8 \times 10^6 M_\odot$ and a diameter

of 45 pc (Schmiedeke et al. 2016), which are well-matched to the Firecracker. It is also in a high pressure environment, with $P/k \sim 10^8 \text{ K cm}^{-3}$ measured for embedded cores in the CMZ (Walker et al. 2018). High resolution ($\sim 0.002 \text{ pc}$) observations see this cloud break into several smaller clumps, the largest of which, Sgr B2 M, has a radius of $\sim 0.5 \text{ pc}$, $M_{\text{gas}} \sim 10^4 M_{\odot}$, and $M_* \sim 1.5 \times 10^4 M_{\odot}$ (Schmiedeke et al. 2016; Ginsburg et al. 2018). This comparison suggests that at higher resolutions, we may see the Firecracker break into smaller protoclusters, which may or may not result in a single bound cluster.

We also note however that the present day CMZ is a different environment from the Antennae overlap region, and the presence of a large SSC population in the Antennae ($>2,700$ clusters with $M_* > 10^5 M_{\odot}$; Whitmore et al. 2010) and no SSCs in the Milky Way (no young clusters with $M_* > 10^5 M_{\odot}$; Portegies Zwart et al. 2010) also suggests that similar massive molecular clouds in the two regions could be expected to form different objects.

Leroy et al. (2018) also examine Sgr B2 as a comparison to their massive clusters and find that at their resolution of 1.9 pc, Sgr B2 would have a wider profile, narrower line width, and lower brightness temperature, suggesting it is a less dense version of the clouds forming clusters in NGC 253. These profiles extend to radii of 10 pc, so cannot be directly compared to the Firecracker, since our resolution is $\gtrsim 10 \text{ pc}$.

2.4.4 Tracing Cluster Evolution

The trend shown in Figure 2.13 indicates that both the ratios HCN/HCO^+ and HCO^+/CO are affected as the cluster evolves. HCN/HCO^+ appears to decrease with age, while HCO^+/CO appears to increase with age. This evolution is shown schematically in Figure 2.14.

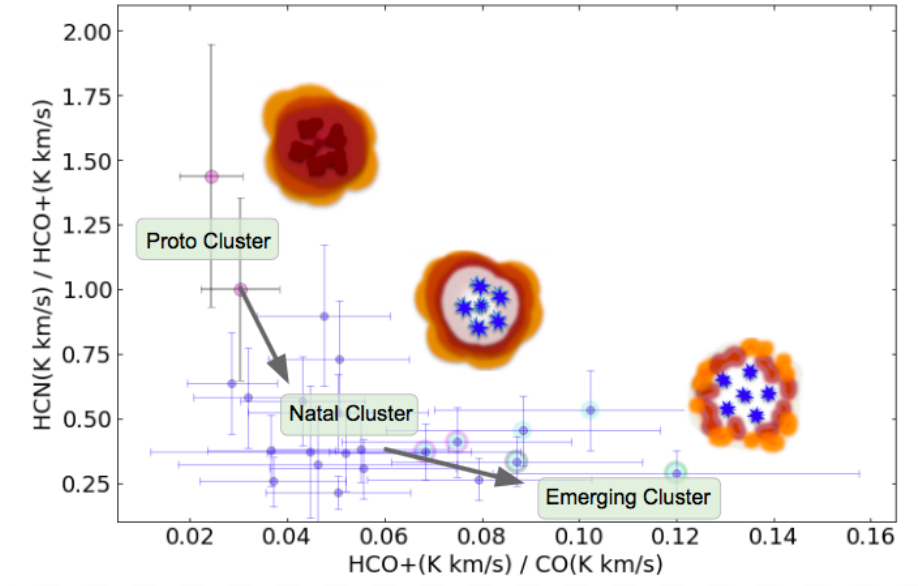


Fig. 2.14.— Ratios of HCN/HCO^+ and HCO^+/CO as shown in Figure 2.12, with a schematic showing the stages of evolution as suggested by the trend in the plot. HCN/HCO^+ appears to decrease with age, while HCO^+/CO appears to increase with age. This trend may allow us to use HCN and HCO^+ as a diagnostic of evolutionary state in unresolved cluster-forming systems.

The mechanisms most likely to be driving the change in HCO^+/CO as discussed in Johnson et al. (2018) are either the photo-enhancement of HCO^+ in the PDRs around newly formed stars (Ginard et al. 2012) or the dissociation of CO due to radiation from massive stars. The HCO^+ enhancement in these more evolved regions would also explain the decrease in HCN/HCO^+ that we observe. This trend could also be caused by a decrease in gas density as the star clusters evolve, causing the density of the gas to drop below the critical density of HCN while remaining higher than the critical density of HCO^+ .

If the increase in the HCO^+/CO ratio is due in part to the dissociation of CO as stars form, this would also be consistent with the analysis of Whitmore et al. (2014), which used CO brightness as a diagnostic of evolutionary stage for clusters.

2.4.5 CO-to-H₂ Conversion Factor

In Figure 2.8, we see that X_{CO} varies spatially by up to $\sim 80\%$ of the average within the Firecracker region, and that this variation is not solely a result of Gaussian noise in the measurements. X_{CO} is expected to vary based on many parameters: high densities will cause X_{CO} to increase, while high gas temperatures and super-virial velocity dispersions will lead to lower X_{CO} values (Bolatto et al. 2013). This results in a complicated picture for starbursting regions which experience all of these effects at once. Computational models by Narayanan et al. (2011) demonstrate that X_{CO} is lowest in regions of high SFR.

Comparing these predictions to the observed spatial variations in the Firecracker, we note that the central peak of the ¹³CO emission, where we expect initial collapse and star formation to occur, does not correspond to a particularly low or high value of X_{CO} in the region as we might expect. Rather, the maximum and minimum locations occur around the edge of the cloud and do not appear to be correlated with the mass surface density, temperature, or velocity dispersion. This may simply be due to the complicated interplay of these three parameters' effects on X_{CO} .

2.4.6 Star Formation Efficiency

Another important parameter for studying the formation of globular clusters is the star formation efficiency (SFE), or how much of the gas in a molecular cloud is converted to stars. This value is defined as $SFE = M_{stars}/(M_{gas} + M_{stars})$. This parameter is important for the survival of the cluster, since much of the remaining gas will be dispersed after stars have formed. If the gas accounts for a large amount of the cluster's mass, the cluster will not remain bound after it has dispersed. Due to this type of argument, we have long believed that SFEs of $\sim 50\%$ are required to

form globular clusters that last for > 10 Gyr (Geyer & Burkert 2001). However, more recent simulations have shown we may be able to relax that constraint to as little as $\sim 5\%$, although a higher SFE makes a cluster more likely to remain bound (Pelupessy & Portegies Zwart 2012). This value more closely matches values of $< 10\%$ for the SFE that has been measured in galactic clouds (Evans et al. 2009).

Recent computational models of massive star cluster formation show that there may be a correlation between the mass surface density, Σ , and the star formation efficiency. Both Kim et al. (2018) and Grudić et al. (2018) show clusters attaining SFEs of $\sim 50\%$ at high surface densities, $1300 M_{\odot} \text{ pc}^{-2}$ in Kim et al. (2018) and $3820 M_{\odot} \text{ pc}^{-2}$ in Grudić et al. (2018). These surface densities are well matched to those we measure in the Firecracker cloud, which range from $1000 - 6000 M_{\odot} \text{ pc}^{-2}$, depending on the assumed mass estimate. This has promising implications for the potential of the Firecracker to form a bound SSC. However, we also note that neither of these models take into account a high external pressure surrounding the precursor cloud as is inferred for the Firecracker for it to be bound. This external pressure would be likely to have strong implications for the outcome of the simulations, as the initial velocity dispersion of the gas would be much higher in this case.

Work done by Matthews et al. (2018) attempts to observationally constrain the SFE, measuring the instantaneous mass ratio (IMR) in the Antennae overlap region. The IMR is an observational analog, defined as $\text{IMR} = M_{stars}/(M_{gas} + M_{stars})$, which would correspond to the SFE of an ideal system that had formed all its stars without yet dispelling its gas. Matthews et al. (2018) find no correlation of IMR with surface density, and find that very few clusters in the region show an IMR greater than 20% despite measuring surface densities up to $\sim 10^4 M_{\odot} \text{ pc}^{-2}$. This suggests the theoretical work may be optimistic in predicting SFEs in starbursting regions such as

the Antennae galaxies.

2.5 Conclusions

We present ALMA observations of the proto-SSC Firecracker cloud in the overlap region of the Antennae, looking at emission from $^{12}\text{CO}(2-1)$, $^{12}\text{CO}(3-2)$, $^{13}\text{CO}(2-1)$, $\text{HCN}(4-3)$, and $\text{HCO}^+(4-3)$. These molecular lines were used to characterize the cloud and the surrounding environment at resolutions as low as $\sim 0.1''$ (10 pc). The findings are summarized below.

- We determine the mass of the cloud to be in the range $1\text{--}9\times 10^6 M_\odot$ and its characteristic radius is 22 pc. These both agree with previous measurements by Johnson et al. (2015) and are consistent with the cloud having the potential to form a super star cluster.
- We do not detect continuum emission at any of the three observed frequencies. This allows us to put an upper limit on the mass ($9\times 10^6 M_\odot$), as well as constrain abundance ratios of $^{12}\text{CO}/^{13}\text{CO}$ and $\text{H}_2/^{12}\text{CO}$ within this region. Certain combinations of these two ratios are disallowed by this upper mass limit.
- We calculate the CO-to- H_2 conversion factor and determine that it varies spatially by up to $\sim 80\%$ of the average, with average values in the range $X_{\text{CO}} = (0.12 - 1.1) \times 10^{20} \text{ cm}^{-2} (\text{K km s}^{-1})^{-1}$. This is consistent with X_{CO} values typically adopted in starburst regions. The spatial variations cannot be explained solely by Gaussian noise in the measurements, and do not align with areas expected to have the greatest SFR. Instead, the variations likely depend on a complex combination of temperature, density, and velocity dispersion.

- We find that the radial profile of the column density can be fit by a Bonnor-Ebert profile characterized by $\xi_{max} = 3.4 \pm 0.4$, and that this profile is also consistent with a Gaussian profile. The Bonnor-Ebert fit would suggest that the Firecracker cloud might be described as an isothermal, self-gravitating, pressure-confined sphere, similar to those forming clusters in our galaxy on smaller scales. This profile would also suggest that the cloud is gravitationally stable. We caution though that simulations of dynamic clouds not in equilibrium have also been shown to be fit by Bonnor-Ebert profiles, which may be the case here for the Firecracker cloud.
- We determine from surface density and size-linewidth parameters that the cloud is not in free-fall or virial equilibrium, and so must be subject to a high external pressure, $P/k \gtrsim 10^8 \text{ K cm}^{-3}$, if it is a bound structure. A comparison with young massive clusters in NGC 253 that have detected star formation suggests a potential trend in which clusters with a low M_{gas}/M_* ratio (and so are likely more evolved) are near virial equilibrium or free fall, while clusters with a higher M_{gas}/M_* would require similar high pressures to remain bound. This would agree with theoretical predictions that high pressure environments are necessary for cluster formation. It also agrees with the Bonnor-Ebert fit’s prediction that the cloud is pressure-bound and gravitationally stable.
- The position-velocity diagram of the Firecracker and its surrounding cloud shows what may be a “broad bridge” feature, which is indicative of cloud-cloud collision. An estimate of the density and relative velocity of the colliding filaments suggests that they are capable of producing a ram pressure of $\sim 1.1 \times 10^9 \text{ K cm}^{-3}$, consistent with the high pressures needed for the cloud to be bound.

- We demonstrate that the Firecracker cloud further supports the findings of Johnson et al. (2018) that HCN and HCO⁺ appear to trace the evolutionary stage of clusters. As stars begin to form, the HCN/HCO⁺ ratio decreases while the HCO⁺/CO is enhanced. This could be due to some combination of enhancement of HCO⁺ in PDRs as stars form, dissociation of CO from massive stars, and changes in gas density as the cluster evolves.
- The measured surface density range of $\Sigma = 1000 - 6000 M_{\odot} \text{ pc}^{-2}$ may indicate that the cloud is capable of a star formation efficiency as high as $\sim 50\%$. A high SFE is predicted to be necessary for a globular cluster to form and remain bound throughout its lifetime.

Chapter 3

A Comparative Study of Spiral Galaxy Environments

The text in Chapter 3 will be submitted for publication in the *Astrophysical Journal* as “ALMA-LEGUS: The Influence of Galactic Environment on Molecular Cloud Properties.”

3.1 Introduction

At low-redshifts, the majority of star formation takes place in spiral galaxies (Brinchmann et al. 2004). This means that to understand star formation in the local universe, we need to understand the influence of spiral structure on the physical conditions of the molecular gas and the processes by which that gas is converted into stars.

Much work has been done on understanding how spiral density waves and stellar feedback impact cloud formation, collapse, and dispersal, both from simulations and observations. There have been several surveys to study the molecular gas in nearby spiral galaxies at the scale of giant molecular clouds (GMCs), such as PAWS

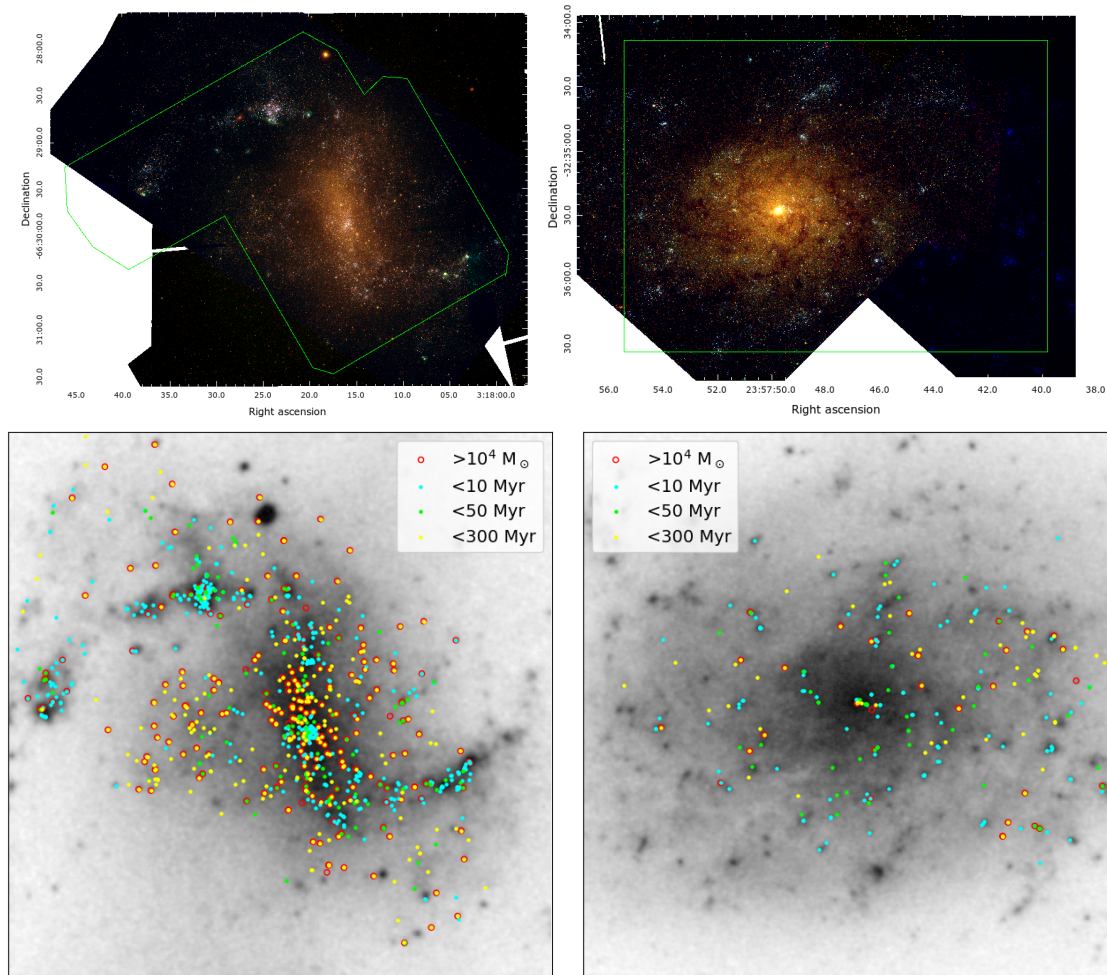


Fig. 3.1.— *Top*: Hubble Space Telescope images of NGC 1313 (left) and NGC 7793 (right) using filters F814W (red), F555W (green), and F336W (blue) from the LEGUS survey. Overplotted are the ALMA CO(2-1) observation footprints. *Bottom*: Positions of clusters identified in the LEGUS catalogs (methodology described by Adamo et al. (2017)), colored by age with clusters younger than 10 Myr in cyan, 10-50 Myr in green, and 50-300 Myr in yellow, plotted overtop the DSS2-red images. Clusters that are more massive than $10^4 M_{\odot}$ are outlined in red. NGC 1313 has significantly more star clusters overall than NGC 7793, even after accounting for their differing SFRs, and especially has more red-outlined massive star clusters, both by number and by fraction of the total cluster mass.

(PdBI Arcsecond Whirlpool Survey), which mapped M51 in CO(1-0) at 40 pc resolution (Schinnerer et al. 2013), CANON (CArma and NObeyama Nearby galaxies), which mapped the inner disks of five spiral galaxies in CO(1-0) at 62-78 pc resolution (Donovan Meyer et al. 2013), PHANGS-ALMA (Physics at High Angular resolution in Nearby Galaxies), which mapped 90 galaxies in CO(2-1) at ~ 100 pc resolution (Leroy et al. 2021), and most recently the barred spiral galaxy M83 was mapped in CO(1-0) at 40 pc resolution (Koda et al. 2023).

These studies have consistently shown that at ~ 40 -100 pc resolutions, the molecular gas in spiral arms tend to be brighter and have higher surface densities, velocity dispersions, and pressures than gas in the interarm regions, especially when a strong bar is present (Colombo et al. 2014; Sun et al. 2018; Sun et al. 2020; Rosolowsky et al. 2021; Koda et al. 2023). They have also shown that the slope of the distribution of cloud masses is shallower and truncates at higher masses in the spiral arms than interarm regions (Koda et al. 2009; Colombo et al. 2014; Rosolowsky et al. 2008), but that despite the greater amount of star formation in the arms, the depletion time in the arms is not significantly shorter (Querejeta et al. 2021). Rather, Yu et al. (2021) find that the depletion time of the gas is more closely related to the strength of the spiral arms, with stronger arms being associated with shorter depletion times and higher specific SFR.

These observations are well-modeled by simulations, especially those of grand design spiral galaxies. Simulations also find that the spiral arms are generally the sites of active star formation rather than the interarm regions (Dobbs et al. 2013), and that GMCs are assembled in the spiral arms and are then sheared into smaller clouds in the interarm regions, resulting in lower mass clouds being found in the interarm regions (Dobbs & Pringle 2013). Breaking up massive clouds via shear is

well-matched to the lifetimes of clouds measured in the interarm region of M51 (Meidt et al. 2015) and of M83 (Koda et al. 2023). Massive clouds are expected to be denser and have longer lifetimes, allowing them to form more massive clusters in the spiral arms before they are dispersed (Dobbs et al. 2011, 2017). Meidt et al. (2013) propose that the higher amount of streaming motion in the interarm regions relative to the arms stabilizes the clouds and suppresses collapse.

Pettitt et al. (2020) find that cause of the spiral pattern (e.g. density wave, interaction, or underlying gravitational instability) has no affect on the simulated GMC properties. However, GMCs show a shallower mass distribution with more massive clouds after the galaxy experiences a tidal fly-by, especially in the spiral arms, and many of the clouds become unbound during this process (Pettitt et al. 2018; Nguyen et al. 2018).

In flocculent spiral galaxies, the distinction between interarm and arm regions is less robust, but Dobbs et al. (2019) still find a difference in the steepness of the cloud mass distribution, where star-forming clouds have a shallower mass distribution than non-star-forming clouds, similar to the difference between arm and interarm regions in grand design galaxies. However, Dobbs et al. (2018) find that to simulate a flocculent spiral with a weak spiral structure, the stellar feedback must be higher than in a galaxy with strong spirals.

These changes in cloud properties have important repercussions not just for where in the galaxy stars form, but also what kind of stars and star clusters form. Measurements of the cluster formation efficiency, or the fraction of stars that form in clusters, indicate that it is correlated with the surface density of the gas, suggesting that higher gas densities and pressures result in more massive star clusters (Adamo et al. 2011; Silva-Villa et al. 2013; Adamo et al. 2015; Johnson et al. 2016; Adamo et al.

Table 3.1: Properties of NGC 1313 and NGC 7793

Galaxy	NGC 1313	NGC 7793
Distance ^a (Mpc)	4.6	3.7
Metallicity ^b ($12 + \log(\text{O}/\text{H})$)	8.4	8.52
SFR ^c (M_{\odot}/yr)	1.15	0.52
M_{*}^d ($\times 10^9 M_{\odot}$)	2.5	3.2
M_{HI}^e ($\times 10^9 M_{\odot}$)	2.1	0.78
$M_{\text{H}_2}^f$ ($\times 10^6 M_{\odot}$)	5.4	10.0
M_{cl}^g ($\times 10^6 M_{\odot}$)	17.3	6.4

References: ^a Qing et al. (2015) and Gao et al. (2016) for NGC 1313 and Radburn-Smith et al. (2011) and Sabbi et al. (2018) for NGC 7793,

^b Walsh & Roy (1997),

^c Calculated by Calzetti et al. (2015) using GALEX far-UV images and corrected for dust with the methods described by Lee et al. (2009),

^d Calculated by Calzetti et al. (2015) using extinction-corrected B -band luminosities and methods described by Bothwell et al. (2009),

^e Calculated by Calzetti et al. (2015) using HI observations from Koribalski et al. (2004),

^f Sum of all CO(2-1) emission and using an average X_{CO} factor for each galaxy as discussed in Section 3.5, does not cover full galaxies,

^g Total mass of clusters in the LEGUS cluster catalogs, based on methodology from Adamo et al. (2017), does not cover full galaxies.

2020). Furthermore, the maximum mass of star clusters where the mass distribution truncates appears to depend on the SFR surface density of the galaxy (Adamo et al. 2015; Johnson et al. 2017; Messa et al. 2018; Wainer et al. 2022). A more extreme version of this has been seen in starburst environments that form massive super star clusters, such as the Antennae galaxies, where clouds have been measured to have extremely high pressures and surface densities (Johnson et al. 2015; Sun et al. 2018; Finn et al. 2019; Krahm et al. *subm.*). The hierarchical clustering of the molecular gas also appears to imprint its structure on the spatial clustering of the star clusters, with implications for the evolution of the star clusters and their potential for dispersal (Grasha et al. 2017a; Grasha et al. 2017b; Grasha et al. 2018; Menon et al. 2021; Turner et al. 2022).

To further understand the role of spiral arm structure on molecular cloud physical conditions and star cluster formation, we present a comparative study of the molecular gas in two spiral galaxies: NGC 1313 and NGC 7793 (Figure 3.1). These two galaxies are included in the Legacy ExtraGalactic UV Survey (LEGUS; Calzetti et al. 2015), a Hubble Space Telescope (HST) Treasury Program that observed 50 nearby (< 12 Mpc) galaxies. As part of the LEGUS survey, they both have comprehensive catalogs of their young star clusters and their masses and ages using the methodology described in Adamo et al. (2017), which allows us to compare the star-forming properties of each galaxy with the molecular gas at scales of ~ 10 pc.

NGC 1313 and NGC 7793 were chosen because they have many similar properties, such as their total stellar mass (2.6×10^9 and $3.2 \times 10^9 M_{\odot}$; Calzetti et al. 2015), their overall metallicities ($12 + \log(\text{O}/\text{H}) = 8.4$ and 8.52 ; Walsh & Roy 1997; Stanghellini et al. 2015), their star formation rates (SFR; 1.15 and $0.52 M_{\odot}/\text{yr}$; Calzetti et al. 2015), and their Hubble type of Sd. They are also both mostly face-on with clear views of the spiral structures in each (inclinations of 40.7 deg and 47.4 deg; Calzetti et al. 2015) and have similar distances (4.6 and 3.7 Mpc; Radburn-Smith et al. 2011; Qing et al. 2015; Gao et al. 2016; Sabbi et al. 2018). Their main properties are listed in Table 3.1.

Despite these many similarities, the two galaxies have starkly different spiral structures, with NGC 1313 being barred with strong spiral arms and NGC 7793 being a flocculent spiral (see Figure 3.1). NGC 1313 also appears to be experiencing a minor interaction (see §3.1.1). Based on the LEGUS cluster catalogs, they also have strikingly different numbers of massive clusters. NGC 1313 has more than six times as many clusters that are more massive than $10^4 M_{\odot}$, despite having a SFR only 2.2 times higher than NGC 7793 and significantly less molecular gas in the observation

footprints presented in this paper (Table 3.1). This makes NGC 1313 and NGC 7793 an excellent pair of galaxies to compare to further understand how the spiral structure of a galaxy influences the types of star clusters that are formed.

3.1.1 NGC 1313

NGC 1313 has an irregular morphology with a strong bar and asymmetric spiral arms, which has historically been compared to the Large Magellanic Cloud (de Vaucouleurs 1963). It is one of the most massive galaxies that shows no gas-phase metallicity gradient across its disk (Walsh & Roy 1997). Its irregular morphology (Sandage & Brucato 1979) and observations of the HI showing a loop of gas around the galaxy and a disturbance in its velocity field in the southwest of the galaxy (Peters et al. 1994) indicate that it is interacting with a satellite galaxy. When measuring the galaxy's star formation history, Larsen et al. (2007) found an increase in recent star formation in the southwest of the galaxy, potentially caused by this interaction. This was further confirmed by Silva-Villa & Larsen (2012), who found that rather than undergoing a starburst across the whole galaxy, there was only an increase in star formation in the southwestern field. They find that the regional starburst occurred ~ 100 Myr ago. Recently, Hernandez et al. (2022) show evidence for a metallicity gradient based on the chemical abundances of young clusters. They also find a constant star formation rate across the disk of NGC 1313 with the exception of the burst in the southwest. This southwestern region where the localized starburst is observed is just outside of the observation footprint for this study. A difference in stellar metallicity tracing a separate population was found throughout the disk by Tikhonov & Galazutdinova (2016), which they attribute to a past merger with a low-mass dwarf satellite that did not gravitationally distort the arms or central region of NGC 1313.

The star cluster population in NGC 1313 has been characterized using the LEGUS cluster catalogs by Grasha et al. (2017b), and the sizes of these clusters were further characterized by Ryon et al. (2017), who found that the clusters are undergoing relaxation but appear to be gravitationally bound. Hannon et al. (2019) studied the morphology of the $H\alpha$ around these clusters and report clearing times for the gas of less than 5 Myr. Messa et al. (2021) added to the LEGUS catalogs by searching for embedded clusters identified with $\text{Pa}\beta$ and in the near-infrared and finding that up to 60% of the star clusters are not accounted for in the UV-optical catalogs.

3.1.2 NGC 7793

NGC 7793 is a member of the Sculptor group of galaxies and has been well-studied due to its proximity and high Galactic latitude. It has no bar, a small bulge with a nuclear star cluster (Kacharov et al. 2018), and a mostly uniform distribution of small, loose spiral arms with little coherent structure (Elmegreen et al. 2014), to the point that it has been called an “extreme” flocculent spiral (Elmegreen & Elmegreen 1984). It has nearby dwarf companions, and the HI disk is warped, suggesting some level of interaction, though they see no sign of tidal effects (Koribalski et al. 2018). It has drawn attention for its unusual discontinuous and positive metallicity gradient in the far outer disk (Vlajić et al. 2011) and its declining rotation curve in the outer edges of the disk (Carignan & Puche 1990; Dicaire et al. 2008), although the latter could be due to a line-of-sight warp in the disk (Bacchini et al. 2019). Studies of its stellar population have also shown that it has a break in the disk, likely caused by radial migration of the stars (Radburn-Smith et al. 2012).

The star formation history of NGC 7793 has been studied by Sacchi et al. (2019) and they found an inside-out growth of the galaxy, with the outer regions undergoing

a greater recent increase in star formation than the inner region. Inside-out growth was also seen in young clumps identified in UV light by Mondal et al. (2021), who also suggest that NGC 7793 is experiencing a recent increase in its star formation rate. Its LEGUS-identified star clusters were included in the same studies as NGC 1313 by Grasha et al. (2017b), Hannon et al. (2019), and Brown & Gnedin (2021) to characterize their populations, cluster boundedness, and gas clearing timescales. The clusters and molecular gas were further studied by Grasha et al. (2018), finding that the younger clusters are more spatially correlated with molecular clouds and that the hierarchical clustering of the clouds is shared by the young clusters. Muraoka et al. (2016) has also mapped the CO(3-2) line in NGC 7793, finding that its emission is well-correlated with infrared tracers of star formation.

To robustly compare the properties of the molecular clouds in this pair of galaxies, we have observed both in CO(2-1) with carefully matched spatial resolutions of 13 pc and surface brightness sensitivities of ~ 0.2 K. These observations allow us to make a direct comparison of clouds in a galaxy with strong spiral arms and in a flocculent spiral without concern for resolution or sensitivity effects. This paper is organized as follows: We present the observations used in this analysis in Section 3.2, and the LEGUS cluster catalogs of the two galaxies in Section 3.3. We then discuss the decomposition of the CO(2-1) emission into substructures in Section 3.4 and the calculation of their properties in Section 3.5. We examine the size-linewidth relations of the clouds in each galaxy in Section 3.6, and the virialization of the clouds in Section 3.7. We compare the distributions of all the measured and derived properties in Section 3.8. We discuss our findings in Section 3.9 and summarize our conclusions in

Section 3.10.

3.2 Observations

3.2.1 NGC 1313 CO(2-1)

NGC 1313 was observed by ALMA in Band 6 (project code 2015.1.00782.S; PI: K. E. Johnson) with the 12m and 7m arrays, and with total power (TP) data. It was originally observed in Cycle 4 in 2016 but did not meet sensitivity requirements and so was observed again in Cycle 5 in 2018. The galaxy is split into two mosaics, one covering the northern arm of the galaxy, and one covering the central region and southern arm. The northern arm mosaic consists of 68 pointings with 1.9 minutes of integration per pointing with a spacing of $12.9''$ for a total integration time of 2.2 hours. The central mosaic consists of 104 pointings with 2.2 minutes of integration per pointing for a total integration time of 3.75 hours, also with a spacing of $12.9''$.

The data were calibrated with the ALMA data pipeline version Pipeline-CASA54-P1-B (Hunter 2023) in CASA 5.4.0-68 using J2258-2758 for bandpass and amplitude calibration and J2353-3037 for phase calibration. It was imaged in CASA 6.1.1.15 with a robust parameter of 0.5, resulting in a synthesized beam of $0.579'' \times 0.486''$ (12.8×11.2 pc at a distance of 4.6 Mpc). The 12m and 7m interferometric data were imaged with the TP data as a starting model, and the final images were then combined using the `feather` task in CASA to ensure the correct flux density at all scales. In Figure 3.2, we show the image data after smoothing to a circular beam size of 13 pc to match the observations of NGC 7793, which corresponds to $0.583''$ for NGC 7793. A summary of the resulting image is shown in Table 3.2.

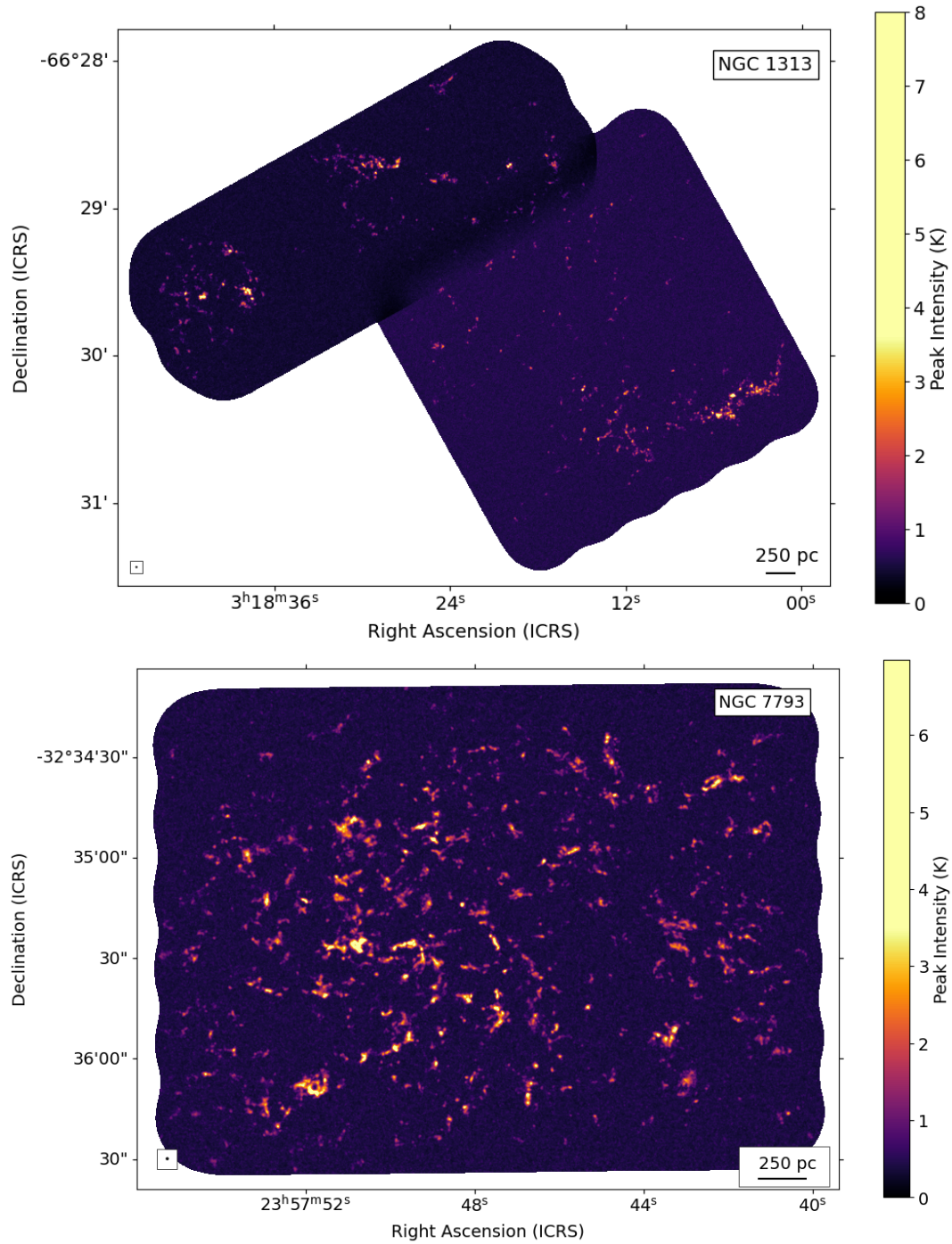


Fig. 3.2.— CO(2-1) peak intensity maps of NGC 1313 (top) and NGC 7793 (bottom), with beam sizes shown in the bottom left corners.

3.2.2 NGC 7793 CO(2-1)

NGC 7793 was observed by ALMA in Band 6 during Cycle 4 in 2016 (project code 2015.1.00782.S; PI: K. E. Johnson) with the 12m and 7m arrays, and with TP data. The observations were a mosaic of the central $180'' \times 114''$ (3×2 kpc) of NGC 7793. The total integration time is 3 hours with the 12-m array with 148 pointings at 1.2 minutes of integration per pointing and a mosaic spacing of $12.9''$ between pointings.

The data were calibrated with the ALMA data pipeline version 2020.1.0-40 (Hunter 2023) in CASA 6.1.1.15 using J0519-4546 and J0334-4008 for bandpass and amplitude calibration and J0303-6211 for phase calibration. It was imaged using a Briggs weighting with a robust parameter of 2.0, resulting in a synthesized beam size of $0.686'' \times 0.595''$ (12.3×10.7 pc at a distance of 3.7 Mpc). The 12m and 7m interferometric data were imaged with the TP data as a starting model, and the final images were then combined using the `feather` task in CASA to ensure the correct flux density at all scales. In Figure 3.2, we show the image data after smoothing to a circular beam size of 13 pc to match the observations of NGC 1313, which corresponds to $0.724''$ for NGC 7793. A summary of the resulting image is shown in Table 3.2. These data also appeared in Grasha et al. (2018).

Table 3.2: ALMA $^{12}\text{CO}(2-1)$ Observations

Galaxy	Beam (arcsec)	Beam (pc)	rms (K)	Velocity Resolution (km/s)
NGC 1313	0.58	13	0.15	1.33
NGC 7793	0.72	13	0.2	1.33

3.2.3 Region Selection

In analyzing these two galaxies, we also are interested in how their properties vary by region within the galaxies. To define these regions, we use contours of the red filter from Digitized Sky Survey (DSS) images of the two galaxies, which traces the bulk of the stellar population. These contours and the defined regions are shown in Figure 3.3.

For NGC 1313, we define regions for the bar, the northern arm, and the southern arm, and any structures that fall outside of those regions are considered interarm (Figure 3.3). The bar region is based on the 75% brightness contour in the DSS2-red image, while the arm regions enclose the emission within the 60% contours, then follow the arm pattern out to the edges of the CO(2-1) map following the 40% contour. We separately consider the northern and southern arms.

Since NGC 7793 is a flocculent spiral and does not have clearly defined arms, we instead split the galaxy up into a circular “center” region that follows the 75% brightness contour in the DSS2-red image, and then a “ring” region surrounding the center following the 60% contour (Figure 3.3). The rest of the structures are considered part of the “outer” region.

3.3 Cluster Catalogs

In addition to the CO(2-1) data, we use catalogs of star clusters and their SED-fitted properties from the LEGUS collaboration, which used the methodology described in Adamo et al. (2017). In this work, we use their catalog that uses Milky Way extinction, averaged aperture correction method, and Padova stellar evolutionary tracks implemented by Yggdrasil (Zackrisson et al. 2011). We include all objects identified

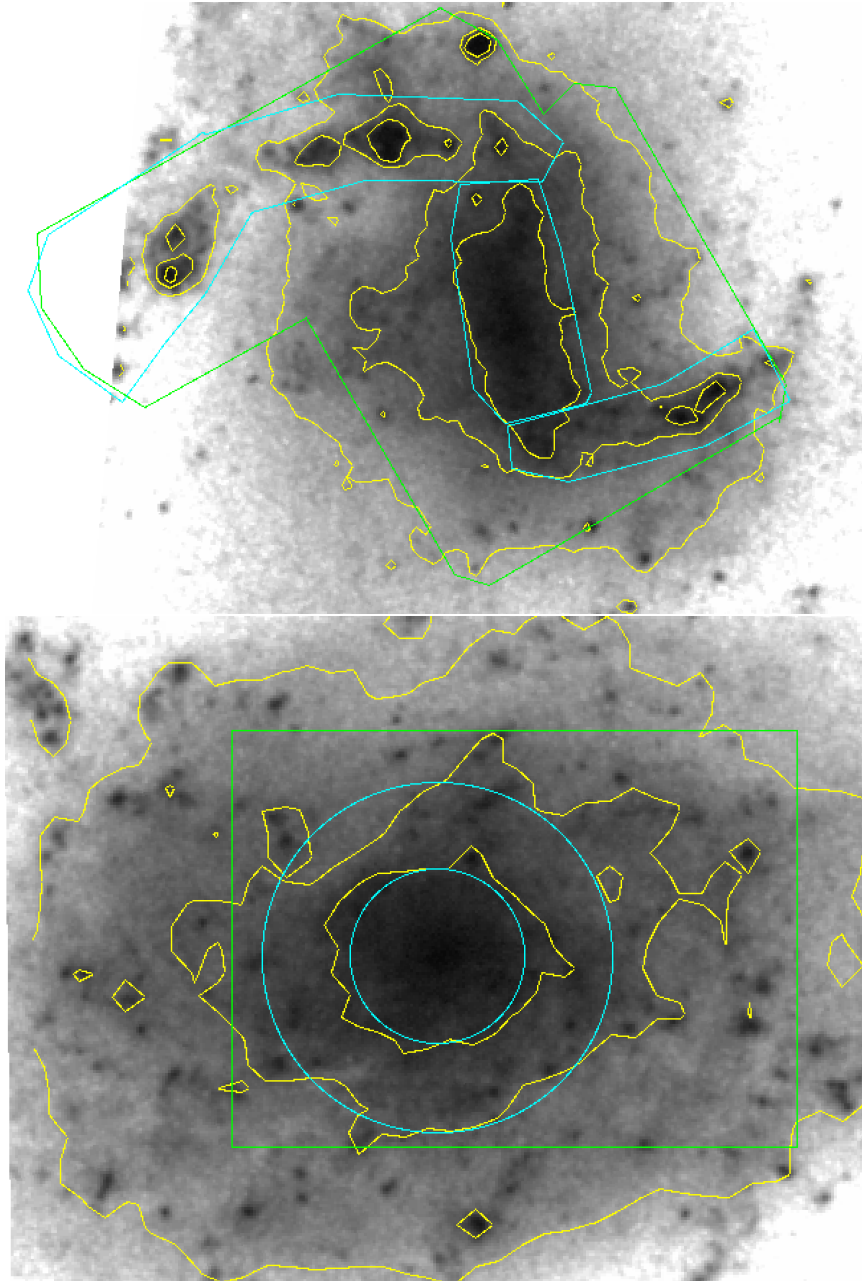


Fig. 3.3.— DSS2-red images of NGC 1313 (top) and NGC 7793 (bottom) in grayscale, with the yellow contours tracing 40%, 60%, and 75% of the maximum brightness in each image. The green outlines show the observational footprints of the ALMA CO(2-1) maps, and the defined regions are shown in cyan. In NGC 1313, those regions are the northern arm, bar, and southern arm, and in NGC 7793 they are the “center” and “ring” regions. The clouds that are not inside any of the regions are defined to belong to the interarm region of NGC 1313 and the outer region of NGC 7793.

by LEGUS as cluster candidates, which required that they were brighter than M_V of -6, detected above 3σ in the UBVI set of filters, and had a visual classification of 1 or 2 (compact) or class 3 (multiply peaked). Adamo et al. (2017) adopt a 90% completeness limit of $5000 M_\odot$ for clusters with ages up to 200 Myr in NGC 602, which has a distance of 10 Mpc. However, at the distances of NGC 1313 and NGC 7793, we expect this limit to be much lower, closer to $1000 M_\odot$ (Grasha et al. 2018). We represent this $1000 M_\odot$ limit as a vertical line in the mass distributions shown in Figures 3.4, 3.5, and 3.6.

Several studies have pointed out that a degeneracy in age and reddening during the fitting results in many old globular clusters incorrectly being assigned much younger ages (Turner et al. 2021; Hannon et al. 2019; Whitmore et al. 2023). In particular, Whitmore et al. (2023) find that the majority of these objects with incorrectly fitted ages fall above a line extending from (6, 1) to (9, 0.1) in a plot of $E(B-V)$ versus $\log(\text{Age})$. They also find that these incorrect ages primarily affect objects on the high mass end ($M > 10^{4.5} M_\odot$). To account for these incorrect ages without biasing our sample against high-mass objects, we remove the clusters that fall above the $E(B-V)$ - $\log(\text{Age})$ line from Whitmore et al. (2023) only when comparing age measurements between the two galaxies. This affects 76 clusters in NGC 1313 and 29 clusters in NGC 7793. Carefully fitting these objects with the degeneracy in mind would likely result in many of them having ages older than 1 Gyr. We also note that there are few enough of these objects that keeping or removing them does not substantially alter our results.

Orozco-Duarte et al. (2022) compared the output of the LEGUS cluster catalog for NGC 7793 with results obtained using synthetic photometry and a stochastically sampled IMF and found masses that were on average 0.11 dex larger and ages that

were 1 Myr younger compared to the Adamo et al. (2017) method. However, we use the original LEGUS catalogs still to maintain a consistent method between the two galaxies.

The cluster catalogs for both galaxies were separated into east and west portions of the map. To combine these, we identified matching pairs of clusters in the overlap region. We then used the cluster properties from the map that had the better fit, based on their reported quality of fit Q parameter. We identified 67 overlapping clusters in NGC 1313 and 47 in NGC 7793. Each of these clumps has a fitted mass, age, and extinction from the catalog.

3.3.1 Cluster Counts

NGC 1313 has ~ 2.6 times as many identified star clusters at all masses as NGC 7793, with a total of 1201 clusters compared to 467 for NGC 7793. Considering that star formation rate in NGC 1313 is ~ 2.2 times larger than that of NGC 7793, this represents a small excess in cluster formation. We can also account for the fraction of the total SFR included in the footprints of the LEGUS observations used to identify these clusters based on the fraction of the GALEX far-UV light. In NGC 1313, 57% of the total SFR is included in the LEGUS footprint, and in NGC 7793 53% is included. Assuming that the cluster populations are well-matched to the SFR within each galaxy, NGC 1313 would have ~ 2110 clusters and NGC 7793 would have ~ 880 clusters within the total star forming area of each galaxy. This suggests then that NGC 1313 has ~ 2.4 times as many clusters than NGC 7793 in the full galaxy, still a slight excess over the difference in total SFR.

This difference in cluster number is more extreme when we consider only the most massive clusters with $M_* > 10^4 M_\odot$. NGC 1313 has over six times as many massive clusters, having 333 massive clusters identified by LEGUS where NGC 7793 has 53. Correcting for the fraction of star formation traced by LEGUS would still leave NGC 1313 with 5.8 times more massive clusters. Furthermore, 37 of those massive clusters are young (< 10 Myr) in NGC 1313, compared to only 3 in NGC 7793. As seen in Figures 3.4, NGC 7793 does have a couple particularly massive clusters, and so we can also compare the mass of clusters in both galaxy above the $M_* > 10^4 M_\odot$ threshold and we find that NGC 1313 has 2.7 times as much mass in massive clusters (2.5 times the mass when including a total SFR correction), which still represents an excess of massive cluster formation in NGC 1313 by this metric.

This demonstrates how NGC 1313 not only has more clusters, but also has more massive clusters than NGC 7793, despite the lower molecular gas content of NGC 1313 (as shown in Table 3.1 and will be discussed in Section 3.5).

3.3.2 Cluster Property Distributions

We further consider how the distributions of cluster masses and ages compare between the two galaxies by looking at histograms, Gaussian kernel density estimations (KDEs) from `scipy` (Virtanen et al. 2020), and cumulative distribution functions (CDFs). Histograms and KDEs are intuitive representations of how the values of a parameter are distributed, but they are also heavily affected by our choice in binning for the histogram and bandwidth for the KDE. We use a scalar estimator bandwidth of 0.5 dex for all KDEs in this section and Section 3.8 for uniformity (Scott’s rule would result in bandwidths between 0.2 and 0.5 dex for the various distributions). CDFs are less intuitive for understanding how values of a property are distributed,

but they are unaffected by binning and so are the most robust depiction of property distributions. When interpreting CDFs, a line further to the right of the plot indicates a distribution with larger values.

In Figure 3.4, we show the distributions of the fitted masses and ages of the clusters for each galaxy, with histograms and KDEs in the left column and CDFs in the right column. The cluster masses in NGC 1313 are skewed towards higher masses, further emphasizing the tendency towards larger masses in NGC 1313. The distribution of cluster ages in the two galaxies appears more similar, though NGC 1313 has slightly older clusters than NGC 7793.

We also consider how the cluster masses and ages vary by region in each galaxy, shown in Figures 3.5 and 3.6. In NGC 1313, there are clear, distinct differences in the mass and age distributions of clusters in these regions. The northern arm has much lower cluster masses than the other regions, but also is most heavily skewed towards young clusters. Meanwhile, the interarm region is more dominated by high-mass, older clusters. The southern arm and the bar have a fairly similar mass distribution, though the bar tends to have older clusters than the southern arm. By number (see Table 3.3), the interarm region has the most massive clusters ($M > 10^4 M_{\odot}$), but the northern arm has the most young, massive clusters (< 10 Myr).

In NGC 7793, the center region has a bump at high masses ($\sim 10^{6.5} M_{\odot}$), but the CDF appears to show that all three regions have nearly identical mass distributions. These two supermassive clusters in the center of NGC 7793 are relatively old, with fitted ages of 0.9 and 12 Gyr. Overall, the age distributions between the regions are also quite similar. This suggests that the properties of the cluster population in NGC 7793 are fairly uniform throughout the galaxy, especially compared to the population in NGC 1313.

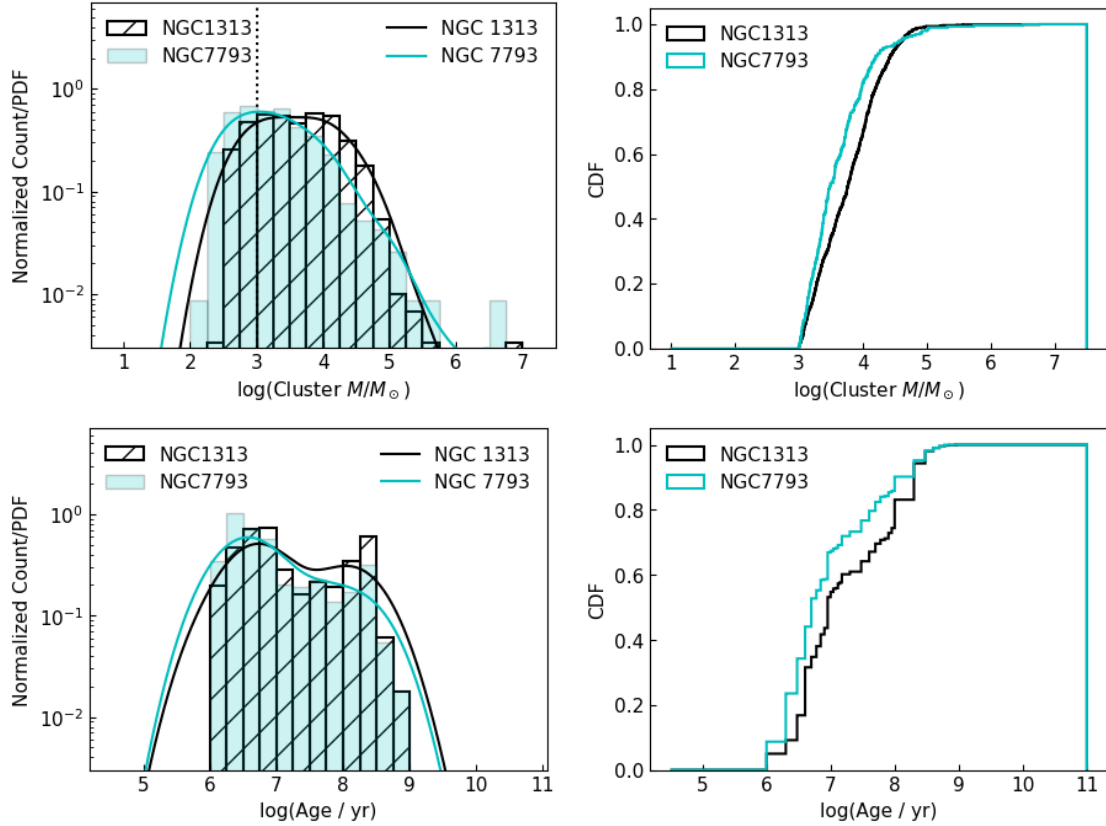


Fig. 3.4.— Normalized distributions of the cluster parameters for the two galaxies, using histograms and KDEs (left) and CDFs (right). The estimated mass completeness limit of $1000 M_{\odot}$ is shown as a vertical line in the top left, and the CDF of the mass distribution only includes clusters above this mass limit. The age distributions do not include clusters that are likely to have incorrect ages due to the age/reddening degeneracy (Whitmore et al. 2023).

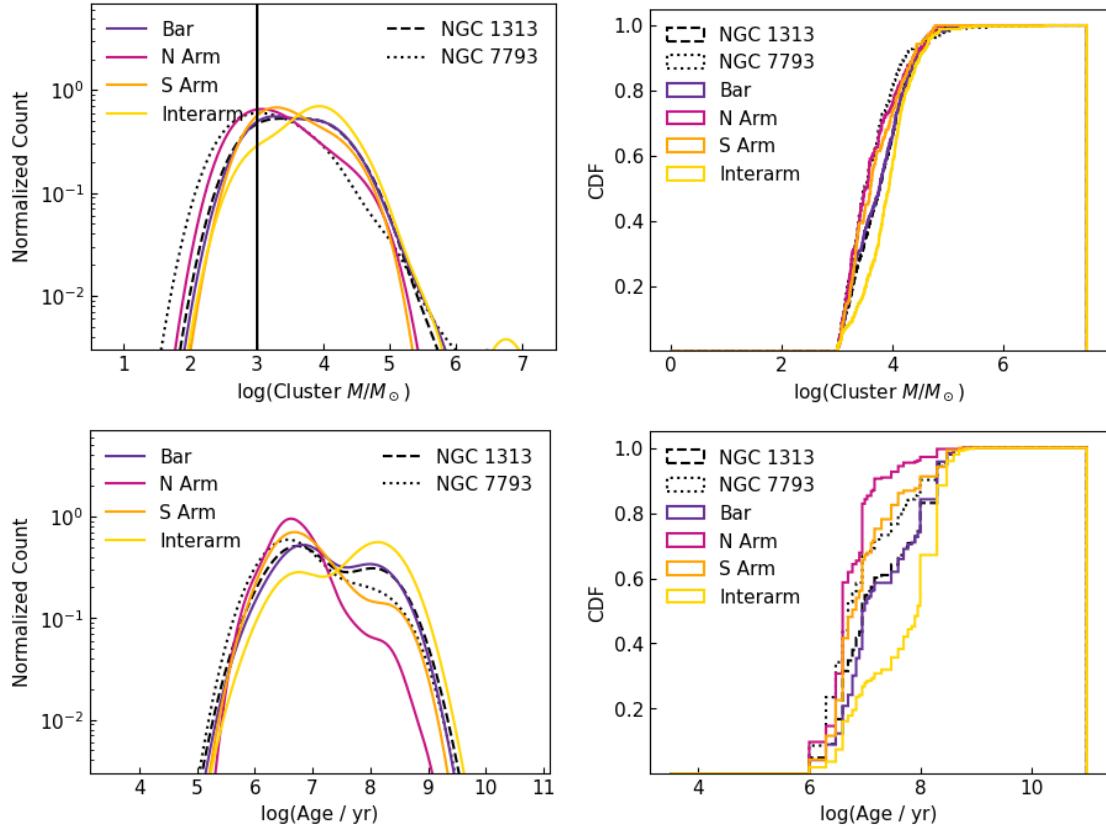


Fig. 3.5.— Distributions of the cluster parameters for the bar, northern arm, southern arm, and interarm regions of NGC 1313 using KDEs (left) and CDFs (right). The global property distributions of clusters in NGC 1313 and NGC 7793 are also shown as black dashed and dotted lines, respectively, and are the same as those in Figure 3.4. The estimated mass completeness limit of $1000 M_{\odot}$ is shown as a vertical line in the top left, and the CDF of the mass distribution only includes clusters above this mass limit. The age distributions do not include clusters that are likely to have incorrect ages due to the age/reddening degeneracy (Whitmore et al. 2023).

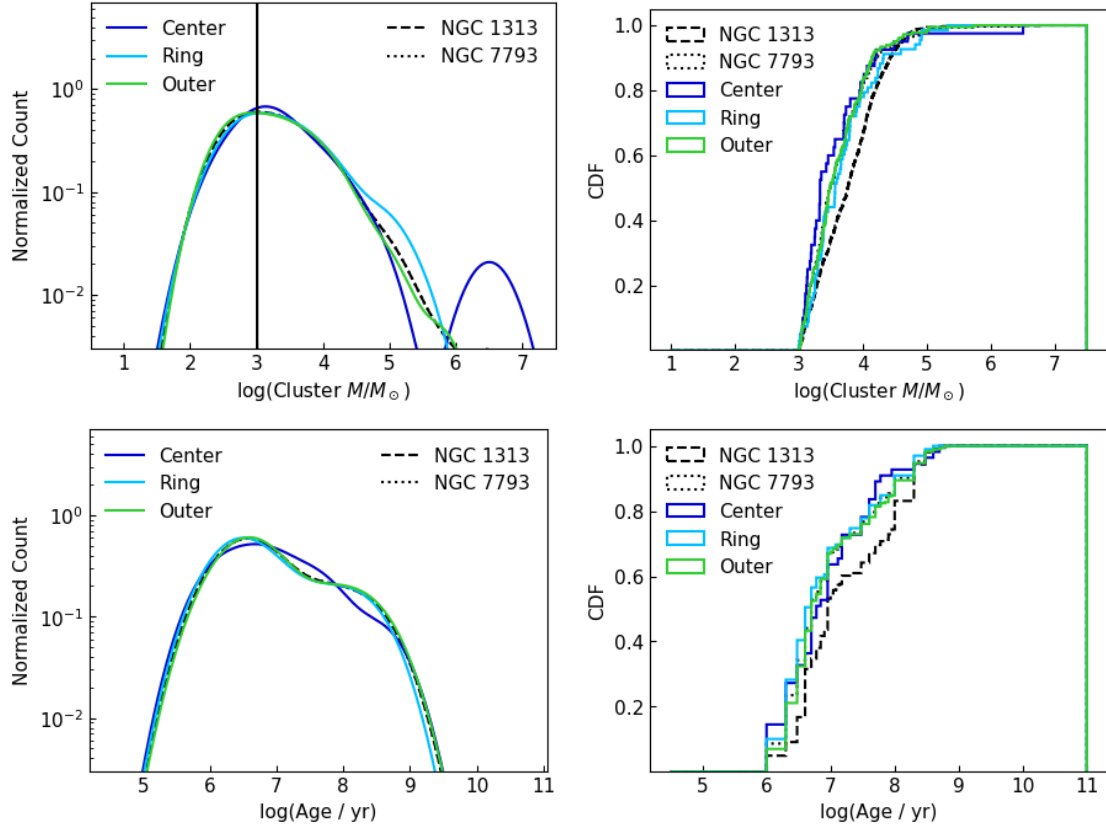


Fig. 3.6.— Distributions of the cluster parameters for the center, ring, and outer regions of NGC 7793 using KDEs (left) and CDFs (right). The global property distributions of clusters in NGC 1313 and NGC 7793 are also shown as black dashed and dotted lines, respectively, and are the same as those in Figure 3.4. The estimated mass completeness limit of $1000 M_{\odot}$ is shown as a vertical line in the top left, and the CDF of the mass distribution only includes clusters above this mass limit.

3.4 Molecular Gas Structure Decomposition

To understand the properties of individual molecular gas structures, we use two different methods of emission decomposition to more robustly compare physical conditions between the two galaxies. One method is to use a dendrogram to hierarchically categorize the structures, and the other is to identify non-overlapping clumps. These segmentation methods are described in more detail below. Dendrograms are superior for examining the full spatial scale of molecular clouds in the region because they are able to capture the hierarchical nature of the gas, from large GMCs to smaller knots. However, dendrograms multiply count emission and so they cannot be used for any counting statistics. We therefore use dendrograms in Sections 3.6 and 3.7 where we want to understand the full spatial scale of the clouds and multiply counted emission is allowable. We use the non-overlapping clumps in Section 3.8, which focuses on property distributions and so cannot include multiply counted emission.

3.4.1 Dendrogram Segmentation

We use the package `astrodendro` (Rosolowsky et al. 2008) to decompose the structures in each galaxy into dendrograms. This results in a hierarchical “tree” of structures that merge together at lower contour levels. The local maxima are called “leaves” and have no further substructure, while the larger merged structures are “branches” and “trunks”. Trunks are not bounded by any other structures. By convention, isolated structures that have no substructure and are also not bounded by any other structure are called leaves instead of trunks. We use the input parameters `min_value=3 σ` , `min_delta=2.5 σ` , and `min_npix=2` beams, where `min_value` is the minimum intensity value of an identified emission peak, `min_delta` is the minimum intensity separation between structures merging, and `min_npix` is the minimum num-

ber of voxels in an identified structure. The breakdown of each type of dendrogram structure for each galaxy is shown in Table 3.3.

3.4.2 Clump Segmentation

We use the algorithm `quickclump` (Sidorin 2017) to decompose the emission into clumps that have no overlap. This algorithm outputs a similar style of clump decomposition to `clumpfind` (Williams et al. 1995), for example. We used the input parameters `Tcutoff`= 4σ , `dTleaf`= 4σ , and `Npixmin`=2 beams (equal to 65 and 70 for NGC 1313 and NGC 7793, respectively). `Tcutoff` is the minimum intensity included in clump assignments, `dTleaf` is the minimum intensity differences for an emission peak to be considered a separate clump, and `Npixmin` is the minimum number of voxels in a clump. The number of clumps identified in each galaxy are shown in Table 3.3.

3.5 Calculating Cloud Properties

3.5.1 Mass

We calculate the mass of each structure using a CO-to-H₂ factor, X_{CO} , where $X_{\text{CO}} = N_{\text{H}_2}/W_{\text{CO}}$, N_{H_2} is the column density of H₂ in cm⁻² and W_{CO} is the observed brightness of CO in K km s⁻¹. We use the $X_{\text{CO}(2-1)}$ calibration from Gong et al. (2020), Table 3, Equation 3b, which determines the $X_{\text{CO}(2-1)}$ conversion factor between N_{H_2} and CO(2-1) based on the peak brightness temperature of the clump (T_{peak} in K), the beam size (r_{b} ; 13 pc), and the metallicity (Z) with the equation

$$X_{\text{CO}(2-1)} = (2.7 \times 10^{20}) T_{\text{peak}}^{-1.07+0.37 \log(r_{\text{b}})} Z^{-0.5} r_{\text{b}}^{-0.13}. \quad (3.1)$$

Table 3.3: Number of cloud structures and clusters in each galaxy and region

Galaxy	Region	Molecular Gas Structures						LEGUS Clusters		
		Trunks	Branches	Leaves	Clumps	Massive Clumps ^a	All	Massive ^a	YMCs ^b	
NGC 1313	All	65	82	442	531	137	1201	333	37	
	Bar	7	1	61	69	7	380	107	8	
	N Arm	20	32	161	193	62	297	48	18	
	S Arm	27	44	156	188	55	145	32	7	
	Interarm	11	5	64	82	13	379	146	4	
NGC 7793	All	130	187	761	965	306	467	53	3	
	Center	22	63	162	203	81	57	7	0	
	Ring	46	63	277	354	118	108	15	2	
	Outer	62	61	322	408	107	302	31	1	

Note: ^a Massive clumps and clusters. The threshold used to define “massive” for both clumps and clusters in this table is $M > 10^4 M_\odot$. ^b YMCs are young, massive clusters, where we use thresholds of $M > 10^4 M_\odot$ and age < 10 Myr.

Using this equation, which is calibrated directly to the CO(2-1) line rather than CO(1-0), means that we do not need to assume a ratio of CO(2-1)/CO(1-0), which is known to vary across galaxies (Koda et al. 2012; Leroy et al. 2022). For NGC 1313, we use an oxygen abundance of $12 + \log(\text{O}/\text{H}) = 8.4 \pm 0.1$ with no radial gradient in the galaxy (Walsh & Roy 1997). NGC 7793 has a measured radial gradient of $12 + \log(\text{O}/\text{H}) = 8.572 - 0.054 \text{ dex kpc}^{-1}$ (Stanghellini et al. 2015). Using a solar oxygen abundance of $12 + \log(\text{O}/\text{H}) = 8.69$ (Asplund et al. 2009), these abundances correspond to metallicities of $Z = 0.51Z_{\odot}$ for NGC 1313 and a range of $Z = (0.56 - 0.76)Z_{\odot}$ for NGC 7793. Using the prescription from Eq. 3.1 results in values of $X_{\text{CO}(2-1)} = (0.69 - 2.56) \times 10^{20} \text{ cm}^{-2}/(\text{K km s}^{-1})$ for NGC 1313 and $X_{\text{CO}} = (0.64 - 2.65) \times 10^{20} \text{ cm}^{-2}/(\text{K km s}^{-1})$ for NGC 7793.

We also consider the metallicity gradient measured for NGC 7793 by Grasha et al. (2022), which instead finds $12 + \log(\text{O}/\text{H}) = 8.945 - 0.083 \text{ dex kpc}^{-1}$, resulting in metallicities of $Z = (1.14 - 1.79)Z_{\odot}$ and values of $X_{\text{CO}(2-1)} = (0.43 - 1.83) \times 10^{20} \text{ cm}^{-2}/(\text{K km s}^{-1})$. We find that the difference in metallicity prescription and resulting masses does not significantly affect any of the results in this paper and so we use the lower metallicities of Stanghellini et al. (2015) throughout for NGC 7793. Hereafter, we refer to $X_{\text{CO}(2-1)}$ as X_{CO} .

We next calculate the mass of each structure using these calibrated X_{CO} values to determine the H_2 column density, then multiply by the pixel size in cm^2 and sum over all pixels to get the mass of H_2 . We then multiply this M_{H_2} by a factor of 1.4 (which is the mean mass per hydrogen atom and assumes all the hydrogen is molecular) to get the total mass of the gas, M . We adopt a 10% error on the resulting masses due to the standard 10% ALMA flux calibration uncertainty (Fomalont et al. 2014), which we add in quadrature with the error from the measured rms noise (Table 3.2).

We also estimate a total mass of H_2 in both galaxies, using the total CO(2-1) emission multiplied by the respective average X_{CO} measured for the clumps in each galaxy (we do not multiply by the factor of 1.4 mentioned above). This total CO mass is shown in Table 3.1, although it is important to note that our observations do not cover the whole galaxy and so this is not the total CO mass of each galaxy. The ALMA observations do, however, cover a similar fraction of the galaxy to the LEGUS observations that clusters are derived from. The CO(2-1) emission identified to be part of a clump structure accounts for approximately 82% of the total CO mass in NGC 1313 and 95% in NGC 7793, which implies that more of the molecular gas in NGC 1313 is diffuse.

3.5.2 Velocity Dispersion

We calculate the velocity dispersion for each structure by finding the intensity-weighted mean line profile and fitting a Gaussian, resulting in a fitted σ_v . We then deconvolve this σ_v with the velocity channel width of the observations, 1.33 km s^{-1} , converted from FWHM to σ with $\text{FWHM} = 2.35\sigma$. The reported error in σ_v comes from the error in the fitting method, propagated through the deconvolution. After deconvolving σ_v , measurements that were smaller than the channel width return non-number values and so are dropped from the analysis. We also remove from our analysis any structures that have a deconvolved σ_v less than a tenth of the velocity resolution. Throughout this work, we also use the term “linewidth” to refer to σ_v .

3.5.3 Radii

To determine the sizes of the structures, we fit ellipses to the half-power contours and take the two axes as the HWHM of the structure. We convert these HWHM

measurements to a σ_R by approximating $\sigma_R = \text{HWHM} \times 2/2.35$, then multiply σ_R by 1.91 to get an “effective radius” (Solomon et al. 1987) in each axis. We deconvolve each axis with the radius of the beam, 6.5 pc, then take the geometric mean of the axes to get a final R . The reported error in the size is determined by how non-circular the structure is, added in quadrature with a measurement error of half a pixel size, propagated through the deconvolution. After deconvolving the radii, measurements that were smaller than the beam size return non-number values and so are dropped from the analysis. We also remove from our analysis any structures that have a reported R less than a tenth of the beam size.

Of the structures that were removed because they were below the resolution limits, there were 113 clumps and 88 dendrogram leaves in NGC 1313 and 166 clumps and 116 dendrogram leaves in NGC 7793. These removed structures account for 4% of the total clump mass in NGC 1313 and 2% in NGC 7793.

3.5.4 **Derived Quantities**

From the measured mass, radius, and linewidth above, we calculate other properties of the structures, including the surface density, Σ , the virial parameter, α_{vir} , the external pressure, P_e , and the free-fall time, t_{ff} . The surface density is simply the total mass divided by the structure’s area.

The virial parameter is the ratio between twice the cloud’s kinetic energy and its gravitational energy, so that a value of one indicates that the cloud is in virial equilibrium. Values greater than one suggest that the cloud is not gravitationally bound and must either disperse or be constrained by an external pressure, while values less than one suggest that the cloud is dominated by gravity and will collapse. We calculate the virial parameter for each structure with the equation

$$\alpha_{\text{vir}} = \frac{5\sigma_v^2 R}{GM}. \quad (3.2)$$

The external pressure is the pressure at the edge of cloud defined by Elmegreen (1989) with the equation

$$P_e = \frac{3\Pi M\sigma_v^2}{4\pi R^3}, \quad (3.3)$$

where Π is defined as the ratio of the density at the edge of the cloud to the mean cloud density ($\rho_e = \Pi\langle\rho\rangle$), and here we take $\Pi = 0.5$.

The free-fall time depends only on the density of the cloud and so we calculate it with the equation

$$t_{ff} = \sqrt{\frac{3\pi}{32G\rho}} = \sqrt{\frac{\pi^2 R^3}{8GM}}. \quad (3.4)$$

Tables of all of these properties and their errors, for both galaxies and for both clumps and dendrogram structures, are given in Appendix A4. Given the large number of structures, we include only the first 5 entries as a demonstration of property values. The full tables are available as supplementary material.

3.6 Size-Linewidth Relations

The sizes and linewidths of molecular cloud structures are expected to follow a power law relation (Larson 1981) of the form

$$\sigma_v = a_0 R^{a_1}. \quad (3.5)$$

The intercept (a_0) and slope (a_1) of this relation have been measured in many

different environments, though the most commonly cited value is that from Solomon et al. (1987), which found $a_0 = 1.0 \pm 0.1$ and $a_1 = 0.5 \pm 0.05$ for clouds mapped in CO(1-0) in the disk of the Milky Way at $45''$ resolution. Solomon et al. (1987) however used a different size parameter, S , than the effective radius also defined in that paper. The size parameter they used was the geometric mean of the spatial dispersions, σ_l and σ_b , so if we convert those to the effective radii that we use in our analysis, the intercept would instead be $a_0 = 0.72 \pm 0.07$.

We show the radii and velocity dispersions of the dendrogram structures in both galaxies with a fitted power law in Figure 3.7, where the power law is fit with orthogonal distance regression to take into account the error in both axes (`scipy.odr`; Virtanen et al. 2020). Due to the large number of clouds, plotting all data points results in the true distribution of points being self-obscured. We instead represent their distribution with a 2-D Gaussian KDE from `scipy.stats`, using the default Scott’s rule to determine the estimator bandwidth.

For NGC 1313 we fit a slope of $a_1 = 1.45 \pm 0.09$ with intercept $a_0 = 0.02 \pm 0.01$, and for NGC 7793 we fit a slope of $a_1 = 0.79 \pm 0.03$ with intercept $a_0 = 0.12 \pm 0.01$ (Figure 3.7 and Table 3.4). The fitted slope for NGC 1313 is steeper than that of NGC 7793 by more than 3σ , and both are significantly steeper than the Solomon et al. (1987) slope for clouds in the Milky Way disk. This suggests that NGC 1313 has higher kinetic energies in larger structures than NGC 7793, and that both have steeper energy cascades than the Milky Way, though this could be because Solomon et al. (1987) do not deconvolve their measured sizes and linewidths with the observation’s beam size and velocity resolution, which most strongly affects the smallest linewidths and sizes, and so would cause us to fit a steeper slope. The fact that we use CO(2-1) instead of CO(1-0) also impacts the measured sizes and linewidths and makes the

comparison with Solomon et al. (1987) less reliable.

Since Solomon et al. (1987), other studies have measured the slope and intercept of this relation in a variety of environments and at many resolutions. In the Milky Way for example, Rice et al. (2016) measure clouds with angular resolutions of 7.5' and measure a slope of $a_1 = 0.52 \pm 0.03$ and Miville-Deschênes et al. (2017) measure clouds with angular resolutions of 8.5' and measure a slope of $a_1 = 0.63 \pm 0.3$, though neither of these studies deconvolve the sizes or linewidths with the beam and velocity channel sizes. Faesi et al. (2016) measure clouds in the nearby spiral galaxy NGC 300 at 40 pc resolution with CO(2-1) and deconvolve their measurements, finding a slope of $a_1 = 0.52 \pm 0.2$. Slopes on the higher side that would better match our measured slope in NGC 7793 have also been found in nearby galaxies, such as $a_1 = 0.6 \pm 0.1$ measured by Bolatto et al. (2008) across many galaxies and with resolutions ranging from 6 to 120 pc with both CO(1-0) and CO(2-1), or $a_1 = 0.8 \pm 0.05$ measured by Wong et al. (2011) across the Large Magellanic Cloud (LMC) at 11 pc resolution with CO(1-0). Neither of these studies deconvolved size and linewidth measurements. Higher resolution studies (0.1-3 pc) in the LMC with CO(2-1) have performed deconvolution and found slopes ranging from $a_1 = 0.49$ to $a_1 = 0.78$ (Nayak et al. 2016; Indebetouw et al. 2020; Wong et al. 2022; Finn et al. 2022). These widely varying measurements demonstrate how resolution, molecular tracer, and the method used to measure size and linewidth all have a large effect on the measured slope. Consequently, we consider comparisons of our measured slopes with other studies less reliable than the comparison between NGC 1313 and NGC 7793 in this work alone.

We also fit the size-linewidth power law relation for the two galaxies and hold the slope constant at a standard value of $a_1 = 0.5$ (Solomon et al. 1987). Fitting only the intercept gives a measure of the amount of kinetic energy in the gas. For NGC 1313,

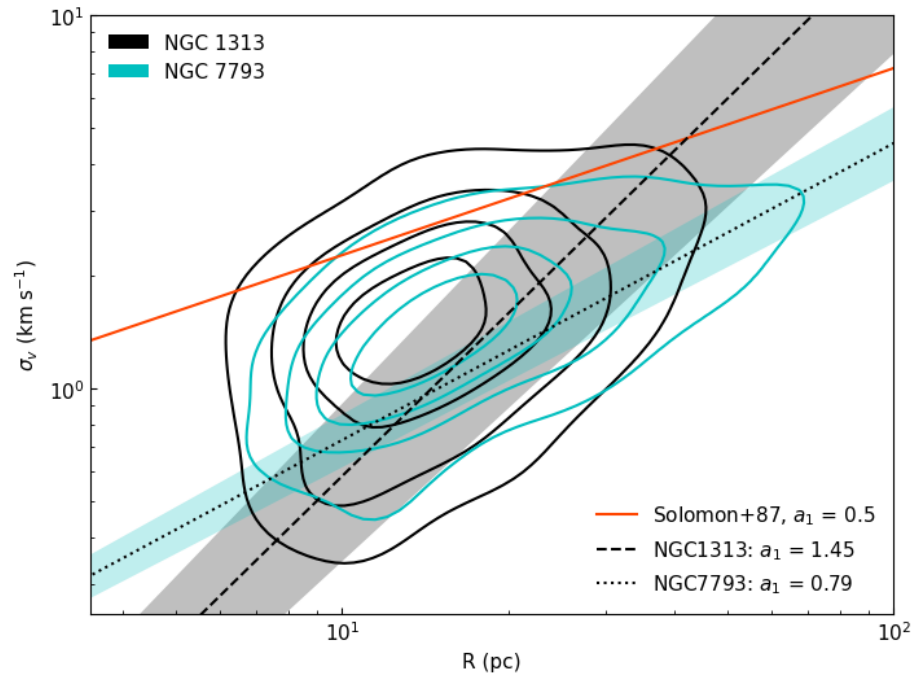


Fig. 3.7.— Kernel density estimates of deconvolved velocity dispersions plotted against deconvolved radii of dendrogram structures in NGC 1313 and NGC 7793 with contours of 20%, 40%, 60%, and 80% of the maximum density. Also shown are the fitted power laws with their respective 1σ errors shown as shaded regions (including error in both the slope and the intercept). The resulting slopes are printed in the bottom right corner. The fitted slope for NGC 1313 is much steeper than that of NGC 7793, which suggests the NGC 1313 has higher kinetic energy at larger size scales.

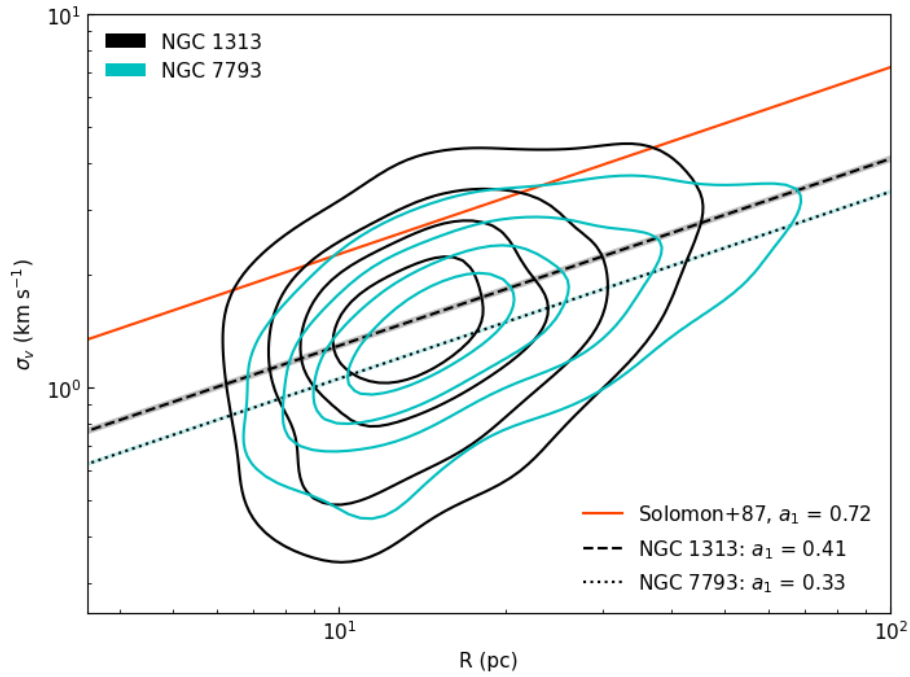


Fig. 3.8.— Kernel density estimates of the deconvolved velocity dispersions plotted against deconvolved radii of dendrogram structures in NGC 1313 and NGC 7793 with contours of 20%, 40%, 60%, and 80% of the maximum density. Also shown are the fitted power laws (where we hold the slope constant at $a_1 = 0.5$) with their respective 1σ errors shown as shaded regions. The resulting intercepts are printed in the bottom right corner. NGC 1313 has a higher intercept than NGC 7793 by more than 3σ , suggesting that the molecular clouds in NGC 1313 have higher kinetic energies.

we fit a value of $a_0 = 0.41 \pm 0.01$, and for NGC 7793 we fit a value of $a_0 = 0.33 \pm 0.004$ (Figure 3.8 and Table 3.4). The intercept of NGC 1313 is significantly higher than that of NGC 7793 by more than 3σ , which suggests that NGC 1313 has more kinetic energy in its molecular clouds than NGC 7793. Both are also significantly lower than the intercept measured in the Milky Way disk, though this could also be because Solomon et al. (1987) of the various inconsistencies discussed above.

3.6.1 Regional Size-Linewidth Relations

We repeat the power law fits of the size-linewidth distribution for the different regions within each galaxy, using the regions defined in Section 3.2.3. The size-linewidth relations are shown in Figure 3.9 and the fitted values for each region and the galaxies as a whole are reported in Table 3.4.

The fitted slopes in NGC 1313 have quite large errors, especially the bar region, and so all of the regions are consistent with each other within the 3σ uncertainties. Despite that, we note that the southern arm of NGC 1313 has a steeper slope than the northern arm, and the interarm region has the shallowest slope of all the regions. The slopes in NGC 7793 mostly are consistent within 3σ , with the exception that the outer region is significantly steeper than the ring region.

Considering the fitted intercepts with fixed slope, NGC 1313 shows a spread of kinetic energies, with the southern arm having the highest intercept, followed by the northern arm, the bar, then the interarm regions. The fitted intercept for the southern arm is significantly higher than the intercepts for the bar and the interarm region, though is just barely consistent within 3σ with the northern arm. Similarly, the northern arm is significantly higher than the interarm region but consistent within 3σ with the bar. The bar and interarm regions are consistent with each other as well.

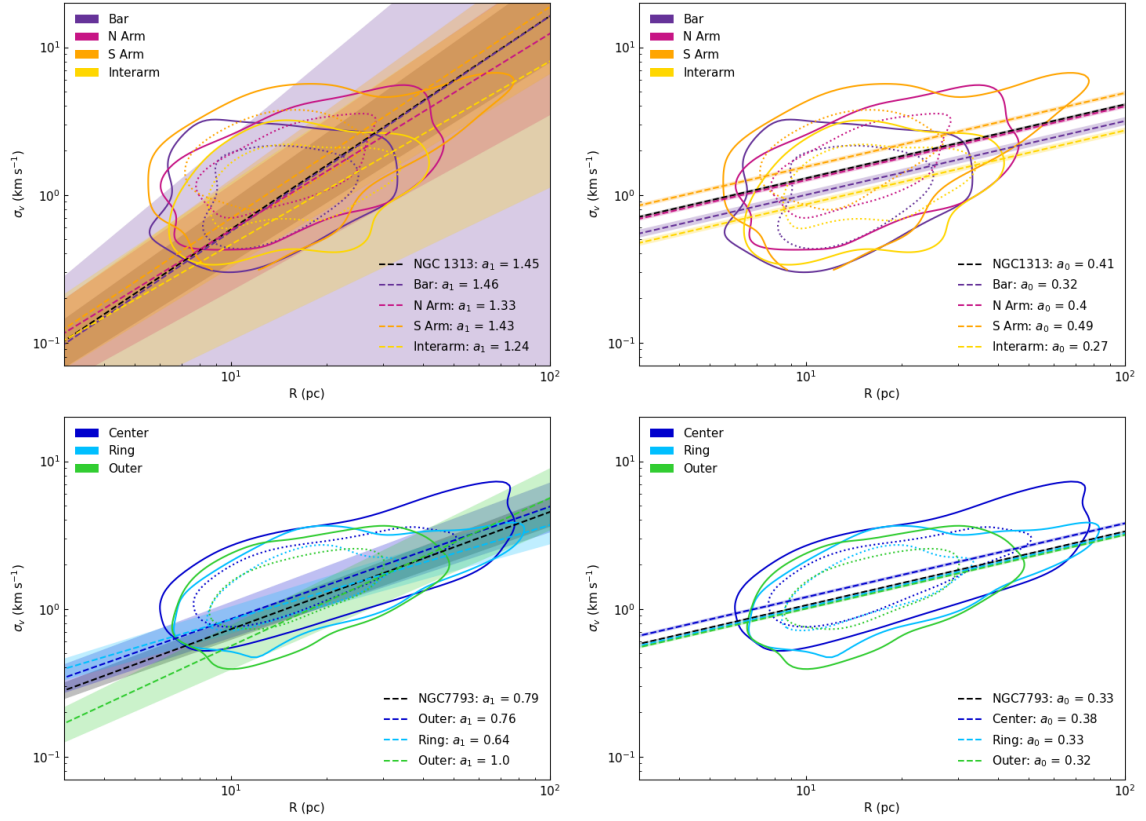


Fig. 3.9.— Deconvolved velocity dispersions plotted against deconvolved radii of dendrogram structures in the different regions of NGC 1313 (top) and NGC 7793 (bottom) showing the 20% KDE contours as solid lines and then 50% contours as dotted lines. The left two plots show the fully fitted power laws, with the resulting slopes shown in the lower right corners, while the plots on the right show fitted power laws with the slope held constant at $a_1 = 0.5$ with the resulting intercepts shown in the lower right corners. Their respective 1σ errors are shown as shaded regions.

These fitted intercepts suggest that the spiral arms of NGC 1313 have higher kinetic energy than the gas in the bar and interarm regions.

In NGC 7793, the fixed-slope intercepts have a much smaller range than in NGC 1313, and all are consistent with each other within 3σ . The center of NGC 7793 is most similar in intercept to the northern arm of NGC 1313, while the outer region is most similar to the bar.

3.7 Virialization

To investigate the gravitational balance of clouds in the two galaxies, we plot the velocity metric, σ_v^2/R , against the surface density, Σ , of each dendrogram structure. The results are shown in Figure 3.10, along with a line indicating where clouds in virial equilibrium would fall in the plot. Falling above the virial equilibrium line indicates that the clouds are super-virial and dominated by kinetic energy, while clouds below the line would be sub-virial and likely to collapse. Being super-virial implies that the clouds are unbound and likely to disperse due to their kinetic energy. However, the kinetic energy of clouds could also be enhanced if they already have begun free-fall collapse, in which case they would fall along the line where $\alpha_{\text{vir}} = 2$ in Figure 3.10. The virial equilibrium line only considers the gravitational and kinetic energies of the cloud, but external pressure or magnetic fields could also affect the boundedness of the clouds by suppressing collapse or dispersal. These environmental effects have been shown to be important in simulations of GMCs in spiral galaxies (Baba et al. 2017).

Both galaxies fall mostly above the virial equilibrium line, suggesting that they are dominated by kinetic energy. Some clouds are consistent with being in free fall, which would enhance their observed kinetic energy. Alternatively, excess kinetic energy

Table 3.4: Fitted slopes and intercepts for size-linewidth relations

Galaxy	Region	Intercept and Slope		Intercept ^a
		a_0	a_1	a_0
NGC 1313	Global	0.02 ± 0.01	1.45 ± 0.09	0.41 ± 0.01
	Bar	0.02 ± 0.02	1.46 ± 0.34	0.32 ± 0.02
	N Arm	0.03 ± 0.01	1.33 ± 0.14	0.40 ± 0.01
	S Arm	0.03 ± 0.01	1.43 ± 0.12	0.49 ± 0.02
	Interarm	0.03 ± 0.02	1.24 ± 0.21	0.27 ± 0.01
NGC 7793	Global	0.12 ± 0.01	0.79 ± 0.03	0.33 ± 0.004
	Center	0.15 ± 0.03	0.76 ± 0.05	0.38 ± 0.01
	Ring	0.19 ± 0.03	0.64 ± 0.04	0.33 ± 0.01
	Outer	0.06 ± 0.01	1.00 ± 0.06	0.32 ± 0.01

Note: ^a Fitted intercept when slope is held fixed at $a_0 = 0.5$.

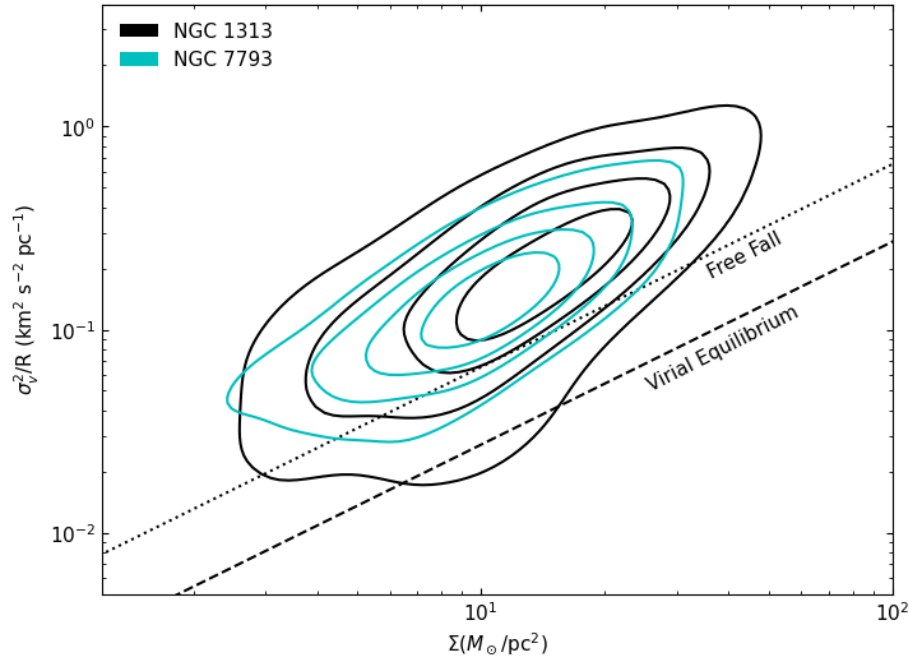


Fig. 3.10.— Kernel density estimates of the velocity metric plotted against surface density of the dendrogram structures in NGC 1313 and NGC 7793, with contours of 20%, 40%, 60%, and 80% of the maximum density. The dashed line shows where clouds in virial equilibrium would fall, above the line being dominated by kinetic energy. Clouds that have begun free-fall collapse would also have enhanced kinetic energy and fall along the dotted line. The structures in both galaxies are mostly super-virial, though the clouds in NGC 1313 appear to have more scatter.

could indicate that many of the clouds in these galaxies are not gravitationally bound, or would require an external pressure to remain bound. This is not unexpected since many studies have found a large number of unbound molecular clouds in galaxy surveys and simulations (Dobbs et al. 2011; Colombo et al. 2014; Sun et al. 2018; Rosolowsky et al. 2021).

While the two galaxies generally occupy the same parameter space in Figure 3.10, NGC 1313 appears to have a larger scatter and have more clouds close to virial equilibrium. This could suggest that more of the clouds in NGC 1313 are close to collapsing into stars and star clusters, which could drive the larger numbers of clusters in NGC 1313 despite its fewer number of clouds. The larger scatter of NGC 1313 clouds towards the unbound parameter space also matches expectations of molecular clouds responding to galaxy interactions, which cause clouds to become unbound (Pettitt et al. 2018; Nguyen et al. 2018). We investigate the boundedness of these structures more quantitatively by examining the spread in virial parameters, α_{vir} , in later sections.

3.7.1 **Regional Virialization**

We also examine where the different regions in each galaxy fall in this parameter space in Figure 3.11. In NGC 1313, all of the regions show more of a dip towards the virial equilibrium line than NGC 7793, though the biggest populations close to virial equilibrium are in the bar and the interarm regions, where the 50% density contours also show that dip. The southern arm appears to extend higher in the plot, suggesting that more of its clouds are either unbound or would require an external pressure to remain bound compared to the other regions. It seems likely that this is related to the interaction history of NGC 1313 in the southwest since simulations

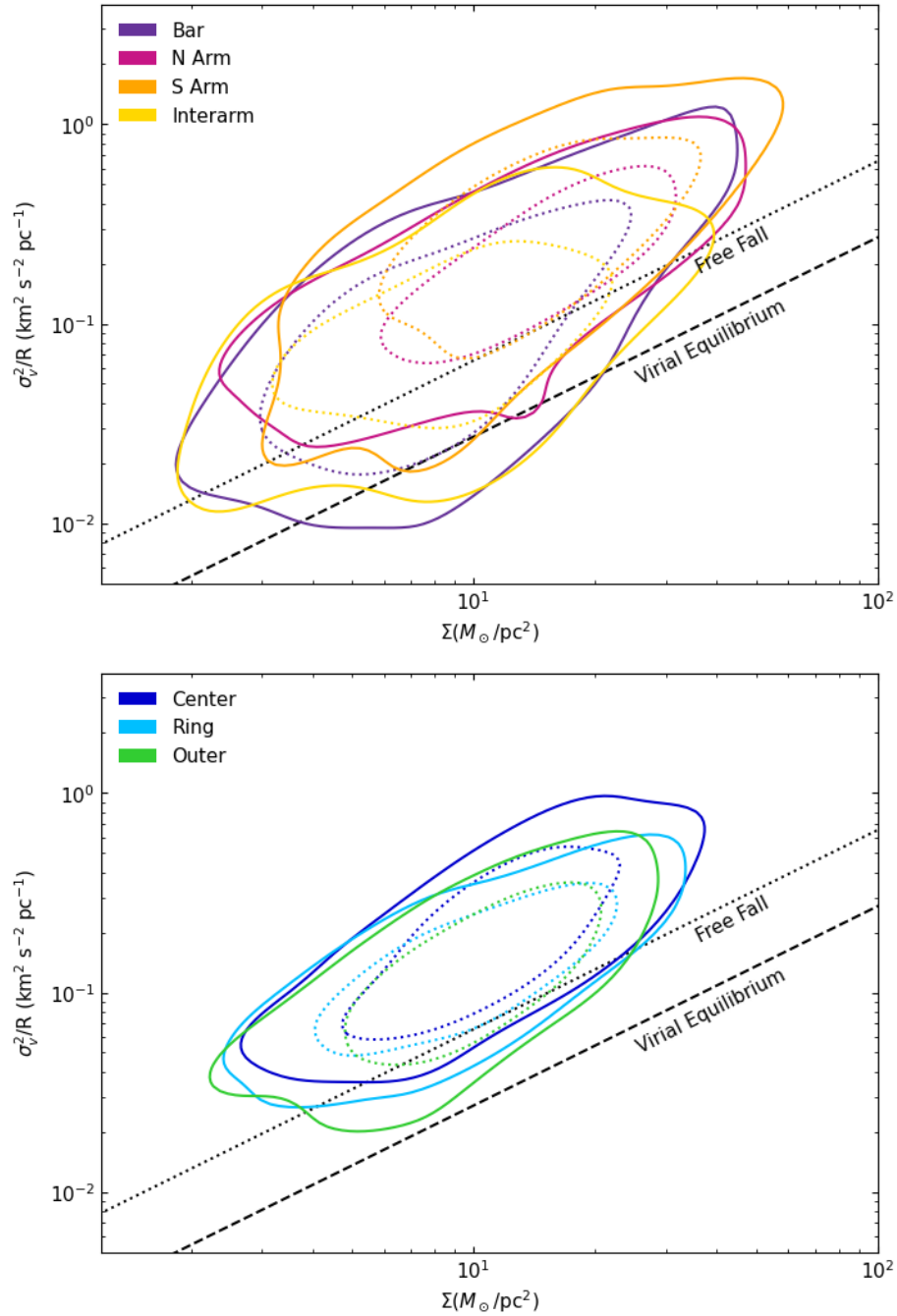


Fig. 3.11.— The velocity metric plotted against surface density of the dendrogram structures in the different regions of NGC 1313 (top) and NGC 7793 (bottom) showing the 20% KDE contours as solid lines and the 50% contours as dotted lines. The dashed line shows where clouds in virial equilibrium would fall, above the line being dominated by kinetic energy. Clouds that have begun free-fall collapse would also have enhanced kinetic energy and fall along the dotted line.

show interaction causing clouds to become unbound (Pettitt et al. 2018; Nguyen et al. 2018). Interestingly, the bar of NGC 1313 does not have more clouds in the unbound or pressure-bound region of the plot than other regions despite that many other galactic centers exhibit high external pressures (Donovan Meyer et al. 2013; Colombo et al. 2014; Kauffmann et al. 2017; Walker et al. 2018; Sun et al. 2018; Sun et al. 2020).

In NGC 7793, the three regions once again appear more uniform than in NGC 1313, although the center region does extend higher in the plots, suggesting that it has more clouds that are unbound or require external pressure than the ring and outer regions as we would expect for a galactic center. The ring and outer regions appear very similar, suggesting there is little variation in the virialization of clouds outside of the galaxy center. None of the regions of NGC 7793 however show a dip towards virial equilibrium like that seen in every region of NGC 1313, except for slightly in the ring region.

3.8 Property Distribution Comparisons

3.8.1 Global Comparison

We next investigate how the distributions of cloud properties compare between the two galaxies by looking at histograms, KDEs, and CDFs of the non-overlapping clump structures. In Figure 3.12, we show the distributions of the three observed quantities (masses, radii, and linewidths) of the two galaxies. By eye, these distributions appear very similar, with NGC 7793 having a slightly broader distribution of masses at both the high and low mass end, and shifted to slightly larger radii.

We see a bit more difference between the galaxies in the properties derived from

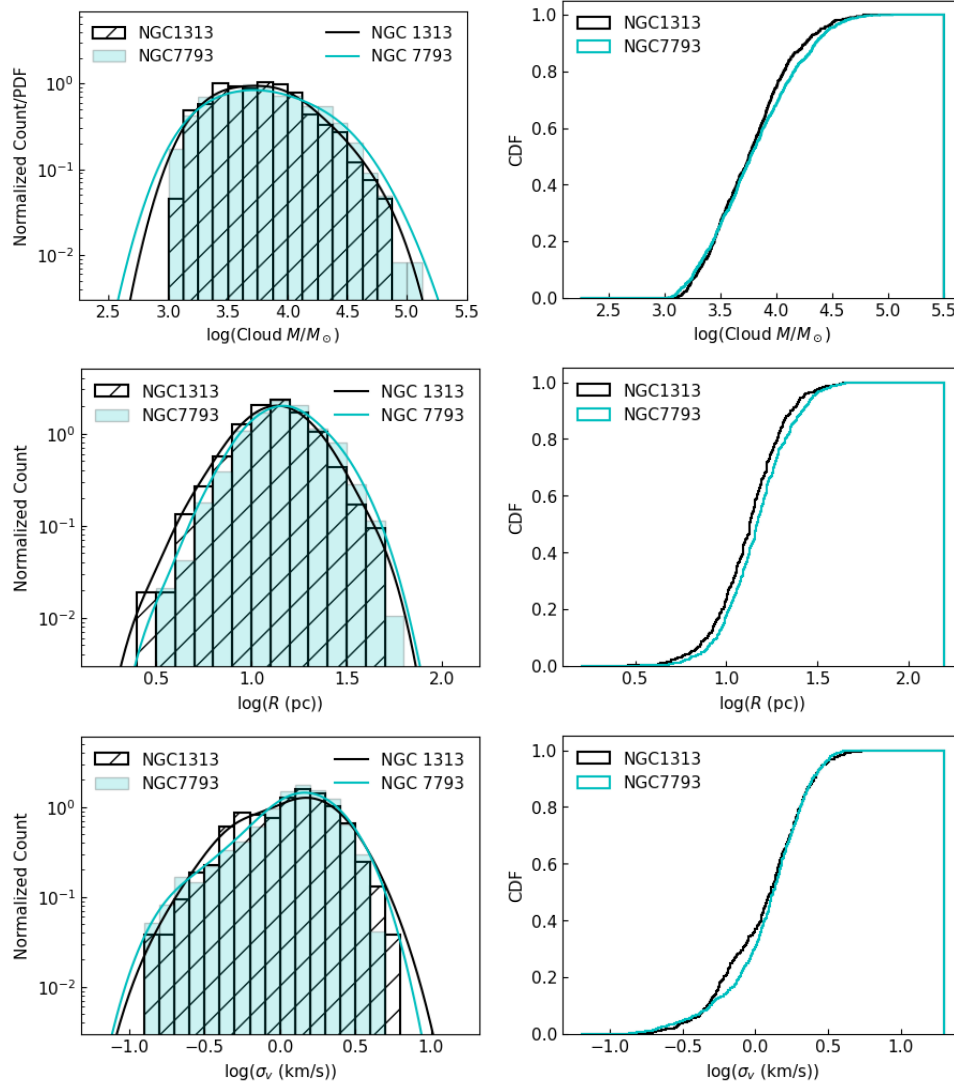


Fig. 3.12.— Distributions of the observed clump parameters for the two galaxies, using histograms and KDEs (left) and CDFs (right). We see minimal difference between the distributions except for a slightly wider mass distribution and slightly larger radii for NGC 7793.

M , R , and σ_v . We show the distributions of the virial parameter, surface density, external pressure, and free-fall time in Figure 3.13. From these we see that NGC 1313 has more clouds at low α_{vir} , which we expected from Section 3.7, as well as higher surface densities, higher external pressures, and lower free-fall times.

We perform the two-sample versions of both the Kolmogorov-Smirnoff (KS) test and the Anderson-Darling (AD) and report a p -value indicating the probability that the two samples are pulled from the same distribution, where a p -value of less than 5% is generally taken to be statistically significant. The KS test is most sensitive to the center of the distribution, while the AD test is more sensitive to the tails. The comparison of every property for the two galaxies have p -values less than 5%, and most are also much less than 1%. This is likely an over-representation of how different the distributions truly are though because the sample sizes of clouds and clusters for the galaxies is so large. As discussed in (Lazariv & Lehmann 2018), as the sample size becomes larger, KS and AD tests have increasingly higher power to discern small differences in the distributions. However, these tests do not take into account the error in the parameters, and so at large sample sizes, these tests can discern differences that are smaller than the error in the measurements, which we consider unreliable.

To combat overpowered statistical tests, we take random subsamples of the distribution for each galaxy and perform a KS and AD test, using a sample size instead of 65. After taking 1000 subsamples, we use the average p -values for each property comparison as the bootstrapped result. We show these results for each property in Table 3.5. This method also means we can better compare the test results between subgalactic regions, which have fewer clumps and clusters, at the same level of discerning power for each statistic. We choose a sample size of 65 because we are limited

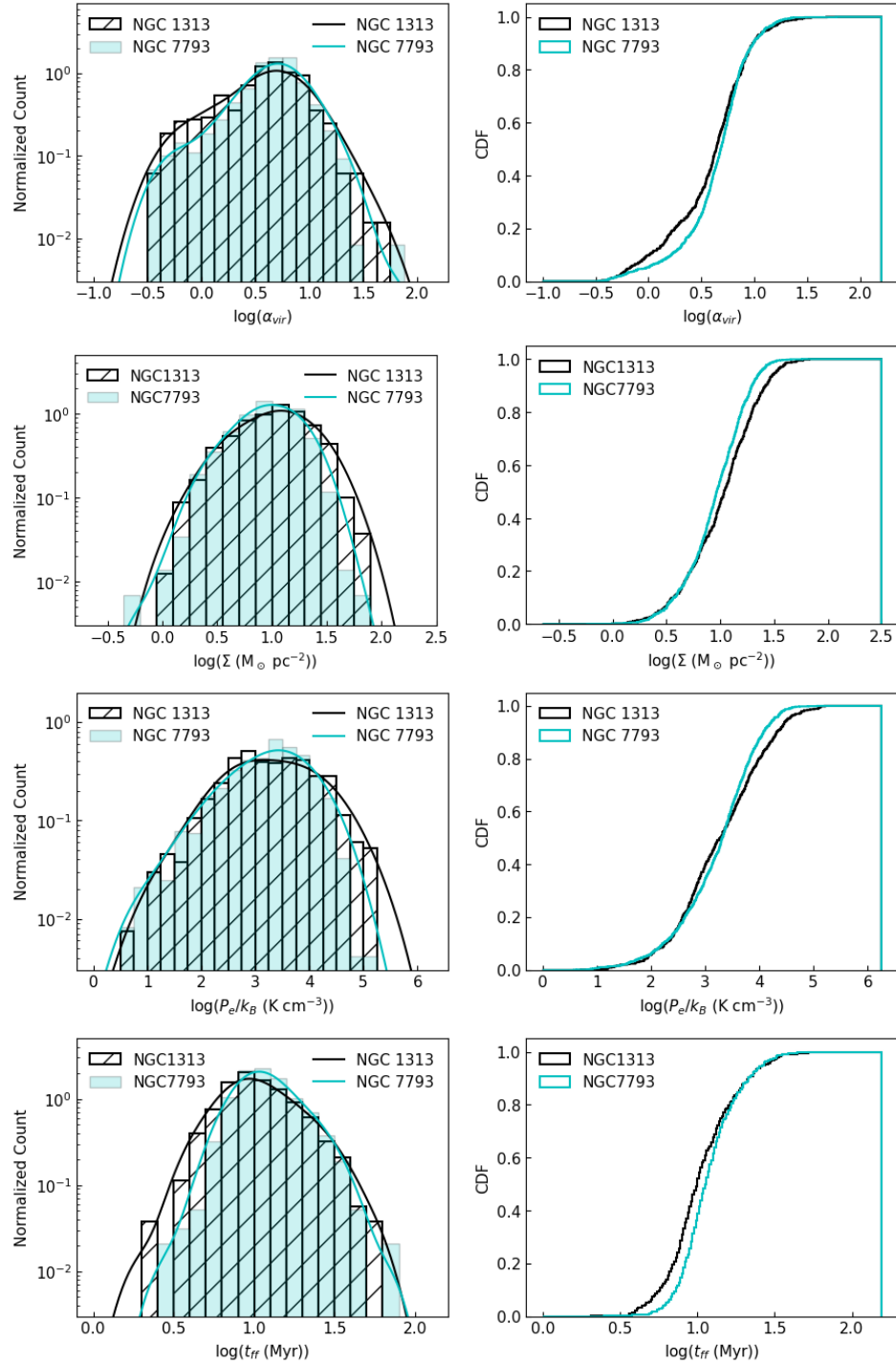


Fig. 3.13.— Distributions of the derived parameters for the two galaxies, using histograms and KDEs (left) and CDFs (right). NGC 1313 appears to have more clouds at low α_{vir} , higher surface densities, higher external pressures, and lower free-fall times than NGC 7793.

by the the number of clumps identified in the bar of NGC 1313. The resulting p -values of these tests are shown in Table 3.5. With this bootstrapped statistic, the only property that crosses a 5% threshold for significance for both KS and AD tests is the distributions of cluster masses - this emphasizes how the cluster populations of the two galaxies appear significantly different, but none of the cloud properties match that level of difference.

The bootstrapped KS and AD tests can be useful for relative comparisons, but we treat the absolute result of whether the distributions are the same or different with much caution. Choosing a sufficiently large sample size causes every property to appear significantly different between the two galaxies, and similarly a sufficiently small sample size makes no property have a statistically significant result. We consider the most reliable use of these bootstrapped tests to be a comparison between properties and regions of which show the greatest differences in their distributions. Plots showing the KS and AD comparisons between every subgalactic region for each property are shown in Section 3.8.1.

These plots and tests indicate that overall, the cloud properties between the two galaxies are not particularly different. The greater number of massive clusters in NGC 1313 compared to NGC 7793 may be driven in part by higher surface densities and pressures. The lower virial parameters and free-fall times in NGC 1313 may suggest that more clouds are close to gravitational collapse and collapse more quickly, which could then result in more clusters being formed on this cloud scale.

To better understand if the highest-surface density clouds in NGC 1313 represent a high-density tail of collapsing clouds, we also plot all of the derived cloud properties against one another for both galaxies in Figure 3.14. These plots show that the surface density, pressure, and free-fall time are all closely correlated with one another,

Table 3.5: Boostrapped two-sample KS and AD test results between NGC 1313 and NGC 7793 global properties

Parameter	KS p -value	AD p -value
Cluster Mass	0.04	0.01
Cluster Age	0.22	0.09
Cloud Mass	0.46	0.20
Radius	0.37	0.16
Linewidth	0.44	0.20
Virial parameter	0.40	0.18
Surface density	0.32	0.14
Pressure	0.38	0.18
Free-fall time	0.20	0.10

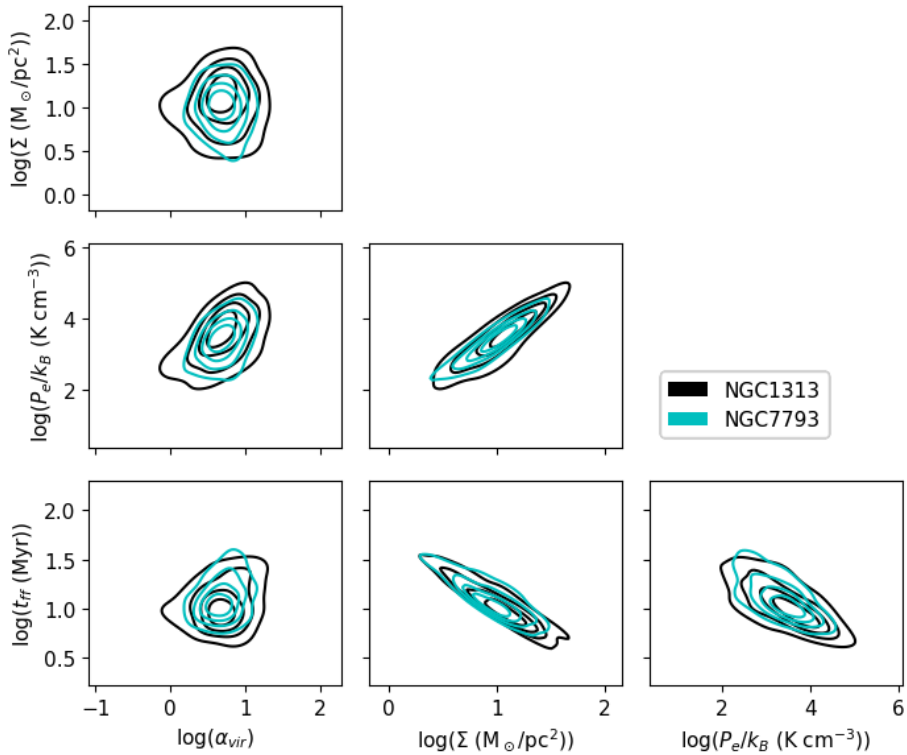


Fig. 3.14.— Gaussian KDEs of the derived dendrogram structure properties plotted against each other for both NGC 1313 and NGC 7793, with contours of 20%, 40%, 60%, and 80% of the maximum density. The virial parameters are much less correlated with the other three properties.

but the virial parameters are much less correlated with all three. This matches results from Sun et al. (2022) that α_{vir} shows the least correlation with other clouds properties while most others are well-correlated, especially the surface density (which is unsurprising since these parameters are calculated from the same three measurements of M , R , and σ_v). The NGC 1313 structures with low virial parameters that may be closest to collapsing do not have particularly high or low surface densities or free-fall times, and slightly low external pressures. This would suggest then that the high surface density clouds in NGC 1313 are not high because they are all collapsing, although the higher surface density clouds also have lower free-fall times.

Kolmogorov-Smirnoff and Anderson-Darling Tests

As thoroughly discussed in Lazariv & Lehmann (2018), as the sample size increases, the discerning power of KS tests increases. However, KS tests cannot take into account error in the measurements, and so it is possible for a test to become over-powered. Even a small difference in the distribution well below the measurement uncertainty can result in a rejection of the null hypothesis that the distributions are the same. This affect is present in AD tests as well.

To combat overpowered statistical tests, we perform a bootstrapping method to measure the difference in the distributions as described in Section 3.8.1. We caution that the resulting p -values are highly dependent on the size of the subsample used, and so these results should only be used to compare the differences between properties and regions on equally-powered statistical footing. This is meant as an indication of which pairings are the most different, not whether the underlying distributions are truly different. It may be possible to select a subsample size based on the error of the measurements being tested, but that is outside the scope of the current work.

Figure 3.15 shows the bootstrapped KS statistic for each cloud and cluster property for each pairing of subgalactic region as well as global distributions for each galaxy. Figure 3.16 shows the same but with an AD test. KS tests are more influenced by the center of the distribution, while AD tests are more sensitive to the tails.

3.8.2 NGC 1313 Region Comparison

We compare the distribution of cloud properties within the bar, northern arm, southern arm, and interarm regions of NGC 1313. The observed mass, radius, and linewidth distributions are shown in Figure 3.17, and the properties derived from them are shown in Figure 3.18. For figure clarity, we show only the KDEs and not the underlying histograms.

There is a large difference in the mass distributions, with the spiral arms having significantly more massive clouds than the bar or interarm regions. The northern arm also appears to have slightly higher masses than the southern arm. These regional mass distribution differences agree with previous results that spiral arms truncate at higher masses than clouds in the interarm regions, seen in both observations (Koda et al. 2009; Colombo et al. 2014; Rosolowsky et al. 2021) and simulations (Pettitt et al. 2018; Nguyen et al. 2018; Dobbs et al. 2019). The differences between cloud size distributions are minimal, though the bar region appears to have slightly fewer clouds with large radii. The spiral arms have similar linewidth distributions and are higher than the other two regions, where the interarm region has the smallest linewidths, again matching previous results (Colombo et al. 2014; Sun et al. 2020; Rosolowsky et al. 2021; Koda et al. 2023).

Despite the large difference in mass distributions, the properties derived from the

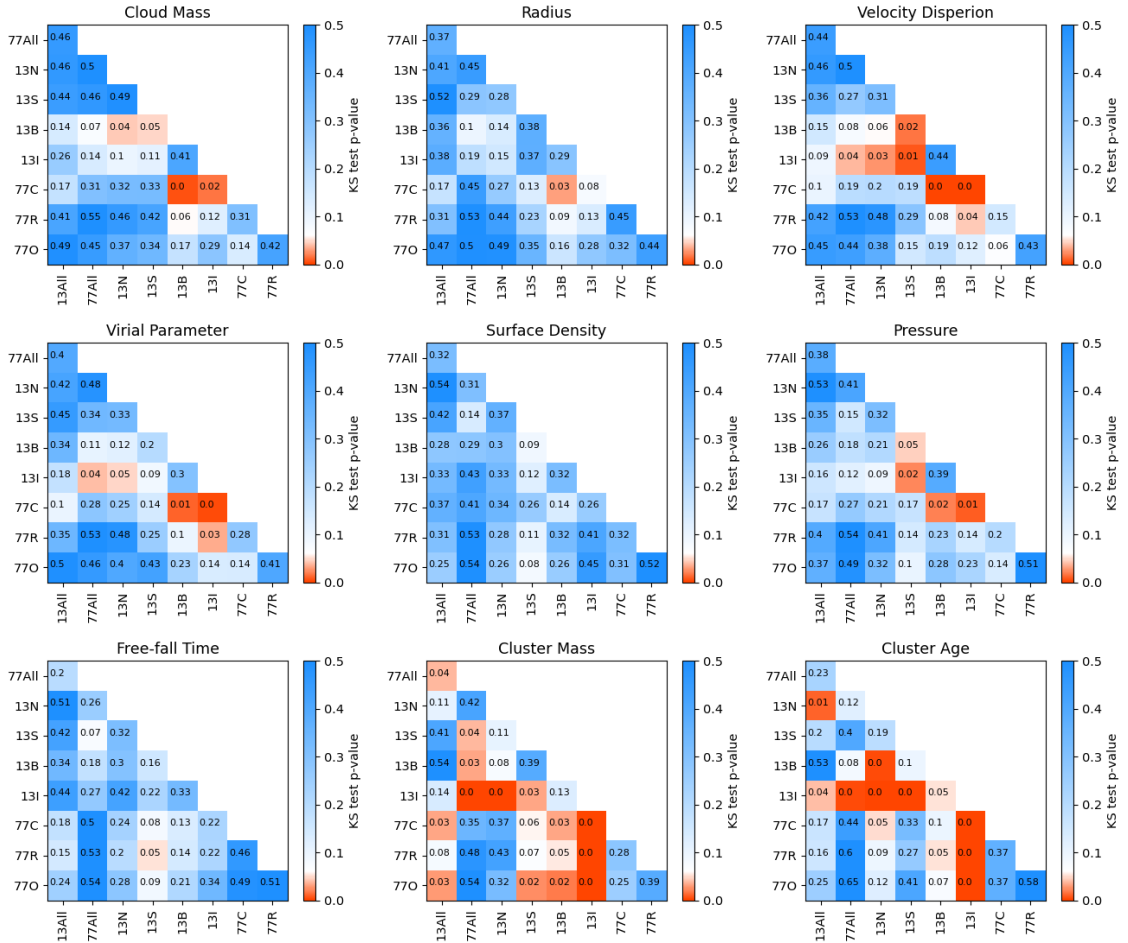


Fig. 3.15.— Bootstrapped KS tests for each cloud and cluster property and for each pairing of subgalactic region as well as global distributions for each galaxy. These p -values should be used as an indication of which distributions are the most different rather than as an absolute metric of whether any one distribution is truly different. Codes for the regions are as follows: “13All” is the global distribution for NGC 1313; “77All” is the global distribution for NGC 7793; “13N”, “13S”, “13B”, and “13I” are the northern arm, southern arm, bar, and interarm regions of NGC 1313; and “77C”, “77R”, and “77O” are the center, ring, and outer regions of NGC 7793.

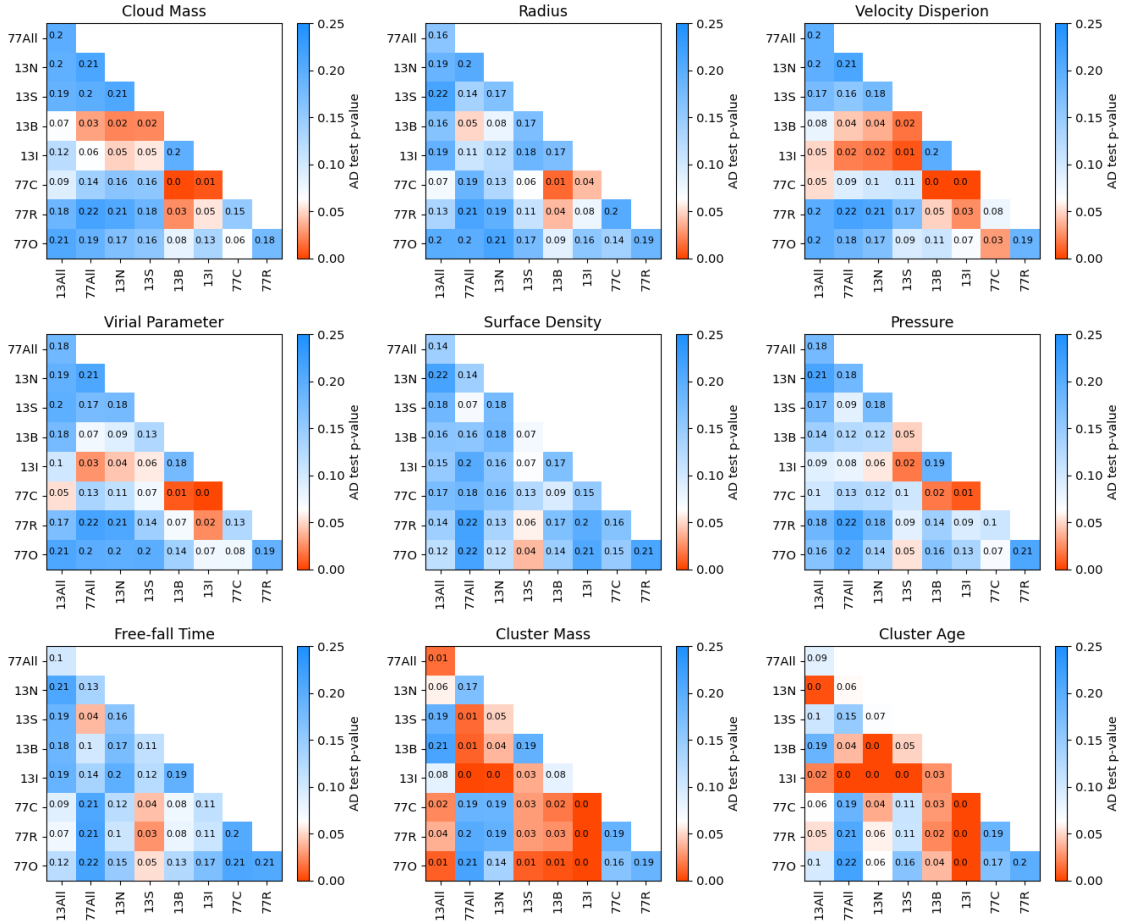


Fig. 3.16.— Bootstrapped AD tests for each cloud and cluster property and for each pairing of subgalactic region as well as global distributions for each galaxy. These p -values should be used as an indication of which distributions are the most different rather than as an absolute metric of whether any one distribution is truly different. Codes for the regions are as follows: “13All” is the global distribution for NGC 1313; “77All” is the global distribution for NGC 7793; “13N”, “13S”, “13B”, and “13I” are the northern arm, southern arm, bar, and interarm regions of NGC 1313; and “77C”, “77R”, and “77O” are the center, ring, and outer regions of NGC 7793.

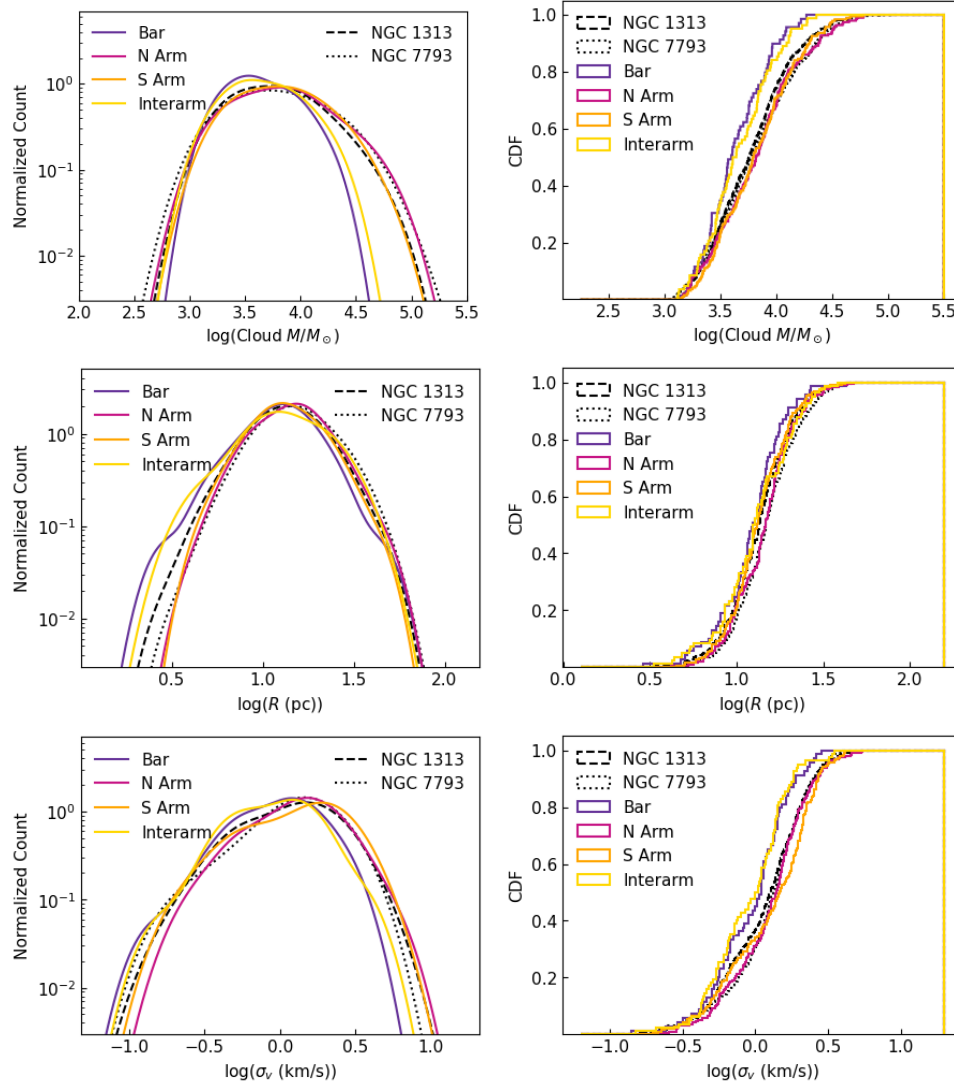


Fig. 3.17.— Distributions of the observed parameters for the bar, northern arm, southern arm, and interarm regions of NGC 1313 using KDEs (left) and CDFs (right). Also shown are the global distributions for each galaxy.

mass, radius, and linewidth do not show strong distinctions between regions. Most notably, the interarm and bar regions appears to have the lowest virial parameters, surface densities, and external pressures. The southern arm also appears to have slightly higher surface densities and pressures compared to the northern arm and other regions.

These differences between the observed and derived property distributions also appear in comparisons of the bootstrapped KS and AD tests shown in Section 3.8.1. None of the derived properties have statistically significant differences (p -values < 0.05) in their distributions between regions for both KS and AD tests except for the southern arm having significantly higher pressure than the bar and interarm regions. There are, however, statistically significant differences in their mass and linewidth distributions. The absolute value of these test results are highly subject to the size of the subsamples used in the bootstrapping, and so we do not take these of indications of whether or not the distributions are actually different, but rather that some are more different than others.

It is particularly surprising that we see so little difference in surface densities between arm and interarm regions, since that has often been a notable difference in other studies (Colombo et al. 2014; Sun et al. 2020; Rosolowsky et al. 2021; Koda et al. 2023). We also note that the clouds in the bar of NGC 1313 mostly have less extreme properties than the arms, whereas other studies have often seen enhancements of the velocity dispersion, surface density, and pressure in bars and galactic centers (Sun et al. 2020; Rosolowsky et al. 2021). This may not be so surprising since Querejeta et al. (2021) report large variations in the properties of molecular gas in bars, potentially because star formation in bars is episodic.

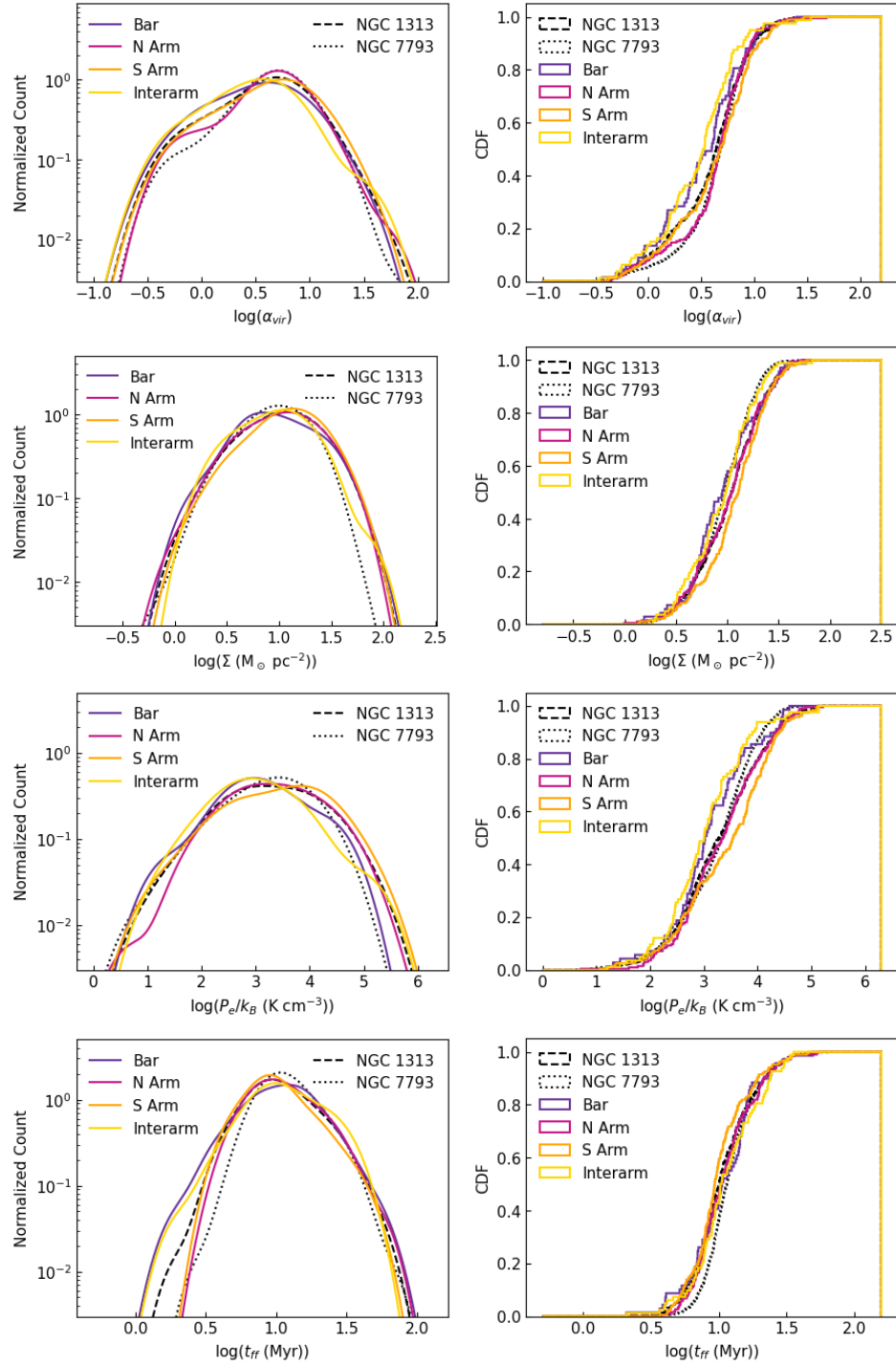


Fig. 3.18.— Distributions of the derived parameters for the bar, northern arm, southern arm, and interarm regions of NGC 1313 using KDEs (left) and CDFs (right). Also shown are the global distributions for each galaxy.

3.8.3 NGC 7793 Region Comparisons

We next examine the distribution of cloud properties within the center, ring, and outer regions of NGC 7793. The observed mass, radius, and linewidth distributions are shown in Figure 3.19, and the properties derived from them are shown in Figure 3.20.

The distributions in NGC 7793 vary from the center of the galaxy to the outer region, with the center having more extreme properties, such as higher masses, higher linewidths, higher virial parameters, and higher external pressures. This generally matches what was found in other surveys for the centers of galaxies (Donovan Meyer et al. 2013; Colombo et al. 2014; Sun et al. 2020; Koda et al. 2023). There is not as much difference, however, in the distributions of radii, surface densities, or free-fall times. In most cases, the ring and outer regions have very similar distributions, while the center deviates more.

These similarities and differences appear as well in comparisons of the bootstrapped KS and AD tests shown in Section 3.8.1. None of the cloud or cluster properties, either observed or derived, have statistically significant differences (p -values < 0.05) in their distributions among the regions of NGC 7793 for both KS and AD tests. The only exception is the center region having significantly higher linewidths than the outer region based on the AD test. Again, the absolute value of these test results are highly subject to the size of the subsamples used in the bootstrapping, so we do not take these results to indicate whether or not the distributions are actually different, but rather that some are more different than others.

3.8.4 Inter-Galaxy Region Comparisons

Based on the regional distributions of NGC 1313 shown in Figures 3.17 and 3.18, none of the regions of NGC 1313 have similar property distributions to the global

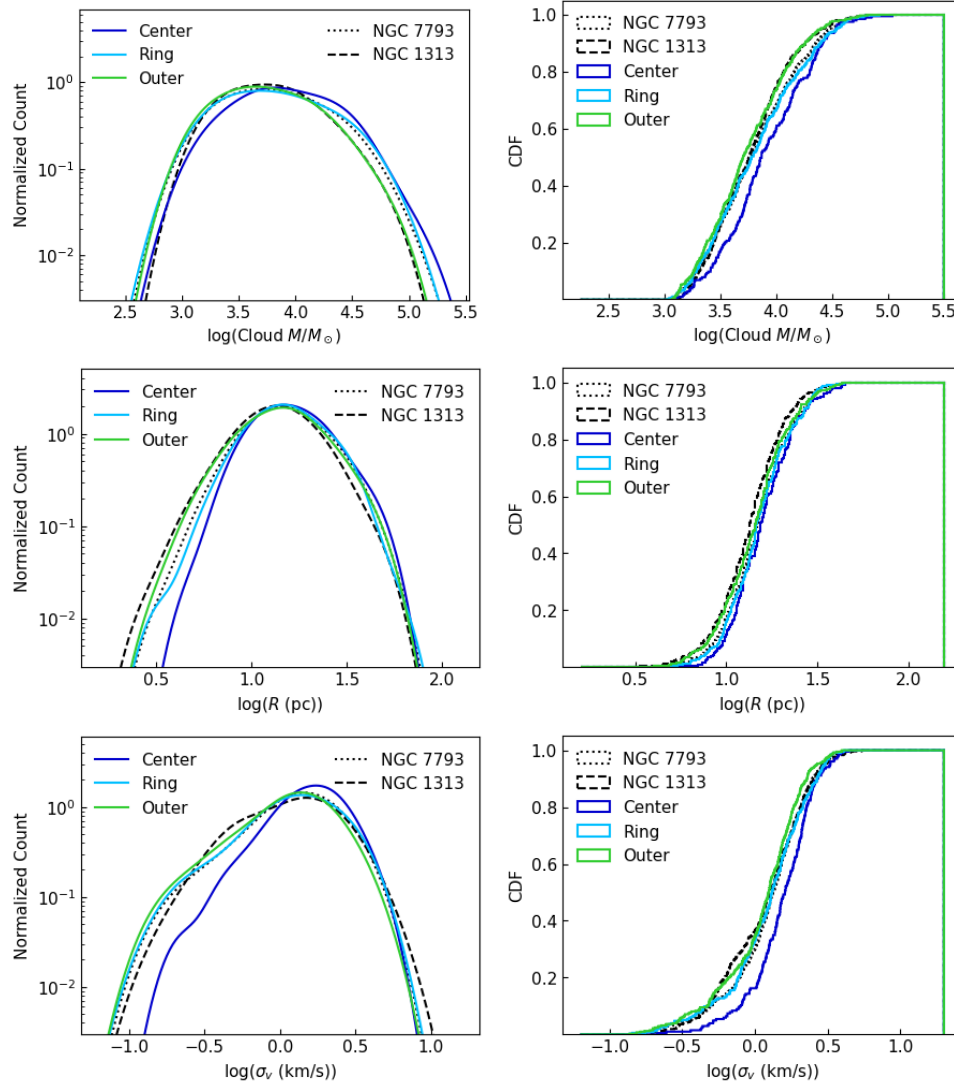


Fig. 3.19.— Distributions of the observed parameters for the center, ring, and outer regions of NGC 7793 using KDEs (left) and CDFs (right). Also shown are the global distributions for each galaxy.

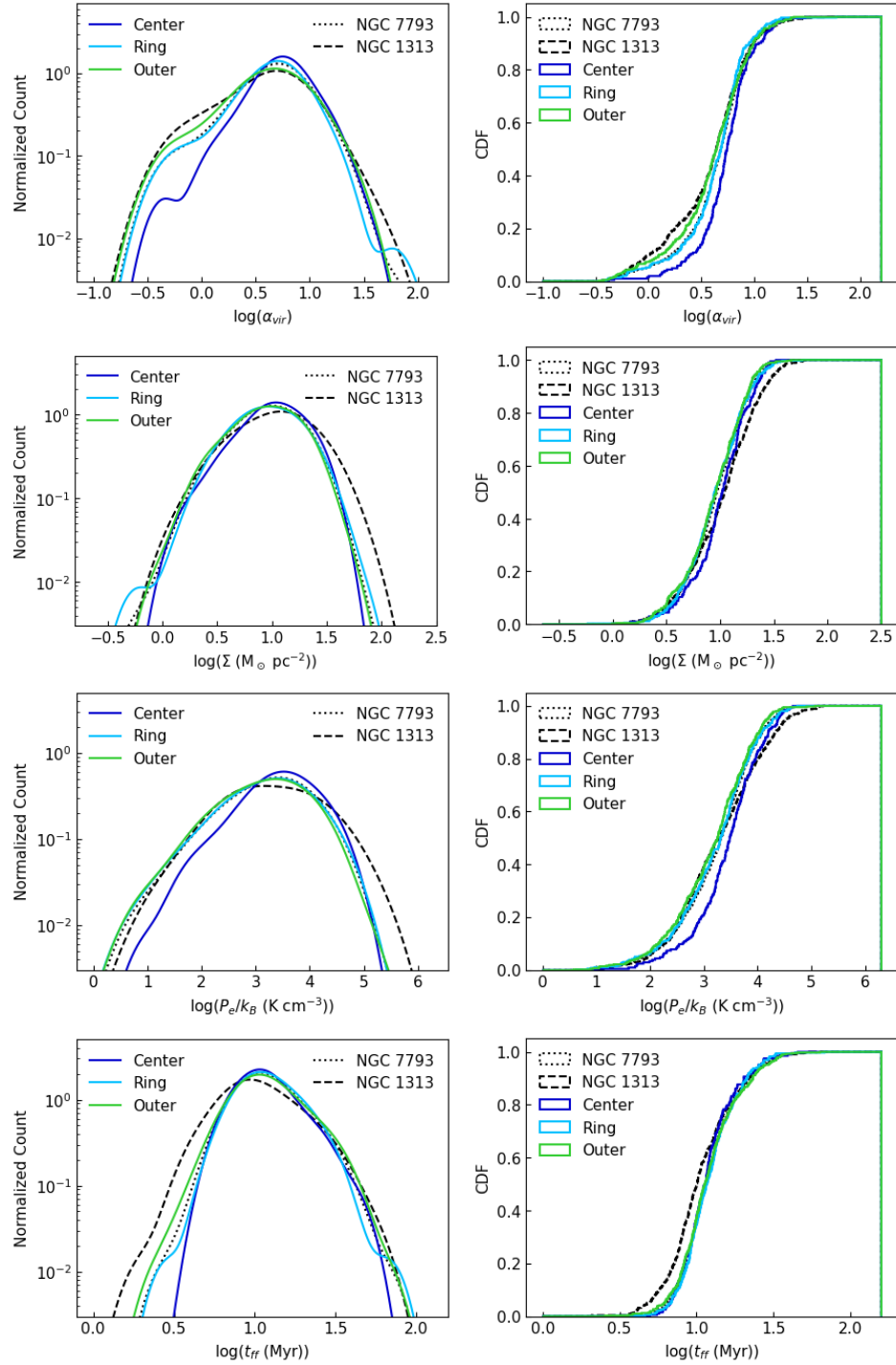


Fig. 3.20.— Distributions of the derived parameters for the center, ring, and outer regions of NGC 7793 using KDEs (left) and CDFs (right). Also shown are the global distributions for each galaxy.

distributions of NGC 7793 clouds across all properties. The northern arm has the most similar mass distribution and α_{vir} distribution to NGC 7793, but the interarm region has the most similar surface density distribution, and in other property distributions, such as external pressure and free-fall time, no NGC 1313 region is similar to the clouds in NGC 7793. This suggests that the environment of a flocculent spiral like NGC 7793 is quite different from both clearly defined arms and their interarm regions. Most notably, every region of NGC 1313 contains, on average, clouds with higher surface densities and shorter free-fall times than NGC 7793.

This differences between the galaxies' regions is seen again in Figures 3.19 and 3.20, which show that none of the regions of NGC 7793 have similar virial parameters, surface densities, external pressures, or free-fall times to the global distributions of NGC 1313. The ring region of NGC 7793 appears to have the most similar mass, radius, and linewidth distributions to the global distribution of NGC 1313.

Considering the comparisons of the bootstrapped KS and AD tests in Section 3.8.1, some of the most significant differences among all the pairings for both tests are between the central region of NGC 7793 and the bar and interarm regions of NGC 1313, for almost every property, with the notable exception of surface density and free-fall time. This is somewhat surprising since the bar of NGC 1313 encompasses that galaxy's own central region. One other notable difference from the KS and AD tests is that the southern arm of NGC 1313 has statistically significant lower free-fall times than all regions of NGC 7793. This is not true for the northern arm. Since the absolute value of resulting p -values of these bootstrapped tests are so easily influenced by subsample size, we do not take these results to indicate whether or not the distributions are actually statistically different, but rather to indicate which distributions are most different.

3.9 Discussion

Overall, the measured cloud properties in the two galaxies are surprisingly similar, especially given the difference in massive star cluster formation between the two. There are slight differences in the distributions of cloud masses, sizes, and linewidths, and these small differences compound to create larger differences in their densities and energy balances. This suggests that star formation variations can be driven by relatively small shifts in these properties, at least on the size scales measured here.

In Table 3.6, we briefly outline the differences in each property between the two galaxies and among regions within each galaxy. There does not appear to be any singular property that has an out-sized influence on the star formation of either galaxy or galactic region.

While the differences between the cloud properties in the two galaxies are surprisingly small, there is much greater variation between regions within the galaxy, especially within NGC 1313. This suggests that the local environment has a much stronger influence on cloud properties than the global galaxy environment. This was also seen when comparing regional variations and galaxy-to-galaxy variations in the PHANGS sample at 100 pc resolution (Sun et al. 2022).

Comparing the regional variations within the two galaxies, NGC 7793 appears much more uniform across the galaxy than NGC 1313, with more extreme properties only being seen in the center of the galaxy. The lack of clearly-defined arm and interarm regions makes direct comparison tricky, but it is at least clear that no part of NGC 7793 contains clouds with surface densities, pressures, or linewidths as high as the arms of NGC 1313. Elmegreen (2009) posits that the degree of dispersion of the density probability distribution function determines the ability of a region to form massive, gravitationally bound star clusters. Regions that have a larger spread

Table 3.6: Comparison of observed properties between environments

Property	Global Difference	NGC 1313 Regional	NGC 7793 Regional
Cluster mass distribution	NGC 1313 more massive	Interarm most and N arm least massive	No difference
Cluster age distribution	NGC 1313 older	Interarm older, N arm youngest	No difference
Size-Linewidth slope	No difference	No difference	No difference
Size-Linewidth intercept	No difference	S arm higher, interarm lower	Center higher
Virialization plot	NGC 1313 closer to virial	Bar and interarm closer to virial	Center further from virial
Cloud Mass distribution	No difference	Arms more massive	Center more massive
Radius distribution	NGC 7793 larger	No difference	No difference
Linewidth distribution	No difference	Arms higher	Center higher
Virial parameter distribution	NGC 1313 lower	Interarm lower	Center higher
Surface density distributions	NGC 1313 higher	S arm higher, interarm lowest	No difference
External pressure distribution	NGC 1313 higher	S arm higher, interarm lowest	Center higher
Free-fall time distribution	NGC 1313 lower	No difference	No difference

in densities will also achieve higher densities, and so be able to form massive clusters. It would follow then that NGC 1313 is able to create more massive star clusters than NGC 7793 because it has a greater variety of subgalactic environments, including strong spiral arm environments that have higher pressures and densities.

It is interesting to note as well that the southern arm of NGC 1313 has slightly more extreme properties than its northern arm. We know from measurements of HI and its star formation history (Peters et al. 1994; Larsen et al. 2007; Silva-Villa & Larsen 2012; Hernandez et al. 2022) that NGC 1313 is experiencing an interaction, which likely caused a recent burst in star formation in the southwest of the galaxy approximately 100 Myr ago. This interaction may also be influencing the difference in cloud properties between the northern and southern arm, suggesting that satellite galaxy interaction can drive variations in local cloud properties.

Meanwhile in NGC 7793, its loose, poorly-defined spiral arms does not result in the majority of the clouds mimicking either the arm or the interarm regions of NGC 1313. Rather, the cloud properties throughout the galaxy have similar masses and kinetic energies to the arms of NGC 1313, but their surface densities and pressures are more similar throughout to the bar and interarm regions of NGC 1313. These differences overall result in higher virial parameters and longer free-fall times throughout NGC 7793 than any other regions in NGC 1313. Essentially, NGC 7793 has clouds that are just as massive and have just as much kinetic energy as NGC 1313, but they are puffier and less pressurized, and so are less inclined to collapse and form stars.

A notable exception to the uniformity of NGC 7793 is the center of the galaxy, where the clouds have higher masses, and fewer clouds have low linewidths, virial parameters, and pressures. These differences between cloud properties may be con-

nected to the presence of supermassive clusters in the center of NGC 7793, though the overall cluster property distribution seems uniform throughout the galaxy based on the CDFs (Figure 3.6). This is reminiscent of the center of our own Galaxy, where the clouds have more extreme properties and some massive star clusters are present, but it is still forming fewer stars than expected based on the gas properties (Kauffmann et al. 2017; Walker et al. 2018).

This work represents the highest resolution direct comparison of the molecular cloud properties in spiral arm, interarm, and flocculent environments to date. Comparing our results at 13 pc to other results at ~ 40 -100 pc resolution reveals further insights about how the molecular gas behaves at different spatial scales. For the most part, we see similar trends in that spiral arms and galaxy centers have higher masses, linewidths, and pressures than interarm and outer regions of the galaxies. However, we see notably less difference in the surface densities between these regions than other studies have found at lower resolution (Colombo et al. 2014; Sun et al. 2020; Rosolowsky et al. 2021; Koda et al. 2023). This could indicate that at lower resolution, the sparse clouds of the interarm and outer regions are spread out to lower apparent surface density by the large beam size. In the arm and central regions, the clouds are sufficiently clustered that the beam is filled by clouds getting blended together, and so the apparent surface density remains high. If this is the case, the surface density seen by lower-resolution studies could be indicative of the sparsity of molecular clouds rather than their true density.

3.10 Conclusions

We present a comparison of the molecular gas of two spiral galaxies from the LEGUS sample (Calzetti et al. 2015), NGC 1313 and NGC 7793, observed in CO(2-1)

with ALMA. These two galaxies have similar stellar masses, metallicities, and star formation rates, yet NGC 1313 is forming significantly more massive star clusters than NGC 7793. With observations of the same molecular tracer at the same physical resolution and the same sensitivity, we compare the properties of the molecular gas to understand what differences in gas conditions give rise to such different star formation outcomes. Our major results are summarized below.

- In addition to NGC 1313 having more massive star clusters than NGC 7793, the cluster populations in NGC 1313 vary by region. The interarm region of NGC 1313 has the oldest and most massive clusters, and the northern arm has the youngest and least massive clusters. The clusters in NGC 7793 show relatively little variation with region of the galaxy, with the exception of a couple supermassive clusters in the center of the galaxy.
- Despite having less star formation, NGC 7793 has significantly more molecular gas by mass, and more identified cloud structures. NGC 1313 has most of its molecular gas mass in its two spiral arms, with relatively few cloud structures identified in the bar or interarm regions.
- We fit power laws to the size-linewidth relations for the two galaxies and find that NGC 1313 has a steeper power law slope than NGC 7793. We also fit solely the intercept of the size-linewidth power law, holding the slope fixed at a value of $a_1 = 0.5$ to determine relative kinetic energies. NGC 1313 also has a significantly higher intercept than NGC 7793, suggesting that the kinetic energy of clouds in NGC 1313 are higher than in NGC 7793. The spiral arms of NGC 1313 have higher fitted intercepts, and so more kinetic energy, than the bar or interarm regions. The fitted intercepts of regions in NGC 7793 meanwhile do not differ by more than 3σ .

- Most of the clouds in both galaxies appear to be unbound and out of virial equilibrium based on plots of their surface densities against their velocity metrics. NGC 1313 has more clouds near virial equilibrium than NGC 7793. This difference in virialized clouds is true for all regions in NGC 1313 and all regions of NGC 7793. The southern arm of NGC 1313 and the center region of NGC 7793 both show a greater spread towards the unbound region of parameter space, suggesting that more of those clouds are either unbound or would require an external pressure to remain bound.
- The distributions of cloud properties between the two galaxies show minimal differences, though the small differences in the observed masses, radii, and linewidths appear to compound into larger differences in the derived properties of virial parameter, surface density, pressure, and free-fall time. NGC 1313 has lower virial parameters and free-fall times and higher surface densities and pressures than NGC 7793. The higher surface densities of NGC 1313 are not correlated with low virial parameters, which would suggest that they are not a log-normal tail caused by clouds with enhanced surface densities because they are collapsing.
- The spiral arms of NGC 1313 tend to have more extreme cloud properties (higher masses, linewidths, surface densities, pressures, and virial parameters) than the bar or interarm regions, and they also host significantly more of the molecular gas mass. In some properties, such as linewidth, surface density, and pressure, the southern arm appears more extreme than the northern arm. This could be because the southern arm is more strongly influenced by the galaxy interaction to the southwest. The greater number of star clusters and the greater masses of those star clusters in NGC 1313 may be driven by its

greater variation in environments and cloud properties within the galaxy. Its greater variation may allow for more extreme cloud properties to arise and so drive more intensive star formation.

- The center region of NGC 7793 has more extreme properties than the ring and outer regions, which are quite similar to each other. This suggests that the disk of NGC 7793 is relatively uniform in cloud properties, which is consistent with finding less variation in cluster properties among the regions than in NGC 1313. The cloud properties in NGC 7793 are not particularly similar to any one region of NGC 1313, suggesting that flocculent environments are distinct from either strong spiral arms or their interarm regions. NGC 7793 has clouds that are as massive and have as much kinetic energy as NGC 1313, but have slightly larger radii and are less dense and pressurized, and so less inclined to collapse and form stars.
- We see surprisingly little variation in surface density between arm and interarm regions in NGC 1313 given previous results. This suggests that differences in surface densities between arm and interarm regions observed in galaxies at ~ 40 pc or coarser resolution could be driven by variations in the number of clouds filling the beam, rather than intrinsic variations in the surface densities of the clouds themselves.

Chapter 4

Structure Analysis of the Quiescent Molecular Ridge

The text in Chapter 4 appeared in the *Astronomical Journal* (Finn et al. 2022) as “Structural and Dynamical Analysis of the Quiescent Molecular Ridge in the Large Magellanic Cloud.”

4.1 Introduction

Star formation is a crucial component of our understanding of galactic environments. As we study galaxies at a wide variety of distance scales and size scales, we look for easily-observable tracers of star formation and molecular gas behavior, such as the Schmidt-Kennicutt law relating molecular gas surface density and galactic star formation rate (Kennicutt 1998). These relations have had success at predicting star formation rates in many environments, but we also know of cases where those relations do not hold. For example, the Central Molecular Zone of our own Galaxy is forming stars an order of magnitude slower than we would expect for a region with so much

molecular gas available (Longmore et al. 2013). It is clear that while these relations hold well on galactic scales, the physical conditions that give rise to such relations are not constant across different environments within a galaxy.

The Large Magellanic Cloud (LMC) is an excellent laboratory in which to study the variations in galactic environments. At a distance of 50 kpc (Pietrzyński et al. 2013), it is close enough that we can resolve individual molecular clouds, while its low inclination angle ($\sim 34^\circ$; van der Marel & Kallivayalil 2014) allows us a clear view of the contents of the galaxy with little line-of-sight or distance confusion. It also hosts a wide variety of star-forming environments, making comparisons between them relatively straightforward since they share a common distance, metallicity ($Z \sim 0.5Z_\odot$; Rolleston et al. 2002), and galactic environment. In this paper, we focus our analysis on the quiescent Molecular Ridge, 30 Doradus (30 Dor), N159, and N113 to span the extremes of star formation in the LMC.

The Molecular Ridge (also referred to throughout this work as “the Ridge”) is a ~ 2 kpc-long structure in the LMC and contains nearly 30% of all the CO-bright molecular gas mass in the galaxy (Cohen et al. 1988; Fukui et al. 2008; Mizuno et al. 2001, see Figure 4.1). Despite this large quantity of molecular gas, the southern part of the Ridge is forming very few massive stars, based on low $H\alpha$ emission and lack of optically-identified young massive clusters (Davies et al. 1976; Bica et al. 1996; Yamaguchi et al. 2001).

Indebetouw et al. (2008) found that the Schmidt-Kennicutt law (Kennicutt 1998) predicts that the Ridge should have a star formation rate of $8 \times 10^{-3} M_\odot \text{ yr}^{-1}$, but the total $H\alpha$ and $24\mu\text{m}$ emission in the Ridge suggests a star formation rate of only $2.6 \times 10^{-4} M_\odot \text{ yr}^{-1}$ (Calzetti et al. 2007). Indebetouw et al. (2008) found that these numbers can be better reconciled by looking for embedded young stellar

objects (YSOs) from the Spitzer Space Telescope survey Spitzer Surveying the Agents of Galaxy Evolution (SAGE; Meixner et al. 2006), which brought the measured star formation rate to approximately $4 \times 10^{-3} M_{\odot} \text{ yr}^{-1}$, within a factor of two of the value predicted by the Schmidt-Kennicutt law. This suggests that the lack of $\text{H}\alpha$ and optical clusters is because the Ridge is preferentially forming low-mass star clusters.

This is a stark contrast to regions just north of the Ridge, such as 30 Dor and N159 (see Figure 4.1), which are some of the most active massive-star-forming regions in the LMC. 30 Dor is home to R136, the closest known super star cluster (SSC), and other young, massive clusters that bring the total mass of recently formed stars in the region up to $\sim 8.7 \times 10^4 M_{\odot}$ (Cignoni et al. 2015). There are still giant molecular clouds (GMCs) forming stars in the region, although the current star formation in 30 Dor is less extreme than it once was, forming primarily low- and intermediate-mass stars (Walborn et al. 2013; Sabbi et al. 2016). Just south of 30 Dor is N159, which contains several embedded high-mass YSOs and HII regions (Chen et al. 2010), suggesting that massive star formation is ongoing in this region. N113 similarly has signs of active high-mass star formation (Sewiło et al. 2010; Seale et al. 2012; Ward et al. 2016). By directly comparing the molecular gas in these regions with that in the Ridge, we hope to identify differences in the physical conditions that could suggest why the regions differ so much in star forming properties.

Finn et al. (2021) fit RADEX models to CO emission in the Ridge and found that the fitted volume density, n_{H_2} , had the strongest correlation with the presence of YSOs associated with the CO clumps. They hypothesized that the Ridge could be forming massive stars so sluggishly either because the molecular gas is lower density than the other star forming regions to its north, or because the threshold density for star formation is higher in the Ridge. For example, the latter could be caused by

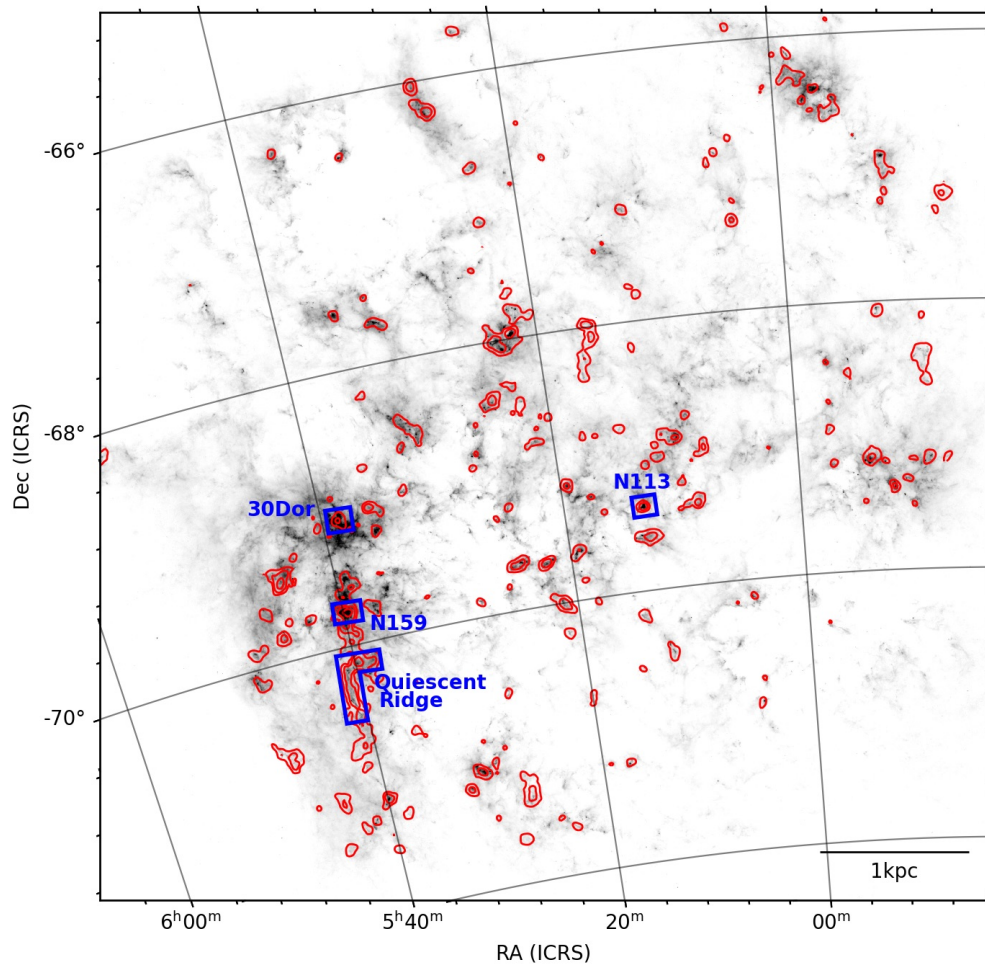


Fig. 4.1.— The LMC with the Molecular Ridge, 30 Dor, N159, and N113 highlighted in blue. The grayscale is PACS 250 μm from the HERITAGE survey (Meixner et al. 2013), and the red contours are $^{12}\text{CO}(1-0)$ from the NANTEN survey (Fukui et al. 2008) showing the extent of all the CO-bright molecular gas in the LMC. Levels are 1.6, 5, and 12 K km s^{-1}

higher amounts of turbulent or magnetic support suppressing collapse in the Ridge.

In this paper, we seek to understand the underlying differences in physical conditions between the Ridge and the other massive star forming regions including 30 Dor, N159, and N113. In §4.2, we present the different observations and regions being compared in this analysis, and in §4.3 we describe how we segment that observed emission into smaller structures using both dendrogram and clump-finding methods. We calculate the mass, velocity dispersion, and radii of these structures in §4.4. We compare the different regions by fitting size-linewidth relations in §4.5 and by considering their virial balance of turbulent and gravitational energy in §4.6. We examine variations in these physical properties within the Ridge in §4.7 and look at the spatial dependence of those variations in §4.8. We bring the results of all of these sections together in §4.9 to discuss the overall picture of the differences in these regions, then summarize our conclusions in §4.10.

4.2 Observations

We examine the Molecular Ridge in $^{13}\text{CO}(1-0)$ and $\text{CS}(2-1)$ and compare it to three other regions in the LMC: 30 Dor, N159, and N113. The observations used in this analysis and their resolutions and measured rms are summarized in Table 4.1.

Table 4.1: Observations used in this analysis

Region	Line	Beam (")	RMS (K)	Velocity Resolution (km/s)
Ridge	$^{13}\text{CO}(1-0)$	13	0.03	0.5
Ridge	$\text{CS}(2-1)$	18	0.017	0.5
30 Dor	$^{13}\text{CO}(2-1)$	13	0.009	0.25
N159	$^{13}\text{CO}(1-0)$	13	0.04	0.5
N113	$^{13}\text{CO}(1-0)$	13	0.0075	0.5

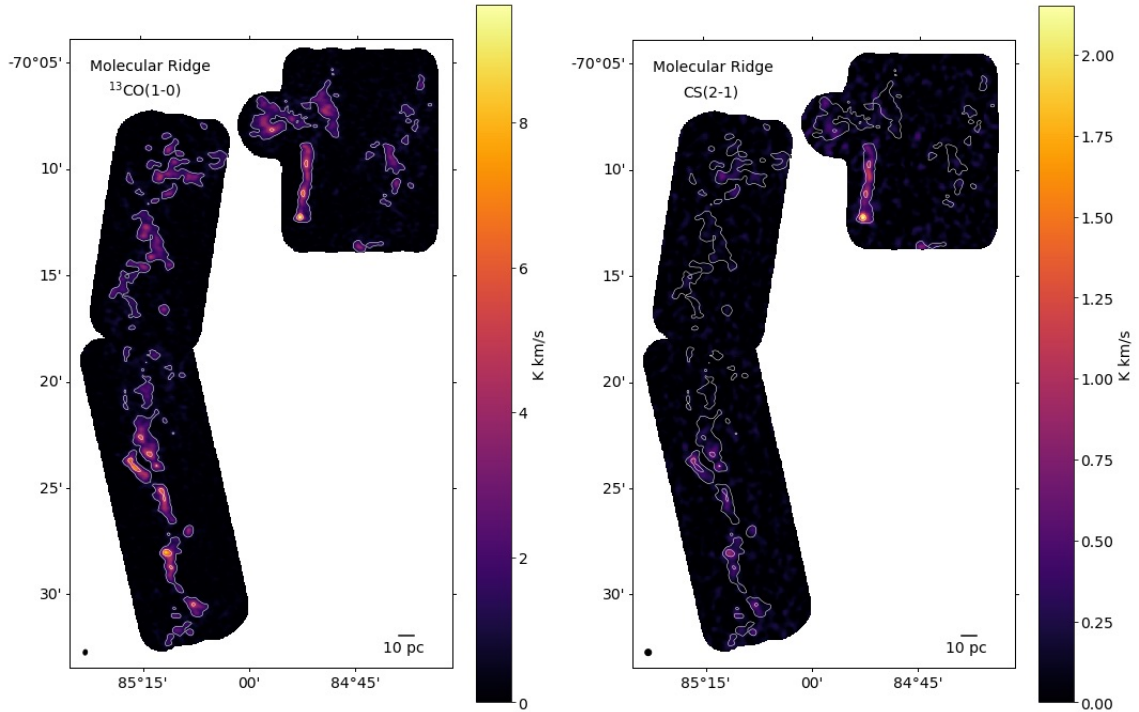


Fig. 4.2.— *Left*: Integrated intensity map of the Molecular Ridge in $^{13}\text{CO}(1-0)$. Contours show 1, 5, and 9 K km/s. *Right*: Integrated intensity map of the Molecular Ridge in $\text{CS}(2-1)$, with the same contour lines from $^{13}\text{CO}(1-0)$ overplotted. In both images, the beam is shown in the lower left corner.

4.2.1 Molecular Ridge

The Molecular Ridge was observed by the Atacama Large Millimeter/submillimeter Array (ALMA) 7m Atacama Compact Array (ACA) in three maps for project 2017.1.00271.S. This data set was combined with ALMA 7m ACA projects 2012.1.00603.S and 2015.1.00196.S, which covered the ~ 2 arcminute region around $5:39:50 -70:08:00$ in the northern center of the maps. These were all also combined with ALMA total power data. The data reduction, calibration, and imaging are described in detail in Finn et al. (2021). The final maps have a resolution of $13''$ and a measured rms in line-free channels of 0.03 K. An integrated intensity map of the $^{13}\text{CO}(1-0)$ and $\text{CS}(2-1)$ emission is shown in Figure 4.2.

4.2.2 30 Doradus

A mosaic of 30 Dor was observed as ALMA project 2019.1.00843.S, and includes 12m and 7m interferometric data as well as total power data. Those data are presented and analyzed at their native resolution of $1.75''$ in Wong et al. (2022). For this analysis, the resolution has been convolved to $13''$ so that it can be directly compared with our data for the Molecular Ridge. After this convolution, the data have a measured rms in line-free channels of 0.009 K. This rms is much lower than the other datasets, but we find that removing structures below the Ridge’s noise level of 0.03 K from the analysis does not significantly change the results. An integrated intensity map of these data is shown in Figure 4.3.

This dataset is $^{13}\text{CO}(2-1)$, rather than $^{13}\text{CO}(1-0)$ like all the other regions. We use a $^{13}\text{CO}(2-1)/^{13}\text{CO}(1-0)$ ratio of 0.84 based on the $^{12}\text{CO}(2-1)/^{12}\text{CO}(1-0)$ ratio measured in Sorai et al. (2001).

4.2.3 N159

N159 is a massive star-forming region to the north of the Ridge but south of 30 Dor. The brightest point in early single-dish surveys of CO in the LMC, this massive star formation region is less evolved than 30 Dor and has a significant remaining reservoir of molecular gas. N159 can be separated into eastern and western components (N159E and N159W), where N159E is thought to be more evolved than N159W (Nayak et al. 2018). There is also another region to the south called N159S that is much more quiescent and is not included in this study. Due to the small number of structures identified at this work’s resolution, we treat N159E and N159W as a single region and this does not significantly affect the results of our analysis.

N159 was observed in $^{13}\text{CO}(1-0)$ by ALMA project 2012.1.00554.S with 12m and

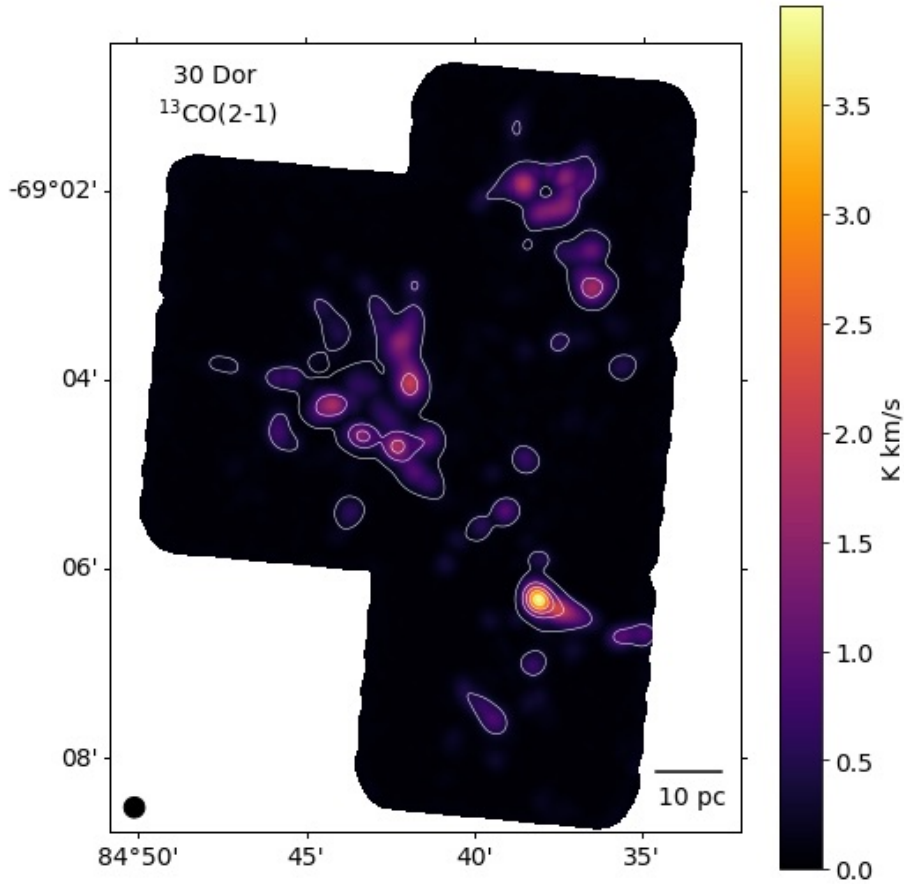


Fig. 4.3.— Integrated intensity map of 30 Dor in $^{13}\text{CO}(2-1)$. Contours show 1, 5, 9, 13, and 17 K km/s. The beam is shown in the lower left corner.

7m interferometric data, and was presented at the native resolution of $2.5'' \times 1.8''$ in Fukui et al. (2015). These data do not include total power data, and so we expect a flux recovery around 66% based on data in the Ridge. We take this correction into account in the mass estimates. As with the other comparison datasets, we convolved the data to $13''$ to match the Ridge data. After this convolution, the data have a measured rms in line-free channels of 0.04 K. An integrated intensity map of these data is shown in Figure 4.4.

4.2.4 N113

N113 is another active massive star-forming region in the LMC with several young, embedded massive YSOs. It is located in the central region of the LMC. N113 was observed in $^{13}\text{CO}(1-0)$ by ALMA project 2015.1.01388.S with 12m interferometric data. These data do not include total power data, and so we expect a flux recovery around 66% based on data in the Ridge. We take this correction into account in the mass estimates. A complete description of the data processing will be discussed in a separate publication at the observations' native resolution of $\sim 2''$. For this work, the data were convolved to $13''$ so they could be directly compared to our Molecular Ridge data. After this convolution, the data have a measured rms in line-free channels of 0.0075 K. This rms is much lower than the other datasets, but we find that removing structures below the Ridge's noise level of 0.03 K from the analysis does not significantly change the results. An integrated intensity map of these data is shown in Figure 4.5.

4.3 Structure Decomposition

To decompose the emission into structures, we used two different methods: splitting the emission into a hierarchy of structures called a dendrogram, and splitting the emission into individual, non-overlapping clumps. Dendrograms better capture the complex and hierarchical nature of molecular clouds, but complicate analysis because the emission is multiply counted and the resulting structures often defy the physics commonly used to describe molecular clouds (for example, we report a single radius for molecular clouds, even though dendrogram structures are frequently non-spherical and have complex and elongated shapes). Clump finding algorithms offer a simpler

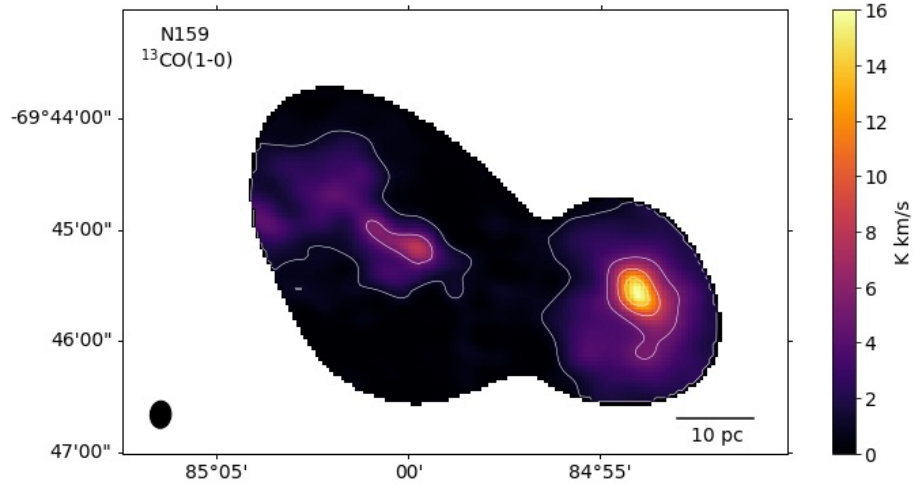


Fig. 4.4.— Integrated intensity map of N159 in $^{13}\text{CO}(1-0)$. Contours show 1, 5, 9, and 13 K km/s. The beam is shown in the lower left corner.

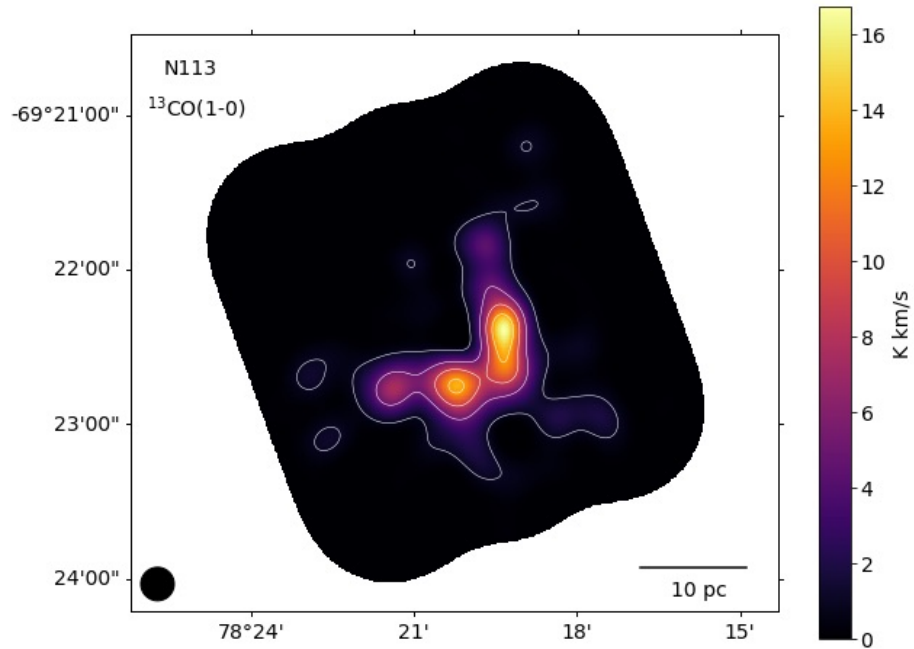


Fig. 4.5.— Integrated intensity map of N113 in $^{13}\text{CO}(1-0)$. Contours show 1, 5, 9, and 13 K km/s. The beam is shown in the lower left corner.

approach to analysis, but are biased towards finding clump structures that are approximately round and the size of the beam, and they cannot capture the hierarchical structure of molecular clouds.

In this study, we use both types of structure decomposition depending on the type of analysis being performed. We use dendrogram structures for the majority of the analysis since they better capture the hierarchical nature of clouds and can demonstrate how the physical properties behave at different size scales. We use clumps for counting-based analyses, such as histograms, since dendrograms multiply count emission.

Due to its bias towards beam-sized structures, the clump segmentation method results in smaller ranges of masses, sizes, and linewidths being calculated in Section 4.4. The ranges of these parameters for the identified clumps align most closely with those for the leaves of the dendrogram.

4.3.1 Dendrogram Segmentation

We decompose the emission in each map into structures using the package `astrodendro` (Rosolowsky et al. 2008) to create a dendrogram. This method of structure decomposition considers how different structures within the data merge as you go to lower contour levels to create a hierarchical categorization of the structures. We used input parameters of `min_value=3 σ` , `min_delta=2.5 σ` , and `min_npix=2` beams, meaning that the algorithm includes only pixels that are above 3σ and finds local maxima that are at least 2.5σ above the point of merging with another structure and bounded by an isosurface with at least as many voxels as two resolution beams.

The local maxima with no resolved substructure are categorized as “leaves”. The algorithm then identifies the points at which these structures merge to define larger

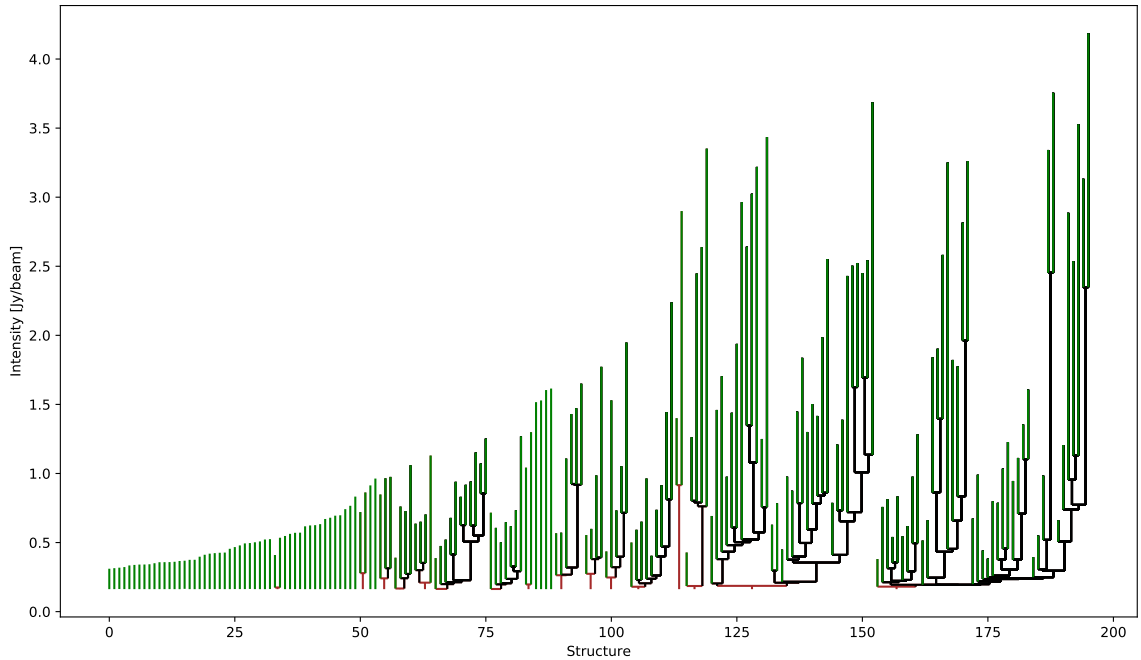


Fig. 4.6.— Dendrogram for the Ridge created by `astrodendro`. Each structure is represented by a vertical line, where the green lines are leaves, black lines are branches, and red lines are trunks. The y-axis indicates the peak of each structure and the intensity at which the structures merge with one another. This plot shows that the Ridge is composed of a few large trunks with a lot of substructure, but also several smaller and more isolated structures.

structures, categorized as “branches” and “trunks”, where trunks are the largest structures that are not bounded by any other structures. Figure 4.6 shows the dendrogram for emission in the Ridge using the above parameters and the breakdown in dendrogram structures for each region is shown in Table 4.2.

4.3.2 Clump Segmentation

To decompose emission into clumps, we use the algorithm `quickclump` (Sidorin 2017). We used the input parameters `Nlevels=1000`, `Tcutoff=4 σ` , `dTleaf=4 σ` , and `Npixmin=50`. The resulting numbers of clumps for each region are shown in Table 4.2.

4.3.3 Fractal Dimension

It is widely found that molecular gas is encountered in fractal structures (i.e., Elmegreen & Falgarone 1996), and that this fractal nature is connected to supersonic turbulence in the interstellar medium (Elmegreen et al. 2001). We consider whether the emission in the Ridge has a fractal morphology that is similar to the morphology in 30 Dor and N113 by measuring the fractal dimension, D_2 , of the structures identified by the dendrogram segmentation in each region. We do this with the area-perimeter relation, $P \propto A^{D_2/2}$ (Falgarone et al. 1991). We measure the perimeter and the area of each structure based on the full contour defined by the `astrodendro` algorithm for the Ridge, 30 Dor, and N113, then fit a power law to each dataset using a non-linear least squares method (`scipy.optimize.curve_fit`; Virtanen et al. 2020). We do not include N159 because the emission on the edges is cut off by the observed map. We fit only the structures that have an area larger than the size of the beam, which is 45 pc². The resulting fits are shown in Figure 4.7.

Each of the datasets are consistent with one another given the error, having fractal dimensions of $D_2 = 1.50 \pm 0.02$, 1.44 ± 0.02 , and 1.42 ± 0.07 for the Ridge, 30 Dor, and N113, respectively. This suggests that the three regions have a similar hierarchical morphology and so likely have similar mechanisms by which turbulence regulates cloud structure.

Table 4.2: Results of dendrogram and clump segmentation, and fractal dimension, D_2 , for each region

Region	Trunks	Branches	Leaves	Clumps	D_2
Ridge ¹³ CO	16	110	196	256	1.50 ± 0.02
Ridge CS	4	6	34	–	–
30 Dor ¹³ CO	6	45	96	75	1.44 ± 0.02
N159 ¹³ CO	1	4	7	9	–
N113 ¹³ CO	1	6	10	10	1.42 ± 0.07

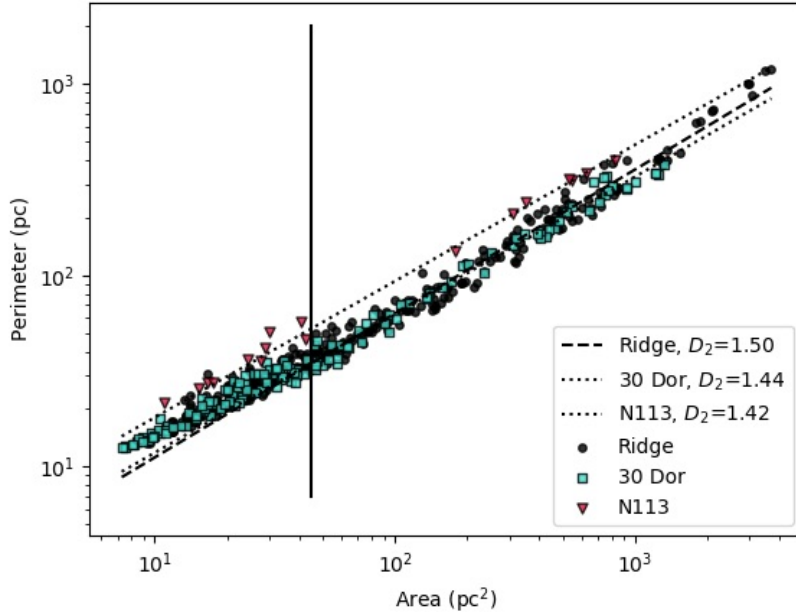


Fig. 4.7.— Perimeter plotted against area of the full contours for dendrogram structures identified in the Ridge, 30 Dor, and N113. We fit power laws to each region to measure the fractal dimension, D_2 , with the area-perimeter relation, $P \propto A^{D_2/2}$. We fit only structures that are larger than the area of the beam, 45 pc, represented by the vertical line. Each of the datasets are consistent with one another, suggesting that they have a similar hierarchical morphology.

These values are higher than the $D_2 = 1.36 \pm 0.02$ measured in galactic molecular clouds with ^{12}CO by Falgarone et al. (1991), but are consistent with the range of 1.2-1.5 measured for HI emission in galactic clouds by Sánchez et al. (2007). These values are also consistent with similar measurements made using stellar structures in the LMC (Miller et al. 2022) and the Small Magellanic Cloud (SMC; Sun et al. 2018), where both find $D_2 = 1.44 \pm 0.2$.

4.4 Derived Properties

To compare the physical conditions of the molecular clouds in each region, we compute the mass, linewidth, radius, and virial parameter, α_{vir} for each structure in each region.

We calculate the mass using an $X_{13\text{CO}}$ factor to convert from integrated $^{13}\text{CO}(1-0)$ intensity to H_2 column density. We adopt a value for $X_{13\text{CO}}$ of $1.6 \times 10^{21} \text{ cm}^{-2}/(\text{K km s}^{-1})$ based on Finn et al. (2021) measurements of non-LTE model-fitted column density in the Ridge. Finn et al. (2021) found that the non-LTE fitted column density of clumps was tightly correlated with the $^{13}\text{CO}(1-0)$ integrated emission, even more so than with the $^{12}\text{CO}(1-0)$ integrated emission. This value of $X_{13\text{CO}}$ is also consistent with using a typical galactic X_{CO} factor of $2 \times 10^{20} \text{ cm}^{-2}/(\text{K km s}^{-1})$ (Bolatto et al. 2013) and a $^{13}\text{CO}(1-0)/^{12}\text{CO}(1-0)$ integrated intensity ratio of 0.12 (Finn et al. 2021). The resulting column densities for 30 Dor also match the ranges of those calculated using LTE assumptions in Wong et al. (2022).

We adopt an error of 10% on the calculated masses based on an assumed 10% flux calibration error (Fomalont et al. 2014). The error associated with the measured σ_{rms} of the image is negligible compared to the flux calibration error. Adopting an $X_{13\text{CO}}$ factor also comes with a large systematic error. Finn et al. (2021) cite an error of 50% based on systematic uncertainties in the $\text{H}_2/^{13}\text{CO}$ abundance ratio, which is added in quadrature to the 10% flux error. The structures in 30 Dor have an additional systematic error since we only have observations of $^{13}\text{CO}(2-1)$ and so we use a $^{13}\text{CO}(2-1)/^{13}\text{CO}(1-0)$ ratio of 0.84 ± 0.3 (Sorai et al. 2001).

To calculate the linewidth of each structure, we fit a Gaussian to the intensity-weighted mean line profile to determine σ_v (not the full-width at half-maximum, FWHM). This linewidth is then deconvolved with the velocity resolution of the data

sets (either 0.5 or 0.25 km s⁻¹, see Table 4.1). To find the error in the measured linewidths, we create 100 noise maps that have been convolved to the same beam size and have the same σ_{rms} as the emission maps and add these to the data then recompute the linewidth. The error is taken to be the standard deviation in the measured linewidths with the added noise.

We performed the above method of error calculation for N159, N113, and 30 Dor, but this was not computationally feasible for the Ridge due to the large size of the data cube and number of clumps. Instead, we found that the fractional error in σ_v ($\sigma_{\sigma_v}/\sigma_v$) from this method in N159, N113, and 30 Dor is closely correlated with the peak brightness temperature (T_{max}) of the structure. We fit this correlation and extrapolated it to the Ridge data set to determine approximate errors for each structure using the following fitted equation:

$$\log\left(\frac{\sigma_{\sigma_v}}{\sigma_v}\right) = -0.69 \log(T_{\text{max}}/K) - 2.23. \quad (4.1)$$

To calculate the sizes, we fit an ellipse to the half-power contour of the structure. To get a single radius value, we used the geometric mean of the major and minor axes of this fitted ellipse, which is then deconvolved with the beam size for the data set. This value is taken to be a HWHM of the structure, from which we approximated $\sigma_R = \text{HWHM} \times 2/2.35$. We then multiplied σ_R by a factor of 1.91 (Solomon et al. 1987) to get our quoted “effective radius”, R . The error was determined with the same method used for the error in the linewidth. In the case of the radius, the fractional errors from N159, N113, and 30 Dor are also closely correlated with the peak brightness temperature (T_{max}) of the structure, and this fitted correlation was extrapolated to the Ridge to approximate errors with the equation

$$\log\left(\frac{\sigma_R}{R}\right) = -1.09 \log(T_{\max}/K) - 1.60. \quad (4.2)$$

Deconvolving the radius with the beam and the linewidth with the velocity resolution resulted in some data points being dropped from the analysis because the half-power contour is smaller than the beam or the fitted linewidth is smaller than the velocity resolution. This left us with 204 structures in the Ridge, 51 structures in 30 Dor, and 9 structures each in N159 and N113.

For N159 and N113, we adopt an additional correction factor of $1/0.66$ in the measured masses to account for the lack of total power data, which we expect to result in a flux recovery of 66% based on data from the Ridge that includes total power. We find that leaving out the total power data in the Ridge does not significantly affect the measured radii or linewidths of the structures.

The three parameters above, mass (M), radius (R), and linewidth, σ_v , are used to calculate the virial parameter, α_{vir} , as a measurement of the balance between gravity and outward pressure, calculated for a spherical cloud. Most molecular cloud structures that we observe are not spherical, which could influence the value of α_{vir} by a factor of order unity. Values of α_{vir} greater than one indicate that the cloud is dominated by kinetic energy, which could mean that the cloud is not bound and will disperse, or that it is constrained by an external pressure to keep it bound. The kinetic energy could also be dominated by potential energy because the cloud is in free fall collapse. Values of α_{vir} less than one indicate that the cloud is dominated by potential energy, and so is likely to begin collapse. We use the equation

$$\alpha_{\text{vir}} = \frac{5\sigma_v^2 R}{GM}. \quad (4.3)$$

The parameters derived in this section are used in the following sections for the

remainder of the analysis. Throughout the analysis, we use the properties derived from ^{13}CO emission rather than CS unless specified otherwise. Tables of all properties used in this analysis are presented in Appendix A5.

4.5 Size-Linewidth Relations

We plot the ^{13}CO linewidths of all the structures against their effective radii. The relation between the two is expected to follow a power law (Larson 1981; Solomon et al. 1987) of the form

$$\sigma_v = a_0 R^{a_1}. \quad (4.4)$$

Solomon et al. (1987) measured sizes and linewidths for molecular clouds in the Galactic disk using a size parameter, S , instead of the effective radius, R , that we use in this study. The size parameter is the geometric mean of the spatial dispersions, σ_l and σ_b , of each cloud, and so is comparable to the σ_R that we measured and then converted to effective radius with the equation $R = 1.91\sigma_R$ (see discussion in §4.4). Solomon et al. (1987) fit values of $a_0 = 1.0 \pm 0.1$ and $a_1 = 0.5 \pm 0.05$, so converting their size parameter to an effective radius would result in an intercept for the power law of $a_0 = 0.72 \pm 0.07$.

In Figure 4.8, we plot the radius and velocity dispersion of the structures and fit both the intercept and slope, a_0 and a_1 , for the Ridge and 30 Dor, using an orthogonal distance regression to take into account the error in both axes (`scipy.odr`; Virtanen et al. 2020). We do not fit these values for N159 and N113 since there are so few data points and the fits are poorly constrained.

For the Ridge, we fit values of $a_0 = 0.41 \pm 0.03$ and $a_1 = 0.44 \pm 0.03$, while for

30 Dor we fit values of $a_0 = 0.72 \pm 0.11$ and $a_1 = 0.56 \pm 0.07$. This indicates that 30 Dor follows a steeper power law than the Ridge, although the two values of a_1 are within 3σ of each other. This means that 30 Dor may have more kinetic energy at larger size scales than the Ridge. The power law slope we fit for 30 Dor structures ($a_1 = 0.56 \pm 0.07$) is comparable to those fit by Nayak et al. (2016), Wong et al. (2019), Indebetouw et al. (2020), and Wong et al. (2022) for dendrogram structures identified in $^{12}\text{CO}(2-1)$ and $^{13}\text{CO}(2-1)$ emission at resolutions ranging from 0.1 to 0.85 pc.

In Figure 4.9, we plot again the size and linewidth of the structures, but now hold the slope of the power law fixed at $a_1 = 0.5$ (Solomon et al. 1987) and fit only the intercept, a_0 . In this case, we fit a value of $a_0 = 0.35 \pm 0.01$ for the Ridge, $a_0 = 0.72 \pm 0.03$ for 30 Dor, $a_0 = 0.90 \pm 0.06$ for N159, and $a_0 = 0.80 \pm 0.05$ for N113. Changing the value of the fixed slope changes the fitted values of the intercept slightly, but does not change the relative differences between data sets. The results above are also unchanged if we use clump-segmented structures instead of dendrogram structures.

The Ridge’s significantly lower intercept from the other three data sets indicates that it has less kinetic energy at a given size scale than the massive-star-forming regions. This result suggests that the lack of massive star formation in the Ridge cannot be caused by excess kinetic energy suppressing star formation. This is quite different from the situation in the Galactic Center, where star formation is also suppressed but the molecular clouds have much higher kinetic energies ($a_0 = 3.0 \pm 0.7$ after converting the size parameter to an effective radius; Oka et al. 2001) than clouds in the disk of the Galaxy ($a_0 = 0.72 \pm 0.07$; Solomon et al. 1987). This indicates that while both regions are examples of deviations from star formation scaling laws, the

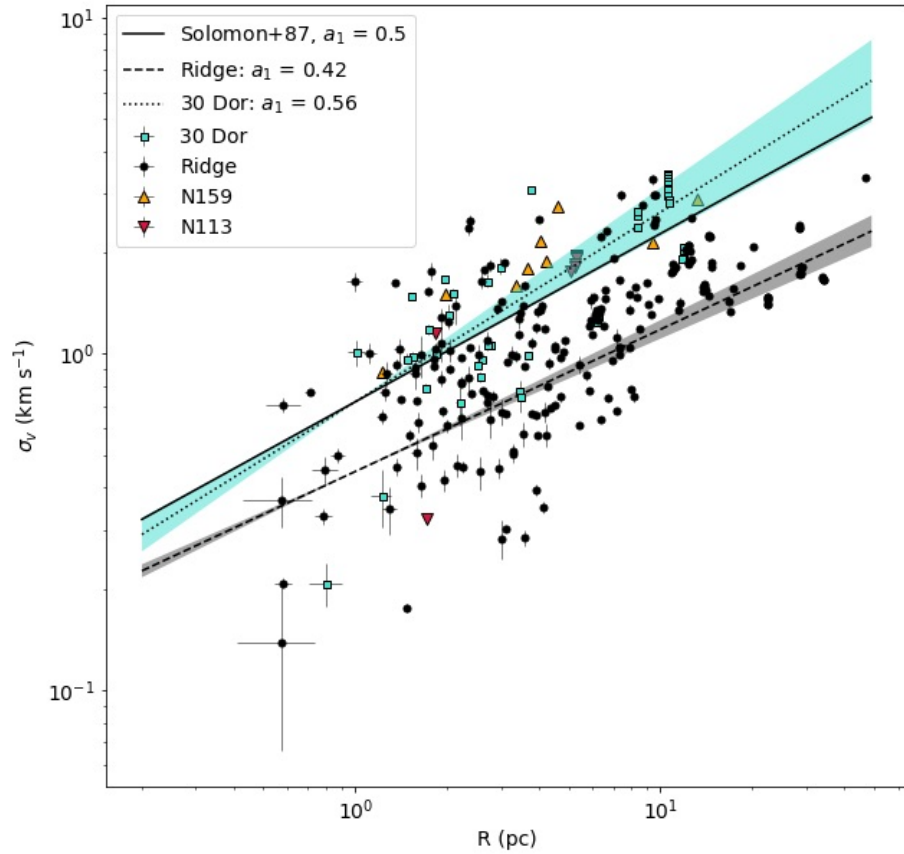


Fig. 4.8.— Linewidths plotted against sizes of structures in the four different regions: the Ridge (black circles), 30 Dor (blue squares), N159 (orange upward-facing triangles), and N113 (red downward-facing triangles). A power law has been fit to the structures in the Ridge (dashed line) and 30 Dor (dotted line) with the error in the fit shown as shaded regions, and the value of the fitted power law slope, a_1 , is written in the legend for each region. We do not fit power laws for N159 and N113 since their small numbers of data points cannot constrain the parameters well. The relation fit by Solomon et al. (1987) for Milky Way clouds is shown as a solid line, where $a_0 = 0.72$ and $a_1 = 0.5$.

physical drivers of that suppression are different.

4.5.1 Size-Linewidth with CS

In Figure 4.10 we plot the size and linewidth of the structures in the Ridge in $^{13}\text{CO}(1-0)$ and CS(2-1) and compare the fitted power law intercept with a fixed slope of $a_1 = 0.5$. The structures from CS(2-1) have a fitted intercept of $a_0 = 0.57 \pm 0.08$, higher than the $^{13}\text{CO}(1-0)$ structure in the Ridge but within 3σ of the $a_0 = 0.35 \pm 0.01$ fitted above. This demonstrates that the dense gas structures traced by CS(2-1) in the Ridge have a higher kinetic energy than the more diffuse gas traced by $^{13}\text{CO}(1-0)$.

It is expected that measuring the sizes and linewidths in a dense gas tracer as opposed to ^{13}CO would result in a size-linewidth relation with a higher intercept (Goodman et al. 1998). However, it is not clear from this plot alone what is causing the higher energy levels in the case of the Ridge presented here. It could be because the gas traced by CS(2-1) is found at the dense centers of clumps throughout the Ridge, where the higher kinetic energy is balanced by a higher gravitational potential. Or it could be that the areas of the Ridge that have CS(2-1) detections are sites where there is more star formation and gravitational collapse occurring, and so those areas have higher kinetic energies than the rest of the Ridge. Finn et al. (2021) see some correlation between the presence of YSOs and the CS(2-1)/ $^{12}\text{CO}(1-0)$ ratio in the Ridge, suggesting some support for the latter scenario, or that a combination of these two effects are at play.

4.6 Virialization

In Figure 4.11, we plot σ_v^2/R against the surface density of each structure. The positions of the structures on this plot indicate the balance between their gravitational

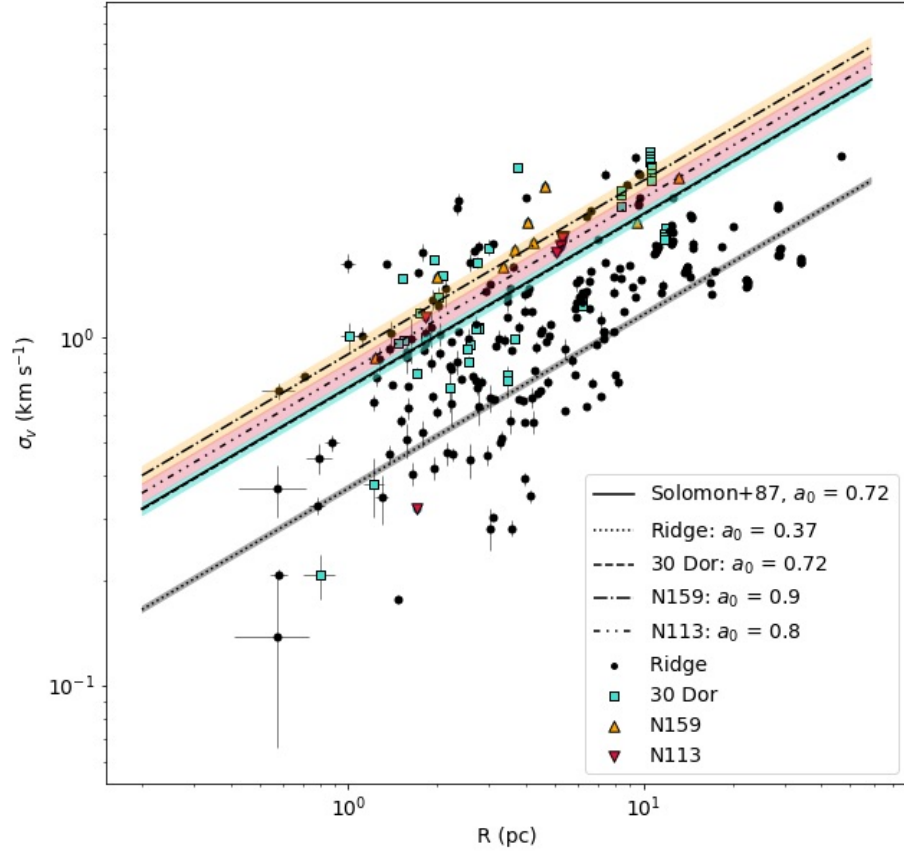


Fig. 4.9.— Linewidths plotted against sizes of structures in the four different regions: the Ridge (black circles), 30 Dor (blue squares), N159 (orange upward-facing triangles), and N113 (red downward-facing triangles). A power law with a fixed slope of $a_1 = 0.5$ has been fit to the structures in each region and the error on each fit is shown as shading colored according to the region, and the value of the fitted power law intercept, a_0 , is written in the legend for each region. The relation fit by Solomon et al. (1987) for Milky Way clouds is shown as a solid line, where $a_0 = 0.72$. The Ridge has a significantly lower fitted intercept than the other three regions, indicating that it has much less kinetic energy for a given size scale.

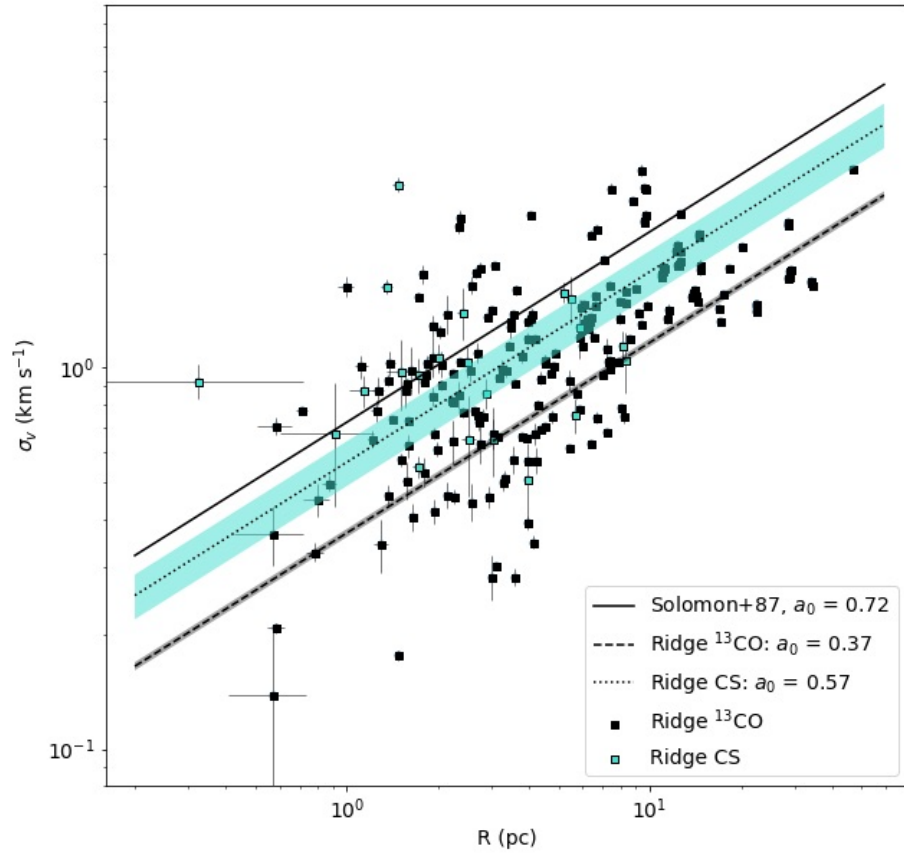


Fig. 4.10.— Linewidths plotted against the sizes of structures in the Ridge identified by $^{13}\text{CO}(1-0)$ (black) and $\text{CS}(2-1)$ (blue). We fit a power law with a fixed slope of $a_1 = 0.5$ to each, which shows that the $\text{CS}(2-1)$ structures have a significantly higher fitted intercept than the $^{13}\text{CO}(1-0)$ structures. This indicates that the dense gas traced by $\text{CS}(2-1)$ has higher kinetic energy at a given size scale.

potential energy and kinetic energy due to turbulence and temperature. If those two are in virial equilibrium, the structures should fall along the virial line, shown in black in Figure 4.11.

Due to the large systematic uncertainties in the measurements of the structures' masses, the absolute positions relative to virial equilibrium on the plot are ambiguous. Instead, we focus this analysis on the relative positions of the data points from different regions. The Ridge structures tend to fall above virial equilibrium more often than structures in the massive-star forming regions 30 Dor, N159, and N113 - 28% of the Ridge structures fall above the virial equilibrium line, where for 30 Dor that fraction is only 3% and none of the structures in N159 or N113 fall above the virial equilibrium line.

To more quantitatively compare the balance of kinetic and gravitational energy in the Ridge and 30 Dor, Figure 4.12 shows the distribution of α_{vir} values in the two regions. Because dendrograms multiply count emission, we use structures from `quickclump` to create all histograms in this analysis. Figure 4.12 clearly shows a difference in α_{vir} values between the two regions, with the Ridge structures tending towards higher α_{vir} . A Kolmogorov-Smirnoff (K-S) test indicates that the two data sets are likely not drawn from the same distribution with a p-value of $\ll 0.01$.

We infer from Figure 4.9 that structures in the Ridge have lower kinetic energies than structures in 30 Dor. That means that for the Ridge to have higher α_{vir} values than 30 Dor, it must have much lower surface densities. In Figure 4.13, we show the distributions of surface densities in the Ridge and 30 Dor, and we do indeed see that those in the Ridge are significantly lower than those in 30 Dor, with a K-S test p-value of $\ll 0.01$. This suggests that the Ridge may be forming fewer massive stars compared to other regions because the Ridge does not have as much dense gas.

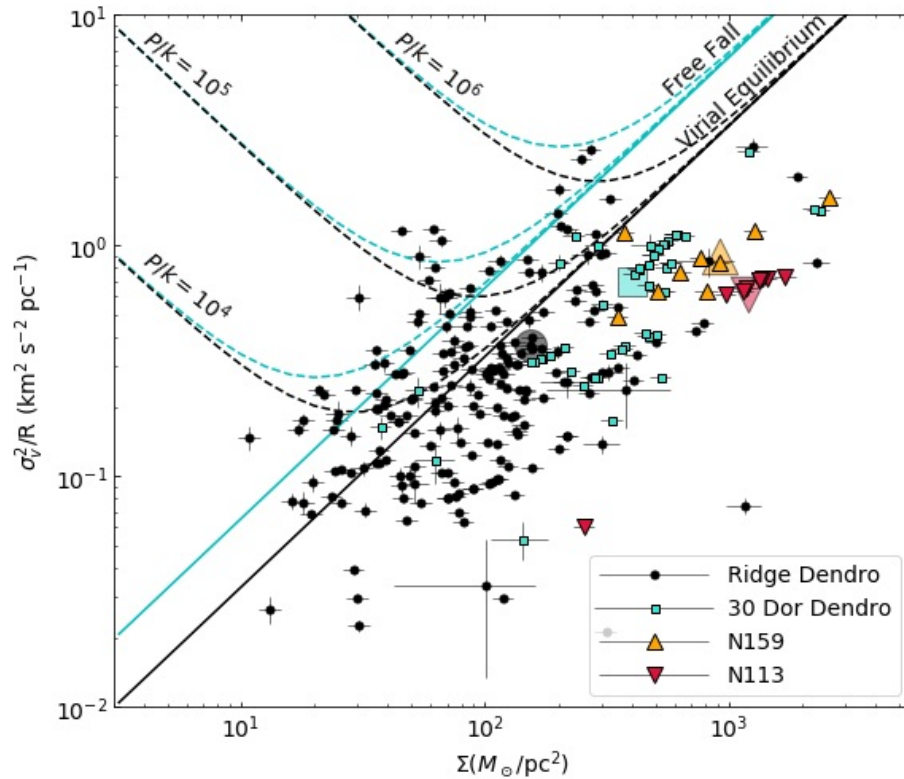


Fig. 4.11.— Surface density plotted against the velocity metric, σ_v^2/R , for the Ridge, 30 Dor, N159, and N113. The black line shows virial equilibrium, the blue line shows how equilibrium shifts when clouds are in free fall, and the dashed lines show those same quantities but when an external pressure is applied (Field et al. 2011). The large, semi-transparent symbols corresponding to each region indicate the average surface density and velocity metric for each region. The systematic uncertainties for all data points are shown in the legend. The structures in the massive-star-forming regions appear to fall below the line of virial equilibrium more than the structures in the Ridge.

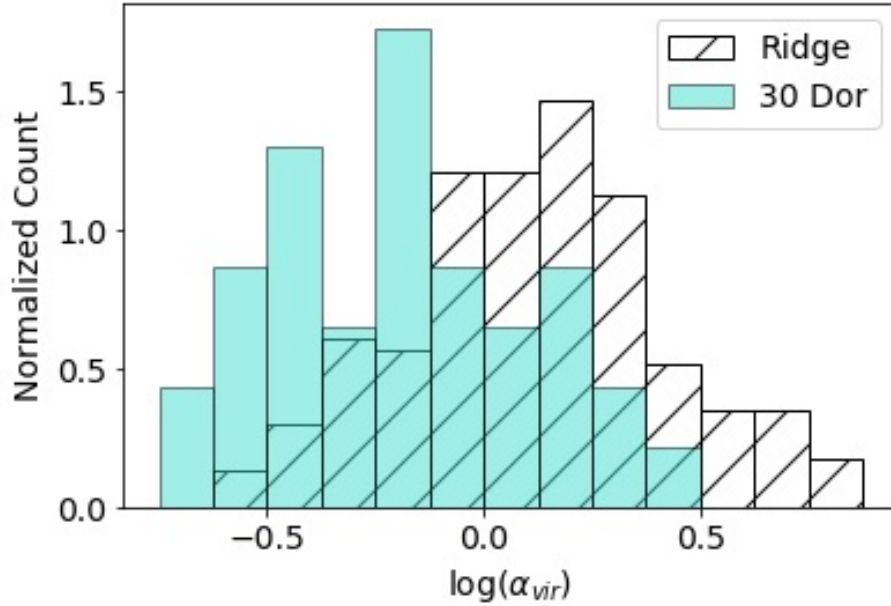


Fig. 4.12.— Distribution of α_{vir} values in the Ridge and 30 Dor, showing that the Ridge tends towards higher values of α_{vir} than 30 Dor. A K-S test indicates that the two datasets are not drawn from the same distribution with a p-value of $\ll 0.01$.

Given the much lower star formation activity in the Ridge and applying the Schmidt-Kennicutt law (Kennicutt 1998), it is expected that the surface density in the Ridge be lower than in 30 Dor. However, it is still higher than what would be predicted with the Schmidt-Kennicutt law based on the star formation rate measured in the Ridge by Indebetouw et al. (2008), $4 \times 10^{-3} M_{\odot} \text{ yr}^{-1}$. From that rate, we would expect a surface density of $\sim 47 M_{\odot} \text{ pc}^{-2}$, but here we measure a mass-weighted average surface density of $\sim 100 M_{\odot} \text{ pc}^{-2}$ in the Ridge. This demonstrates that while the Ridge is lower in surface density than 30 Dor, there is still a discrepancy with the Schmidt-Kennicutt law in the Ridge.

We compare these measured surface densities to the often-cited threshold for massive star formation of $A_V > 8$ mag measured by Lada et al. (2010). Finn et al. (2019) calculate that based on measurements of $\frac{A_V}{N_H}$ in the LMC (Dobashi et al.

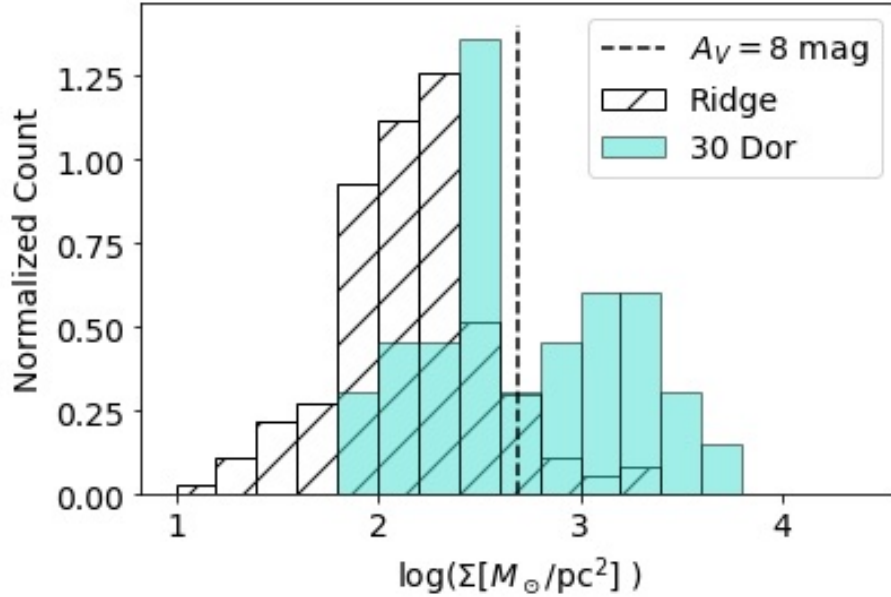


Fig. 4.13.— Distribution of surface densities in the Ridge and 30 Dor. The Ridge has significantly lower surface densities than 30 Dor, which results in structures in the Ridge having higher α_{vir} values despite their lower kinetic energies. Also shown is the $A_V > 8$ mag threshold for massive star formation from Lada et al. (2010), converted to $\Sigma_{\text{gas}} > 490 M_{\odot} \text{pc}^{-2}$. This indicates that the Ridge is likely not forming massive stars because it lacks dense gas.

2008), this threshold would correlate to $\Sigma_{\text{gas}} > 490 M_{\odot} \text{pc}^{-2}$. Plotting this threshold on Figure 4.13 indicates that the majority of structures in the Ridge fall below this threshold, while 30 Dor structures are distributed around this threshold and have a mass-weighted average of $500 M_{\odot} \text{pc}^{-2}$. There were too few structures in N159 and N113 at this resolution to include them in a histogram, but their mass-weighted average surface densities were 1100 and $1260 M_{\odot} \text{pc}^{-2}$, respectively. This is all consistent with the Ridge having little massive star formation because it falls below a density threshold compared to the other massive star forming regions.

It is expected that highly irradiated clouds, such as those in 30 Dor close to R136, will have a higher dark-gas fraction due to photodissociation and so a higher X_{CO} factor (Chevance et al. 2020b). This effect would also cause us to see less of the diffuse

envelope of the cloud, meaning that both the measured radii and linewidths may be underestimated. O’Neill et al. (submitted) make a thorough study of the effect of CO-dark gas on the measured properties of clouds. Their analysis suggests that in extreme cases of compactness for clouds in 30 Dor, the discrepancy in Figure 4.11 could be explained by a significantly higher dark gas fraction than in the Ridge. However, the effect of CO-dark gas on the size-linewidth relation, such as is shown in Figure 4.9, would be to move up and to the right, mostly parallel to the relation. This suggests that it is quite unlikely that the difference in fitted a_0 intercept values is due to differences in the amount of CO-dark gas in the regions. Differences in the abundance ratio of ^{13}CO would cause similar effects, but the abundances have not been measured well enough to make any strong comment on this effect.

The use of $^{13}\text{CO}(2-1)$ in 30 Dor and $^{13}\text{CO}(1-0)$ in the Ridge and the other regions likely also affects their relative distributions of α_{vir} , even after applying a correction factor of $^{13}\text{CO}(2-1)/^{13}\text{CO}(1-0) = 0.84$ to the 30 Dor masses. Since we expect $^{13}\text{CO}(2-1)$ to be fainter and not as well detected as $^{13}\text{CO}(1-0)$, this probably has a similar effect to that of CO-dark gas, although a thorough study taking into account excitation would be necessary to draw any firm conclusions.

4.7 Variation within the Ridge

To further investigate the physical conditions in the Ridge, we next look for variation in α_{vir} values and other physical properties within the region. Figure 4.14 shows a map of the Ridge colored by the α_{vir} parameter measured for the structure. In this map, we use structures found with `quickclump` to minimize overlap in the map. Where there is overlap along the line of sight, the average is shown. Also shown in the map are YSOs from Whitney et al. (2008), Gruendl & Chu (2009), and Seale et al. (2014),

as well as HII regions and their sizes from Henize (1956). There appears to be some regions that tend toward higher or lower α_{vir} parameters, but there does not seem to be any consistent trend north-to-south along the Ridge.

We split the structures in the Ridge into four main regions - a Southern region, then an Eastern, a Central, and a Western region to the north (hereafter referred to as NE, NC, and NW, respectively). The boundaries between these regions are shown in Figure 4.14. There is one major clump not included in any region, just below the borders of the NC and NW regions. This clump is partly cut off by the edge of the observation footprint and so does not have a reliable α_{vir} measurement. It is left out of the analysis.

To compare the α_{vir} values in each of the four regions, we plot histograms of their values in Figure 4.15. The shape of these distributions appear by eye primarily Gaussian. We perform a K-S test on each pairing of regions to determine if their values of α_{vir} are drawn from a common distribution. The resulting p-values of the K-S test for each pairing are presented in Table 4.3, where a p-value of less than 0.05 means we reject the null hypothesis (that the α_{vir} values for the two regions are drawn from the same distribution) with at least 95% confidence.

The South, NC, and NW regions are all consistent with being drawn from the same distribution. The NE region, however, has K-S test p-values less than 0.05 when paired with each of the other regions, suggesting that its α_{vir} values are not

Table 4.3: K-S test p-values of α_{vir} distributions in pairings of regions within the Ridge, derived from $^{13}\text{CO}(1-0)$.

	N East	N Center	N West
South	0.016	0.702	0.305
N East	-	0.002	0.001
N Center	-	-	0.751

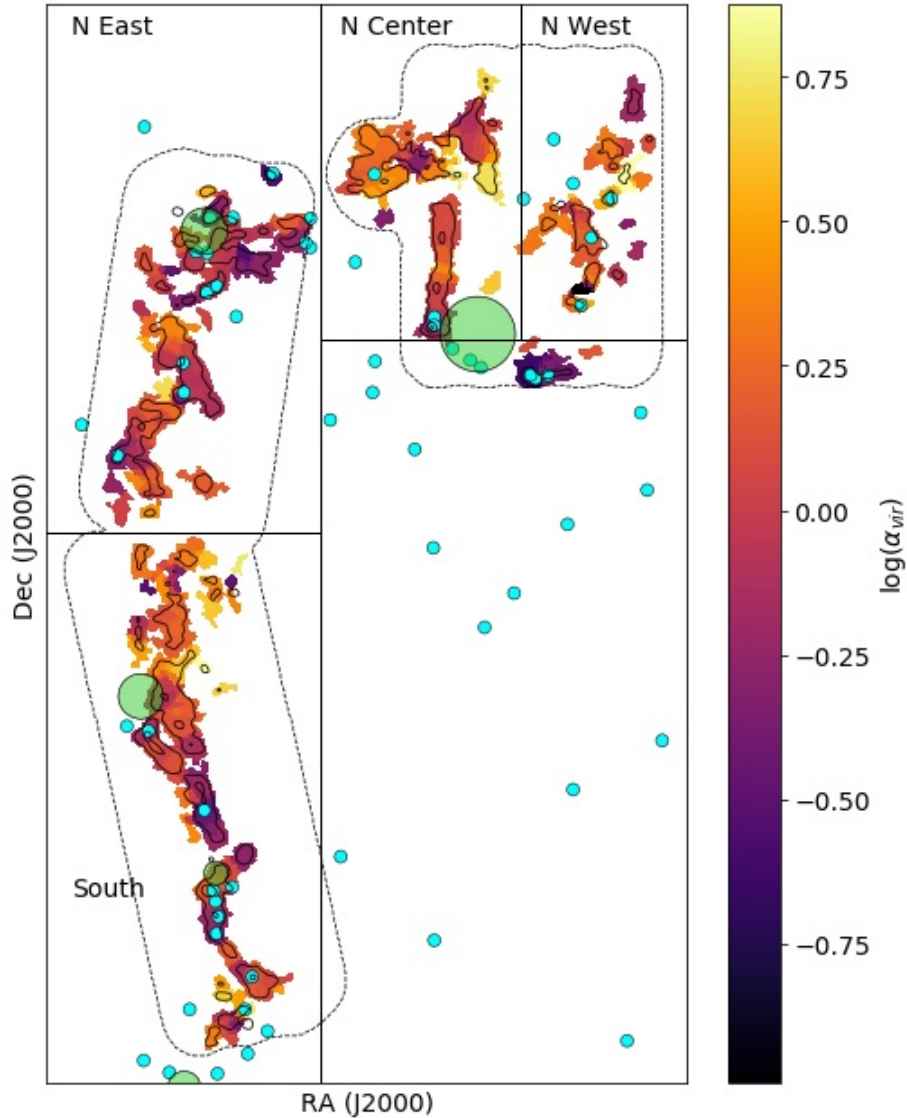


Fig. 4.14.— Map of the Molecular Ridge colored by each structure’s α_{vir} parameter. For this map we used structures found with `quickclump` to minimize structure overlap. Where there is overlap along the line of sight, we show the average α_{vir} . The small blue circles indicate YSOs from infrared surveys (Whitney et al. 2008; Gruendl & Chu 2009; Seale et al. 2014) and the large green circles indicate HII regions and their sizes from Henize (1956). The black lines show the boundaries used to split the Ridge into four different regions to analyze and the dashed lines show the observation footprint.

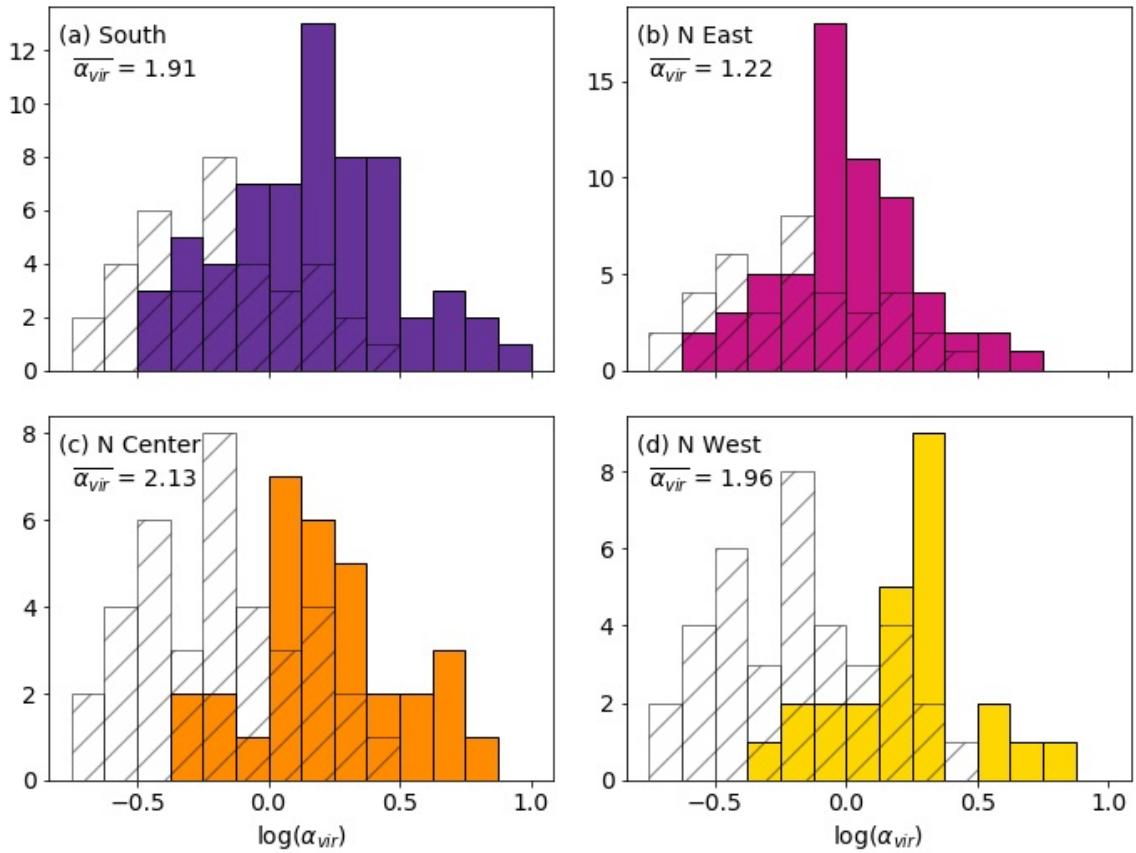


Fig. 4.15.— Histograms of the α_{vir} parameter by region in the Ridge, derived from $^{13}\text{CO}(1-0)$ (Figure 4.14 shows the extent of the regions). Overplotted in black hatching is the α_{vir} distribution of 30 Dor. The average α_{vir} parameter is shown in the top left of the panel for each region. A series of K-S tests indicates that the NE region (pink) has a different distribution than each of the other regions in the Ridge. The NE region tends towards lower values of α_{vir} than the rest of the Ridge.

drawn from the same distribution. This suggests that there is a difference in the physical conditions in the NE region that is causing lower values of α_{vir} in that region compared to the rest of the Ridge.

We look into this difference further by comparing the size-linewidth relation in these different regions within the Ridge. Similar to §4.5, we fit the power law relation between σ_v and R for the structures in each of these regions with the slope of the power law fixed at $a_1 = 0.5$ (Figure 4.16). For these regions, we fit $a_0 = 0.33 \pm 0.01$, 0.35 ± 0.01 , 0.55 ± 0.03 , and 0.46 ± 0.03 for the South, NE, NC, and NW regions, respectively. This indicates that the South and NE regions have similarly low kinetic energies, while the NW region has higher kinetic energy and the NC has the highest kinetic energy. This makes sense since the NC region hosts the large HII region, N171 (Henize 1956).

The low kinetic energy in the NE region relative to the NC and NW regions could explain why its α_{vir} values are lower. However, the kinetic energy in the Southern region appears nearly as low and its α_{vir} values are comparable with those in the NC and NW regions. To explain these variations in α_{vir} values, we also consider maps of n_{H_2} in the Ridge based on fitting RADEX models to low resolution ^{12}CO and ^{13}CO emission in Finn et al. (2021). This map indicates that the NE region has higher gas densities than the Southern region, which would result in the NE having lower α_{vir} values despite having comparably low kinetic energy. It is unclear from these plots what might be causing the higher densities in the NE region.

4.8 Spatial Dependence

To investigate what is driving the variations in α_{vir} values in the Ridge, we consider how α_{vir} varies with proximity to the nearest YSO, the nearest HII region, and to

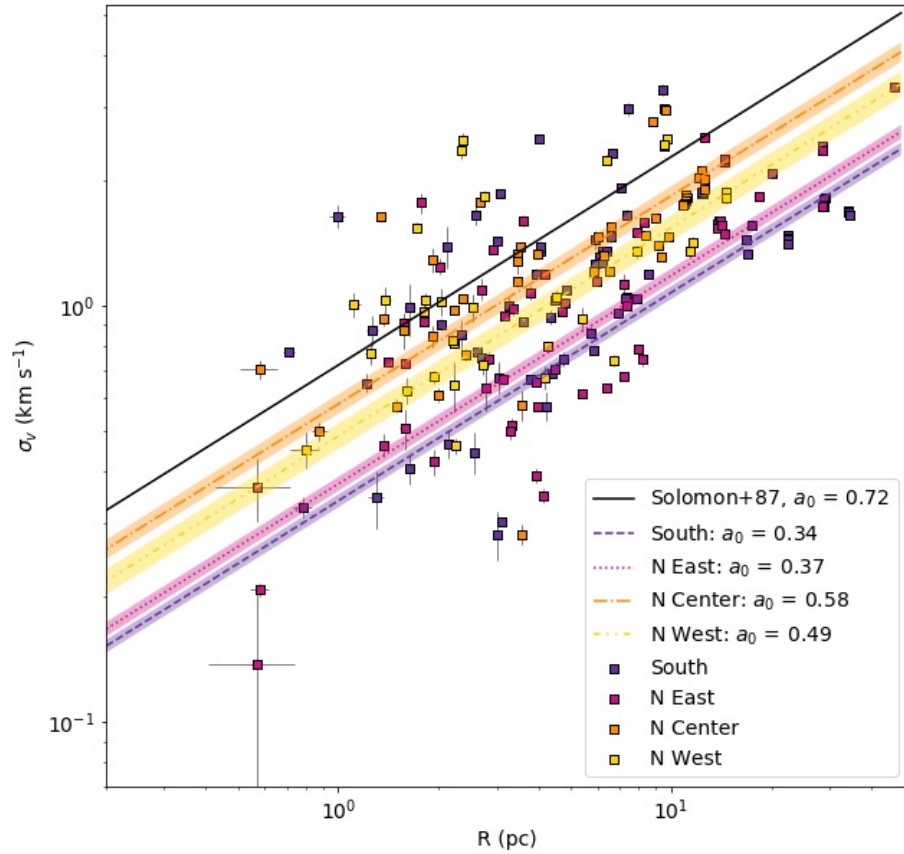


Fig. 4.16.— Linewidths plotted against sizes of structures in the Ridge, colored by their region within the Ridge. We fit a power law with a fixed slope of $a_1 = 0.5$ to each region's structures and find that the South and NE regions have the lowest intercepts, indicating low kinetic energy in these regions. The NC region has the highest intercept, indicating that it has the highest kinetic energy.

R136 in 30 Dor. These plots are shown in Figure 4.17 and for each we calculate a Pearson's correlation coefficient, r .

All three of these show similarly weak correlations. The variation of α_{vir} with distance to R136 shows the weakest correlation, with a coefficient of -0.27. This agrees with our by-eye assessment of Figure 4.14 that there appears to be little cohesive north-to-south trend across the Ridge. This result suggests that the super star cluster R136 and in general that massive star formation to the north is not strongly affecting the physical conditions in the Ridge at this distance. This is consistent with the findings of Wong et al. (2022) that there is little correlation with α_{vir} for clouds in 30 Dor and their distance to R136.

The weak correlation in the figure appears most dominated by lower α_{vir} values around a distance of 1.1 kpc from R136, which corresponds to a declination of approximately $-70^{\circ}26.4'$. This falls halfway along the South region defined in Figure 4.14, and is near several YSOs and an HII region.

The correlation coefficient between α_{vir} and distance to the nearest YSO is 0.29, and between α_{vir} and distance to the nearest HII region is 0.28. The weak correlation suggests that local influences such as radiation and thermal pressure from nearby star formation have a small effect on molecular gas conditions. Structures that have a nearby YSO or HII region tend to have lower α_{vir} . This could be because the YSOs and HII regions are creating gas conditions that are conducive for further star formation, or because they are more likely to be associated with gas that has the right conditions for star formation.

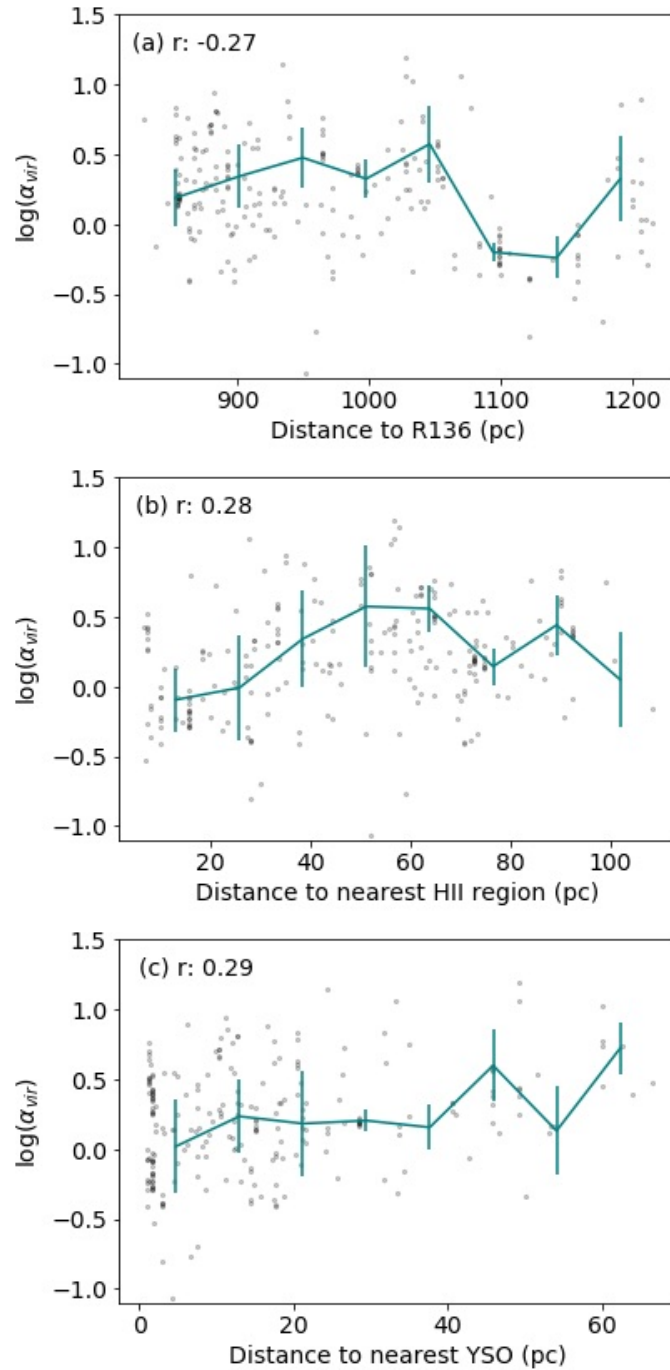


Fig. 4.17.— Values of α_{vir} in the Ridge plotted against the structure's distance to R136 (*top*), the nearest HII region (*middle*), and the nearest YSO (*bottom*). All three show similarly weak correlations based on Pearson's correlation coefficients, shown in the top left corner.

4.9 Discussion

With this analysis, we hope to better understand what is driving the differences in star formation activity between the Molecular Ridge and the nearby massive-star-forming regions 30 Dor, N159, and N113. By comparing the fractal dimensions of 30 Dor and the Ridge, it seems that the hierarchical morphology in the two regions is similar and thus the state of fragmentation is not driving the difference in star formation.

From Figure 4.8, we conclude that the Ridge has significantly lower kinetic energy per size scale than the massive star forming regions, while Figure 4.12 demonstrates that despite the low kinetic energy, the Ridge still has higher values of α_{vir} on average. This must be driven by relatively low surface densities in the Ridge, which is confirmed by Figure 4.13. All of this evidence suggests that the Ridge’s lack of massive star formation is likely driven by a paucity of dense gas relative to regions like 30 Dor, rather than collapse being suppressed by excess turbulence in the Ridge. However, as Finn et al. (2021) point out, surface density cannot account for differences in line-of-sight length and cannot directly trace the true volume density of the gas. To directly compare the volume density of the gas in the Ridge and the massive star forming regions, we would need to observe multiple ^{12}CO and ^{13}CO emission lines in other regions and perform the same RADEX fitting done in Finn et al. (2021).

As shown in Figure 4.11, the systematic uncertainty in the mass estimates makes it difficult to discuss the absolute position of the structures relative to virial equilibrium. The Ridge could have a higher distribution of α_{vir} values for a few different reasons: the clouds are subjected to an external pressure, the clouds are in free fall, or the clouds are unbounded. The even distribution of the Ridge clouds along the virial line in Figure 4.11 rather than clustering around a consistent range of pressures makes

it seem unlikely that an external pressure has a large influence here. The clouds being in free fall collapse could also explain the higher α_{vir} values, but this scenario seems inconsistent with the low kinetic energies indicated in the size-linewidth plots (Figure 4.9) and the low amount of star formation. It seems most likely that the clouds in the Ridge tend to be less gravitationally bound than the clouds in the other star forming regions. This could be due to low gas density, which would make it harder for the clouds to hold together or begin gravitational collapse.

This finding may also have implications for the types of stars and clusters formed based on the density of gas forming those stars. Indebetouw et al. (2008) find that the Ridge is still forming stars, but preferentially forms low-mass clusters that do not sample a standard initial mass function (IMF; such as Kroupa 2002) well and so do not produce many massive stars. This aligns well with our finding that at this resolution, structures in the Ridge have surface densities that fall below the threshold for massive star formation of $A_V > 8$ mag from Lada et al. (2010). Meanwhile, 30 Dor structures are distributed around that threshold, and the massive star forming regions N159 and N113 have average surface densities well above that threshold.

The gradient in star forming potential from 30 Dor, N159, and through the Ridge seems consistent with the interaction histories of the LMC and SMC proposed by Besla et al. (2012) in which the SMC collided with the LMC in the past 250 Myr. Recent numerical simulations have further constrained that interaction to the SMC colliding with the LMC 140-160 Myr ago with an impact parameter of ~ 5 kpc (Choi et al. 2022). The Magellanic Bridge connecting the two galaxies is likely the result of such an interaction, and the Molecular Ridge extends from 30 Dor in the direction of the Bridge, suggesting a potential connection between the two structures. The current relative velocity of the LMC and SMC are estimated to be $\sim 100 \text{ km s}^{-1}$

(Zivick et al. 2019), meaning that during such a collision, the SMC’s motion through the LMC would be supersonic for the molecular gas, creating shocks and over-densities in the molecular clouds. The extended Magellanic Streams seen in HI gas are also likely caused in part by close interactions between the LMC and SMC, as well as their interactions with the Milky Way (e.g., Lucchini et al. 2021), although this structure occurs on much larger size scales than the regions studied here.

This interaction scenario is also supported by the findings of Furuta et al. (2019) that the gas in the regions around 30 Dor and N159 has a lower measured $A_V/N(\text{H})$ than the rest of the LMC and is instead consistent with gas in the SMC. Furuta et al. (2021) proposed a geometry in which gas from the SMC is colliding with the LMC disk moving north to south, forming R136 in 30 Dor and then N159.

The LMC-SMC interaction and subsequent tidal effects would have increased the turbulent motion in the molecular gas, which could have led to the formation of R136 as well as the older populations in the 30 Dor region (Rahner et al. 2018). To create an SSC like R136 that has a mass of $\sim 10^5 M_\odot$, the initial molecular cloud would have needed to start with a mass of at least $\sim 2 \times 10^5 M_\odot$, assuming a maximum star formation efficiency for SSCs of 50% (Ashman & Zepf 2001; Kroupa et al. 2001; Grudić et al. 2018). Johnson et al. (2015) further required that to form an SSC, the initial molecular cloud must contain this large mass within a maximum radius of 25 pc. None of the molecular cloud structures in 30 Dor meet these criteria, and so are not capable of creating an SSC like R136, suggesting that the gas conditions during the peak of star formation in 30 Dor were much more extreme than they currently are. The molecular cloud that created R136 more likely appeared similar in physical conditions to the potential SSC precursor cloud observed in the merging Antennae galaxies (Johnson et al. 2015). Finn et al. (2019) observed that this cloud has a large α_{vir} parameter

and would require high external pressure in order to remain bound. They also found evidence that this pressure is supplied by cloud-cloud collision. Fukui et al. (2017) presented evidence that R136 was also created by a tidally-induced collision of large scale HI clouds, which would align with the idea that the molecular cloud precursor to R136 was subject to high external pressure from a galactic interaction.

Fukui et al. (2015) also found evidence for a cloud-cloud collision triggering the formation of high-mass YSOs in N159, and follow-up work by Fukui et al. (2019) and Tokuda et al. (2019) suggests that this collision is associated with the same large scale colliding flows that triggered the formation of R136 cited above. N159 is currently forming more massive star clusters than the 30 Dor region and hosts a massive molecular core of $\sim 10^4 M_{\odot}$ within a ~ 1 pc radius (Tokuda et al. 2022), but it does not have any molecular cloud structures measured in this analysis that meet the SSC-forming criteria cited above (a mass of at least $2 \times 10^5 M_{\odot}$ within a radius of 25 pc; Johnson et al. 2015). This ongoing star formation in N159 is consistent with our finding that the structures are currently near or below virial equilibrium, and so are likely to collapse and form stars, but they do not show signs of requiring a high external pressure to be bound as seen in SSC-forming clouds.

If 30 Dor and N159 experienced cloud collisions induced by the interaction of the SMC and LMC, it would be reasonable to expect that as the SMC moved away from the LMC, the gas conditions became less extreme (and so N159 is not forming stars as intensely as 30 Dor once was) and some molecular gas may also have been pulled out of the SMC in the direction of the Magellanic Bridge, meaning that the Ridge may even be a denser extension of the Magellanic Bridge. The Ridge could be this gas, and our finding that it is less dense than the gas in 30 Dor and N159 is consistent with that interpretation. It is also consistent with our finding that the northern regions

have higher kinetic energy and densities and so are more similar to 30 Dor and N159 than the molecular gas towards the south of the Ridge.

This proposed scenario demonstrates how galaxy interactions can create regions that both over- and under-produce stars when compared to often-applied scaling relations. This effect can be important when accounting for star formation in galaxy simulations, especially given the importance of dwarf galaxy mergers in the evolution of galaxies over cosmic time. It would be interesting to see if any simulations of dwarf galaxy interactions, especially of the SMC and LMC interaction specifically, are able to recreate the morphology of the Ridge and the gas conditions that we see along its extent. Such simulations may also help clarify the timescales of the interaction between the galaxies and the subsequent tidal effects that may lead to further cloud collisions and the eventual onset of star formation in regions like 30 Dor.

4.10 Conclusions

We present a comparison of ^{13}CO observations of the Molecular Ridge, 30 Dor, N159, and N113 in the LMC. The latter three regions are all actively forming massive stars, while the Ridge is not, despite its large reservoir of molecular gas. We use dendrograms and clump-finding algorithms to segment the emission and analyze the physical conditions of those structures. Our major findings are summarized below.

- The Ridge, 30 Dor, and N113 have fractal dimensions of $D_2 = 1.50 \pm 0.02$, 1.44 ± 0.02 , 1.42 ± 0.07 respectively. These are similar enough that it seems unlikely the difference in star formation activity between the regions is related to a difference in cloud morphology and hierarchical structure. These values are also consistent with other measurements of the fractal dimension within the LMC, SMC, and Milky Way. (§4.3.3)

- Comparing size-linewidth relations in the Ridge, 30 Dor, N159, and N113 indicates that the Ridge has significantly lower kinetic energy at given size scales when compared to the massive star forming regions. This would rule out the possibility that the Ridge has lower rates of massive star formation because it is supported against collapse due to excess kinetic energy. (§4.5)
- The Ridge has higher values of α_{vir} than 30 Dor, although the absolute scaling of these values relative to virial equilibrium is unclear due to large uncertainties in the mass estimate. This appears to be driven by significantly lower surface densities in the Ridge, since we know from the size-linewidth relations that the Ridge also has lower kinetic energy than 30 Dor. We find as well that the structures in the Ridge fall below the Lada et al. (2010) threshold of $A_V > 8$ mag for massive star formation, while 30 Dor structures are distributed around this threshold and the average surface densities in N159 and N113 are well above this threshold. These results suggest that the Ridge has lower rates of massive star formation because it has significantly less dense gas than 30 Dor, although from Finn et al. (2021) we know that the surface density of the gas does not necessarily trace the non-LTE-fitted volume density of the gas. (§4.6)
- Within the Ridge, there is some variation in physical properties. The region in the northeast has a significantly lower α_{vir} distribution than the other regions, likely partially driven by having a low specific kinetic energy and relatively high densities. (§4.7)
- The α_{vir} values measured for structures are only weakly correlated with distance from the super star cluster R136 in 30 Dor, suggesting that such star clusters do not affect gas properties at kiloparsec distances. The α_{vir} values similarly show

only a weak correlation with the distances to the nearest YSO and the nearest HII region, suggesting that local star formation has a minimal influence on gas conditions or that the YSOs are slightly more likely to be spatially coincident with gas that has the right conditions for further star formation. (§4.8)

Chapter 5

Fitting Non-LTE Models to Map Physical Conditions

The text in Chapter 5 appeared in the *Astrophysical Journal* (Finn et al. 2021) as “Physical Conditions in the LMC’s Quiescent Molecular Ridge: Fitting Non-LTE Models to CO Emission.”

5.1 Introduction

Our understanding of star formation is heavily dependent on our understanding of molecular clouds and the physics that governs them. It is difficult, and in many cases impossible, to determine those physical conditions without relying on assumptions or scaling relations (e.g., Kennicutt 1998). These assumptions appear to be sufficient in many cases, but there are examples of clouds and regions of galaxies that are not forming stars as we would expect based on these scaling relations. For example, “Maddalena’s Cloud” G126-2.5 is a giant molecular cloud in the Milky Way that has unusually low star formation (Maddalena & Thaddeus 1985), and the star formation

rate in the Central Molecular Zone in the Galactic Center is an order of magnitude lower than would be predicted by Galactic trends (Longmore et al. 2013). To understand why, we must determine physical conditions without making assumptions that molecular clouds are behaving in the "typical" way.

One of the most common mass estimates for molecular clouds comes from the CO-to-H₂ conversion factor, X_{CO} , which is discussed in detail in Bolatto et al. (2013). It is often calibrated with the virial mass or dust mass and is used to convert the integrated intensity of ¹²CO(1-0) emission to a column density of H₂. The X_{CO} factor method is most valid when determining masses on large size scales where many molecular clouds are smoothed together, averaging over the varying physical conditions. On the scale of individual star-forming clouds or individual lines-of-sight, the conversion of CO flux to H₂ column density with an adopted X_{CO} factor cannot be expected to be constant (Bolatto et al. 2013, and references therein).

Another measure of mass can be made by assuming local thermal equilibrium (LTE) to get excitation temperature, optical depth, and column density (Mangum & Shirley 2015). This method is based on the assumption that the gas is sufficiently dense for the molecular excitation levels to have a Boltzmann distribution corresponding to an excitation temperature, T_{ex} , and that the excitation temperatures of ¹²CO and ¹³CO are equal. This method also often assumes that ¹²CO is optically thick, allowing for an easy estimate of the excitation temperature (T_{ex}) from the brightness temperature (T_B), while ¹³CO is optically thin, which makes it possible to determine the optical depth with an assumption of the relative abundance of ¹²CO and ¹³CO (Koeppen & Kegel 1980).

However, these calculations break down if ¹²CO becomes optically thin, or if either line's level population is not well described by a Boltzmann distribution. Studies

have shown regimes in which the LTE calculations overestimate the column density by up to a factor of two in bright ($T_B > 40$ K) clouds (Indebetouw et al. 2020), and underestimate the mass by up to a factor of 7 when the ^{13}CO becomes sub-thermally excited (Castets et al. 1990; Padoan et al. 2000; Heyer & Dame 2015). Assuming LTE also requires that the density is sufficiently high such that the excitation is entirely governed by temperature, meaning that any dependence on density drops out of the equations and so cannot be solved for.

Ratios of isotopologues (e.g. $^{13}\text{CO}/^{12}\text{CO}$) can trace volume density in the case where one line is optically thick and the other line is sub-thermally excited (Nishimura et al. 2015). Ratios of upper to lower excitation levels of CO (e.g. $^{12}\text{CO}(2-1)/^{12}\text{CO}(1-0)$) scale with excitation temperature and density when both lines are optically thin, and the ratio approaches unity as the lines get increasingly optically thick (Sakamoto 1994; Nishimura et al. 2015; Peñaloza et al. 2017). These ratios are also dependent on optical depth and local abundance ratios and so can only provide rough diagnostics of the density and temperature (Peñaloza et al. 2017).

In this study, we fit molecular line observations to the results of non-LTE escape probability models from RADEX (van der Tak et al. 2007). This avoids many of the assumptions required for other methods, such as those listed above, and so allows us to better characterize the actual physical conditions of the gas. With this method, we obtain estimates of not just the temperature and column density, but also the volume density. Our only assumptions in this case are that the different molecular lines are tracing the same gas with a constant abundance ratio throughout the cloud, and that the gas in each voxel is homogeneous—we fit only one set of physical conditions for each pixel and velocity channel despite the fact that temperature and density almost certainly vary along the line of sight and within the beam. Through this

model-fitting study, we determine the physical conditions of molecular clouds in the Large Magellanic Cloud (LMC) and compare those results to other common methods: adopting an X_{CO} factor, assuming LTE, or using line diagnostics.

We use as a case study the quiescent southern end of the Molecular Ridge in the LMC, extending 1-2 kpc south from 30 Doradus (Figure 5.1). We assume a distance to the LMC of 50 kpc (Schaefer 2008). Cohen et al. (1988) first noted the Ridge as a striking feature in low resolution maps of $^{12}\text{CO}(1-0)$, and further observations of ^{12}CO by the NANTEN survey (Fukui et al. 2008) revealed that it contained $\sim 30\%$ of all CO-bright molecular gas mass in the LMC (Mizuno et al. 2001). Despite the large reservoir of molecular gas, the Ridge is surprisingly quiescent, showing little sign of star formation based on the presence of young optical clusters or $\text{H}\alpha$ emission (Davies et al. 1976; Bica et al. 1996; Yamaguchi et al. 2001). Indebetouw et al. (2008) find the $\text{H}\alpha$ emission (Calzetti et al. 2007) would predict a star formation rate of $2.6 \times 10^{-4} M_{\odot} \text{ yr}^{-1}$, while the star formation rate predicted by the molecular gas surface density and the Schmidt-Kennicutt law (Kennicutt 1998) would be $8 \times 10^{-3} M_{\odot} \text{ yr}^{-1}$, over a factor of 30 larger. There are only five HII regions in the Ridge that were identified and named by Henize (1956), most notably N171, as well as some fainter HII regions (see Figure 5.1).

By looking for embedded stellar objects in the Ridge from the *Spitzer* SAGE survey (Meixner et al. 2006), Indebetouw et al. (2008) showed that the lack of young, blue clusters and low $\text{H}\alpha$ emission is likely due to the Ridge preferentially forming relatively low mass star clusters rather than having deeply-embedded high mass objects or simply not forming stars at all (the star formation measured by modeling the YSO population was a factor of two lower than that predicted from the extragalactic Schmitt-Kennicutt law (Kennicutt 1998), but agreed within the uncertainties). This

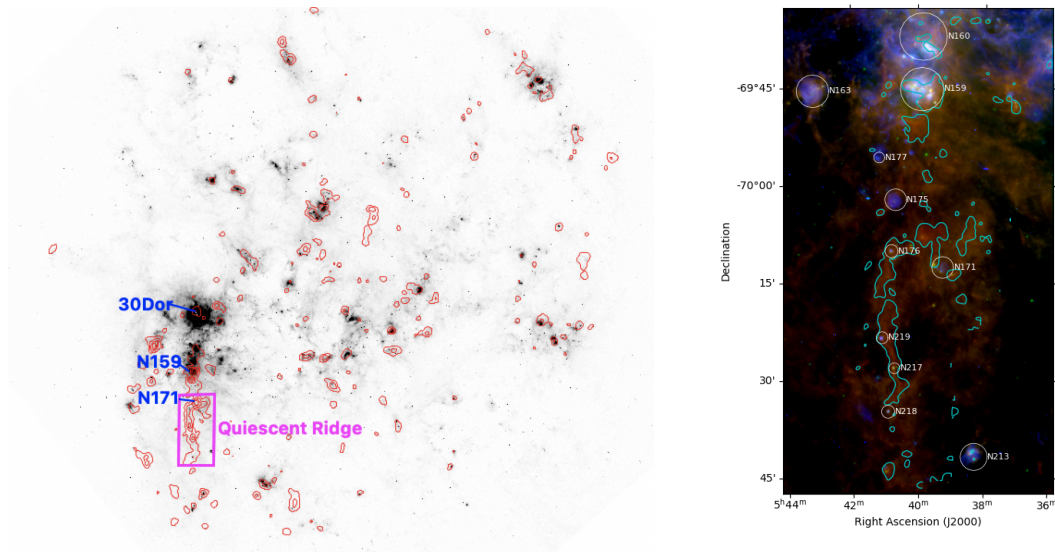


Fig. 5.1.— *Left:* The LMC with the Molecular Ridge highlighted in pink and active star-forming regions 30 Doradus (30 Dor), N159, and N171 in blue. The grayscale is MIPS 24 μm from the SAGE survey (Meixner et al. 2006), and the red contours are $^{12}\text{CO}(1-0)$ from the NANTEN survey (Fukui et al. 2008). We can see from this that the Ridge is a unique feature, showing up prominently in the red $^{12}\text{CO}(1-0)$ contours, but lacking any strong emission in the 24 μm grayscale, which is a common star formation tracer. *Right:* RGB image zoomed in on the Ridge. The red is PACS 250 μm from the HERITAGE survey, green is the same 24 μm as the grayscale on the left, and blue is H α from MCELS survey (Smith & MCELS Team 1998). The cyan contours are $^{12}\text{CO}(1-0)$ from the MAGMA survey, and HII regions identified by Henize (1956) are shown as white circles.

is a stark contrast to 30 Doradus and the active massive star formation regions N159 and N160 directly to the north of the Ridge that are forming massive stars prodigiously. This makes the Molecular Ridge a particularly interesting region for studies of the molecular gas properties.

The quiescence of the Ridge could be due to atypical gas conditions, so a robust, assumption-minimizing approach is needed to analyze its physical conditions. To do this, we use four molecular lines - $^{12}\text{CO}(1-0)$, $^{13}\text{CO}(1-0)$, $^{12}\text{CO}(2-1)$, and $^{13}\text{CO}(2-1)$, the observations of which are described in §5.2. We fit non-LTE RADEX models to those observed lines as described in §5.3, and so avoid assumptions about stability, local excitation, or optical depth. We evaluate the performance of this fitting and details of methodology choices in the Appendices A1 through A3.

In §5.4, we segment the emission into clumps and determine the physical properties of these clumps. We then discuss YSOs detected in the Ridge and match them to those CO clumps in §5.5. We evaluate how the derived properties of the clumps compare with other common methods of determining physical conditions in §5.6, and how the derived properties correlate with star formation as traced by the presence of associated YSOs in §5.7. Our major results are summarized in §5.8.

5.2 Observations

In this analysis, we make use of new $^{13}\text{CO}(1-0)$ and $\text{CS}(2-1)$ data from the Atacama Large Millimeter/submillimeter Array (ALMA) 7m Atacama Compact Array (ACA), described in §5.2.1. We also use $^{12}\text{CO}(1-0)$ data from the Mopra Telescope taken as part of the Magellanic Mopra Assessment (MAGMA) survey (Wong et al. 2011), and new observations of $^{12}\text{CO}(2-1)$ and $^{13}\text{CO}(2-1)$ from the Atacama Pathfinder Experiment (APEX), described in §5.2.2. These observations are summarized in Table 5.1,

and the integrated intensity maps are shown in Figure 5.2. The errors reported in Table 5.1 are the rms noise in line-free regions of the data cubes in a single channel of 1 km s^{-1} . Though Table 5.1 and Figure 5.2 show the resolutions obtained for each set of observations, the majority of the analysis presented in this paper is performed with all data sets convolved to $45''$ and 1.0 km s^{-1} velocity resolution to compare among the data sets. The final data cubes used in the analysis are available as supplementary material¹.

5.2.1 ALMA Data

Interferometric data were obtained in three maps with the ALMA 7m ACA for project 2017.1.00271.S. The data contain 3 spectral windows centered on $^{13}\text{CO}(1-0)$, $\text{C}^{18}\text{O}(1-0)$, and $\text{CS}(2-1)$, each with 2048 61.035 kHz channels (125 MHz bandwidth). An additional 2 GHz wide spectral window with coarse channels (0.98 MHz) was observed centered on $\text{H}40\alpha$ at 99 GHz . The north-west 96-pointing map was observed 9 times between 2017-11-07 and 2017-11-15 for a total of 438 minutes on source. J0522-3627 ($5-5.5 \text{ Jy}$) and J0529-7245 ($600-700 \text{ mJy}$) were used for bandpass and amplitude, and for phase calibration, respectively. The central 76-pointing map was observed 9 times

¹<https://doi.org/10.5281/zenodo.4838414>

Table 5.1: Observations used in this analysis

Source	Line	Beam ($''$)	RMS (K)	Velocity Channel
ALMA ACA	$^{13}\text{CO}(1-0)$	16	0.033	0.5 km/s
ALMA ACA	$\text{CS}(2-1)$	18	0.025	0.5 km/s
ALMA TP	$^{13}\text{CO}(1-0)$	63	0.0078	0.19 km/s
ALMA TP	$\text{CS}(2-1)$	70	0.0062	0.19 km/s
MAGMA	$^{12}\text{CO}(1-0)$	45	0.11	0.5 km/s
APEX	$^{12}\text{CO}(2-1)$	29	0.23	1.0 km/s
APEX	$^{13}\text{CO}(2-1)$	30	0.065	1.0 km/s

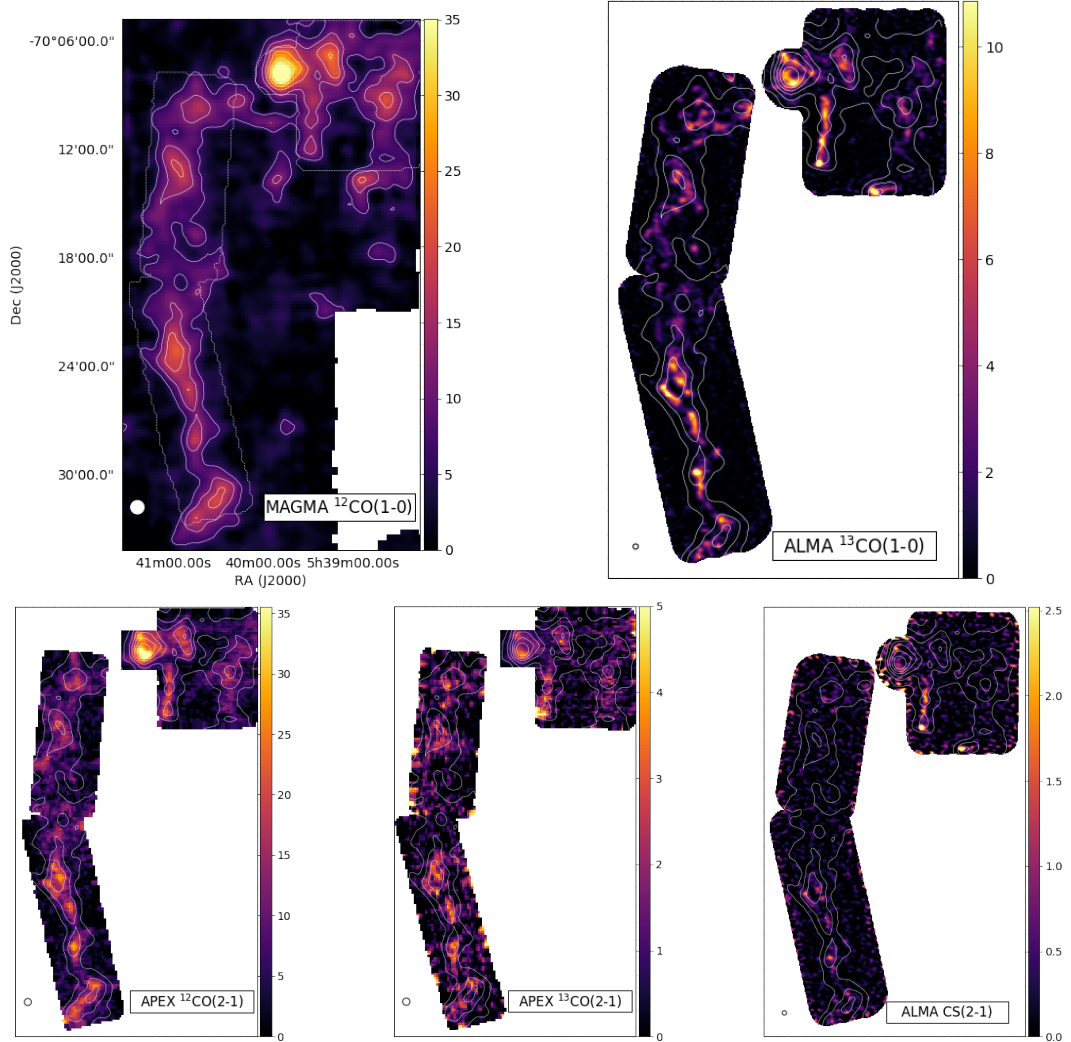


Fig. 5.2.— Integrated intensity maps of the observations used in this analysis. The contours are the integrated intensity of $^{12}\text{CO}(1-0)$ at intervals of 6, 12, 18, 24, and 30 K km s^{-1} . The dotted contour in the MAGMA $^{12}\text{CO}(1-0)$ map shows the common observational footprint of all the maps. All maps are in units of K km s^{-1} , and the beams are shown in the lower left corners.

between 2017-10-15 and 2017-11-06 for a total of 346 minutes on source, and the southern 106-pointing map 11 times between 2017-10-15 and 2017-11-06 for a total of 470 minutes on source. Those maps used the same bandpass and amplitude calibrator as the northern. In a given execution, either J0635-7516 (1.25 Jy) or J0529-7245 was used for phase calibration.

The data were calibrated with the ALMA data pipeline Pipeline-CASA51-P2-B, v.40896² (Davis 2021), packaged with CASA 5.1.1-5³ (McMullin et al. 2007). The standard pipeline recipe and default parameters were used as described in the ALMA pipeline User’s Guide. Visibilities are calibrated at full spectral resolution. Time-varying gains are solved on the phase calibrator using the 2 GHz wide spectral window, and transferred to the narrow spectral windows using a constant spw-spw phase offset during each 1.5-hour execution block. Gains are transferred to the science target on the scan timescale with linear interpolation in time. Weights are set correctly by the ALMA correlator and propagated through the calibration process, so no statwt is required. Continuum and line spectral channels are found in each spectral windows by the pipeline task findCont described in the manual. A linear per-visibility fit is performed and subtracted in the uv domain. The pipeline images data at full spectral resolution, but we re-imaged the calibrated continuum-subtracted visibilities as described below.

By design, project 2017.1.00271.S did not cover the ~ 2 arcminute HII region at 5:39:50 -70:08:00 because it was already observed with ALMA ACA by projects 2012.1.00603.S and 2015.1.00196.S. These projects also have three narrow spectral windows centered on $^{13}\text{CO}(1-0)$, $\text{C}^{18}\text{O}(1-0)$, and $\text{CS}(2-1)$, and a 2 GHz wide spectral window. The narrow windows have 30.518 kHz and 122.07 kHz channels in

²<https://almascience.nrao.edu/processing/>

³casa.nrao.edu

2012.1.00603.S and 2015.1.00196.S, respectively, but all have 125MHz bandwidth like the primary dataset. The wide window is centered at 96.8 GHz in project 2015.1.00196.S, but that spectral window is not analyzed here. Project 2012.1.00603.S was observed 8 times between 2013-12-17 and 2015-04-28, using Ganymede, J0519-4546 (1.3Jy), Uranus, Callisto or Mars as the amplitude calibrator, J0538-4405, J0519-4546, J0635-7516, or J1037-2934 as the bandpass calibrator, and J0635-7516 or J0601-7036 as the phase calibrator. Those data were calibrated manually by ALMA staff, using a script accessible in the ALMA archive. That script solves for time-varying gains on each spectral window individually, and transfers the gains from phase calibrator to science target, but not between spectral windows.

Project 2015.1.00196.S was observed 8 times between 2016-05-01 and 2016-06-12, using J0538-4405 (2.6 Jy) or J1107-4449 (1.3 Jy) for bandpass calibration, J0538-4405 or Uranus for amplitude calibration, and J0529-7245 (700-850 mJy) for phase calibration. The data were calibrated with Pipeline-CASA56-P1-B v.42866 packaged with CASA 5.6.1-8, following the same procedure as the primary dataset 2017.1.00271.S.

There were no detections in C¹⁸O(1-0) above a 3σ upper limit of 200 mJy. The ¹³CO(1-0) visibility data from 2012.1.00603.S and the CS(2-1) data from 2012.1.00603.S and 2015.1.00196.S were added to the 2017.1.00271.S NW tile data before imaging.

For all projects, total power ALMA data was obtained for rectangular regions corresponding to the interferometric maps, extended by one primary beam in both dimensions. Project 2012.1.00603.S was observed 4 times between 2013-12-16 and 2014-12-14, and processed with Pipeline-Cycle2-R1-B v.31667 in CASA 4.2.2. Project 2015.1.00196.S was observed 13 times between 2016-03-23 and 2016-04-08 and processed with Pipeline-Cycle3-R4-B v.36660 in CASA 4.5.3. Project 2017.1.00271.S NW, central, and southern maps were observed 23 times between 2018-03-30 and

2018-04-23, 25 times between 2018-01-09 and 2018-04-05, and 22 times between 2018-01-24 and 2018-03-21, respectively. All 2017.1.00271.S data were calibrated and imaged with Pipeline-CASA51-P2-B v.40896 packaged with CASA 5.1.1-5. The ALMA single dish pipeline is also described in the User’s Manual, and the standard procedure was used: application of system temperature amplitude calibration, subtraction of an OFF position, line detection by clustering analysis, fitting and removal of a polynomial baseline, and a second iteration of line detection and baseline removal. The spectra are then gridded to produce image cubes at native spectral resolution, with beams and rms as noted in Table 5.1.

The interferometric data were imaged and combined with the total power data using CASA 5.6.1-8. For the line cubes, total power images were Hanning smoothed and used as a starting model for interferometric deconvolution with the `tclean` task. The images have a cell size of $2.1'' \times 2.1'' \times 0.5 \text{ km s}^{-1}$, were cleaned to a 1σ threshold (0.6 Jy/bm for $^{13}\text{CO}(1-0)$ and 0.3 Jy/bm for $\text{CS}(2-1)$) using the mosaic gridded, hogbom deconvolver, briggs weighting with `robust=0.5`, and auto-multithresh masking using the pipeline default automasking parameters. Use of the total power starting model increases the signal-to-noise on the “overlap” spatial scales to which the interferometric and total power are both sensitive, but can overestimate the total flux density after nonlinear deconvolution. To correct the flux, the final deconvolved image is combined with the total power image (multiplied by the interferometric sensitivity map) using the `feather` task, which adds the two images in the Fourier domain and ensures the correct total flux density on all spatial scales. The interferometer recovered 40% of the total flux across the region, with individual clouds recovering between 15 and 99%. The final combined image is then divided by the interferometric sensitivity map to obtain the correct flux scale as a function of position. We then convolved the three

regions to a common circular beam of $16.0''$ and $18.2''$ for $^{13}\text{CO}(1-0)$ and $\text{CS}(2-1)$, respectively, and mosaiced them into a single map, linearly weighted by each tile's sensitivity image.

5.2.2 APEX Data

$^{12}\text{CO}(2-1)$ and $^{13}\text{CO}(2-1)$ were observed with the Atacama Pathfinder Experiment 12m telescope, APEX, between August 14 and 24, 2017 under project number 0100.F-9313(A). The observations were taken with the APEX-1 receiver, resulting in a beam size of $27.8''$ – $29.0''$. Three maps were obtained, corresponding to the three ALMA maps, using on-the-fly (OTF) mapping. Standard calibration was performed using R-Dor, Venus, RAFGL1235, and 07454-7112. Data reduction was carried out using GILDAS/CLASS; to increase the signal-to-noise ratios in individual channels, contiguous channels were smoothed to a velocity resolution of 1.0 km s^{-1} and then baseline subtracted, resulting rms ~ 0.24 and 0.09 K for ^{12}CO and ^{13}CO , respectively. The APEX data cubes were gridded to $9'' \times 9''$ (~ 3 pixels per beam) to facilitate comparisons with the ALMA data cubes. As with the interferometric ALMA data, the 2 arcmin region at 5:39:50 -70:08:00 was not observed with APEX, but instead, the archival ALMA total power data for $^{12}\text{CO}(2-1)$ and $^{13}\text{CO}(2-1)$ from projects 2012.1.00603.S and 2015.1.00196.S were added to our APEX mosaic. The APEX and ALMA images were combined after convolving the images to a common beam size and gridding as an average weighted by each image's sensitivity map.

5.3 RADEX Fitting

5.3.1 Fitting Method

To determine physical parameters from the observed ^{12}CO and ^{13}CO emission lines, we compared the line intensities at each pixel and velocity to model intensities for a range of physical parameters from the non-LTE escape probability code RADEX (van der Tak et al. 2007). This was done by computing a three-dimensional grid of RADEX models for a range of kinetic temperatures (T_{kin}), H_2 volume densities (n_{H_2}), and ^{12}CO column densities (N_{CO}). The four emission cubes— $^{12}\text{CO}(1-0)$, $^{13}\text{CO}(1-0)$, $^{12}\text{CO}(2-1)$, and $^{13}\text{CO}(2-1)$ —were all convolved to $45''$ and 1 km s^{-1} to match the lowest common resolutions among the data sets. The errors used in calculating probabilities are the rms errors in these newly convolved maps, measured in emission-free slices of the cubes. The lower-resolution errors for $^{12}\text{CO}(1-0)$, $^{13}\text{CO}(1-0)$, $^{12}\text{CO}(2-1)$, and $^{13}\text{CO}(2-1)$ are 0.11 K, 0.017 K, 0.1 K, and 0.035 K, respectively. We show the the $^{13}\text{CO}(1-0)$ map at this lowered resolution in Figure 5.3 and example input spectra for the lines in Figure 5.4.

When computing RADEX models, we used a homogeneous spherical escape probability geometry with a line width of 1 km s^{-1} to match our observations' velocity channels, and a background temperature of 2.73 K. We also assume that the ratio of ^{12}CO to ^{13}CO (R_{13}) is in the range 50–100 (Nikolić et al. 2007) and that $N_{^{12}\text{CO}}/N_{^{13}\text{CO}} = R_{13}$.

We limited the ranges of the parameters to be T_{kin} between 2 and 200 K, n_{H_2} between $10^{1.5}$ and 10^7 cm^{-3} , and N_{CO} between 10^{14} and 10^{18} cm^{-2} . The ranges of n_{H_2} and N_{CO} are evenly spaced in log space, T_{kin} is spaced linearly. When computing the RADEX grid, we also excluded regions of the parameter space where RADEX predictions

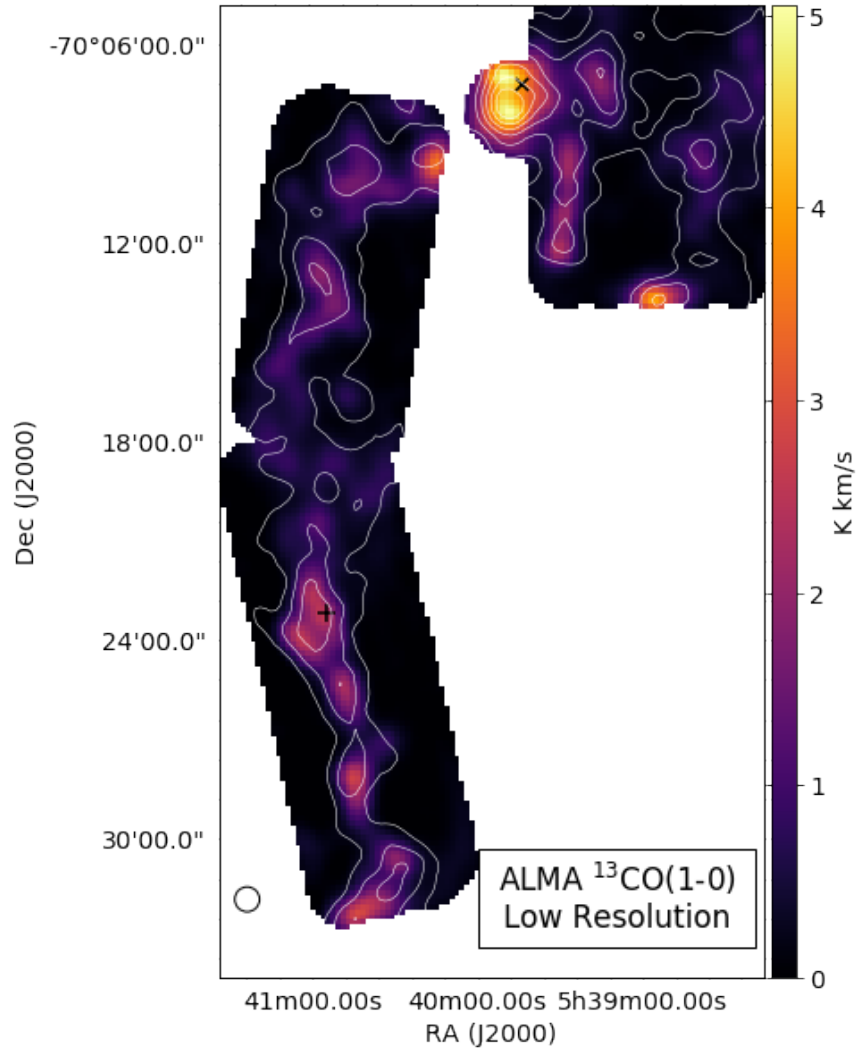


Fig. 5.3.— Integrated intensity map of $^{13}\text{CO}(1-0)$ convolved to a resolution of $45''$ (beam shown in lower left corner) to match the limiting resolution of the $^{12}\text{CO}(1-0)$ map. The contours are the integrated intensity of $^{12}\text{CO}(1-0)$ as shown in Figure 5.2, and locations of the example spectra shown in Figure 5.4 are marked with a cross for panel (a) and an X for panel (b). The majority of the analysis in this paper is performed at this lowered resolution, including the RADEX fitting.

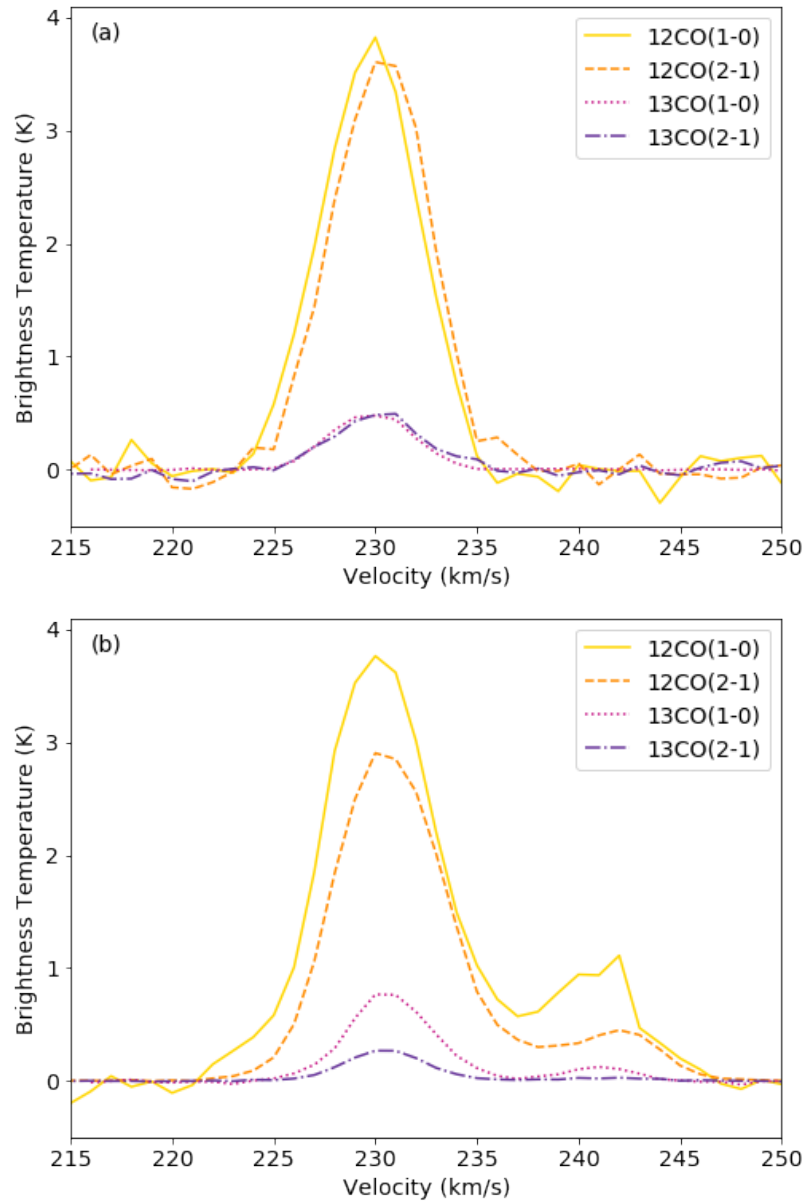


Fig. 5.4.— Example spectra of $^{12}\text{CO}(1-0)$, $^{12}\text{CO}(2-1)$, $^{13}\text{CO}(1-0)$, and $^{13}\text{CO}(2-1)$ from two different peaks. These are examples of spectra that are used in the RADEX fitting, and so are taken from maps that have all been convolved to a beam size of $45''$. The top panel shows a spectra that is typical throughout the region, while the bottom panel shows an example with more velocity structure from the northern region of the map. The locations of these two spectra are shown in the $^{13}\text{CO}(1-0)$ map in Figure 5.3.

are less reliable, such as where the optical depth gets very large ($\tau > 300$), where ^{12}CO becomes overpopulated and the excitation gets inflated ($T_{ex} > 2.5 \times T_{\text{kin}}$, Koeppen & Kegel 1980), where any output values become unphysically negative, and where RADEX took more than 999,000 iterations to solve.

For each combination of the three parameters, $\vec{p} = (T_{\text{kin}}, n_{\text{H}_2}, N_{\text{CO}})$, the resultant model brightness temperatures from RADEX, $R(\vec{p})$, and the beam filling factor, f , were used to compute a probability given the observed brightness temperature for some voxel, I , and its error, δ , for each observed line, j , using the equation

$$P(\vec{p}|I) = \prod_j \frac{-1}{\delta_j} \exp \left[\frac{1}{2} \left(\frac{(I_j - R(\vec{p})_j \times f)}{\delta_j} \right)^2 \right] \quad (5.1)$$

We find the combination of parameter values that yields the greatest probability, \vec{p}_{max} . We then find the odds ratio for all other parameter combinations in the grid:

$$O = \frac{P(\vec{p}_{\text{max}}|I)}{P(\vec{p}|I)} \quad (5.2)$$

In the case of uniform priors (so $P(\vec{p}_{\text{max}}) = P(\vec{p})$, which we assume here for all parameters), this reduces to the Bayes Factor:

$$B = \frac{P(I|\vec{p}_{\text{max}})}{P(I|\vec{p})} \quad (5.3)$$

To compare \vec{p}_{max} with all other combinations of parameters, we use the ‘‘Jeffreys’’ scale (Trotta 2008) to determine if p_{max} is ‘‘inconclusively’’, ‘‘weakly’’, ‘‘moderately’’, or ‘‘strongly’’ preferred to the other parameter combinations. Trotta (2008) defines this empirically derived scale as follows: a value of $|\ln B| < 1$ corresponds to inconclusive evidence, $1 \leq |\ln B| < 2.5$ is weak evidence, $2.5 \leq |\ln B| < 5$ is moderate evidence, and $|\ln B| \geq 5$ is strong evidence. The value of $|\ln B|$ is zero for \vec{p}_{max} , and increases

for parameter combinations that have lower probabilities of matching the observed intensities.

After excluding the regions of parameter space for which $|\ln B| \geq 5.0$ (\vec{p}_{\max} is strongly preferred over all the excluded parameter combinations) we determine the ranges of the remaining parameter space for each parameter to obtain what we call here “Bayesian intervals”. We do the same to get intervals excluding parameter combinations with $|\ln B| \geq 2.5$ and $|\ln B| \geq 1.0$ to get intervals outside of which \vec{p}_{\max} is “moderately” and “weakly” preferred, respectively. In this case, the “strong” 5.0 Bayesian interval is the largest and least constrained of the three since parameter combinations that \vec{p}_{\max} is only moderately or weakly preferred over are included within the interval. The “weak” 1.0 Bayesian interval is the narrowest and most constrained, since \vec{p}_{\max} only needs to be weakly preferred over a parameter combination for it to be excluded.

The Bayesian intervals and \vec{p}_{\max} all depend entirely on the 3-dimensional probability density function (PDF). In addition to these intervals, we also consider each individual parameter’s probability density profile, integrated over the other two parameters. From these profiles, we determine one-sigma and two-sigma, 67% and 95%, confidence intervals, defined as the smallest ranges of the parameters for which the sum under their normalized probability profiles is 0.67 and 0.95, respectively. The confidence intervals depend only on the integrated 1-dimensional profiles instead of the 3-dimensional PDF and therefore depend on the spacing of intervals used in the parameter ranges. Since the n_{H_2} and N_{CO} ranges span several orders of magnitude, the confidence intervals are determined in log space so as not to overly weight the higher values. The confidence interval of T_{kin} is calculated with linear spacing.

An example corner plot showing a resultant distribution for one pixel of data

is shown in Figure 5.5. The profiles along the diagonal show some of the metrics described above: \vec{p}_{\max} , the collapsed 1-dimensional probability profiles, and the two smallest Bayesian intervals.

We attempted to independently constrain R_{13} in the same way as the other parameters, adding it as a fourth dimension to the tested parameter space. However, R_{13} was rarely constrained and including it significantly increased the computational requirements. We therefore assumed a range of $R_{13} = 50$ – 100 instead (Nikolić et al. 2007) and performed the fitting once with $R_{13} = 50$ and once with $R_{13} = 100$. With additional observations of higher J ^{12}CO and ^{13}CO lines, we might be able to constrain R_{13} on a pixel-by-pixel basis, making it worth the additional computational requirements.

We similarly attempted to include fitting the beam filling factor as a fourth parameter with minimal success. Appendix A1 goes into detail about the various attempts at fitting and measuring the beam filling factor. After examining the results of these attempts, we used a range of filling factors from 10%–20%. The lower limit of this range comes from unphysical fitting solutions (primarily defined as excessively large line-of-sight path lengths) and the upper limit comes from measured upper limits when comparing the high resolution $^{13}\text{CO}(1-0)$ observations at $13''$ to the low resolution maps at $45''$. The exception to this is the ~ 2 arcminute region at 5:39:50–70:08:00, where we found a lower limit on the filling factor to be 15% rather than 10%. A filling factor of 10% results in line-of-sight path lengths that are > 100 pc while the radius of the clouds in the region are measured to be ~ 20 pc. We do not take into account any potential difference in beam filling factors between different lines, despite them likely having different spatial distributions.

Using simulated data from the full range of the parameter space based on expected

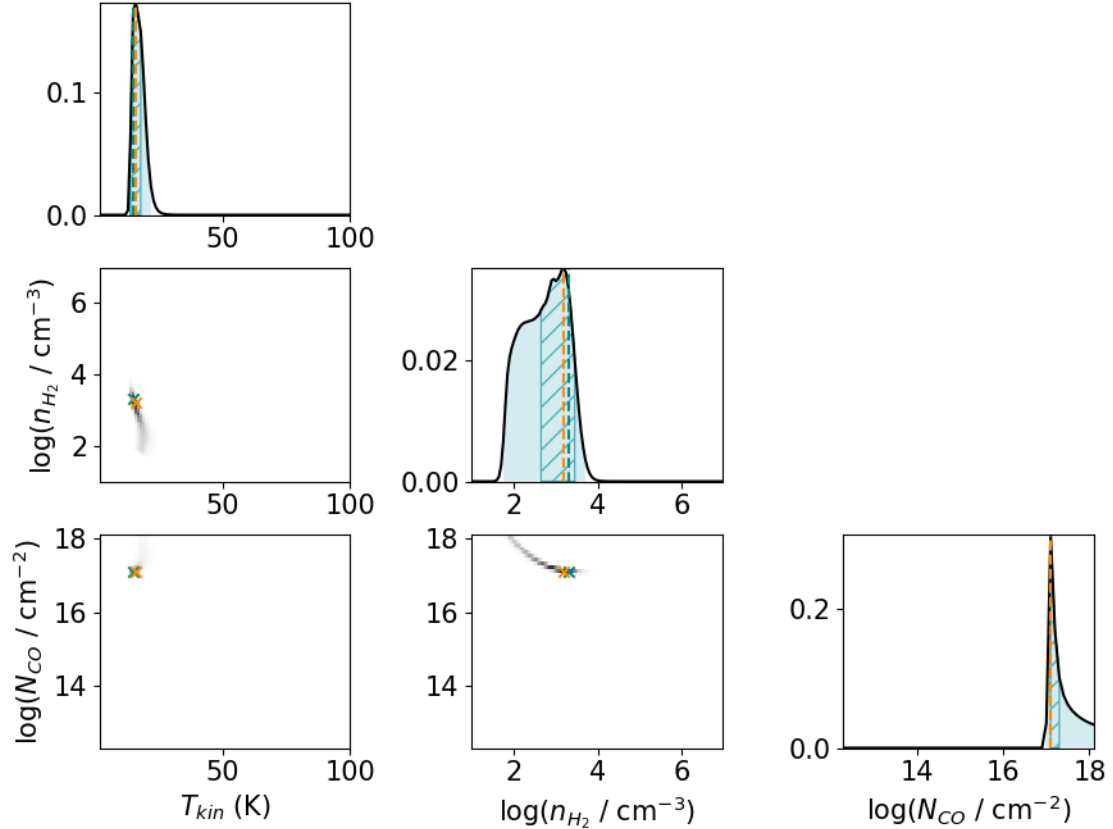


Fig. 5.5.— Example of a probability distribution from representative data with line intensities of 1.7 K, 0.2 K, 1.2 K, and 0.14 K for $^{12}\text{CO}(1-0)$, $^{13}\text{CO}(1-0)$, $^{12}\text{CO}(2-1)$, and $^{13}\text{CO}(2-1)$, respectively, using a 15% beam filling factor, and $R_{13} = 100$. The ranges on the axes show the full tested parameter space. The blue shading shows the 2.5 Bayesian intervals (“moderate” evidence), and the blue hatching shows the 1.0 Bayesian intervals (“weak” evidence). The vertical blue dashed lines and blue crosses indicate p_{max} , and the orange dashed lines and orange crosses indicate the maximum value of the probability profiles. This plot indicates that this pixel most likely has $T_{\text{kin}} = 15$ K, $n_{\text{H}_2} = 10^{3.3} \text{ cm}^{-3}$, and $N_{\text{CO}} = 10^{17.1} \text{ cm}^{-2}$.

emission from RADEX and the measured rms error in the observed maps, we evaluated how well our data can be fit by the process described here. We also evaluated which of the Bayesian and confidence intervals best recovered true parameter values while still constraining their values. The full evaluation process is described in Appendix A2 and additional related plots are available as supplementary material⁴. The true parameter values were almost always recovered at $N_{\text{CO}} > 10^{15} \text{ cm}^{-2}$ and for the full range of T_{kin} and n_{H_2} . The intervals that were determined to best characterize the true parameter values were a combination of the 95% confidence interval and the 1.0 Bayesian interval. They showed similarly high recovery rates of the true parameter values and had the tightest constraints on those values. In some regions the 95% confidence interval was better constrained than the 1.0 Bayesian interval, and vice versa, hence the combination of the two.

We also consider how the fitting process depends on including all four observed lines— $^{12}\text{CO}(1-0)$, $^{13}\text{CO}(1-0)$, $^{12}\text{CO}(2-1)$, $^{13}\text{CO}(2-1)$ —and how it would change if we included only the three lines with the best angular resolution and dropped $^{12}\text{CO}(1-0)$, which has a resolution of $45''$. This would allow us to do the entire fitting process at higher resolution since we would instead be limited by the $^{13}\text{CO}(2-1)$ at $30''$. We consider this case in Appendix A2.1 using the fitting evaluation methods described in Appendix A2. We find that dropping the $^{12}\text{CO}(1-0)$ results in a loss of sensitivity to moderate values of N_{CO} . While the resulting fitted intervals still include the correct value almost all the time for $N_{\text{CO}} > 10^{15} \text{ cm}^{-2}$, they are only well-constrained for $N_{\text{CO}} > 10^{16} \text{ cm}^{-2}$. We decided that the improvement in resolution is not worth the loss in sensitivity to this range of column densities.

⁴<https://doi.org/10.5281/zenodo.4646288>

5.3.2 **Generating Maps of Physical Parameters**

We perform the RADEX fitting on each of the pixels in the map. For each velocity component within each pixel, we find the peak of the $^{13}\text{CO}(1-0)$ line profile for a single velocity component and perform a full fit of the three physical parameters— T_{kin} , n_{H_2} , N_{CO} —for the peak value. We then assume that T_{kin} and n_{H_2} are constant for that line of sight and fit the rest of the line only considering the T_{kin} and n_{H_2} that were in the fitted interval of the line peak to get N_{CO} across the line. We include only velocities for which at least two lines have detections above 5σ . N_{CO} is then summed over the line to get a total value for the pixel. Upper and lower errors come from the upper and lower bounds of the fitted interval for each parameter, and for N_{CO} , the upper errors and lower errors are propagated separately to get upper and lower errors on the total N_{CO} for the line.

We also considered two other methods for this fitting process: fitting all three parameters for each voxel along the line of sight or holding T_{kin} and n_{H_2} fixed for the entire cloud after segmenting the emission into clumps. These alternative methods are compared in Appendix A3, where we find that the method described here of holding T_{kin} and n_{H_2} fixed for the line of sight yielded the most reliable realistic results.

This process was done once with $R_{13}=50$ and once with $R_{13}=100$, and also once each with a filling factor of 10% and 20% for a total of four runs, with the exception of the region around 5:39:50 -70:08:00, for which we used a lower limit on the filling factor of 15% rather than 10% as described in Appendix A1. To correct our final results for this filling factor, we multiplied the fitted N_{CO} by the assumed filling factor for the clump. We did not correct the n_{H_2} values for the filling factor, so the values reported are those of clump structures on the scale of the assumed filling factor (4.5'' 6.75'' or 9'' for filling factor of 10%, 15%, or 20%, respectively).

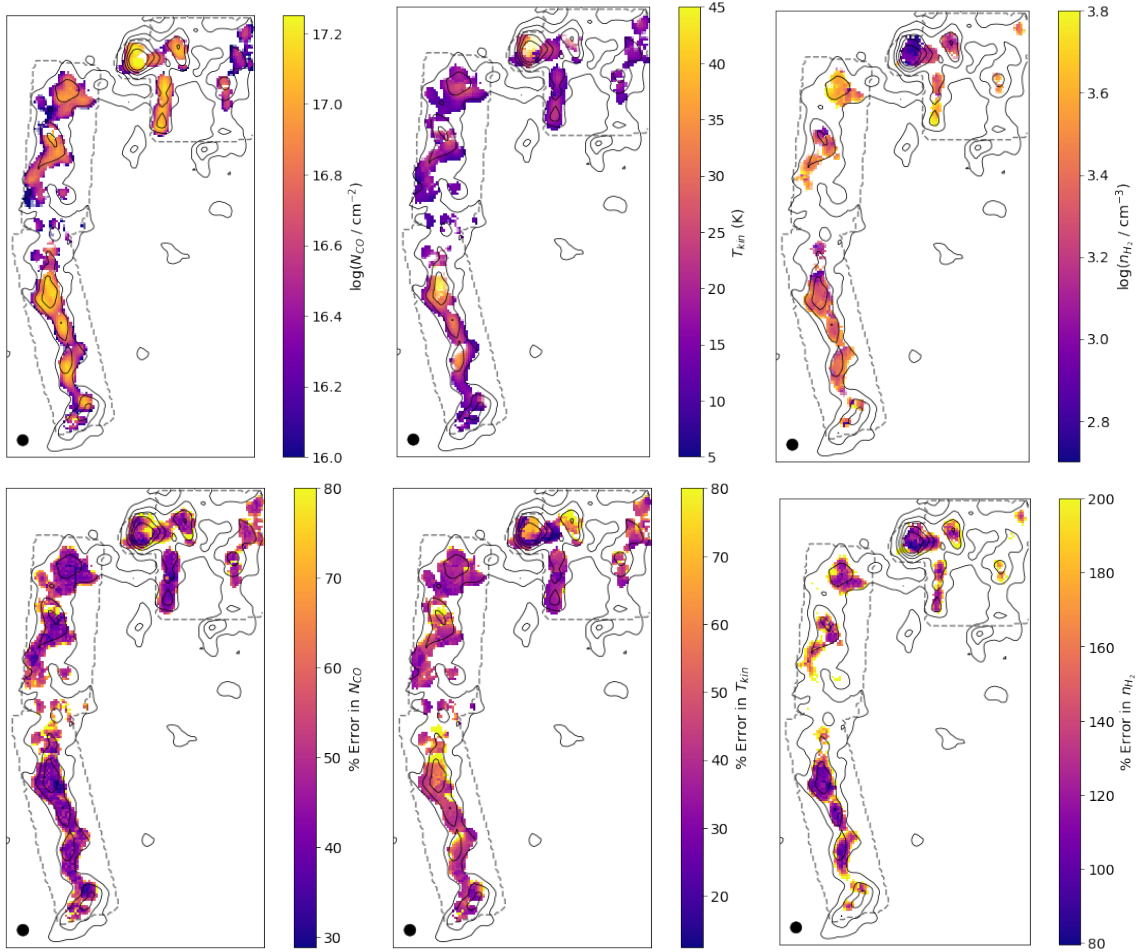


Fig. 5.6.— RADEX-fitted maps of N_{CO} , T_{kin} , and n_{H_2} (top row, left to right) and the percent error in N_{CO} , T_{kin} , and n_{H_2} (bottom row, left to right). N_{CO} was masked where the error was more than 80%, T_{kin} where the error was more than 50%, and n_{H_2} where the error was more than 200%. The values shown have been averaged between the values fit with $R_{13} = 50$ and $R_{13} = 100$ and filling factors of 10% and 20%, which can result in errors larger than the described cutoffs. The pixel transparency in the maps of the fitted parameters (top row) is proportional to the error in those parameters (bottom row). All N_{CO} values are corrected for the assumed beam filling factor, but the n_{H_2} values are those fitted to the structures at the filling factor scale (4.5'' or 9'' for filling factors of 10% and 20%, respectively). The solid contours are the integrated intensity of MAGMA $^{12}\text{CO}(1-0)$, as shown in Figure 5.2, and the dashed contours show the common observational footprint. The 45'' beam is shown in the bottom left corner.

When approaching a boundary between two velocity components, both spatially and in velocity space, we drew a hard barrier rather than doing any partial pixel assignments to account for overlapping line wings or spatial overlap. To check if this affected the fitting results, we did the RADEX fitting for three overlapping velocity components, but this time fitting Gaussian line profiles to each pixel to appropriately assign partial emission to the overlapping clumps. The RADEX fitting code used this partial emission assignment and continued the fitting as before. This did not result in any significant change in any of the derived quantities, and so fortunately the detailed accounting of multiple velocity components does not need to be added in general to this kind of analysis. This is likely because the line wing that was cut from Component A and assigned to Component B is well accounted for by the line wing of Component B that was assigned to Component A, so the amount of emission is not significantly changed. This result might change if there is a large temperature difference between overlapping components, but that seems unlikely to occur in most scenarios.

The results for each velocity component were combined into maps of the whole Ridge shown in Figure 5.6 by adding N_{CO} along each line of sight and using a mass-weighted average for T_{kin} and n_{H_2} . We masked fits that were not well-constrained since our results from Appendix A2 showed that poorly constrained fits often were also not accurate. How well each parameter could be expected to be constrained varied largely, as shown in Appendix A2. T_{kin} and N_{CO} were both usually tightly constrained, while the fitted n_{H_2} is not as well constrained. This appears to be a reflection of how well the data at hand can inform the physical parameters rather than a reflection of how reliable the fitting process is. For both Figure 5.6 and deriving quantities in §5.4.2, we masked values of N_{CO} where the error was more than 80%, T_{kin} where the error was

more than 50%, and n_{H_2} where the error was more than 200%. We also masked values of T_{kin} that were less than 3 K, and values of n_{H_2} that rose sharply at the edges of clumps. In the case of the Molecular Ridge, we accomplished this by masking where n_{H_2} was greater than 10^4 cm^{-3} since values larger than that only occurred in edge pixels, but this would change if the range of fitted n_{H_2} had been higher.

After cutting pixels that had poorly constrained or unphysical fits, we combined fitted values from the runs with different R_{13} and filling factors. The reported values for T_{kin} , n_{H_2} , and N_{CO} are the mean of the best fit values from the $R_{13}=50$ and $R_{13}=100$ results and the 10% and 20% filling factor results. The upper and lower errors are from the highest and lowest values included in any of the fitted intervals (i.e. if T_{kin} is 26 ± 3 K for $R_{13}=50$ and 30 ± 5 K for $R_{13}=100$, the reported T_{kin} is 28^{+7}_{-5} K). When reporting a single error, we use the geometric mean of the upper and lower error. This results in the maps shown in Figure 5.6 sometimes having larger errors than the cutoffs described here.

5.4 Clump Definitions and Properties

5.4.1 Clump Definitions

We used `quickclump`⁵(Sidorin 2017), which is a Python clump-finding algorithm that is similar in methodology to `clumpfind` (Williams et al. 1994) and `DENDROFIND` (Wünsch et al. 2012). These clumps are based on the ALMA $^{13}\text{CO}(1-0)$ cube convolved to $45''$ to match the lowest resolution observation (the $^{12}\text{CO}(1-0)$ from MAGMA), and the input parameters used were `Nlevels=1000`, `Tcutoff=4 σ =1.4 K`, `dTleaf=4 σ =1.4 K`, and `Npixmin=5`. A map of the 32 clumps identified by `quickclump` is shown in

⁵<https://github.com/vojtech-sidorin/quickclump/>

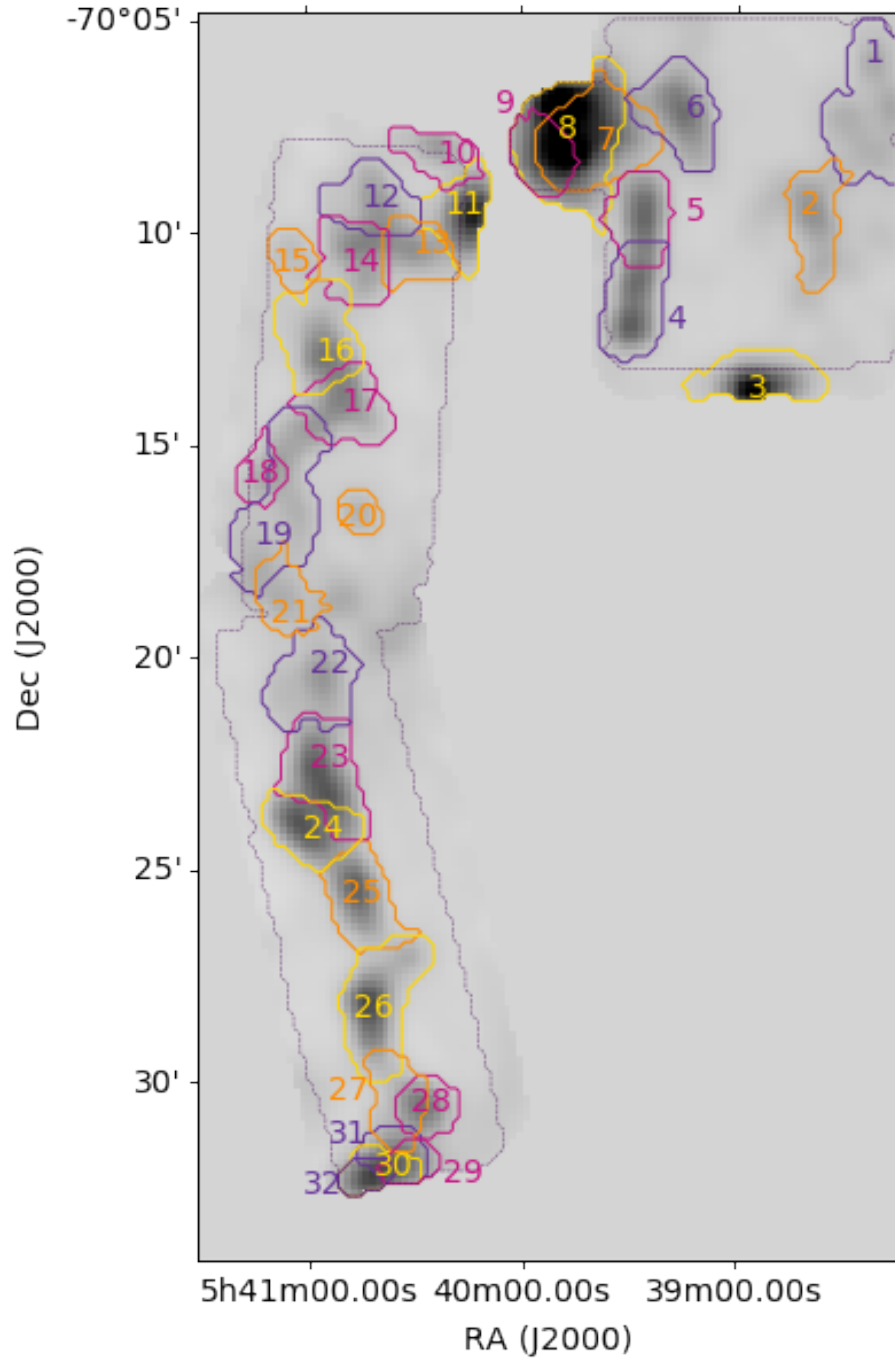


Fig. 5.7.— Projection of the 32 clumps identified by `quickclump` with identifying numbers. The grayscale is the integrated intensity of $^{13}\text{CO}(1-0)$ (same map as Figure 5.3). Overlapping clump borders indicate that the clumps overlap along the line of sight and are differentiated by their velocity structure. The dotted contour shows the common observational footprint of the four observed emission lines.

Figure 5.7 where they are also given identifying numbers. Each voxel in the data cube was assigned to at most a single clump, so overlapping clump borders in Figure 5.7 indicate that the clumps overlap along the line of sight and are differentiated by their velocity structure. The integrated line fluxes for each of these clumps and each observed line are given in Appendix A6, Table 8.13. Clumps 3, 10, and 11 do not have corresponding APEX data and so were not included in the RADEX fitting.

If any clump had more than 75% of the pixels masked in any parameter, we removed the entire clump from the following analysis; this was only the case for n_{H_2} in clumps 1, 20, 29, 30, and 32. We also discarded the fits of clumps 9, 15, and 21 because they had very few pixels with successful fits, the fitted parameters had large variations from pixel-to-pixel, and they were major outliers in later trends.

5.4.2 Derived Clump Properties

For each clump, we calculated the mass by summing the N_{CO} within the clump, then multiplying by the area of each pixel in cm^2 , the ratio of H_2/CO , and a factor of 1.3 to convert from H_2 mass to total mass based on cosmic abundances. The H_2/CO ratio is based on the values of R_{13} for the map (either 50 or 100), and $\text{H}_2/^{13}\text{CO}$ in the outer Milky Way, where the metallicity is similar to the LMC ($\sim 1/3$ of solar). This has been measured to be between $\text{H}_2/^{13}\text{CO} = 10^6$ (Heyer et al. 2001) and $\text{H}_2/^{13}\text{CO} = 3 \times 10^6$ (Brand & Wouterloot 1995), so we adopt $\text{H}_2/^{13}\text{CO} = 2 \times 10^6$ in this work. Previous works in the LMC have used similar values: $2\text{--}6 \times 10^6$ in Heikkilä et al. (1999), and 3×10^6 in Wong et al. (2019). We keep $\text{H}_2/^{13}\text{CO}$ constant rather than H_2/CO since ^{13}CO is optically thinner; ^{12}CO is usually optically thick, so the column density is more correlated with the ^{13}CO lines. Keeping $\text{H}_2/^{13}\text{CO}$ constant minimizes our dependence on the value assumed for R_{13} and instead leaves us with

the value of $\text{H}_2/^{13}\text{CO}$ as the major systematic uncertainty.

The final mass estimate for the clump is the mean of the masses from assuming $R_{13}=50$ and $R_{13}=100$ and assuming a filling factor of 10% and 20%. The upper and lower errors come from the full range included in the upper and lower errors on the two masses, as described in §5.3.2. When a single error is reported, it is the geometric mean of the upper and lower errors. To get temperatures and densities for each clump, we took the mass-weighted average of all pixels in the clump, with the upper and lower errors propagated through separately. The resulting clump masses are in the range $(3.4 - 35.5) \times 10^3 M_{\odot}$, temperatures are in the range 13–36 K, and densities are in the range 650–3940 cm^{-3} .

To measure the linewidths, we found the mass-weighted mean line profile using the map of N_{CO} . We then fit a Gaussian to this average line profile and report σ_v , not FWHM. The resulting linewidths are in the range 1.2–2.1 km s^{-1} . Shuffling the line profiles to a common central velocity first would change the linewidths by $\sim 10\%$.

To get the radius of the clumps, we fit ellipses to the half-light contour, giving us major and minor axes for the clump. We convert these FWHM values to σ of a gaussian profile ($\text{FWHM} = 2.35 \times \sigma$). The reported radius is the geometric mean of the major and minor axes.

We also compare the radii from the fitted ellipse to two other methods. One is finding the area of the clump within the half-light contour and then finding the radius of a circle with equivalent area. This is taken to be an effective FWHM, which is then converted to σ of a Gaussian profile. This results in an effective radius that is usually almost identical to the geometric mean of the fitted ellipse, differing by a factor of 0.99 on average.

The other method is to take the spatial second moment of the clump projected

along the axes of the fitted ellipse. This results in σ for the major and minor axes of the clump. The geometric mean of these major and minor radii is a factor of 0.72 lower on average than that fitted by the ellipse.

In the rest of this paper, we use the radius from the ellipse fitting method, and the error in the radius takes into account how non-circular the clump boundary is. The resulting σ_r are in the range 5–10 pc.

The values of all derived properties for each of the clumps with RADEX fits are given in Appendix A6, Table 8.14.

5.5 Associated YSOs

Current star formation in a molecular clump is expected to affect the gas in that clump - heating and changes in optical depth due to bulk gas motions and photodissociation will change the excitation conditions. In this section we describe the young stellar objects in the region, and how they are associated with CO clumps. In the next section, we will compare our non-LTE fitting to other techniques of determining gas properties, and will find that the presence of YSOs does not appear to affect one's ability to calculate gas properties using those different methods. In section 7, we will address the different question of whether the presence of the YSOs is correlated with changes in the physical properties.

5.5.1 YSO Selection

Complete infrared surveys of the LMC with Spitzer (SAGE Meixner et al. 2006) and Herschel (HERITAGE Meixner et al. 2013) enabled the uniform selection of massive young stellar objects (MYSOs) across the entire galaxy. Whitney et al. (2008, henceforth W08) used PSF-fit photometry from the SAGE legacy catalog and color

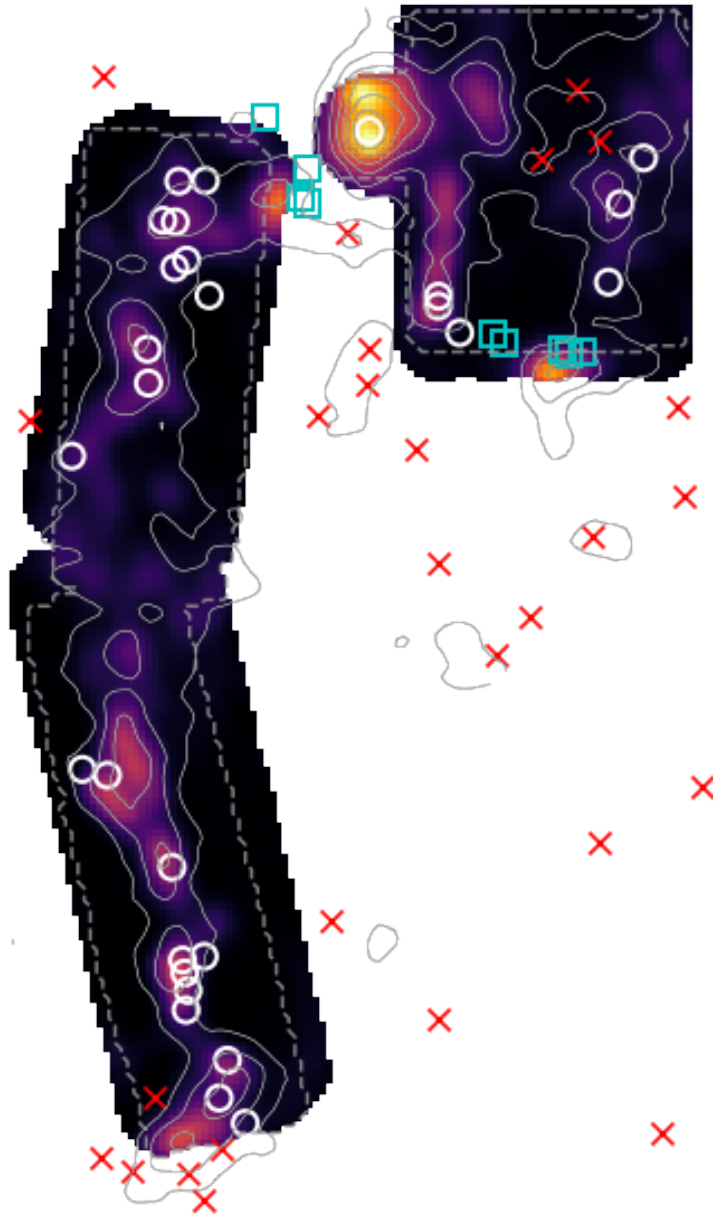


Fig. 5.8.— The 28 YSOs that were matched to CO clumps with RADEX fits are shown as white circles, the 9 YSOs that were matched to CO clumps that could not be fitted are shown as cyan squares, and the YSOs with no associated clump in $^{13}\text{CO}(1-0)$ are shown as red Xs. The color image is the integrated intensity of $^{13}\text{CO}(1-0)$ (same maps as Figure 5.3), which is the map that was used to assign clumps with `quickclump`. The contours are the integrated intensity of $^{12}\text{CO}(1-0)$ as in Figure 5.2.

selections between 1 and $10\mu\text{m}$, chosen to include MYSO models and exclude evolved and main sequence stars. Gruendl & Chu (2009, henceforth GC09) used aperture photometry of SAGE images and the $4.5\text{-}8.0\mu\text{m}$ color plus manual examination of images and source environment. Seale et al. (2014, henceforth S14) used $250\mu\text{m}$ PSF-fit photometry from the HERITAGE legacy catalog and $24\mu\text{m}$ emission to include MYSOs and resolved morphology to exclude background galaxies.

We combined the three existing MYSO catalogs in the Ridge region, first by matching all GC09 and W08 sources within $10''$ of each S14 source. This resulted in the same associations that S14 published with a $5''$ matching radius, with the addition of a single matched source J85.202523-70.17060. Visual examination of $8.0\text{-}24\text{-}250\mu\text{m}$ 3-color images prompted the removal of three S14 sources which were blended with other S14 sources - the guiding principle being to identify the sources that could be reliably photometered over a wide wavelength range.

The resulting list of 109 sources contains 24 MYSO candidates identified only from the shorter-wavelength lists GC09 and W08, 45 identified only from the longer-wavelength list S14, and 40 sources identified in multiple lists and matched. Next, we generated cutout images from $1.0\text{-}500\mu\text{m}$ and calculated aperture photometry at all bands.

The datasets used are 2MASS J, H, and K_s ($1.2\mu\text{m}$, $1.6\mu\text{m}$, $2.1\mu\text{m}$, angular resolution $\sim 2''$, aperture radius $3''$) (Skrutskie et al. 2006), SAGE IRAC bands 1-4 (3.6 , 4.5 , 5.8 , and $8.0\mu\text{m}$, resolution $\sim 2''$, aperture radius $3''$) and MIPS $24\mu\text{m}$ and $70\mu\text{m}$ (resolution $6''$, $18''$, aperture radius $9''$, $18''$), HERITAGE PACS 110 and $170\mu\text{m}$ (resolution $8''$, $13''$, aperture radius $11''$, $18''$), and HERITAGE SPIRE $250, 350$, $500\mu\text{m}$ (resolution $18''$, $25''$, $36''$, aperture radius $18''$, $25''$, $37''$). A local annular background was subtracted from each flux, and the uncertainty of the flux measurement is calculated

from the standard deviation of values in the annulus.

We combined the published photometry with the new aperture photometry by visually inspecting the cutout images and spectral energy distribution (SED) of the two. For most sources, the published photometry agreed with the new aperture photometry within uncertainties, so the average was used. For sources and bands in which the published photometry was lacking, the aperture photometry smoothly filled in the SED.

The Spitzer MIPS $70\mu\text{m}$ resolution of $18''$ is significantly worse than the neighboring points in our spectral energy distributions (Spitzer MIPS $24\mu\text{m}$ and Herschel PACS $100\mu\text{m}$ at $\sim 6''$). Consequently, the $70\mu\text{m}$ flux density was clearly affected by blending for many sources, so was used as an upper limit in the subsequent SED fitting. If the image cutouts were confused, or the aperture and published photometry were very discrepant for a given source and band, we either eliminated that band from the fitting or used the largest photometric value as an upper limit.

5.5.2 YSO Fitting

We fit the YSO SEDs with the Robitaille (2017) grid of single-YSO dust radiative transfer models⁶ and the Robitaille et al. (2007) χ^2 fitting code⁷. Following many other studies (e.g. Carlson et al. 2012; Chen et al. 2010), we used a minimum uncertainty in each band of 10%, and calculated χ^2 for every model. Central sources in the Robitaille (2017) model grid are parameterized by the radius and temperature of the YSO, R_\star and T_\star . We interpolated the $Z=0.004$ PARSEC stellar evolutionary models (Bressan et al. 2012) that include the PMS phase⁸ to determine the mass of

⁶<https://zenodo.org/record/166732>

⁷<https://sedfitter.readthedocs.io/en/stable/index.html>

⁸<http://stev.oapd.inaf.it/cgi-bin/cmd>

the YSO, M_\star , and age for each Robitaille YSO model. The Robitaille circumstellar dust distribution is that of a rotating flattened toroid in analytical form Ulrich (1976) parameterized by centrifugal radius R_C and scaling density ρ_0 . Using the central source mass assigned to each model, the envelope accretion rate \dot{M} is a function of M_\star , ρ_0 , and R_C (Robitaille 2017, equation 5). The envelope accretion rate relative to the central source mass is a measure of evolutionary stage under the assumption that mean accretion rate decreases with time for protostars.

Finally, we assigned M_\star and \dot{M} to each source in the Ridge by marginalizing the model probability distributions over all other model parameters and measuring the first and second moments of each 1D probability distribution. We visually inspected the 2D probability distribution of M_\star and \dot{M} for each source and verified that the second moments that we are using as uncertainties for those parameters do indeed span the range of well-fitting models, even in the minority of cases where the probability distribution is not single-peaked. A table of M_\star and \dot{M} for each YSO that was matched with a CO clump is given in Appendix A6, Table 8.15.

It is important to recognize that despite the use of a specific set of models, fundamentally the quantities being measured and parameterized are the total luminosity of the central source, which is tightly correlated with the derived M_\star , and the amount of dust extinction around that central source, which is highly correlated with the envelope accretion rate \dot{M} (except for more evolved sources that have little envelope in which case the disk has more of an effect on the SED).

Comparing the detection limits of the SAGE and Herschel surveys to all of the Robitaille (2017) models, we expect that all protostars with a mass above $6 M_\odot$ will be detected. At $2.5 M_\odot$, half of all protostars would be detected, though it is possible to detect some protostars down to $1 M_\odot$, depending on their evolutionary state.

5.5.3 YSO Matching

We then matched the YSOs to CO clumps by eye, assigning them to a clump only if their positions coincided with CO emission (see Figure 5.8). In cases where the YSO overlapped with strong emission from more than one clump, it was assigned to the clump that was brightest in its location. This process resulted in 37 of the YSOs being matched to CO clumps in the Molecular Ridge. Of these 37, nine were associated with the three clumps that do not have data for $^{12}\text{CO}(2-1)$ and $^{13}\text{CO}(2-1)$ from APEX (clumps 3, 10, and 11) and so could not be included in all parts of the analysis. Table 8.15 in Appendix A6 includes the number of the clump assigned to each of these 37 YSOs.

5.6 Comparing RADEX Fitting to Other Methods

5.6.1 LTE Method

We compared the clump masses derived by the RADEX fitting to the results of LTE assumptions with both the (1-0) lines and the (2-1) lines. For LTE, we use the peak of the ^{12}CO line for each pixel, divided by a beam filling factor of 10% or 20% that we used in the RADEX fitting (results for each were combined after as described in §5.3.1), to get T_{ex} :

Table 5.2: Comparison of different methods of determining mass and temperature.

	M/M_{RF}	$T_{\text{ex}}/T_{\text{kin,RF}}$
LTE (1-0)	1.66 ± 0.19	0.71 ± 0.10
LTE (2-1)	0.55 ± 0.10	0.78 ± 0.15
X_{CO}	1.20 ± 0.33	NA

Note: These values are the average of the ratios for all the clumps that were fit with these methods and the standard deviation among the clumps. M_{RF} , $T_{\text{kin,RF}}$ are the values derived from the RADEX fitting as described in §5.3.2.

$$T_B = T_{ul}(1 - e^{-\tau_\nu}) \left[\frac{1}{e^{T_{ul}/T_{ex}} - 1} - \frac{1}{e^{T_{ul}/T_{bg}} - 1} \right], \quad (5.4)$$

where we assume optically thick ^{12}CO , so $e^{-\tau_\nu} \approx 0$. T_B is the peak brightness temperature for the pixel divided by the filling factor, $T_{ul} = 5.532$ K for $^{12}\text{CO}(1-0)$, $T_{ul} = 11.06$ K for $^{12}\text{CO}(2-1)$, and $T_{bg} = 2.73$ K. Then, we calculate the optical depth of ^{13}CO from

$$\tau_\nu = -\ln \left[1 - \frac{T_B}{T_{ul}} \left[\frac{1}{e^{T_{ul}/T_{ex}} - 1} - \frac{1}{e^{T_{ul}/T_{bg}} - 1} \right]^{-1} \right] \quad (5.5)$$

where now T_B is from $^{13}\text{CO}(1-0)$ divided by the filling factor of 10%, $T_{ul} = 5.289$ K for $^{13}\text{CO}(1-0)$, and $T_{ul} = 10.58$ K for $^{13}\text{CO}(2-1)$. Then, the column density of ^{13}CO is

$$N_{13} = \frac{8\pi\nu_0^2 Q}{c^2 A_{ul} g_u} \frac{1}{1 - e^{-T_{ul}/T_{ex}}} \int \tau_\nu d\nu \quad (5.6)$$

where we use $Q = \frac{T_{ex}}{B_0} + \frac{1}{3}$ and $B_0 = 2.644$ K for ^{13}CO . We adopt $\text{H}_2/^{13}\text{CO} = 2 \times 10^6$ and sum over all pixels in the clump to get masses from the LTE assumptions. A comparison of the results using the (1-0) and (2-1) lines against our RADEX-fitting method is given in Table 5.2.

Using (2-1) lines with the LTE assumptions results in a much lower mass estimate and a lower T_{ex} estimate than the RADEX-fitted T_{kin} (by average factors of 0.55 ± 0.10 and 0.78 ± 0.15 , respectively). A low mass estimate from LTE calculations is expected if ^{13}CO is sub-thermally excited and $T_{\text{ex}}^{13} < T_{\text{ex}}^{12}$: The T_{ex} derived from ^{12}CO is too high for ^{13}CO , which makes the optical depth of ^{13}CO underestimated, and so the column density and mass are underestimated (e.g. Castets et al. 1990; Padoan et al. 2000; Heyer & Dame 2015). The temperature estimate being lower than the non-LTE

T_{kin} could mean that ^{12}CO is also sub-thermally excited, but less so than ^{13}CO .

The mass estimate when using the (1-0) lines is higher than our fitted RADEX (by an average factor of 1.66 ± 0.19), which is harder to explain though not unprecedented (Indebetouw et al. 2020). One way this could happen is if the ^{12}CO is not actually optically thick, which would make the LTE T_{ex} estimate too low and shift the optical depth estimate higher. This could be exacerbated if the beam filling factor we use is too large, which would also artificially lower the measured excitation temperature. The non-linearity of the LTE equations means that an underestimated T_{ex} due to a high filling factor would cause a larger shift to high column density than is corrected for with the filling factor being multiplied back in at the end. This filling factor was also used in the RADEX fitting, but the non-linearity of that is even more extreme, making it difficult to predict how much it would affect our results relative to the LTE calculations.

5.6.2 X_{CO} Method

We also include in Table 5.2 a comparison of the mass from a typical Milky Way value of $X_{\text{CO}} = 2 \times 10^{20} \text{ cm}^2 / (\text{K km s}^{-1})$ (Bolatto et al. 2013). These masses are on average slightly higher than those fit with RADEX—though they are consistent within the deviation between clumps (the average factor is 1.20 ± 0.33).

We fit the linear relation between the RADEX-fitted total N_{H_2} and the summed $^{12}\text{CO}(1-0)$ flux of the clump in units of K km s^{-1} (W_{CO}), both divided by the number of pixels in the clump with N_{H_2} solutions (Figure 5.9a). The linear trend was fit to the linear values, not in log space. Values of individual pixels within the clumps with N_{H_2} solutions are also shown behind the clump average points. The slope of this trend is the X_{CO} conversion factor ($N_{\text{H}_2} = X_{\text{CO}} \times W_{\text{CO}}$). This relation is subject to

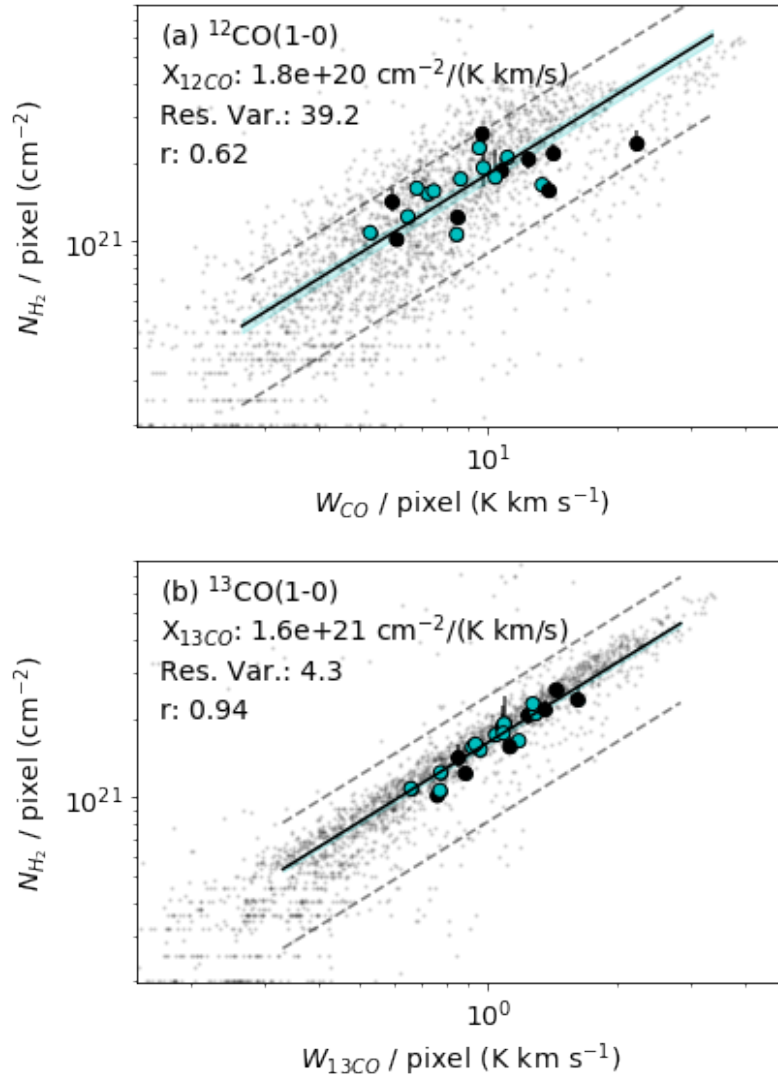


Fig. 5.9.— Fitted values of N_{H_2} per pixel against the integrated flux per pixel of $^{12}\text{CO}(1-0)$ (top) and $^{13}\text{CO}(1-0)$ (bottom). Blue circles indicate clumps with at least one associated YSO, while the black circles are clumps without any associated YSOs. The small black points show the values of individual pixels. The fitted linear trend (fitted linearly, not in log space as is plotted here) corresponds to a value of $X_{CO} = (1.8 \pm 0.1) \times 10^{20} \text{ cm}^{-2}/(\text{K km s}^{-1})$ and $X_{13\text{CO}} = (1.6 \pm 0.03) \times 10^{21} \text{ cm}^{-2}/(\text{K km s}^{-1})$, respectively. The dotted lines on either side show the systematic range from the uncertainty in the ratio $H_2/^{13}\text{CO}$ used to get N_{H_2} . ^{13}CO has a tighter trend with N_{H_2} with a residual variance of 4.3 and correlation coefficient of 0.94 while ^{12}CO has a residual variance of 39 and correlation coefficient of 0.62, suggesting that the $X_{13\text{CO}}$ factor may be a better tool for estimating mass than the typical X_{CO} .

the systematic error in the ratio $H_2/^{13}CO$ used in §5.4.2. We use $H_2/^{13}CO = 2 \times 10^6$ with a range of $(1 - 3) \times 10^6$ (Brand & Wouterloot 1995; Heikkilä et al. 1999; Heyer et al. 2001). A higher $H_2/^{13}CO$ value results in higher derived masses and a larger derived X_{CO} .

Fitting a linear relation results in a value for X_{CO} of $(1.81 \pm 0.1) \times 10^{20} \text{ cm}^{-2}/(\text{K km s}^{-1})$, and taking into account the full systematic range due to the uncertainty in $H_2/^{13}CO$ and the error in the fitted X_{CO} results in a value of X_{CO} in the range $(0.85 - 2.87) \times 10^{20} \text{ cm}^{-2}/(\text{K km s}^{-1})$, shown in Figure 5.9a. This is lower than we expect for the Ridge since the LMC has a metallicity of 1/3 solar and has been estimated to have a value closer to $X_{CO} \sim 4 \times 10^{20} \text{ cm}^{-2}/(\text{K km s}^{-1})$ (Hughes et al. 2010; Bolatto et al. 2013). This discrepancy could be because the non-LTE fitting is more accurate than previous measures or could be due to an underestimate of the $H_2/^{13}CO$ ratio; a ratio of $H_2/^{13}CO \sim 4 \times 10^6$ would make our fitted X_{CO} consistent with other estimates for the LMC.

We also perform this fitting with the summed $^{13}CO(1-0)$ intensities to get a value of $X_{^{13}CO}$ (Figure 5.9b). We find a value of $X_{^{13}CO} = (1.62 \pm 0.03) \times 10^{21} \text{ cm}^{-2}/(\text{K km s}^{-1})$, and taking into account the systematic range of $H_2/^{13}CO = (1 - 3) \times 10^6$ and the error in the fitted $X_{^{13}CO}$ results in a $X_{^{13}CO}$ range of $(0.80 - 2.48) \times 10^{21} \text{ cm}^{-2}/(\text{K km s}^{-1})$.

The relation between N_{H_2} and ^{13}CO emission is tighter than the relation of N_{H_2} with ^{12}CO . The fitted X_{CO} has a 5.8% error and a residual variance of 39, while the fitted $X_{^{13}CO}$ has a 1.9% error and a residual variance of 4.3. Calculating a Pearson correlation coefficient for the two trends results in a value of $r = 0.62$ for X_{CO} and $r = 0.94$ for $X_{^{13}CO}$. This shows that using a $X_{^{13}CO}$ would be a more precise method of determining mass than X_{CO} , which makes sense since ^{13}CO is more optically thin

and so can better trace the quantity of gas, while ^{12}CO is usually optically thick.

Another possible source of scatter for ^{12}CO could be the faint pixels that do not have corresponding ^{13}CO emission. Since detections in three of the four lines were required before the fitting proceeded, there are several pixels that have $^{12}\text{CO}(1-0)$ emission above 5σ but no emission in two of the other lines. These are the faintest of the pixels and so would have correspondingly low N_{CO} , so including them would not make large changes to the reported N_{H_2} or W_{CO} , but could account for some of the scatter.

We also show in both panels of Figure 5.9 the values of N_{H_2} and W_{CO} for individual pixels. In both cases, the pixels have shallower slopes than the clump-averaged values and fitting the pixels instead would result in a value of $X_{\text{CO}} = (1.13 \pm 0.01) \times 10^{20} \text{ cm}^{-2}/(\text{K km s}^{-1})$ and $X_{^{13}\text{CO}} = (1.32 \pm 0.01) \times 10^{21} \text{ cm}^{-2}/(\text{K km s}^{-1})$. For X_{CO} , the pixels show a stronger correlation between W_{CO} and N_{H_2} than the clump-averaged values, with a correlation coefficient of $r = 0.74$. In contrast, the clump-averaged values for $X_{^{13}\text{CO}}$ have a stronger trend than the pixels, which have a correlation coefficient of $r = 0.89$. We would expect the clump-averaged values to show a stronger trend since the X_{CO} method works best when integrating over variations in physical conditions (Bolatto et al. 2013).

5.6.3 Diagnostic Line Ratios

Isotopologues

Ratios of isotopologues (e.g. $^{13}\text{CO}/^{12}\text{CO}$) can trace volume density in the case where one line is optically thick and the other line is sub-thermally excited (Nishimura et al. 2015). We examine how well the ratios of the ^{13}CO and ^{12}CO lines' total fluxes in K km s^{-1} predict the fitted RADEX volume density, n_{H_2} . Figure 5.10 shows that the

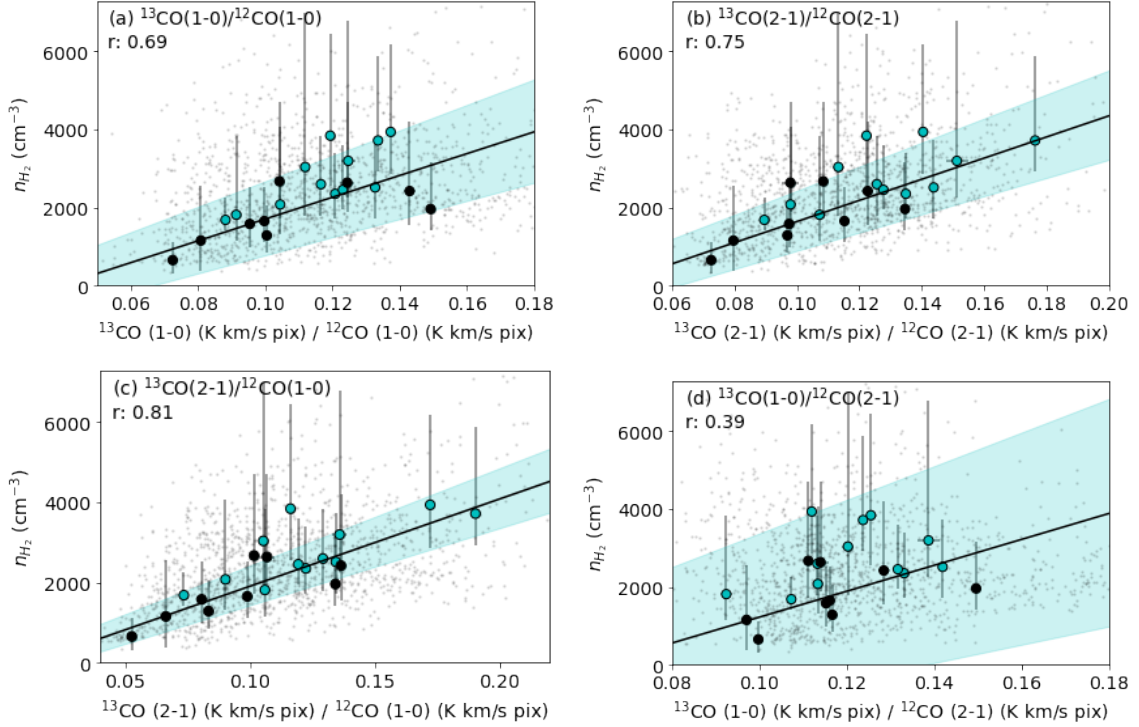


Fig. 5.10.— Volume density fitted by RADEX plotted against ratios of ^{13}CO to ^{12}CO . The ratio with the strongest correlation is $^{13}\text{CO}(2-1)/^{12}\text{CO}(1-0)$ in panel (c), with a residual variance of 0.18 and Pearson correlation coefficient of $r = 0.81$. The ratios $^{13}\text{CO}(1-0)/^{12}\text{CO}(1-0)$ and $^{13}\text{CO}(2-1)/^{12}\text{CO}(2-1)$ both also show strong trends with residual variances of 0.32 and 0.24, respectively, and $r = 0.69$ and $r = 0.75$, respectively. The ratio of $^{13}\text{CO}(1-0)/^{12}\text{CO}(2-1)$ shows very little trend with a residual variance of 0.57 and $r = 0.39$. Plot symbols are the same as in Figure 5.9. The blue points indicate clumps with at least one associated YSO, demonstrating that YSO presence does not appear to affect the trends at all.

strongest combination of lines to predict n_{H_2} is $^{13}\text{CO}(2-1)/^{12}\text{CO}(1-0)$, with a residual variance of 0.18 and Pearson correlation coefficient of $r = 0.81$. This makes sense since we expect $^{13}\text{CO}(2-1)$ to be the most sub-thermally excited of the lines, especially from the LTE comparison in §5.6.1, and we expect $^{12}\text{CO}(1-0)$ to be the most optically thick.

The weakest predictor of n_{H_2} is $^{13}\text{CO}(1-0)/^{12}\text{CO}(2-1)$, with a residual variance of 0.57 and $r = 0.39$. $^{13}\text{CO}(1-0)/^{12}\text{CO}(1-0)$ and $^{13}\text{CO}(2-1)/^{12}\text{CO}(2-1)$ have residual variances of 0.32 and 0.24, respectively, and $r = 0.69$ and $r = 0.75$, respectively. All of these combinations do show a positive trend, indicating that $^{13}\text{CO}/^{12}\text{CO}$ is indeed a good diagnostic of gas density in this physical regime, where the ^{13}CO is sub-thermally excited. In areas of higher temperature and density where all lines become thermalized, this relation would likely no longer hold.

The fitted n_{H_2} has asymmetrical error bars, and when fitting the trends in Figure 5.10, we simply use the mean of the upper and lower errors. This results in overestimated errors (Barlow 2004), but a proper treatment of the errors would require a computationally rigorous analysis to properly account for the non-gaussian nature of the n_{H_2} probability distribution. We decided to report the simpler analysis with the acknowledgement that the errors are overestimated. Since the mean errors are usually lower than the upper errors and larger than the lower errors, the fit is also likely biased towards lower values of n_{H_2} .

In all plots, we indicate the clumps that have at least one associated YSO as blue instead of black. Although YSOs could potentially affect the excitation, we do not see any indication that the presence of YSOs affects our ability to recover and understand that excitation, using different methods.

We also show in Figure 5.10 the values for individual pixels. In all panels, the correlations of the pixels is much weaker than that of the clump-averaged values,

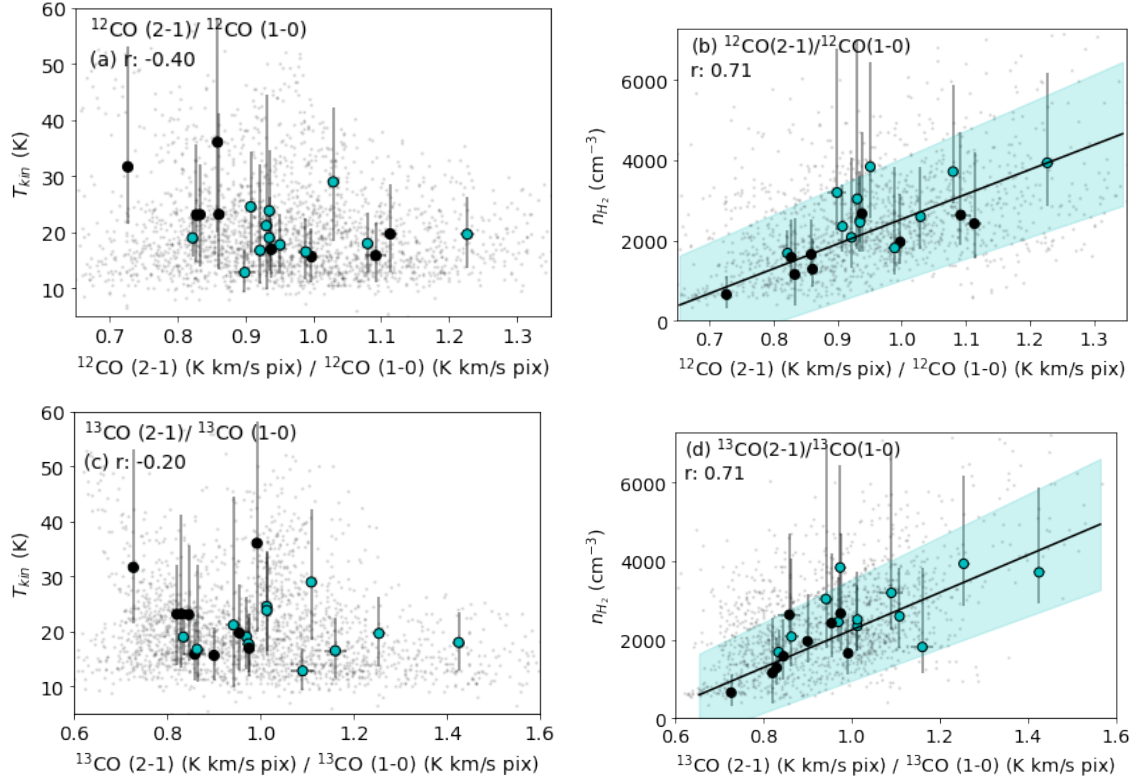


Fig. 5.11.— Kinetic temperature (left column) and RADEX-fitted density (right column) against ratios of upper and lower transitions ($^{12}\text{CO}(2-1)/^{12}\text{CO}(1-0)$ above and $^{13}\text{CO}(2-1)/^{13}\text{CO}(1-0)$ below). There is not a strong correlation with T_{kin} for either ^{12}CO or ^{13}CO , suggesting that such line ratios are not a good diagnostic of kinetic temperature in this physical regime. They do, however, show a correlation with density, which has been fitted with a linear trend. The two ratios have a similar correlation, both with $r = 0.71$ and residual variances of 0.22 and 0.25, respectively, though this is not as strong as the correlation of n_{H_2} with $^{13}\text{CO}(2-1)/^{12}\text{CO}(1-0)$ (Figure 5.10c). Plot symbols are the same as in Figure 5.9. Blue points indicate clumps with at least one associated YSO, which shows that YSO presence seems to have no affect on these trends, except that all clumps that have $^{13}\text{CO}(2-1)/^{13}\text{CO}(1-0) > 1$ also have at least one associated YSO.

having correlation coefficients of 0.35, 0.43, 0.53, and 0.11, respectively, for panels (a) through (d). This indicates that these trends are most accurate when averaged over the whole clump.

Excitation Levels

Ratios of upper to lower excitation levels of CO (e.g. $^{12}\text{CO}(2-1)/^{12}\text{CO}(1-0)$) scale with excitation temperature and density when both lines are optically thin, and the ratio approaches unity as the lines get increasingly optically thick (Sakamoto 1994; Nishimura et al. 2015; Peñalosa et al. 2017). Figure 5.11 show the measured ratios of the total flux in $\text{K km s}^{-1} \text{ pix}$ for $^{12}\text{CO}(2-1)/^{12}\text{CO}(1-0)$ and for $^{13}\text{CO}(2-1)/^{13}\text{CO}(1-0)$ plotted against the RADEX-fitted T_{kin} and n_{H_2} .

The plots of T_{kin} against $^{12}\text{CO}(2-1)/^{12}\text{CO}(1-0)$ and $^{13}\text{CO}(2-1)/^{13}\text{CO}(1-0)$ in Figure 5.11 do not show a strong linear trend ($r = -0.40$ and $r = -0.20$, respectively). This could be because the line ratios do not correlate with the excitation temperature, or because the excitation temperature is not correlated with the kinetic temperature in these clumps. We have seen in §5.6.1 and §5.6.3 that the lines are likely sub-thermally excited, which would be consistent with the excitation temperature not tracing the kinetic temperature as well.

The ratios of excitation levels seem much more correlated with n_{H_2} than T_{kin} . For these, we were able to fit a linear relation as shown in Figure 5.11. The two ratios have a similar correlation, both with $r = 0.71$ and residual variances of 0.22 and 0.25, respectively, though neither are as good a tracer as the $^{13}\text{CO}(2-1)/^{12}\text{CO}(1-0)$ relation from Figure 5.10c.

The ratios of (2-1)/(1-0) shown in Figure 5.11 are greater than unity for many of the clumps. This could happen if the lines are optically thin and the gas is hot,

allowing the (2-1) lines to be excited. This is consistent with the results of the LTE mass estimate with (1-0) lines being an overestimate, which would require optically thin lines. The clumps with the high (2-1)/(1-0) ratios may have an embedded source of internal heating.

As in Figure 5.10, we indicate the clumps that have at least one associated YSO as blue instead of black. Again in these plots, the presence of YSOs seems to have no strong relation to the trends, except that all clumps that have $^{13}\text{CO}(2-1)/^{13}\text{CO}(1-0) > 1$ do have at least one associated YSO. This is not the case for $^{12}\text{CO}(2-1)/^{12}\text{CO}(1-0)$.

We also show in Figure 5.11 the values for individual pixels. In all panels, the correlations of the pixels are much weaker than that of the clump-averaged values, having correlation coefficients of -0.15, 0.49, -0.01, and 0.52, respectively, for panels (a) through (d). This indicates that these trends are most accurate when averaged over the whole clump.

Dense Gas Tracer, CS(2-1)

CS is a commonly observed dense gas tracer in molecular clouds with an optically thin critical density of 10^5 cm^{-3} at 20 K for CS(2-1) (Shirley 2015). We examine here how the ratios of CS(2-1) to CO correlate with the RADEX-fitted density.

Figure 5.12 shows the ratio of the integrated intensities across a clump in units of $\text{K km s}^{-1} \text{ pix}$ of CS(2-1) to $^{12}\text{CO}(1-0)$ and CS(2-1) to $^{13}\text{CO}(1-0)$. For both ratios, there is a weak linear trend with n_{H_2} , with correlation coefficients of $r = 0.40$ and $r = 0.28$ for the ratio with $^{12}\text{CO}(1-0)$ and $^{13}\text{CO}(1-0)$, respectively. This demonstrates that CS(2-1)/ $^{12}\text{CO}(1-0)$ may be a slightly better indicator of density than CS(2-1)/ $^{13}\text{CO}(1-0)$.

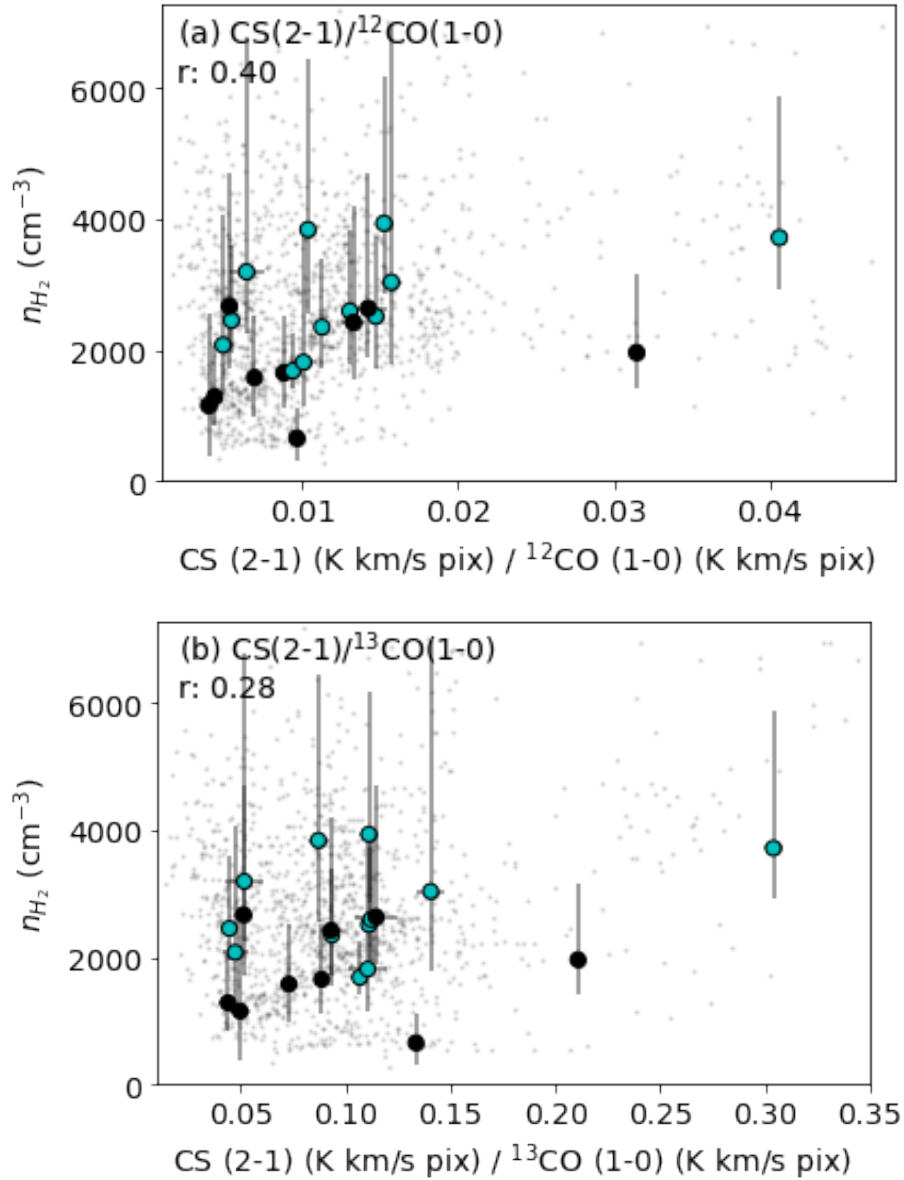


Fig. 5.12.— Density fitted by RADEX against ratios of CS(2-1) to $^{12}\text{CO}(1-0)$ (*top*) and to $^{13}\text{CO}(1-0)$ (*bottom*). CS(2-1)/ $^{12}\text{CO}(1-0)$ has a stronger correlation with density than CS(2-1)/ $^{13}\text{CO}(1-0)$ with correlation coefficients of $r = 0.40$ and $r = 0.28$, respectively. The small black points show the values of individual pixels, which have slightly weaker trends than the clump-averaged values. Despite the high critical density of CS, neither of the ratios are as strong as most of the trends of density with CO line ratios shown in Figures 5.10 and 5.11. This could be due to molecular abundance variations or because of the scales traced by the CO in the RADEX fitting. Plot symbols are the same as in Figure 5.9.

We also show in Figure 5.12 the values of individual pixels, which have slightly weaker correlations with $r = 0.35$ and $r = 0.26$, respectively. We also indicate clumps that have at least one associated YSO as blue instead of black circles, which shows that YSO presence appears to have no effect on these trends.

Despite the high critical density of CS, Figure 5.12 suggests that CS(2-1) cannot predict the density as strongly as most ratios of ^{13}CO to ^{12}CO shown in Figure 5.10 or the ratios of excitation levels shown in Figure 5.11b and 5.11d. This could be because of variations in molecular abundance that influence the strength of the CS emission in addition to the density. This could also be because the RADEX fitting is primarily tracing the CO density at scales of 1-2 pc, while the CS emission may be coming from more compact cores within the clumps. With higher resolution multiline observations and parameter fitting, we may begin to see more correlation between the fitted density and the CS emission.

5.7 Trends with Star Formation

5.7.1 Trend with Fitted Density

We looked for correlations between any of the derived quantities from §5.4.2 and star formation. Our measures of star formation for a clump are the number of YSOs associated with it and their masses (§5.5). We use a Pearson correlation coefficient, r , to evaluate how strong a relation there is between the two variables, though we acknowledge a linear trend may not best describe the expected relationship between the variables. For that reason, we are more interested in the relative values of the correlation coefficients than the absolute values.

By far the strongest correlation of YSO presence is with the mass-weighted RADEX-

fitted volume density, n_{H_2} . The density appears correlated with the number of YSOs associated with each clump ($r = 0.60$), the total mass of all YSOs associated with the clump ($r = 0.62$), and even the average mass of YSO associated with the clump ($r = 0.63$). Figure 5.13 shows that clumps fit with a higher n_{H_2} have more associated YSOs, and more massive associated YSOs, and that clumps with lower values of n_{H_2} have no associated YSOs, or less massive YSOs.

5.7.2 Other Common Star Formation Tracers

We investigated whether or not a threshold or trend appears in other, more commonly or easily observed properties: the mean volume density ($\bar{n} = 3M/4\pi R^3 \mu m_{\text{H}_2}$, corrected to match the filling factor scale of n_{H_2} by dividing \bar{n} by $f^{3/2}$), the ratio of the integrated intensities of CS(2-1) to $^{12}\text{CO}(1-0)$, the gas surface density ($\Sigma = M/\text{Area}$), and the virial parameter, α_{vir} . The gas surface density is directly proportional to N_{H_2} and A_V , which are cited as showing star formation thresholds (i.e. Kennicutt 1998; Lada et al. 2010). The relation between these four parameters and the total mass of associated YSOs, as well as with the fitted density, n_{H_2} , are shown in Figure 5.14.

Mean Density

The mean density (Figures 5.14a and 5.14b) does not show much of a trend with the total mass of associated YSOs ($r = 0.37$) and shows almost no trend with the fitted density ($r = 0.06$). Figure 5.14b shows a line indicating a one-to-one correlation between mean density and fitted density, and the fitted density is almost always larger than the mean density. This is expected since the mean density is an average over the whole clump, while the fitted density is a mass-weighted average. Since more of the clump's mass is in the denser regions, the fitted density is higher. The mass

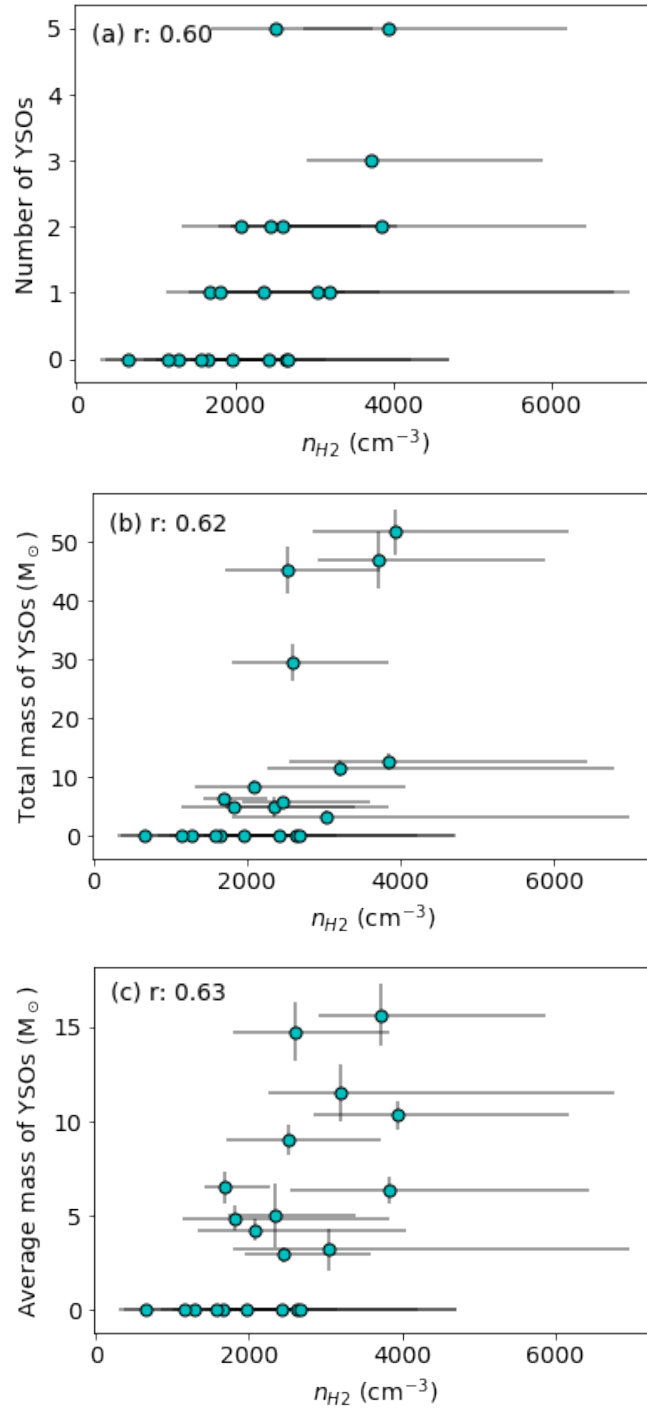


Fig. 5.13.— The number of YSOs associated with a given clump (*top*), their total mass (*middle*), and their average mass (*bottom*) plotted against the RADEX-fitted volume density, n_{H_2} . These three trends have correlation coefficients of 0.60, 0.62, and 0.63, respectively.

weighting also means the fitted density depends on the internal structure and density profile of the clump, while the mean density contains none of that information.

Dense Gas Ratio

The ratio of dense gas tracers with critical densities above 10^4 cm^{-3} (e.g. HCN, HCO^+ , CS) to CO is often used as a tracer of the star formation rate in galaxies (Gao & Solomon 2004; Wang et al. 2011; Zhang et al. 2014; Li et al. 2021). In §5.6.3, we examined how ratios of CS(2-1) to CO correlated with RADEX-fitted density and found that CS(2-1)/ $^{12}\text{CO}(1-0)$ shows a slightly stronger correlation with n_{H_2} than CS(2-1)/ $^{13}\text{CO}(1-0)$, though neither ratio is as good a predictor of n_{H_2} as most of the ratios between CO lines (§5.6.3 and §5.6.3).

In Figures 5.14c and 5.14d, we see that the ratio of CS(2-1)/ $^{12}\text{CO}(1-0)$ shows the strongest correlation with the RADEX-fitted density of the star formation-tracing parameters ($r = 0.40$) and an even stronger correlation with associated YSO presence ($r = 0.47$), although this is still not as strong a correlation as with fitted density (Figure 5.13). This measurement is difficult to relate to other observations since it cannot be directly compared with dense gas ratios of other common dense gas tracers, such as HCN or HCO^+ .

The two clumps in Figure 5.14c and 5.14d that have much larger CS(2-1)/ $^{12}\text{CO}(1-0)$ ratios than the rest are clumps 4 and 5, which have particularly bright CS(2-1) emission in Figure 5.2. It is not immediately clear what is causing this enhanced CS(2-1) emission in the region, since it does not appear particularly unique in any of the fitted physical conditions (see Figure 5.6). The enhanced CS emission could be related to variations in the molecular abundance of CS across the region. It also could be that the region would appear more unique at higher resolutions where dense

cores would be detected and not convolved with the surrounding more diffuse gas.

Surface Density

Gas surface density, Σ_{gas} , is one of the most commonly used star formation threshold measures. It is correlated with star formation rate via the Kennicutt-Schmidt Relation on several scales (see reviews in Elmegreen 2018; Kennicutt & Evans 2012). One of the most commonly cited star formation thresholds is $A_V > 8$ from Lada et al. (2010), which corresponds to $\Sigma_{\text{gas}} > 116 M_{\odot} \text{ pc}^{-2}$ in their sample of Milky Way clouds.

In the LMC, Dobashi et al. (2008) found a global relation of $\frac{A_V}{N_H} = 1.7 \times 10^{-22} \text{ mag} / \text{H cm}^2$, although this value varies from $2.5 \times 10^{-22} \text{ mag} / \text{H cm}^2$ near 30 Dor, to $0.63 \times 10^{-22} \text{ mag} / \text{H cm}^2$ near the outskirts of the LMC. Assuming that all the hydrogen in the Ridge is molecular, a threshold of $A_V > 8$ corresponds to $N_{H_2} > 2.4 \times 10^{22} \text{ cm}^{-2}$, based on the global estimate, and this in turn corresponds to a gas surface density of $\Sigma_{\text{gas}} > 490 M_{\odot} \text{ pc}^{-2}$, with a lower limit of $\Sigma_{\text{gas}} > 330 M_{\odot} \text{ pc}^{-2}$ based on $\frac{A_V}{N_H}$ measured in the outskirts of the LMC.

The threshold of $A_V > 8$ from Lada et al. (2010) was measured on $\sim 0.1 \text{ pc}$ scales, so at $45''$ (11 pc) resolution, a threshold of $490 M_{\odot} \text{ pc}^{-2}$ would correspond to $\sim 4.5 M_{\odot} \text{ pc}^{-2}$ if all of the emission is coming from compact sources with no diffuse component. The smallest gas surface density measured for a clumps in the Ridge with an associated YSO is $\Sigma = 10 M_{\odot} \text{ pc}^{-2}$, and since a diffuse envelope is likely, this would be consistent with the $A_V > 8$ star formation threshold on smaller scales.

The surface density shows the weakest correlation with the presence of YSOs ($r = 0.06$) and weak, surprisingly negative correlation with fitted density as well (-0.31) (Figures 5.14e and 5.14f). There are clumps with high surface density and no associated YSOs, and clumps with low surface density in the Ridge that do have

associated YSOs.

Virial Parameter

The last metric we considered is the virial parameter, α_{vir} , calculated as

$$\alpha_{\text{vir}} = \frac{5\sigma_v^2 R}{GM}, \quad (5.7)$$

where R in this equation is 1.91 times the σ_R reported in Table 8.14 to get an “effective radius” (Solomon et al. 1987). This parameter indicates whether or not the clumps are in virial equilibrium. The correlation between α_{vir} and associated YSOs is weak, but negative as we would expect, since clumps with a high α_{vir} are less prone to collapse ($r = -0.26$; Figure 5.14g). Clumps with a high α_{vir} have a few associated YSOs, but clumps with a low α_{vir} seem to have the most massive associated YSOs. Plotting α_{vir} against fitted density shows almost no trend ($r = -0.1$; Figure 5.14h)).

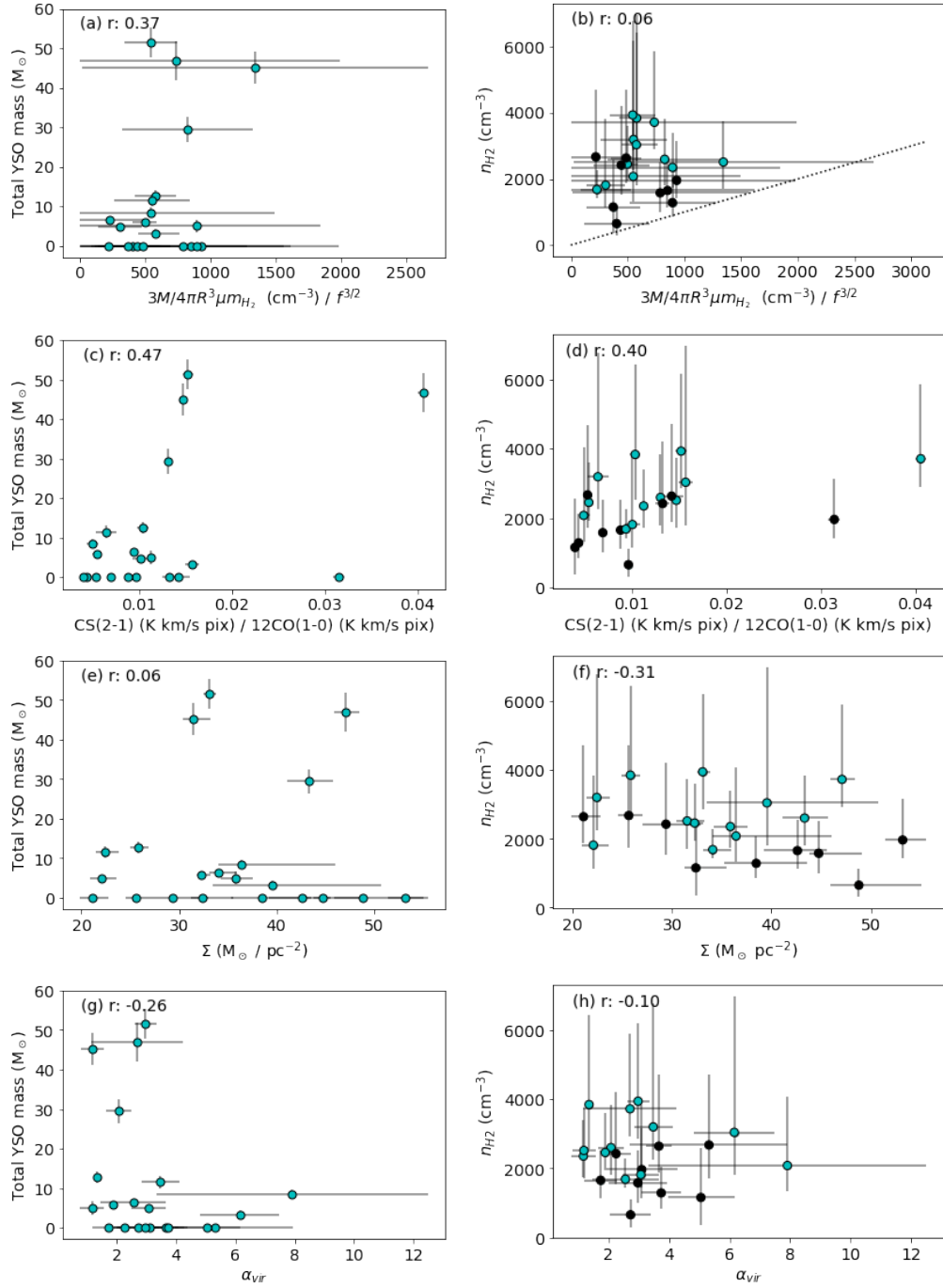


Fig. 5.14.— *Left column:* The total mass of YSOs associated with a clump plotted against four parameters commonly used as indicators or thresholds for stars formation: the mean density, the dense gas fraction, the gas surface density, and the virial parameter α_{vir} . *Right column:* The same four parameters, plotted against the fitted density, n_{H_2} . In panel (b), the dotted line shows a one-to-one correlation between the fitted and mean densities. The blue points indicate clumps that have at least one associated YSO, while the black points have no associated YSOs.

5.7.3 Discussion of Density Correlation

The correlation with RADEX-fitted density and YSO presence could indicate a threshold density for star formation, which is commonly invoked in theories of star formation (Evans 1999, and references therein). Typically, density thresholds measured in the Milky Way are $n_{\text{H}_2} > 10^4 - 10^5 \text{ cm}^{-3}$ (Evans 1999), though these are often measured on scales of $\sim 0.1 \text{ pc}$. Since the densities in the Ridge are measured on scales of 4.5–9'' (1-2 pc) depending on the filling factor, finding clumps with associated YSOs and densities of $\gtrsim 10^3 \text{ cm}^{-3}$ is not inconsistent with these Milky Way density threshold measurements. However, with a detection limit for YSOs around $\sim 2.5 M_{\odot}$ and a trend with YSO mass, there could be lower mass, undetected YSOs associated with the lower density clumps as well. Also, the trends we see in Figure 5.13 appear more continuous, rather than the step-function that would be expected of a strict density threshold.

To understand other star formation thresholds that have been observed, we need to relate the actual physical conditions of the gas to the observational measurements we use to describe them, which are usually only projections of those conditions. The strong correlation of our RADEX-fitted density with the presence of YSOs may indicate that the fitting more directly measures the actual physical condition of the gas than any of the other parameters tested in Figure 5.14. Unlike measurements of mean density or surface density, the fitting allows us to probe the conditions of the gas that is the source of the emission, without being as affected by line-of-sight effects or optical depth.

Khullar et al. (2019) find in their simulations that while a high n_{H_2} is necessary for efficient star formation, typical star formation thresholds such as surface density do not actually correspond to that physical threshold. It seems like the virial parameter,

α_{vir} ought to probe the actual physical conditions and be a good predictor of star formation and collapse; however, most measured α_{vir} use Equation 5.7, which depends on the total mass and estimations of the radius of clouds that are not symmetric or spherical. The resulting measurement is subject to the same projection effects and averaging as measuring the mean density instead of the fitted density.

While the fitted density seems to be a better predictor of star formation than any of the other measurements, we cannot directly relate that to the conditions of the clouds when they actually formed the associated YSOs, or whether those are even the same clouds that we are observing now. Furthermore, there are many other factors that determine whether or not a cloud will form stars, and it seems unlikely that there is a single one-size-fits-all density threshold that guarantees the formation of stars, as discussed in Elmegreen (2018).

What we are seeing in Figure 5.13 is more likely an indicator of the local environment in the Ridge, and what density is required for the molecular gas to form stars above $\sim 2.5 M_{\odot}$ when averaged over ~ 1 pc. It would be interesting to test if the Ridge is forming fewer massive stars than regions to the north because the densities in the Ridge are lower, or if the threshold for forming stars is higher, making it more difficult to form stars than in other regions of the LMC. If the Ridge is more turbulent or more magnetically supported, it could raise the density threshold compared to other regions.

As shown in Figure 5.14, we cannot accurately compare this fitted density by measuring the mean density, surface density, dense gas ratio, or α_{vir} . However, as we saw in §5.6.3, ratios of ^{13}CO to ^{12}CO do show a strong correlation with the fitted gas density. We cannot easily say how those trends or specific numbers translate to other regions or size scales though, since the trend is likely dependent on the excitation and

optical depth of the observed lines and a full non-LTE analysis like the one presented here would be necessary. To make a robust comparison of star formation in the Ridge to other massive-star-forming regions in the LMC, we would need to perform the full RADEX fitting process described in this work in other regions of the LMC. Such a study could give insights into whether the Ridge has lower densities on average compared to those regions or whether stars in those regions are able to form at lower densities, suggesting that the gas density required for star formation to occur may depend on galactic environment.

Indebetouw et al. (2013) published fluxes of $^{12}\text{CO}(2-1)$ and $^{13}\text{CO}(2-1)$ at < 1 pc resolution for 103 clumps they identified in the region of 30 Dor. The ratios of $^{13}\text{CO}(2-1)/^{12}\text{CO}(2-1)$ for those clumps ranged from 0.05 to 0.46, where the clumps in the Ridge range from 0.06 to 0.14. Furthermore, Indebetouw et al. (2013) flag six of those clumps as being associated with YSOs or clusters. These six clusters have $^{13}\text{CO}(2-1)/^{12}\text{CO}(2-1)$ ratios that range from 0.14 to 0.22. These are higher than the ratios for most of the Ridge clumps, though they are not the highest ratios of the clumps measured in 30 Dor. If the numbers from the trend in Figure 5.10 hold in 30 Dor and at smaller size scales, this could indicate that 30 Dor does indeed have higher densities than in the Ridge. To be sure how these two regions compare in densities though, we intend to perform our RADEX fitting on observations at a similar resolution.

5.8 Conclusions

We present new observations of the Molecular Ridge in the LMC, including $^{13}\text{CO}(1-0)$ and $\text{CS}(2-1)$ from ALMA at $16''$ resolution, and $^{12}\text{CO}(2-1)$ and $^{13}\text{CO}(2-1)$ from APEX at $30''$ resolution, as well as archival $^{12}\text{CO}(1-0)$ from MAGMA at $45''$ resolution. We

analyzed these observations by fitting them to RADEX models and assessed how well this fitting technique was able to recover T_{kin} , N_{CO} , and n_{H_2} from simulated line emission. The results are summarized below:

- We were able to reliably recover T_{kin} , n_{H_2} , and N_{CO} from simulated line emission by using a combination of the 95% confidence interval and 1.0 Bayesian interval. The performance of the fitting varied across the range of T_{kin} , n_{H_2} , and N_{CO} that we tested, and is dependent on the expected rms error in the line observations. We also determined that dropping one of the four lines— $^{12}\text{CO}(1-0)$, which had the lowest resolution—would result in a significant loss of fitting sensitivity, especially in moderate values of N_{CO} . We found that it was unnecessary to account for sharp boundaries between clumps, as fitting Gaussian line profiles did not change the results significantly.
- LTE calculations from the (2-1) lines result in much lower clump masses than the RADEX fitting, which implies that the lines are sub-thermally excited and the excitation temperatures of $^{12}\text{CO}(2-1)$ and $^{13}\text{CO}(2-1)$ are not equal. When calculating LTE masses from the (1-0) lines, the masses are higher than the RADEX fitting. This could happen if the ^{12}CO lines are actually optically thin rather than thick or if the adopted beam filling factor was too large, though the relative effects of the filling factor are nonlinear and difficult to predict.
- We calculated a value for X_{CO} in the Ridge based on the RADEX fitted masses, getting $X_{\text{CO}} = 1.8 \times 10^{20} \text{ cm}^{-2} / (\text{K km s}^{-1})$, which is lower than we would expect for the LMC with 1/3 solar metallicity. This could be because the non-LTE fitting is better tracing the molecular mass or because the abundance ratio of $\text{H}_2/^{13}\text{CO} = 2 \times 10^6$ that we used was too low. We also calculated a value

for $X_{13\text{CO}}$, where the total N_{H_2} is related to the integrated flux of $^{13}\text{CO}(1-0)$ rather than $^{12}\text{CO}(1-0)$. We get $X_{13\text{CO}} = 1.6 \times 10^{21} \text{ cm}^{-2} / (\text{K km s}^{-1})$, and the correlation is much tighter than it is with ^{12}CO . This indicates that using $^{13}\text{CO}(1-0)$ for mass estimates would be more accurate than using $^{12}\text{CO}(1-0)$.

- The ratio $^{13}\text{CO}(2-1)/^{12}\text{CO}(1-0)$ had the tightest trend with the RADEX-fitted gas density, n_{H_2} , though all ratios of ^{13}CO to ^{12}CO fluxes are diagnostic of the volume density to a lesser extent. Ratios of upper level transitions to lower ($^{12}\text{CO}(2-1)/^{12}\text{CO}(1-0)$) are also correlated with density and not kinetic temperature. These relations are likely due to the observed lines being sub-thermally excited, so the density of the gas is important for excitation and the excitation temperature is lower than the kinetic temperature. Six clumps had a $^{12}\text{CO}(2-1)/^{12}\text{CO}(1-0)$ ratio greater than 1 in K km/s pix units, meaning that the ^{12}CO may actually be optically thin and relatively hot in some clumps to allow $^{12}\text{CO}(2-1)$ to be brighter than $^{12}\text{CO}(1-0)$. The $^{13}\text{CO}(2-1)/^{13}\text{CO}(1-0)$ ratios were above 1 for eight clumps, and all eight clumps have an associated YSO, which could be a source of heating to excite the (2-1) line. We also find that neither the ratio of $\text{CS}(2-1)/^{12}\text{CO}(1-0)$ nor $\text{CS}(2-1)/^{13}\text{CO}(1-0)$ show as strong a correlation with density as most of the $^{13}\text{CO}/^{12}\text{CO}$ or (2-1)/(1-0) ratios, despite CS being commonly used as a dense gas tracer.
- We find that no star formation parameter that can be calculated from simple mass estimates, like the mass based on an X-factor, showed a strong trend with star formation. Rather, the strongest predictor of the presence of YSOs associated with a clump was its RADEX-fitted gas density, n_{H_2} . This fitted density is correlated with the number of associated YSOs, as well as the total and average mass of those YSOs. The simpler parameters we investigated were the

mean density calculated from total mass and size, the ratio of the dense gas tracer CS(2-1) to $^{12}\text{CO}(1-0)$, the surface density (which is directly related to A_V and N_{H_2}), and the virial parameter, α_{vir} . The correlation of n_{H_2} with YSO presence demonstrates that the RADEX fitting may better probe the physical conditions of the gas on these scales, though the actual relationship between the fitted density and some critical “threshold” density required for star formation is uncertain.

- We hypothesize that the Molecular Ridge may not be actively forming massive stars as much as the northern regions either because its gas density is lower than those other regions or because it has a higher density threshold for stars to form. A higher density threshold could be due to turbulent or magnetic support for example. The results of this study show that the RADEX-fitted volume density of the gas cannot be traced accurately by easily measured observables, such as surface density or a global mean density. While ratios of ^{13}CO to ^{12}CO are diagnostic of gas density, the scaling of this relationship is likely dependent on the local physical conditions and may not be accurate for determining relative gas density in other regions. To test these hypotheses, we will conduct a follow-up study of other active star-forming regions in the LMC with the RADEX fitting method presented here.

Chapter 6

Elementary Student Perceptions Of Science

The text in Chapter 6 has been accepted for publication in the Journal of STEM Outreach (Finn et al. 2023) as “How Informal Science Education Influences Elementary Students’ Perceptions Of Science And Themselves.”

6.1 Introduction

Despite decades of effort to improve diversity in science careers, women and people of color remain largely underrepresented, especially in the physical sciences (Fry et al. 2021). In a study of children in the 10-18 age range in the UK, the majority of those surveyed admire scientists and find science interesting, but only 16% aspired to become scientists (Archer et al. 2020). This difference between students’ science interest and science aspiration, which the authors refer to as the “being/doing” divide (Archer et al. 2010), is more pronounced for female students than for male students. In this study we focus on the factors that influence elementary students’ science aspirations,

including their interest in science, their self-efficacy, and how their identity aligns with being a scientist.

Many studies indicate that science interest is high and shows no difference between genders for younger students, but a gap in interest between male and female students develops around grade six (Pell & Jarvis 2001; Murphy & Beggs 2005; Baram-Tsabari & Yarden 2011). Several studies also show that around this age, female students begin to have a weaker belief in their abilities to do science and math (Andre et al. 1999; Gunderson et al. 2012; Bian et al. 2017). The differences in elementary student science interest and self-efficacy by ethnicity/race are not as prominent as by gender (Archer et al. 2020; Vandenberg et al. 2021), although significant achievement gaps exist (Quinn & Cooc 2015; Curran & Kellogg 2016) as well as aspiration gaps (DeWitt & Archer 2015). There is much less work done examining the role of socioeconomic status in elementary student science aspirations, but Archer et al. (2020) do find that students from socio-economically disadvantaged families are significantly less likely to aspire to science careers.

Studies find that differences in science aspirations around this age may be due in part to students becoming more aware of cultural stereotypes that make them believe their personal identity is incompatible with being a scientist (Schreiner & Sjøberg 2007; Ceci et al. 2009; Archer et al. 2010; Cheryan et al. 2015; Carli et al. 2016). This is noted both based on gendered stereotypes (Vincent-Ruz & Schunn 2018) as well as ethnic/racial stereotypes (Aschbacher et al. 2010; Archer et al. 2015; Rahm et al. 2022). Students may enjoy science and consider themselves good at science, but still think that science is “not for me.” Many aspects of the scientist stereotype are inherently contradictory to society’s concepts of being feminine (Archer et al. 2010) or to students’ perceptions of their cultural identity (Archer et al. 2015). To

encourage more students from underrepresented populations to consider pursuing science careers, science educators need to address all of these different effects in the way that science is presented to children, especially in the age range where they begin to develop their personal identities.

Traditionally, many prominent depictions of science and scientists in the media (Steinke 2005), which are often shared and perpetuated by parents and elementary teachers (Keller 2001), reinforce ideas about science being a series of facts to be learned rather than a process, or that science is only done by “brilliant” white men in lab coats. Representation in science has improved over the last several decades, both in the media and in real life (Long et al. 2010; Previs 2016; Steinke & Tavarez 2017), but children are still more likely to draw a man than a woman when asked to draw a scientist (Miller et al. 2018; Hayes et al. 2020). When asked to draw themselves doing science, fifth grade students often drew themselves reading a book or taking notes, while the scientists they drew were mostly white men in a laboratory setting (Barman et al. 1997). While student perceptions of themselves doing science may have improved since the Barman et al. (1997) study, incorporating hands-on, interactive activities into science curricula has been shown to help students develop positive attitudes towards science and better understand the many different ways that science happens (Bredderman 1983; Aydede & Kesercioğlu 2010; Satterthwait 2010).

Another means of improving students’ perceptions of science and enhancing their interest in science is to teach them about nature of science (NOS; Tobias 1990; van Griethuijsen et al. 2015). Here we use the definition from (Schwartz et al. 2004, pg. 611) that NOS is “the values and underlying assumptions that are intrinsic to scientific knowledge, including the influences and limitations that result from science as a human endeavor”, and which are characterized by the following features from the

National Science Teacher Association (NSTA 2000):

1. Scientific knowledge is reliable, yet still tentative.
2. Science uses a variety of methods.
3. Science involves creativity.
4. Science investigates questions related to the natural world.
5. The terms “theories” and “laws” have specific meanings in science.
6. Contributions to science have been made by people all over the world.
7. Science occurs in a social and cultural context.
8. The history of science shows science can both gradually and suddenly change.
9. There is a relationship between science and technology, but basic scientific research is not concerned with practical outcomes.

In this study, we examine the influence of the astronomy out-of-school time (OST) program Dark Skies, Bright Kids (DSBK), which targets elementary students from underrepresented populations. OST programs have been shown to impact student perceptions of science, scientists, and their own science identity, and they provide an excellent opportunity for them to learn science more interactively (Krishnamurthi & Porro 2008; Bhattacharyya et al. 2011; McCreedy & Dierking 2013; Riedinger & Taylor 2016; Hayes et al. 2020). We investigate the impact of DSBK programs on the students’ perceptions of science, NOS concepts, and their own self-identity in relation to science.

6.2 Program Background

6.2.1 Organization Overview

Dark Skies, Bright Kids (DSBK) is a graduate-student-run volunteer organization based at the University of Virginia (UVA). DSBK was founded in 2008 to provide OST outreach opportunities for elementary-aged children in underserved communities - primarily in Charlottesville, Virginia and the greater surrounding area, but also across the state of Virginia. The majority of DSBK's members are graduate student volunteers in the UVA Astronomy Department, which includes the authors of this paper. Though our outreach activities are astronomy-themed, our mission is more generally aimed toward fostering the curiosity and imagination of students through hands-on, group-oriented science activities. We aim to provide children with the opportunity to see science as fun and exciting, and to see themselves as scientists, through engagement in inquiry-based learning activities that occur outside the traditional classroom environment.

6.2.2 Program Structure

The two main ways that DSBK interacts with our target demographic are through after-school clubs and week-long summer clubs. For the after-school variant, each semester (i.e., twice per year, once in the spring and once in the fall) we coordinate with a single elementary school in the City of Charlottesville or Albemarle County to host a club. Schools are selected on a rotating basis, with priority given to schools with a large population of students from backgrounds underrepresented in STEM fields (especially non-white or low socioeconomic status). Typical after-school clubs meet for approximately two hours on Friday afternoons for eight weeks. Each week

a particular topic in astronomy serves as the theme for the day, and we lead the students through several activities related to the topic. To provide the students with a varied learning experience, we do different kinds of activities such as demonstrations, hands-on interactive activities, and physically active kinesthetic activities. The week-long summer clubs are led and structured much the same way, but with the content delivered in a single week. Summer camps are conducted in rural areas of Virginia and are available to students from any local elementary school. We cover the same daily topics and activities in the form of ten half-day sessions (morning and afternoon) from Monday to Friday.

Typically, all DSBK events are done in-person, with the exception of Summer 2020, Spring 2021, and Summer 2021, which were operated virtually due to COVID. To facilitate compatibility with the remote learning environment, we modified several aspects of camp, such as rewriting some activities so they could be safely performed at home with minimal supervision, providing students with prepackaged materials and instructions, and introducing the content and activity descriptions in synchronous video sessions. The video sessions gave students the opportunity to interact with DSBK volunteers in real time and ask questions as they worked through the activities. We made recordings of the video sessions available so that students had an asynchronous option in cases of poor internet connection or unreliable device availability. A more thorough discussion of the structures and differences between virtual and in-person DSBK events can be found in Finn et al. (2020).

Club Date	Format	Number of students with data	Number of before-club surveys	Number of daily surveys	Number of after-club surveys
2019 Summer	In-person	10	10	77	10
2019 Summer	In-person	12	12	79	12
2019 Fall	In-person	21	21	99	18
2020 Spring	In-person	16	15	16	0
2020 Summer	Virtual	34	34	124	18
2021 Spring	Virtual	10	10	47	8
2021 Summer	Virtual	9	9	48	6
2022 Summer	In-person	8	8	50	8

Table 6.1: Summary of data sources from the seven clubs conducted during the data collection period.

6.3 Methods

6.3.1 Participants

We began collecting the data presented here in 2019 from students who participated in a DSBK program between Fall 2019 and Summer 2021. In that time period, there were a total of three semester after-school clubs and five summer clubs offered, for a total of 135 students with at least some data. The Spring 2020 semester club was cut short due to COVID, so no after-club surveys were collected. All club participants were elementary students between 3rd and 5th grade, or in the case of the summer clubs, rising 3rd-6th graders, corresponding roughly to ages 8-12. In Table 6.1, we summarize the data obtained from each club.

Elementary students were asked to apply to participate in the programs. For semester clubs, we gave applications to all students within the eligible grade window

at the school, and for summer clubs we used online advertisements and provided copies of the applications to local elementary schools. The number of applicants rarely exceeded the capacity of the club, but in those cases applicants were randomly selected (the number of participants for each club, which is almost always the number of applicants, is shown in Table 6.1). This means that our sample is primarily composed of students who chose to join our astronomy OST program. Most often this is because the student was already interested in science or astronomy, but there could be other reasons that a student or their guardian signed them up, such as wanting a free after school program or summer camp to provide adult supervision. We discuss the ways this selection affects our results in the Limitations section.

There were a total of 135 students with at least some data across all the programs analyzed in this work. We included on the applications the option to disclose demographic information for the students. Of those who included this data, 47% were female, 35% were non-white, and 29% qualified for free or reduced lunch (a measure of socioeconomic status). The number of students who identified as Black, Hispanic, Asian, or a combination of two or more races is too small for individual group statistics, and so in this analysis we have grouped them together.

6.3.2 Data Sources

Data was collected in the form of surveys that students filled out at different stages during the club. We developed these surveys to test student beliefs about NOS concepts, their science ability and aspiration, if they identified with being a scientist during out programs, and how different daily activities correlated with their science identity. We designed all of the questions to be simple and easily understood by children, and all forms were limited to one page to accommodate short attention

spans. Each of these surveys included a variety of qualitative (short answer) and quantitative questions (Likert scale, true false, or check mark). In this work, we consider only the responses given to the quantitative questions . There were three types of surveys:

- Before-club survey (“Getting to Know You”): This form was filled out by participants once, at the beginning of the first day of club. The quantitative questions diagnosed the students’ perceptions of their science ability, their creativity, their aspiration to become a scientist, and their beliefs about NOS concepts.
- Daily survey (“Wrap-Up”): This form was filled out by participants at the end of each full day of the club. For an eight week semester club, each student was given eight wrap-up surveys over the course of the club, while for a week-long summer camp, each student was given five wrap-up surveys. Each of these asked quantitative questions about if they felt like a scientist that day, were interested in that day’s topic, if they had any questions about the topic, and what activities they performed throughout the day (such as asking questions or doing experiments).
- After-club survey (“Saying Goodbye”): This form was filled out by participants once, at the end of the last day of club. The quantitative questions asked were identical to those on the before-club survey.

To help promote student engagement with the Likert scale questions, we presented the possible answer choices as a kid-friendly graphic, shown in Figure 6.1. In Tables 6.2 and 6.3, we list the full set of questions analyzed in this paper for the before/after-club survey and the daily survey, respectively.

Do you feel like you are good at science? (Circle one)

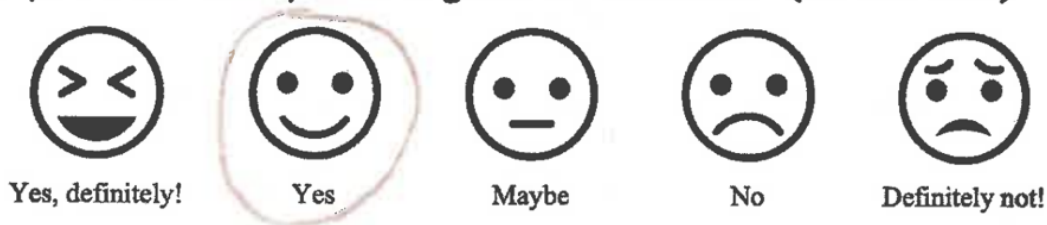


Fig. 6.1.— An example of one of the questions on the before-club survey as it was presented to the students in graphical format. For our analysis, student answers to these Likert scale questions were translated to a 1 to 5 scale, where “Yes, definitely!” = 5 and “Definitely not!” = 1.

We include in the before- and after-club surveys statements about NOS concepts written in kid-friendly language. There is no one definition of NOS (Abd-El-Khalick & Lederman 2000), but in Table 6.2 we highlight in bold the answer that better aligns with NOS principles listed in the introduction (NSTA 2000) and which we aimed to convey throughout the program. During DSBK clubs, NOS concepts are not explicitly mentioned or taught, but were implicitly modeled in our activity design and discussions. Entering this work, we hypothesized that participation in a DSBK club would improve students’ understanding of NOS, and that this would be reflected in the after-club survey.

Question	Answer Format
Do you feel like you are good at science?	Likert scale, 1-5
Do you feel like you are creative?	Likert scale, 1-5
When you grow up, do you want to be a scientist?	Likert scale, 1-5
Science is based on observations.	<u>True</u> or False
There is a right way to do science.	True or <u>False</u>
Science requires creativity.	<u>True</u> or False
Teamwork is part of science.	<u>True</u> or False
Science can change.	<u>True</u> or False
Science teachers do science	<u>True</u> or False
Science is challenging.	True or <u>False</u>

Table 6.2: Summary of the quantitative questions asked on the before- and after-club survey, given at the beginning of the first day of club and the end of the last day of club, respectively. For the True or False statements, the bold and underlined answer is the one that better aligns with NOS concepts.

Question	Answer Format
Today I was creative.	Check mark
Today I asked questions.	Check mark
Today I had fun.	Check mark
Today I made observations.	Check mark
Today I did experiments.	Check mark
Today I worked with others.	Check mark
Today I learned.	Check mark
Today I changed my mind about something.	Check mark
Today I felt like a scientist.	Likert scale, 1-5
[Today's activity] is interesting.	Likert scale, 1-5

Table 6.3: Summary of the quantitative questions asked on the daily surveys, given at the end of each day of club.

6.4 Data Analysis and Results

In this section, we address three main research questions:

1. How did the students' perceptions of their science ability, creativity, and science aspirations change before and after the astronomy club?
2. How did the students' perceptions of the nature of science change before and after the astronomy club?
3. What daily activities or actions identified by the students resulted in them feeling more like a scientist or interested in the topic that day?

6.4.1 Research Question 1

How did the students' perceptions of their science ability, creativity, and science aspirations change before and after the astronomy club?

To investigate this question, we compared responses on the before- and after-club surveys to the questions “Do you feel like you are good at science?”, “Do you feel like you are creative?”, and “When you grow up, do you want to be a scientist?”. We matched before and after responses and only included in this analysis students who had completed both surveys, for a total of 74 pairings. We show the mean response to the three questions before and after the astronomy club in Figure 6.2. The responses to each question are mostly positive, especially the first two questions measuring their perceived science competency and creativity, for which there were no responses of “No” or “Definitely not”. Their science aspirations were on average lower than the other two questions, which aligns with previous findings (e.g. Archer et al. 2020), but still were on average more positive than negative or neutral.

Confidence in science, creativity, and science aspiration before and after club

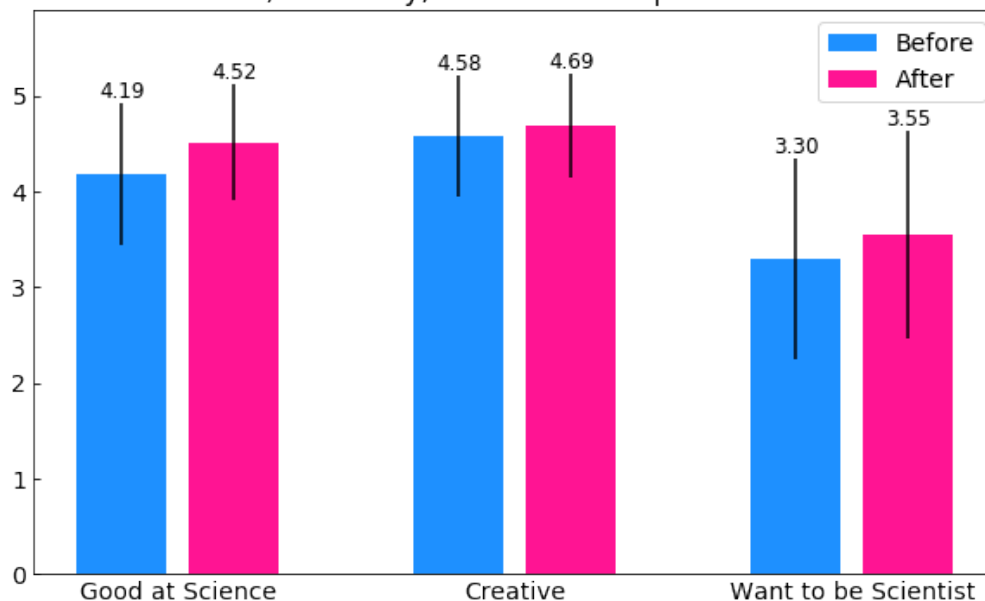


Fig. 6.2.— Mean and standard deviation of before- and after-club responses to the questions “Do you feel like you are good at science?”, “Do you feel like you are creative?”, and “When you grow up, do you want to be a scientist?”, where 5 is the most positive response.

A Shapiro-Wilk test for normality revealed that before and after data for each question did not follow a normal distribution ($p < 0.01$ for all 6 tests). We then used a non-parametric Wilcoxon signed-rank test to show that the before and after responses did not change significantly over the course of our programs, at the 95% confidence threshold for the questions “Do you feel like you are creative?” ($p = 0.096$) and “When you grow up, do you want to be a scientist?” ($p = 0.082$). For the question “Do you feel like you are good at science?”, students’ perceptions of their science ability significantly increased after participation in our program at the 95% confidence threshold ($p = 0.0034$). This indicates that our program positively impacts students’ perceptions of their science abilities.

Demographic Effects

We investigated how these differences varied for students based on their gender, race, and socioeconomic status. We compared before- and after-club responses to each of the questions with Wilcoxon signed-rank tests for subsets of participants who self-reported as male, female, white, non-white, qualifying for free-or-reduced lunch (FRL), and not qualifying for FRL. Since some participants chose not to disclose one or more of these demographics, these subsets do not reflect the total number of students with before- and after-club survey pairings.

The average response to the question “Do you feel like you are good at science?” increased after the program for each demographic subset, but was only statistically significant based on a 95% confidence threshold for female students, white students, and students who do not qualify for FRL. We show the mean response to the question “Do you feel like you are good at science?” for each demographic subset in Figure 6.3. The Wilcoxon signed-rank test indicated that there was no significant difference between responses for the questions “Do you feel like you are creative?”, and “When you grow up, do you want to be a scientist?”, therefore we do not show those here.

We also performed Mann–Whitney U tests, a non-parametric test to determine if the average responses to each question were consistent between gender, race, and FRL status. Using a 95% confidence threshold for significance, we find that male students have a significantly higher average response to “Do you feel like you are good at science?” than female students before club, but not after club. There is also a significant difference between white and non-white students’ responses to that question before club, but not after club, with non-white students having more positive responses than white students. We find no significant difference between students who qualify for FRL and those who do not and no differences in either of the other

Confidence in science abilities before and after club by demographic group

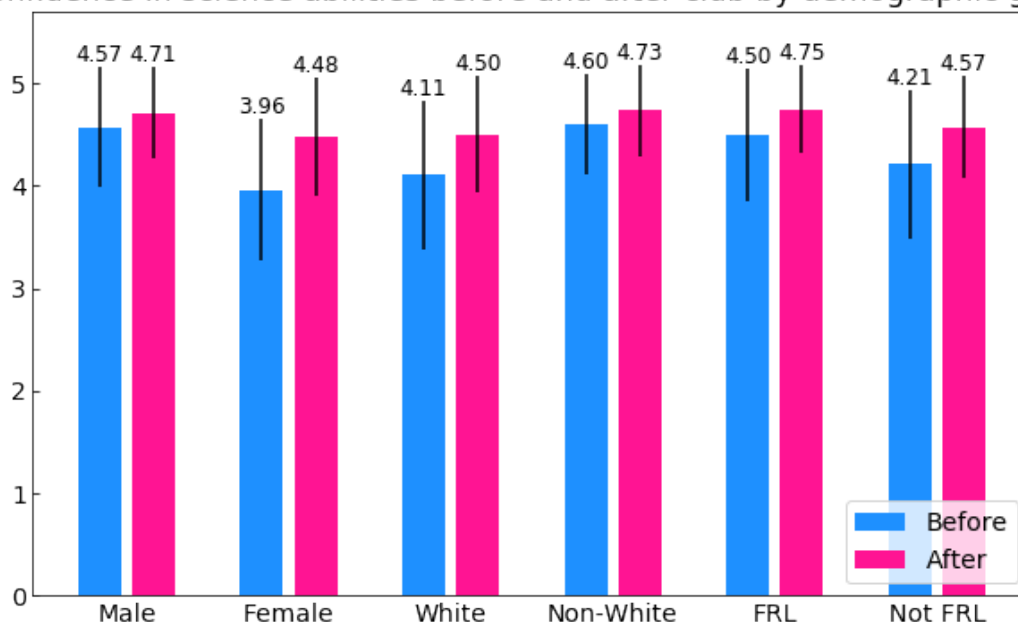


Fig. 6.3.— Mean and standard deviation of before- and after-club responses to the question “Do you feel like you are good at science?”, where 5 is the most positive response, broken up into demographic subsets.

questions. These test results are summarized in Table 6.4.

The lack of statistical significance in some of these cases could be due to the smaller sample sizes involved when we isolate demographic groups (the minimum size is $N = 18$ for students who qualify for FRL). While the Mann-Whitney U test and Wilcoxon signed rank test are still valid for small sample sizes, they are only sensitive to larger differences. In the case of comparing the Mann-Whitney U tests before and after club, the sample sizes for each group have not changed. This means that while there was a statistical difference in male vs. female and white vs. non-white student responses before club, after club those differences at least decreased enough that they were no longer statistically significant.

Comparison Groups	Mann-Whitney U test p -value
Male/Female before club	0.0022
Male/Female after club	0.088
White/Non-white before club	0.017
White/Non-white after club	0.10
FRL/Not before club	0.13
FRL/Not after club	0.15

Table 6.4: Results of the Mann-Whitney U test to determine if there is a significant difference in responses to “Do you feel like you are good at science?” between demographic groups before and after the club. Pairings with a significant difference based on a 95% confidence threshold ($p < 0.05$) are highlighted in green. There were no pairings with a significant difference for either of the other questions on the survey.

6.4.2 Research Question 2

How did the students’ perceptions of the nature of science change before and after the astronomy club?

We next compared before- and after-club responses to the series of True/False questions concerning NOS concepts. Figure 6.4 shows the fraction of responses that were “True” before and after the club. All of the statements show a small change before and after the club. Most of those changes are in the expected direction (see Table 6.2), with the exception of “There is a right way to do science”, “Teamwork is part of science”, and “Science can change.” To determine whether the changes in responses were statistically significant, we computed a 95% confidence interval for each. Considering this confidence interval, none of the observed changes in the fraction of “True” responses are statistically significant. We also looked at these responses as a function of gender, race, and socioeconomic status and found no significant differences or changes before and after club.

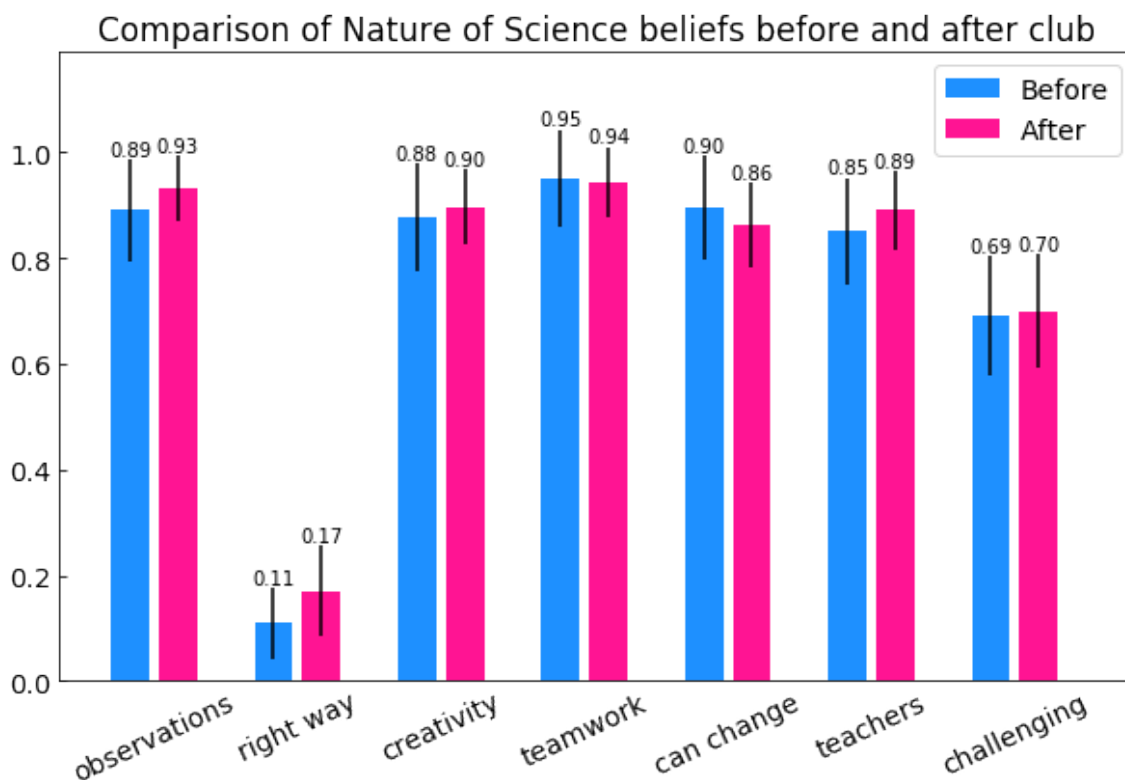


Fig. 6.4.— Fraction of student responses that were “True” for each NOS statement, before and after the astronomy club. While all of the statements show a small change in responses, the error bars indicate that none of the changes are significant based on a 95% confidence threshold.

The lack of a statistically significant change in NOS perceptions aligns with other findings that an implicit teaching approach is not effective in teaching NOS concepts (Abd-El-Khalick & Lederman 2000). While we cannot comment further on the effect of the astronomy club on changing students’ perceptions, it is still interesting to consider their overall perception of science. We show the fractions of “True” responses averaged between before and after club with respective errors in Table 6.5. The majority of students demonstrated perceptions that align with NOS concepts for every statement, notably including the ideas that science requires creativity, that there is more than one right way to do science, and that science can change, which are some

Nature of Science Statement	Fraction of “True” Responses and Error
Science is based on observations.	0.91±0.11
There is a right way to do science.	0.14±0.11
Science requires creativity.	0.89±0.13
Teamwork is part of science.	0.95±0.11
Science can change.	0.88±0.13
Science teachers do science.	0.87±0.12
Science is challenging.	0.70±0.16

Table 6.5: Fraction of responses that aligned with NOS principles (see Table 2). These are averaged between before and after clubs with a 95% confidence interval reported.

of the more common misconceptions about NOS (Lederman et al. 2002). Students mostly recognized the collaborative nature of science, with the highest fraction of agreement with the statement that “Teamwork is a part of science.”

We expected that students would come to view science as less challenging through participation in our programs. However, this statement elicited the largest spread in student responses. We know that after the program, 98% of students responded with either “Yes” or “Yes, definitely!” in response to the statement “I am good at science”, so it seems that the belief that science is challenging does not come from them feeling that they struggle with science or science class, but rather a recognition of the inherent challenge in science.

6.4.3 Research Question 3

What daily activities or actions identified by the students resulted in them feeling more like a scientist or interested in the topic that day?

To answer this question, we looked at student responses to the daily “Wrap-Up”

surveys. Students checked boxes of whether or not they performed various activities that day during camp, and responded to the Likert scale questions “Today, I felt like a scientist.” and “[The day’s topic] is interesting.” We look for a relationship between students performing a given activity and a higher score in either of those two Likert scale questions.

To quantify such a relationship, we used a proportional odds logistic regression model using the `polr()` function from the MASS package in R. This model analyzes how different factors affect the odds that a student will respond with a higher value on a Likert scale question. We input into this model the responses from each day’s wrap-up form from each student, where we have a total of 540 completed forms from a total of 124 students. We looked for a dependence of the ordinal responses to the two Likert scale questions on whether students reported performing an activity, represented in the model as a 1 or a 0. We also included in the model a dependence on which program the response is from to control for variations in student personalities, the format of the program, and the volunteers leading the program.

To determine that the above inputs to the model resulted in the best fit of the data, we minimized the Akaike Information Criterion (AIC) score, where a lower score indicates a better model fit. For example, including which program the response came from resulted in a lower AIC than not including the club information. Other parameters we considered including, but which resulted in higher AIC values, were whether the program was a week-long summer camp or a semester-long weekly after school club, whether the program was virtual or in-person, and which topic was being covered that day. The first two of these options are both accounted for by including which program the response is from as an input parameter. The fact that the model fits better without including the day’s topic indicates that it is not correlated with

	"Today, I felt like a scientist"		"[The day's topic] is interesting"		
"Today, I..."	p-value	Odds ratio	p-value	Odds ratio	% of responses
Was creative	<0.01	3.11	<0.01	2.19	74%
Did experiments	<0.01	2.25	0.90	0.97	72%
Asked questions	<0.01	1.83	0.014	1.85	56%
Worked with others	0.78	0.94	0.58	0.86	60%
Had fun	0.97	0.99	0.045	1.90	87%
Learned something	1.00	1.00	0.32	1.34	79%
Made observations	0.040	1.66	0.29	1.33	67%
Changed my mind about something	0.079	0.68	<0.01	0.51	42%

Table 6.6: Results of the proportional odds logistic regression model to determine the odds that performing an activity resulted in the student reporting a higher ordinal response to the Likert scale question. We highlight factors that fall below a 95% confidence threshold for statistical significance. The final column shows how often students reported doing each activity.

how the students responded to the two Likert scale questions.

The outputs from the model are the odds ratios and p-values for each input. Together, these indicate which of the various inputs resulted in a statistically significant higher-level ordinal response. So in our case, the model outputs the odds that when a student reported doing a given activity, they would also give a more positive response to "Today, I felt like a scientist" or "[The day's topic] is interesting". An odds ratio above 1 indicates a positive association, while an odds ratio below 1 indicates a negative association. The results for each of the questions are shown in Table 6.6.

Both questions had four factors with a statistically significant relationship with the responses. For the responses to “Today, I felt like a scientist”, those four factors were being creative, doing experiments, asking questions, and making observations. All of these factors had a positive relationship with how much students felt like a scientist. Being creative had the strongest positive relationship with the responses.

For the responses to “[The day’s topic] is interesting”, being creative, asking questions, and having fun had positive associations with the students’ responses, while changing their mind had a negative relationship. Again, being creative was the strongest of these.

6.5 Discussion

Overall, our data indicate that students felt more confident about their science abilities after participating in a DSBK program. This finding aligns well with other studies evaluating the effects of OST programs (Chun & Harris 2011; McCreedy & Dierking 2013). Of the 74 paired before and after responses, only three students responded to “Do you feel like you are good at science?” with “Maybe” at the end of the program, and all other responses were “Yes” or “Definitely yes”. While 70% said that “Science is challenging”, 94% of the students said that they were good at science, which indicates that while students acknowledge the difficulty of science, they do not think that it is too difficult for them to excel at the subject.

We do not see similar increases in students’ responses to the questions “Do you feel like you are creative?”. This is unsurprising since it is not a skill that we emphasize in our program or a skill that is traditionally associated with science. However, all but four students responded with either “Yes” or “Definitely yes” to “Do you feel like you are creative?” before the program, so the lack of difference before and after club

may also be because there was little room for improvement in the first place.

We also do not see a statistically significant increase in responses to the question “Do you want to be a scientist when you grow up?”. This is also unsurprising and agrees with prior work that even when students have positive attitudes towards science, a much smaller fraction aspire to be scientists when they grow up (Archer et al. 2020).

When considering the influence of student demographics, we find that female students, white students, and students who do not qualify for free-or-reduced lunch showed the greatest increase in science confidence over the course of DSBK programs. This could potentially be due in part to the fact that a majority of our volunteer base is white and female, and so students with this identity are exposed to representation among the scientists that they meet through the program. Future work could include tracking volunteer demographics more closely to investigate this connection. We were surprised to see that before club, non-white students had higher science confidence responses than their white counterparts, based on the history of whiteness in STEM disciplines. This could be due in part to the selection effect of which students decide to join DSBK programs. The fact that we combined several racial groups together also makes this result harder to interpret, though it aligns with recent findings from Archer et al. (2020) that among 10-19 years old in the UK, South-Asian, Chinese, and Black students had higher science aspirations than white students.

We find that in the daily surveys, students who said that on a given day they were creative or that they asked questions were more likely to also say that they felt like a scientist and that they were interested in that day’s topic. Being creative had a particularly strong association, with this activity having the greatest positive relationship with answers to both questions. We found this result surprising,

since creativity is not traditionally associated with being a scientist and is more often associated with artistry and perceived as the opposite of science (Kind & Kind 2007). We know that scientists do require creativity though, as is included in our NOS understanding (NSTA 2000), and the students in this study also recognized this idea, as demonstrated by 89% of them agreeing with the statement “Science requires creativity.”

A commonality between creativity and asking questions is that both are a form of having ownership in what you are learning. Being able to impart some of their personal ideas into the activities can make students feel more like a part of the process, and so feel more like they are scientists. Similarly, asking questions requires internalizing what you have learned and either identifying what you still do not understand or thinking of what new information would be interesting. Both of these activities can make the students feel more engaged with the material and like they have agency in what they are learning. This may be why students were more interested in the topic and more likely to feel like they were scientists when they partook in creative activities or asked questions.

It is less surprising, but still important to note, that doing experiments and making observations were both also correlated with students feeling like scientists. Many of the activities that we do during DSBK programs are led with a focus on experimentation, especially when leading activities that would otherwise be based on more passive demonstration. We present the activities to students with language that makes it explicitly clear that we are doing an experiment. One example of an activity that has worked well for our group is when we frame the Coke and Mentor demonstration as an experiment of whether diet or regular Coke creates a bigger reaction. This language can help the students recognize that the activity is an experiment and that they need

to make observations to uncover the answer, which in turn can help them realize they are taking part in a scientific process. These activities were correlated with students feeling more like scientists, but not with being more interested in the science topic.

It is similarly unsurprising that when students say that they had fun during the program, they were more likely to find the day's topic interesting. What is more surprising is that a student responding that they had fun during the day did not have a much stronger correlation with their interest in the day's topic than being creative or asking questions. This suggests then that students' interest in the learning material taught during the day is not their primary source of fun during the program.

We find no correlation with either feeling like a scientist or being interested in the topic for the statements "Today I learned something new" and "Today I worked with others". This is surprising to us since we would have expected that learning science topics would increase students' science identity and students generally agreed with the statement "Teamwork is a part of science" (95% respond "True"). This may be because students frequently work together in many contexts, and so while they recognize teamwork is important to science, teamwork is not inherently scientific on its own.

The fact that learning something new shows so little correlation with feeling like a scientist or being interested in the days' topics could be because learning new things can be positive, negative, or neutral and may also feel more like a traditional school activity. Students are expected to learn new things all the time in school whether they are interested in the topic or not and learning about science, math, or writing in school does not necessarily make them think of themselves as scientists, mathematicians, or writers. This result demonstrates how active learning and hands-on experiences can be more important for developing science identity than gaining

knowledge about science.

While students for the most part recognize that science is tentative and subject to change (88% responded that the statement “Science can change” is True), they still seemed uncomfortable with changing their minds. On days that students reported changing their minds, the odds of them saying they were interested in the day’s topic was half as much as on days they did not change their minds. Changing their minds also resulted in an odds ratio of less than one for responding positively to “Today I felt like a scientist”, although that result is less statistically significant. This suggests that while students acknowledge that science changes, they may have been turned off from the topic when they themselves changed their minds. It is a natural reaction to be uncomfortable when confronted with something that changes your mind, and in our society changing one’s mind often comes with strong negative connotations about being wrong. It would be helpful to find a framework for leading students through that process while maintaining their interest in and excitement for the topic. There have been many studies on what science misconceptions exist among elementary students (e.g. Stein et al. 2008; Soeharto et al. 2019) and how educators can address and correct those misconceptions (e.g. Gooding & Metz 2011; Karpudewan et al. 2017). However, there is much less literature on how correcting misconceptions affects students’ interest in science or their confidence in their science abilities.

6.5.1 Actionable Suggestions

Below we list actionable suggestions for elementary OST science education:

- Incorporate student creativity into science activities.
- Encourage students to think of questions about what they have learned.

- Frame lessons or science demonstrations as experiments with observations and inferences.
- Aspects of activities that make a student feel more like a scientist do not necessarily make students more interested in the topic; carefully consider goals for an activity as you craft it.
- In cases where the goal of a program or lesson is to increase interest in science or to help students feel like scientists, focus on students having science experiences rather than learning science knowledge.
- If you are interested in teaching the nature of science, use explicit instruction on these topics.

6.6 Limitations

The biggest limitation of this study is that the sample of students that participated all chose to be a part of the DSBK programs, and so were more likely to already have a favorable view of science and their science abilities. Furthermore, we only received daily responses from students who attended club on a given day, and if a student chose to stop coming to our program or missed the last day of club, they did not complete an after-club survey and so were not included in those comparative parts of the analysis (of the 118 students who completed before-club surveys, only 74 completed after-club surveys). This likely biased the responses to questions about students' perceptions of their science competency, science aspirations, daily science identity, and interest in the daily science topics. It may also have influenced their prior knowledge and perceptions of NOS concepts. This could be improved by instead conducting this

study in a setting where all students in a class are expected to participate in the activities.

Similarly, students who experienced behavior problems during a day of the program and students who may be on the ADHA-spectrum are more likely to not complete our daily wrap-up survey forms. We do not collect data on these issues, and so they may bias our results on the daily surveys towards students with longer attention spans or those who had more positive experiences during the day.

A drawback of the check mark format that we used for the daily activities was that it allowed for straightlining and there were several cases of students checking every box. It is possible that the students thoughtfully believed they had engaged in all of the activities listed, but there were also likely many cases of the students checking every box without giving much thought to the exercise. Since we cannot meaningfully distinguish between those two cases, all data was included. To account for this in future iterations of this work, we could consider including an attention check to distinguish whether students are giving genuine responses to the surveys.

We find that our approach of implicitly demonstrating NOS concepts without explicit discussion of them throughout the program did not result in any significant change in student perceptions of those NOS ideas. To better understand how such programs could influence student understanding of NOS concepts, it would be helpful to incorporate explicit discussion of these concepts into our program.

6.7 Conclusions

In this work, we present survey results from elementary students participating in DSBK astronomy programs, both in 8-week-long after school clubs and week-long full-day summer camps. Students were asked about their perceptions of their science

competency, creativity, science aspirations, and understanding of NOS concepts both before and after the programs, and throughout the programs were asked about the activities they took part in, their perceptions of themselves as scientists, and their interest in the daily astronomy topic. Our major findings are summarized below:

- Students' confidence in their science abilities increased after participating in DSBK programs. Their belief in their creativity and their aspiration to pursue a scientific career also both increased, but not statistically significantly based on a 95% confidence threshold. Female students, white students, and students who do not qualify for free-or-reduced lunch showed the greatest increase in science confidence over the course of the programs.
- Before the program, male students and non-white students showed a significantly higher science confidence than female students and white students, respectively. After the club, there was no statistically significant difference between their responses. This was due to the increase in science confidence of female and white students.
- There was no statistically significant change in students' understanding of NOS concepts after the program, suggesting that an implicit teaching approach is insufficient to convey NOS ideas. However, the majority of students' beliefs did still align with accepted NOS tenets, both before and after the program.
- Being creative was the daily activity that had the strongest association with both students feeling like scientists and with students being interested in the day's topic. Students who said they had been creative on a given day were 3 times more likely to say they felt like a scientist and 2 times more likely to say they were interested in the day's topic.

- In addition to being creative, there was a positive association between feeling like a scientist and the daily activities of asking questions, doing experiments, and making observations. For interest in the day's topic, there was also a positive association with asking questions and having fun.
- There was no significant correlation between learning something new and either feeling like a scientist or being interested in the day's topic. The same is true for working with others.
- There was a negative correlation between students reporting that they had changed their mind about something and saying they were interested in the day's topic, with students half as likely to be interested on days that they changed their minds.

These conclusions can be actively incorporated into future STEM education programs by emphasizing student creativity and questioning in science activities, performing experiments and making observations, and taking an explicit approach to teaching NOS concepts.

Chapter 7

Conclusions

In this work, I present several studies that focus on understanding the physical conditions that give rise to star formation in a variety of environments, from quiescent to starbursting. Understanding the physics of the ISM that lead to star formation in a wide range of environments in the local universe is critical to our understanding of star formation throughout cosmic time.

These studies have primarily focused on understanding the molecular gas using spectral observations of emission lines from carbon monoxide, CO. I have used ALMA observations to determine molecular clouds' properties and how they relate to associated star formation. By measuring the sizes, masses, and velocity dispersions of molecular clouds, we can learn about their relative turbulence, gravitational potential, and kinematics. I have measured these cloud properties in several regions with a wide range of star formation activity to investigate how the environment affects the clouds' physical conditions, and in turn how those conditions affect star formation outcomes.

The specific environments I presented here include the Antennae galaxies, a starbursting pair of merging spiral galaxies that are in the process of forming thousands

of SSCs (Whitmore et al. 2010). The Antennae galaxies also contains a cloud nicknamed the Firecracker, which is the only known example of a cloud that is thought to have the potential to form an SSC, but has not yet been disrupted by star formation (Johnson et al. 2015; Finn et al. 2019). I have also measured cloud properties in the LMC, which is home to the only SSC in the Local Group, R136 in the 30 Doradus (30 Dor) region. Immediately south of 30 Dor and massive star-forming region N159 is the quiescent Molecular Ridge, which contains nearly a third of all CO-bright molecular gas in the LMC, and yet is forming shockingly few massive stars (Indebetouw et al. 2008). I have most recently turned to a pair of galaxies, NGC 1313 and NGC 7793, which have similar galactic properties (e.g. mass, star formation rate), but have vastly different environments and star cluster populations (Calzetti et al. 2015). NGC 1313 is a barred spiral galaxy with many massive clusters, while NGC 7793 is a flocculent spiral with almost none of its star formation happening in the form of massive star clusters.

This series of work shows a trend that clouds with more extreme properties (higher surface densities, pressures, and turbulence) yield more intensive star formation. I find evidence that external pressure is essential for forming massive clusters, which agrees remarkably well with theoretical predictions (Elmegreen & Efremov 1997).

In Chapter 2, I present observations the “Firecracker.” Using emission from $^{12}\text{CO}(2-1)$, $^{12}\text{CO}(3-2)$, $^{13}\text{CO}(2-1)$, $\text{HCN}(4-3)$, and $\text{HCO}^+(4-3)$ molecular lines, I am able to resolve the cloud’s structure and find that it has a characteristic radius of 22 pc and a mass of $1-9 \times 10^6 M_{\odot}$. Based on the calculation of the mass, we determine that the commonly used CO-to- H_2 conversion factor in this region varies spatially, with average values in the range $X_{\text{CO}} = (0.12 - 1.1) \times 10^{20} \text{ cm}^{-2} (\text{K km s}^{-1})^{-1}$. I demonstrate that if the cloud is bound (as is circumstantially suggested by its bright,

compact morphology), an external pressure in excess of $P/k > 10^8 \text{ K cm}^{-3}$ is required. This would be consistent with theoretical expectations that globular cluster formation requires high pressure environments, much higher than typical values found in the Milky Way. The position-velocity diagram of the cloud and its surrounding material suggests that this high pressure may be produced by ram pressure from the collision of filaments. The relative line strengths of HCN and HCO⁺ in this region also suggest that these molecular lines can be used as a tracer for the evolutionary stage of a cluster.

In Chapter 3, I present a comparative study of two galaxies from the LEGUS sample: barred spiral NGC 1313 and flocculent spiral NGC 7793. These two galaxies have similar masses, metallicities, and star formation rates, but NGC 1313 is forming significantly more massive star clusters than NGC 7793. I directly compare the molecular gas in these two similar galaxies to determine the physical conditions responsible for their large disparity in cluster formation. I find surprisingly small differences between the molecular cloud populations in the two galaxies, though the largest of those differences are that NGC 1313 has higher surface densities and lower free-fall times. I find that there are much larger variations in cloud properties between different regions within each galaxy than there are between the galaxies on a global scale, especially for NGC 1313. There are higher masses, linewidths, surface densities, pressures, and virial parameters in the arms of NGC 1313 and center of NGC 7793 than in the interarm and outer regions of the galaxies. The massive cluster formation of NGC 1313 may be driven by its greater variation in environments, allowing more clouds with the necessary conditions to arise, although no one parameter seems primarily responsible for the difference in star formation. Meanwhile NGC 7793 has clouds that are as massive and have as much kinetic energy as clouds in the arms of

NGC 1313, but have densities and pressures more similar to the interarm regions and so are less inclined to collapse and form stars. The cloud properties in NGC 1313 and NGC 7793 suggest that spiral arms, interarm regions, and flocculent spirals each represent distinct environments with regard to molecular cloud populations.

In Chapter 4, I present a comparison of low- J ^{13}CO and CS observations of four different regions in the LMC—the quiescent Molecular Ridge, 30 Doradus, N159, and N113, all at a resolution of ~ 3 pc. The regions 30 Dor, N159, and N113 are actively forming massive stars, while the Molecular Ridge is forming almost no massive stars, despite its large reservoir of molecular gas and proximity to N159 and 30 Dor. I segment the emission from each region into hierarchical structures using dendrograms and analyze the sizes, masses, and linewidths of these structures. I find that the Ridge has significantly lower kinetic energy at a given size scale and also lower surface densities than the other regions, resulting in higher virial parameters. This suggests that the Ridge is not forming massive stars as actively as the other regions because it has less dense gas and not because collapse is suppressed by excess kinetic energy. I also find that these physical conditions and energy balance vary significantly within the Ridge and that this variation appears only weakly correlated with distance from sites of massive star formation such as R136 in 30 Dor, which is ~ 1 kpc away. These variations also show only a weak correlation with local star formation activity within the clouds.

In Chapter 5, I analyze ALMA and APEX observations of the Molecular Ridge of molecular lines $^{12}\text{CO}(1-0)$, $^{13}\text{CO}(1-0)$, $^{12}\text{CO}(2-1)$, $^{13}\text{CO}(2-1)$, and CS(2-1) with a new multi-line non-LTE fitting tool to produce maps of T_{kin} , n_{H_2} , and N_{CO} across the region based on models from RADEX. These maps only depend on assumptions about the abundance ratio between isotopologues. In addition to being less dependent on

assumptions than other techniques, this method is the only way to determine the volume density of the gas without making any assumptions about line-of-sight sizes. Using simulated data for a range of parameter space for each of these variables, I evaluate how well our fitting method can recover these physical parameters for the given set of molecular lines. I then compare the results of this fitting with LTE and X_{CO} methods of obtaining mass estimates and how line ratios correspond with physical conditions and find that the fitted properties differ from properties based on assuming LTE or a conversion factor by as much as 66%, indicating that those assumptions do not hold on this scale. This fitting tool allows us to more directly probe the physical conditions of the gas and estimate values of T_{kin} , n_{H_2} , and N_{CO} that are less subject to the effects of optical depth and line-of-sight projection than previous methods. The fitted n_{H_2} values show a strong correlation with the presence of YSOs, and with the total and average mass of the associated YSOs. Typical star formation diagnostics, such as mean density, dense gas fraction, and virial parameter do not show a strong correlation with YSO properties. This indicates that the fitted volume density is uniquely able to capture the relevant star-forming ability of the cloud.

Finally, in Chapter 6 I discuss the Dark Skies, Bright Kids program, an out-of-school time astronomy program that focuses on enriching science education in under-served school systems. Before, after, and throughout the program, we survey students on their perceptions of science, themselves, and their activities. I find that over the course of our program, students become more confident in their science abilities. Student ideas about science remain unchanged, but largely align with Nature of Science ideals. I also find that on days that students report they were creative and asked questions, they were more likely to say they felt like a scientist and were

interested in the day's topic, suggesting that creativity can be just as important as doing experiments for generating interest in and a sense of participating in science. Our results suggest that incorporating creativity and opportunities to ask questions can be just as important as doing experiments for generating interest in and a sense of participating in science.

Chapter 8

Appendices

A1 Beam Filling Factor in RADEX Fitting

A filling factor (defined as $f = T_{B,45''}/T_{B,\text{true}}$) is required to get accurate physical conditions. We attempted two methods of dealing with this issue: fitting the filling factor as a fourth dimension in the fitting process, and fitting ratios of the intensities rather than their absolute values to avoid the need for the filling factor at all. However, both of these methods reduce the degrees of freedom in the fitting to zero, and we found they were unable to constrain the physical parameters or the beam filling factor reliably.

There are two common types of results when fitting the filling factor. An example of the first of these is shown in Figure 8.1, using the same representative data as in Figure 5.5 that has a high signal to noise ratio (ranging from 5 for $^{13}\text{CO}(2-1)$ to 16 for $^{12}\text{CO}(1-0)$). In this plot, the filling factor is not constrained and the 4-dimensional probability distribution is multimodal. This results in a maximum likelihood point in 4-D parameter space (the blue line in Figure 8.1) that is inconsistent with the maximum of the collapsed probability profile for the filling factor (the orange line in Figure 8.1), making the results difficult to interpret.

The other common behavior when fitting the filling factor is shown in Figure 8.2 using the peak of one of the fainter clumps (numbered 21 in Figure 5.7). In this case, the filling factor is well constrained on a low value, but the resulting fit for the other parameters are highly unlikely to occur physically. The temperature is poorly constrained but pushed to high temperatures, and N_{CO} is extremely high and n_{H_2} is low, which would require a very long path length along the line of sight ($\gtrsim 80$ pc) that is inconsistent with the size of the clump being fitted (~ 10 pc). We concluded that this type of result was unphysical and unreliable, so could not be used to determine the filling factor.

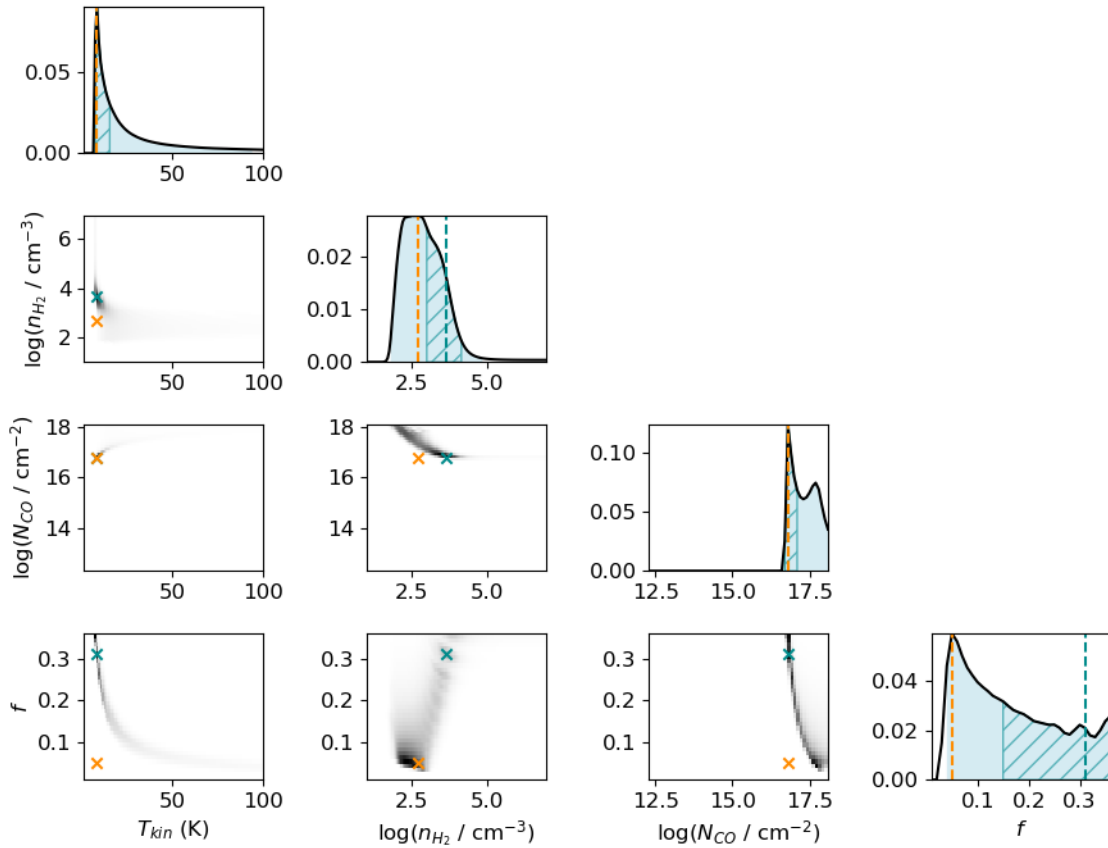


Fig. 8.1.— Example of a probability distribution from representative data (1.7 K, 0.2 K, 1.2 K, and 0.14 K for $^{12}\text{CO}(1-0)$, $^{13}\text{CO}(1-0)$, $^{12}\text{CO}(2-1)$, and $^{13}\text{CO}(2-1)$, respectively; same data, shading, and lines as in Figure 5.5) with the beam filling factor, f , added a fourth dimension to fit, with $R_{13}=100$. This results in a poorly constrained filling factor and a multimodal 4-D probability distribution. The multimodality of the probability distribution results in a major inconsistency between the peak of the 4-D probability distribution and the peak of the collapsed probability profile for the filling factor.

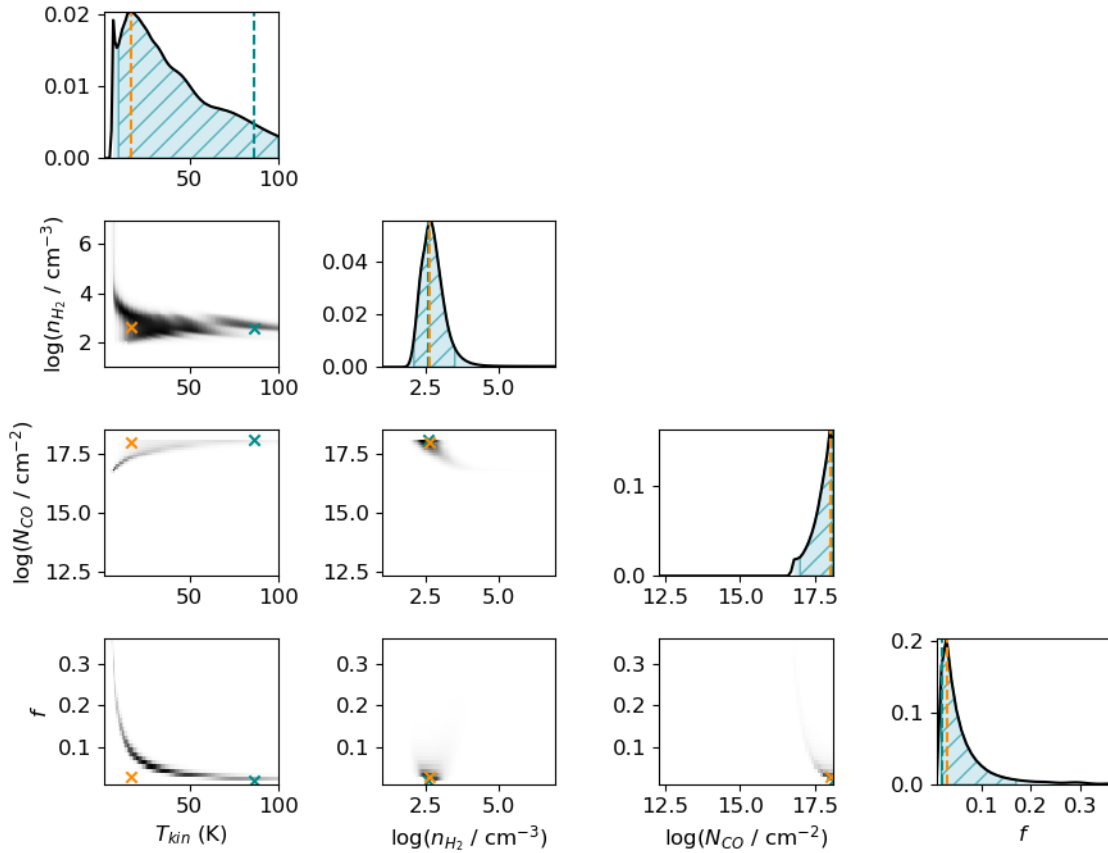


Fig. 8.2.— Example of a probability distribution from fainter data (0.96 K, 0.17 K, 0.91 K, and 0.10 K for $^{12}\text{CO}(1-0)$, $^{13}\text{CO}(1-0)$, $^{12}\text{CO}(2-1)$, and $^{13}\text{CO}(2-1)$, respectively) with the beam filling factor, f , added a fourth dimension to fit, and the same shading and lines as in Figure 5.5. This results in a well-constrained fit for the filling factor at a low value, but an unconstrained, unphysically high T_{kin} and a combination of a high N_{CO} and low n_{H_2} which would require a much longer path length than is consistent with the size of the clump ($\gtrsim 80$ pc compared to ~ 10 pc). We consider this type of fit unreliable and unphysical.

Fitting ratios from the four observations removes the filling factor from the equation entirely, assuming that all four lines are tracing the same gas with the same filling factor. However, one line must be selected as the denominator, and so the number of data points to fit is reduced to three. The resulting fit has the same issues as fitting the filling factor: either the parameters are poorly constrained or the constrained values are unphysical. Figure 8.3 shows an example of an unphysical fit from ratio fitting, where the fitted temperature is almost entirely unconstrained and the combination of a high N_{CO} and low n_{H_2} requires a long path length that is inconsistent with the size of the clump.

Since fitting the filling factor or the ratios resulted in either an unreliable or unconstrained result, and because fitting the filling factor also significantly increases the computational requirements, we assumed a range of filling factors for the region, similar to our handling of R_{13} . The upper limits were determined by calculating the ratio of the high resolution (16") ALMA $^{13}\text{CO}(1-0)$ data to that same data convolved to 45" to get an observed upper limit.

We ran `quickclump` on the high resolution ALMA $^{13}\text{CO}(1-0)$, then took the ratio of the peak of the fifty brightest clumps and the peak of the corresponding low resolution clump as defined in §5.4.1. This results in an upper limit for the filling factor of these high resolution clumps ($f < T_{B,45''}/T_{B,16''}$). Each low resolution clump had multiple corresponding high resolution clumps, so we looked at the minimum upper limit of those. All low resolution clumps had an upper limit above 20%, so we adopt an upper limit on the filling factor of 20% across the region.

The lower limit of the range comes from the fits becoming unphysical below $f \sim 10\%$. Taking lower beam filling factors results in unrealistically large temperatures with large errors, and large path lengths along the line of sight that are inconsistent

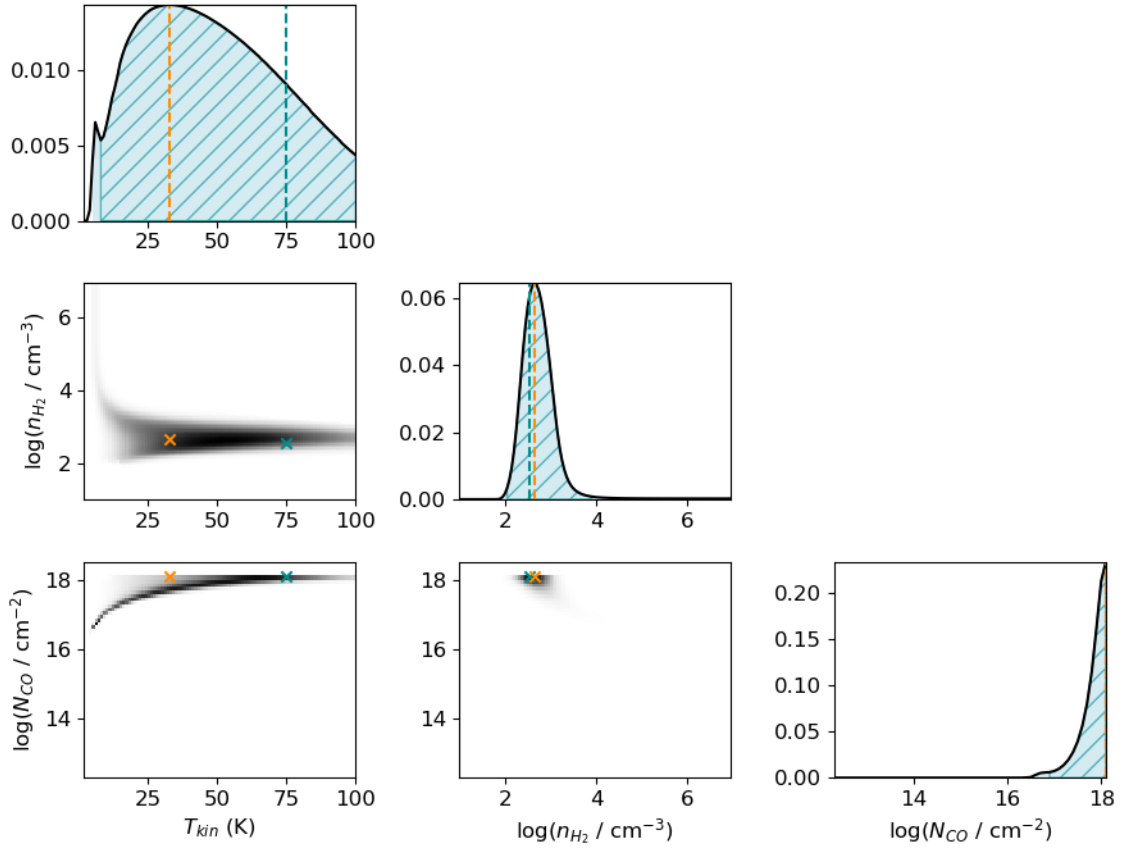


Fig. 8.3.— Example of a probability distribution from fitting the ratios of the line intensities, using $^{13}\text{CO}(1-0)$ as the denominator. This plot uses the same intensities as Figure 8.2, so the fitted ratios are 5.6, 5.3, and 0.59 for $^{12}\text{CO}(1-0)/^{13}\text{CO}(1-0)$, $^{12}\text{CO}(2-1)/^{13}\text{CO}(1-0)$, and $^{13}\text{CO}(2-1)/^{13}\text{CO}(1-0)$, respectively. The shading and lines are the same as in Figure 5.5. This results in an unconstrained, unphysically high T_{kin} and a combination of a high N_{CO} and low n_{H_2} which would require a much longer path length than is consistent with the size of the clump ($\gtrsim 80$ pc compared to ~ 10 pc). We consider this type of fit unreliable and unphysical.

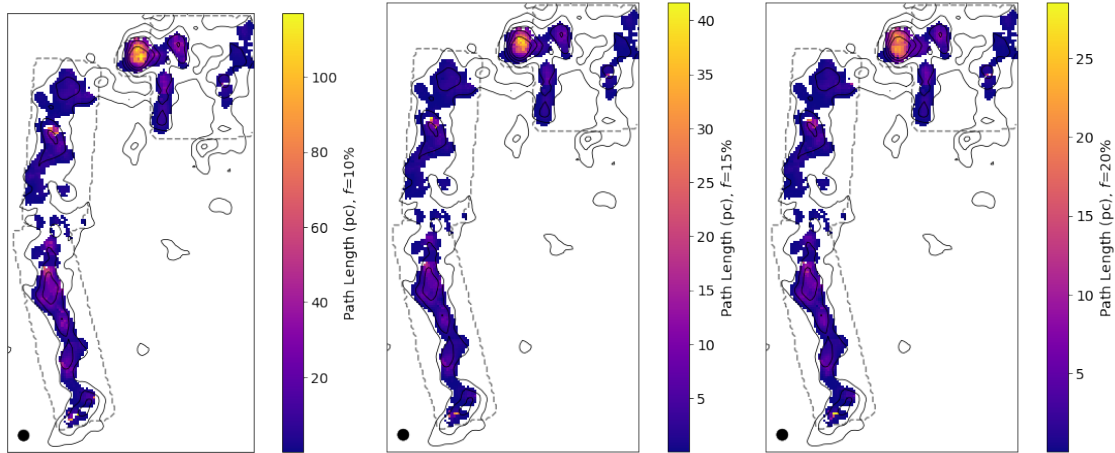


Fig. 8.4.— Line-of-sight path length of the fitting results with beam filling factors of 10%, 15%, and 20%. The path length is determined by dividing the H_2 column density in units of cm^{-2} by the H_2 volume density in units of cm^{-3} , and converted to parsecs. With a beam size of ~ 11 pc, the path length becomes unrealistically large around clumps numbered 7, 8, and 9 (Figure 5.7) when we assume $f = 10\%$, so we instead use a filling factor lower limit of 15% in that region. The contours are the $^{12}\text{CO}(1-0)$ integrated intensity as shown in Figure 5.2, and the dashed line is the common observation footprint.

with the projected size of the clumps.

We make an exception to the 10% filling factor lower limit for the clumps numbered 7, 8, and 9 in Figure 5.7. Each of these clumps return unphysical values similar to those shown in Figure 8.2 when fitted with a 10% filling factor. We show the resultant line-of-sight path length when adopting filling factors of 10%, 15%, and 20% to demonstrate the unphysical nature of the 10% results in that region. The path length is determined by dividing the H_2 column density (N_{H_2}) in units of cm^{-2} by the H_2 volume density (n_{H_2}) in units of cm^{-3} , and converted to parsecs. These types of unphysical values occur primarily when the fitted filling factor is too low, and so for these three clumps we use a filling factor of 15%, which is large enough that the results are no longer unphysical.

The assumed filling factor has the strongest effect on the fitted temperature. Due

to the highest-probability line for T_{kin} and f in the bottom left corner plots of Figures 8.1 and 8.2, at low filling factors the temperature quickly gets high with large errors, while at higher filling factors the variation in temperature levels off at lower values and varies much less. Because of this, taking a filling factor that is too low strongly affects the fitted temperature.

The density is also affected by the filling factor, though not nearly as strongly as temperature. A higher filling factor results in a higher density most, but not all, of the time. When reporting values of N_{CO} , we multiply the filling factor back into the results ($N_{\text{CO}} \times f$) to get an accurate mass calculation. This results in a value of N_{CO} that is almost entirely unaffected by the assumed filling factor.

A2 Evaluating RADEX Fitting Performance

We tested how well our multiline data with similar signal-to-noise as our Ridge measurements can be fit by this process and which of the five intervals described in §5.3.1 is best to accurately constrain the parameters (the five intervals are the three Bayesian intervals based on the 3-dimensional probability distribution and the two confidence intervals based on 1-dimensional probability profiles for each parameter). To do this evaluation, we simulated data for a range of physical parameters, covering the tested parameter space (T_{kin} between 5 and 55 K, n_{H_2} between $10^{2.5} \text{ cm}^{-3}$ and 10^6 cm^{-3} , and N_{CO} between $10^{14.5} \text{ cm}^{-2}$ and 10^{18} cm^{-2}). For each combination of these three parameters, we used RADEX to determine the expected emission from the four lines that we observe: $^{12}\text{CO}(1-0)$, $^{13}\text{CO}(1-0)$, $^{12}\text{CO}(2-1)$, and $^{13}\text{CO}(2-1)$. We then added random Gaussian noise based on the observed rms error for each line after convolving to a resolution of $45''$ in each cube to match the $^{12}\text{CO}(1-0)$ resolution: 0.11 K, 0.017 K, 0.1 K, and 0.035 K, respectively, for $^{12}\text{CO}(1-0)$, $^{13}\text{CO}(1-0)$, $^{12}\text{CO}(2-1)$, and

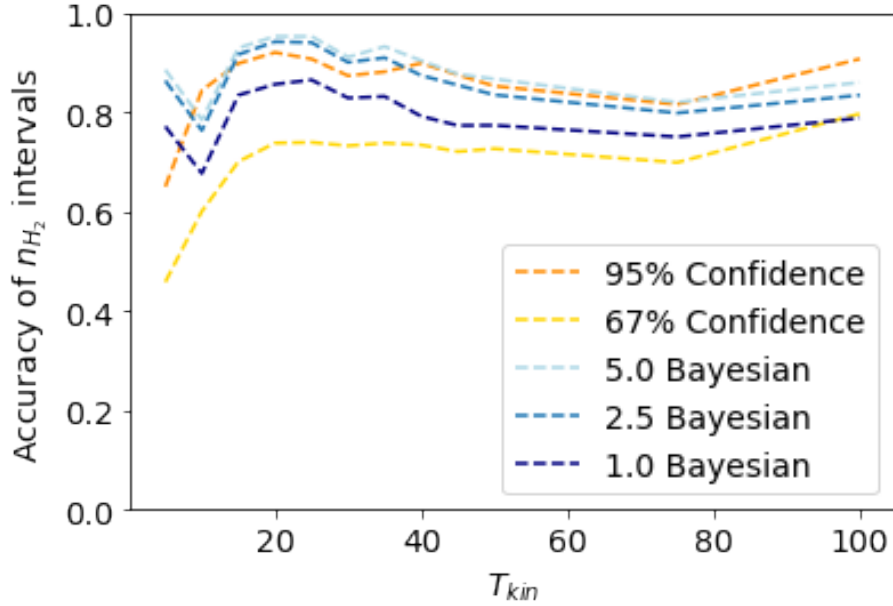


Fig. 8.5.— An example of how well we recover n_{H_2} as a function of T_{kin} . For each of the five intervals, we plot the fraction of runs in which the true model value was within the interval, averaged over all n_{H_2} and N_{CO} to get a function of T_{kin} . This plot shows that we do not robustly recover n_{H_2} when T_{kin} is low. Also, the 67% confidence interval is much less accurate than the other four intervals.

$^{13}\text{CO}(2-1)$. We did not include any beam filling factors in this process.

For each combination of physical parameters, we generated 100 instances of random Gaussian noise and then determined \vec{p}_{max} , Bayesian intervals, and confidence intervals for each instance (see §5.3.1 for a description of these calculations). In all cases we used $R_{13} = 100$. We then considered how often in these 100 instances the true model values were recovered within each of the five intervals. The recovery of each parameter depends on all three parameters (e.g., N_{CO} is better recovered at higher T_{kin} , as well as at higher N_{CO}), so to compare the five intervals' performances, we examine how each parameter is recovered as a function of each of the other two parameters as well as itself.

An example of such a plot is shown in Figure 8.5, where we compare how often

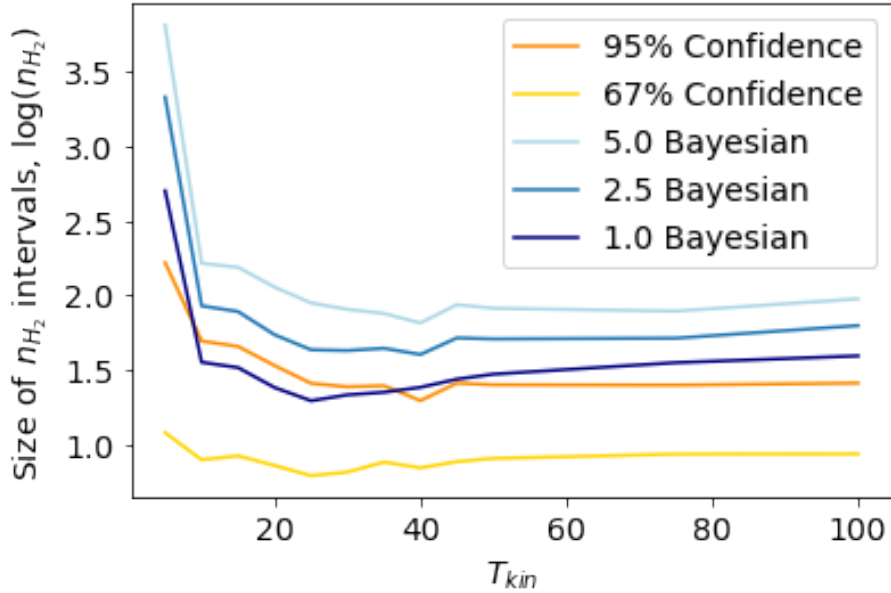


Fig. 8.6.— An example of how precise our fitting of n_{H_2} is as a function of T_{kin} . For each of the five intervals, we plot the total size of the n_{H_2} interval in dex, averaged over all n_{H_2} and N_{CO} to get a function of T_{kin} . The size shown here does not account for where within the interval the best fit value is, and it is frequently not symmetrical. At $T_{\text{kin}} < 10$ K, n_{H_2} is less constrained, by approximately an order of magnitude in most cases. Also, the 67% confidence interval constrains n_{H_2} most precisely (although we know from Fig 8.5 that it is much less accurate). Unsurprisingly, the most accurate intervals are also the least constrained.

the correct value of n_{H_2} falls in each of the five intervals as a function of T_{kin} (and so collapsed over all values of n_{H_2} and N_{CO}). This shows that we do not robustly recover the true value of n_{H_2} when T_{kin} is low. Also, the 67% confidence interval is a smaller range and contains the correct answer a much lower fraction of the time than the other wider confidence intervals, which is exactly what we would expect from a 1-sigma confidence interval.

How often the model value is in the interval tells us how accurate our fitting is, but we also want to know how precise our fitting can be. If the interval includes the entire parameter range, the true value will always be in it, but we have also done nothing

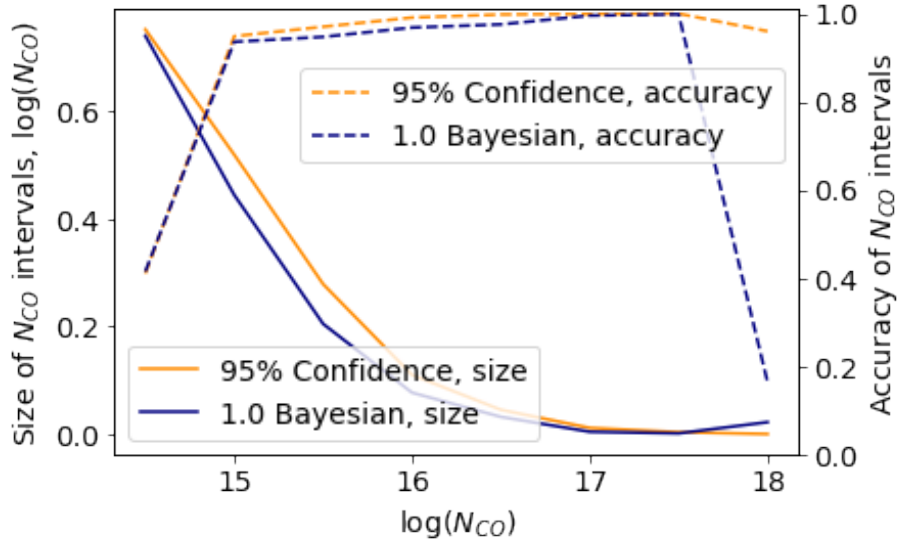


Fig. 8.7.— The accuracy and precision of the 95% confidence interval and the 1.0 Bayesian interval for N_{CO} as a function of N_{CO} (averaged over n_{H_2} and T_{kin}). At low N_{CO} , neither interval is able to accurately predict the true N_{CO} value despite the size of the interval increasing. At high N_{CO} , the Bayesian interval drops sharply in accuracy, while the confidence interval does not.

to constrain it. So, we also consider the size of each interval for each parameter, as a function of each parameter. We show an example plot of this in Figure 8.6, where the size of the five n_{H_2} intervals are again plotted as a function of T_{kin} . In this plot, n_{H_2} is better constrained when T_{kin} is high. As we would expect, the most constrained interval (the 67% confidence interval) is the least accurate (as shown in Figure 8.5), while the least constrained interval (the 5.0 Bayesian interval) is the most accurate.

From an examination of plots similar to Figures 8.5 and 8.6 for all of the parameters, the combination of the 95% confidence interval and the 1.0 Bayesian interval delivers the desired balance of accuracy and precision to fit the physical parameters to the data. There are some regions of parameter space where one is preferred over the other and vice versa, and so a combination of the two is used to fit the actual data. This is demonstrated in Figure 8.7, where at high N_{CO} ($> 10^{17.5} \text{ cm}^{-2}$), the

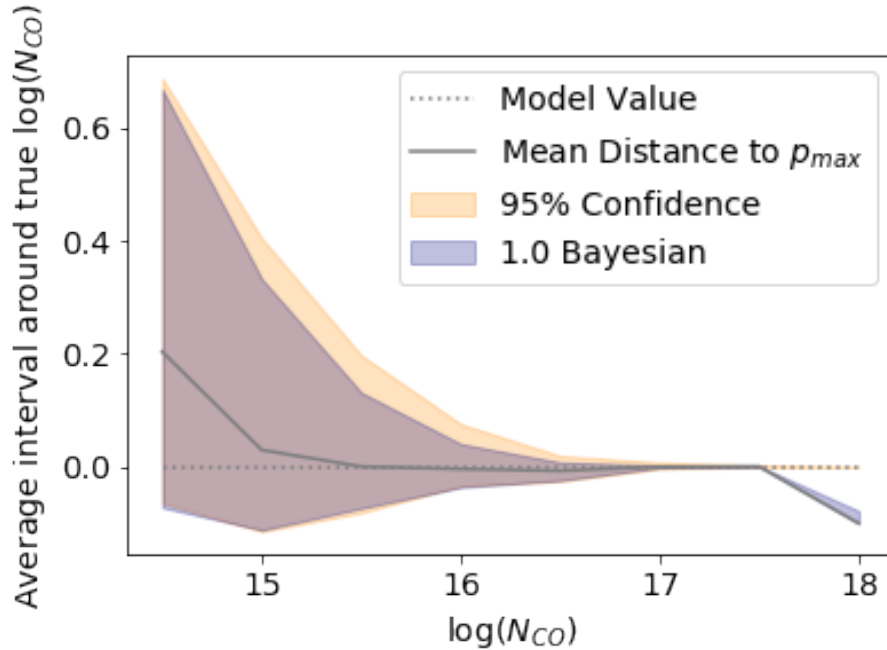


Fig. 8.8.— Offset of the 95% confidence interval, the 1.0 Bayesian interval, and \vec{p}_{\max} from the true value of N_{CO} , averaged over all T_{kin} and n_{H_2} , to get a function of N_{CO} . At low N_{CO} , both intervals as well as \vec{p}_{\max} overestimate N_{CO} . At high N_{CO} , the confidence interval is accurate and well-constrained. The Bayesian interval however is precise and inaccurate - it tightly fits an under-estimate.

1.0 Bayesian interval returns a tight constraint on the wrong value, while the 95% confidence interval tightly constrains the correct value. In other regions of parameter space, the 1.0 Bayesian interval is just as accurate as the 95% confidence interval but more precise. We use a combination of the two intervals by selecting the more precise one to determine the correct value, with one exception: When the 95% interval fits a high N_{CO} value ($> 10^{17.5} \text{ cm}^{-2}$), we always use the 95% interval since Figure 8.7 demonstrates the Bayesian interval cannot be trusted in this range.

We also consider systematic offsets (e.g., consistent over- or under-estimates) between the model values and the fitted intervals as measured by the mean distances of the model values to the edges of the intervals. We do this for the 95% confi-

dence interval, the 1.0 Bayesian interval, and \vec{p}_{max} for each parameter as a function of each parameter. We show an example of one such plot in Figure 8.8. At low N_{CO} , both intervals accurately include the true N_{CO} value, but most of the interval is an overestimate, while at high N_{CO} , the 1.0 Bayesian interval underestimates N_{CO} .

A2.1 Dependence on $^{12}\text{CO}(1-0)$

We tested the performance of the model fitting when we included only the highest resolution lines: $^{13}\text{CO}(1-0)$, $^{12}\text{CO}(2-1)$, and $^{13}\text{CO}(2-1)$. We dropped the $^{12}\text{CO}(1-0)$ since it had the worst resolution at $45''$. We then simulated data once again using the RADEX model from the same range of parameter space as above. This time we added random Gaussian noise based on the error after convolving each cube to $30''$ instead of $45''$ to match the new limiting resolution of $^{13}\text{CO}(2-1)$.

We compared the fitting performance using the measures described above to determine how much sensitivity we lose by not including the information from $^{12}\text{CO}(1-0)$. We show example plots from this comparison in Figures 8.9 and 8.10. By dropping the $^{12}\text{CO}(1-0)$, we are less sensitive to intermediate N_{CO} values: While the resulting fitted intervals still include the correct value almost all the time for $N_{\text{CO}} > 10^{15} \text{ cm}^{-2}$, they are only well-constrained for $N_{\text{CO}} > 10^{16} \text{ cm}^{-2}$. Since we expect that much of the Ridge may fall in this range of N_{CO} values, we decided that the improved sensitivity to the physical parameters is worth losing some resolution.

A comprehensive set of plots comparing the performance of fitting in the case of three lines instead of four for all parameters similar to Figures 8.5–8.10 is available as supplementary material¹.

¹<https://doi.org/10.5281/zenodo.4646288>

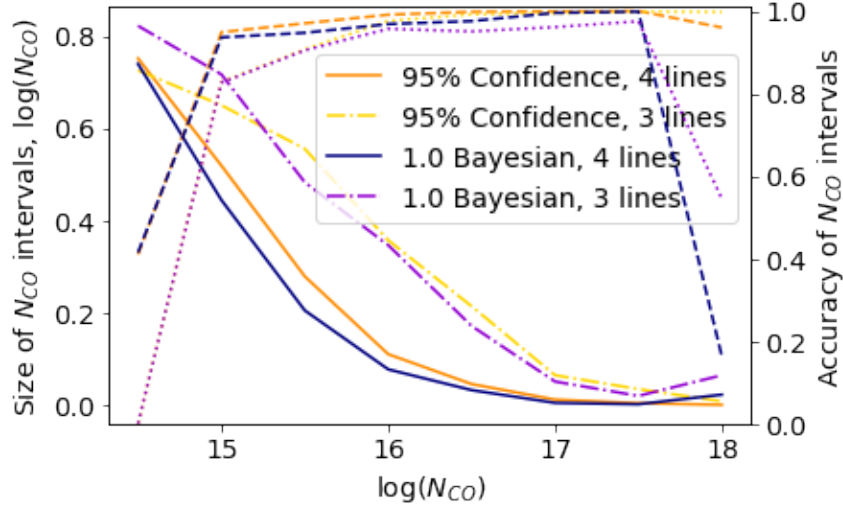


Fig. 8.9.— A comparison of how the 95% confidence interval and 1.0 Bayesian interval fit N_{CO} as a function of N_{CO} when four lines are included ($^{12}\text{CO}(1-0)$, $^{12}\text{CO}(2-1)$, $^{13}\text{CO}(1-0)$, and $^{13}\text{CO}(2-1)$), and when only three lines are included (no $^{12}\text{CO}(1-0)$). The solid lines show the sizes of the intervals, while the dashed lines show how often the true value is in the interval.

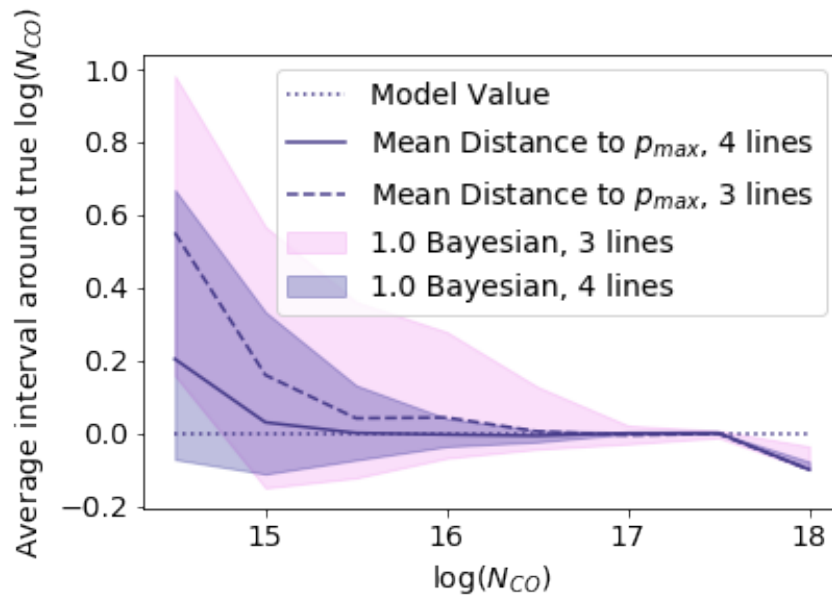


Fig. 8.10.— Offset of the 1.0 Bayesian interval and \vec{p}_{max} from the true value of N_{CO} as a function of N_{CO} when four lines are included ($^{12}\text{CO}(1-0)$, $^{12}\text{CO}(2-1)$, $^{13}\text{CO}(1-0)$, and $^{13}\text{CO}(2-1)$), and when only three lines are included (no $^{12}\text{CO}(1-0)$).

A3 RADEX Fitting Method

In addition to the method described in §5.3.2, we tested holding T_{kin} and n_{H_2} fixed for the whole clump (Clump Fixed method) and fully fitting T_{kin} and n_{H_2} for every velocity and every pixel (Full Fit method). We decided to hold T_{kin} and n_{H_2} fixed for only the line (Line Fixed method, described in §5.3.2) because this had the best physical motivation and gave the most realistic results. The Full Fit method resulted in the line edges becoming unrealistically low in T_{kin} and high in N_{CO} and having poor fits at the line edges. The Full Fit method is also less consistent with the assumptions of escape probability codes including RADEX, which assumes constant excitation across a finite-sized cloud.

The Clump Fixed method had similar results to the Line Fixed method, but the N_{CO} fits were much less constrained on the edges of the clump. Also, a uniform temperature and density profile is unrealistic for a clump, and holding these values fixed for the whole clump made the fit overly dependent on the single peak pixel, which we wanted to avoid.

We compared the resulting masses, temperatures, and densities for each clump to the masses from the Full Fit and Clump Fixed methods, rather than the Line Fixed method. A table summarizing how our measurements would change with different fitting methods is given in Table 8.1, where we show the ratio of the derived

Table 8.1: Comparison of RADEX fitting methods

	M/M_{LF}	$T_{\text{kin}}/T_{\text{kin,LF}}$	$n_{\text{H}_2}/n_{\text{H}_2,\text{LF}}$
Full Fit	1.07 ± 0.09	0.92 ± 0.12	0.81 ± 0.17
Clump Fixed	0.83 ± 0.11	1.15 ± 0.14	1.04 ± 0.42

Notes. Comparison of different methods of determining mass (from N_{CO}), T_{kin} or T_{ex} , and n_{H_2} . These values are the average of the ratios for all the clumps that were fit with these methods. M_{LF} , $T_{\text{kin,LF}}$ are the values derived from the Line Fixed RADEX fitting method.

mass, temperature, and density from alternate fitting methods and our preferred Line Fixed method, averaged across all clumps included in this analysis and the standard deviation of these ratios.

The Full Fit method results in mass, temperature, and density estimates that seem largely consistent with the Line Fixed method. The difference between these two methods is in the fitting of the line wings, and since the line wings have a much lower column density than the line peak, the mass and the mass-weighted T_{kin} and n_{H_2} are not much higher or lower than when we use the Line Fixed method. When using the Full Fit method, the lower intensities in the line wings cause the fitting to prefer lower temperatures and densities, which is compensated for with higher N_{CO} values, causing a slightly higher mass than the Line Fixed method.

The Clump Fixed method results in a lower mass and higher temperature than the Line Fixed method on average. The density is consistent with the Line Fixed method, but with larger variations. A lower mass is expected from this method, since the fitting compensates for a higher temperature by preferring a lower N_{CO} . On the edges of the clump where we would expect the temperature to be lower, it is instead fitted with the temperature from the center of the clump, causing lower N_{CO} estimates and a lower mass overall. The temperature is also expected to be higher, though the effect is not as large because T_{kin} is mass-weighted and the center of the clump where N_{CO} is highest is less affected by the constant temperature assumption.

A4 Data for Chapter 3: LEGUS Galaxy Comparison

We include demonstrative tables of the properties derived in Section 3.5, where only the first 25 entries are shown. The full tables are available as supplementary materials at the University of Virginia Dataverse² (Finn 2023). We include tables for NGC 1313 dendrogram structures (Table 8.2) and clumps (Table 8.3), and NGC 7793 dendrogram structures (Table 8.4) and clumps (Table 8.5).

²<https://doi.org/10.18130/V3/P3APTZ>

Table 8.2: Catalog of NGC 1313 dendrogram properties

ID	RA (deg)	Dec (deg)	W_{CO} (K km s ⁻¹)	CO _{max} (K)	Mass (×10 ³ M _⊙)	Radius (pc)	σ_v (km s ⁻¹)	α_{vir}	Σ (M _⊙ pc ⁻²)	$\log(P_e/k_B)$ (K cm ⁻³)	t_{ff} (Myr)
1	49.5522	-66.5107	1690±8	2.7	26±2.6	55±1.1	2.4±0.06	14±1.6	2.8±0.31	2.7±1.8	41±2.4
2	49.5517	-66.5104	234±2	2.6	3.8±0.38	19±1.1	0.59±0.03	2±0.29	3.3±0.52	2±1.2	22±2.3
3	49.5378	-66.5084	102±2	1.4	2.5±0.26	11±1.1	2.1±0.2	22±5.6	7.2±1.7	3.8±3.1	11±1.9
4	49.5662	-66.5064	96±2	1.1	2.6±0.27	15±1.1	0.69±0.007	3±0.4	4±0.73	2.4±1.4	18±2.3
5	49.5522	-66.5107	399±3	2.7	6.2±0.62	18±1.1	0.56±0.02	1±0.14	6.3±1	2.3±1.4	16±1.7
6	49.5498	-66.5087	3795±12	3.6	49±4.9	62±1.1	6±0.3	53±7.1	4±0.43	3.6±2.8	37±2.1
7	49.5382	-66.5077	1079±7	2.1	20±2	13±4	1.4±0.07	1.6±0.53	36±22	4±3.1	5.6±2.6
8	49.5374	-66.5079	116±2	1.6	2.5±0.26	7.3±1.1	2.3±0.2	18±4.4	15±4.9	4.3±3.6	6.5±1.5
9	49.5532	-66.5103	132±3	1.4	3.2±0.32	14±1.1	0.64±0.03	2.1±0.34	5.4±1	2.5±1.6	15±2
10	49.5513	-66.5094	75±2	1.6	1.6±0.17	9.3±1.1	0.44±0.002	1.2±0.2	6.1±1.6	2.4±1.4	12±2.2
11	49.5498	-66.5087	2902±10	3.6	37±3.8	62±1.1	5.5±0.2	57±6.9	3.1±0.33	3.5±2.5	41±2.4
12	49.5496	-66.5081	1120±5	3	16±1.6	19±1.1	3.2±0.08	13±1.7	15±2.2	4.1±3.2	11±1.1
13	49.5467	-66.5111	1205±7	2.7	19±1.9	38±1.1	3.5±0.2	28±4.7	4.2±0.48	3.4±2.6	28±1.9
14	49.5467	-66.5111	1636±8	2.7	26±2.6	39±1.1	3±0.09	16±1.9	5.3±0.61	3.3±2.4	25±1.7
15	49.5355	-66.5079	1955±9	2.7	31±3.1	30±35	1.7±0.04	3.2±3.7	11±25	3.3±2.3	15±27
17	49.5479	-66.5136	260±4	1.7	5.5±0.56	14±10	1.2±0.02	4.4±3.3	8.9±13	3.2±2.3	12±13
18	49.5467	-66.5108	159±2	1.8	3.2±0.33	17±3.2	0.66±0.001	2.6±0.56	3.5±1.3	2.2±1.2	21±5.8
19	49.5814	-66.5184	583±5	2.3	10±1	16±1.1	2.8±0.2	14±3.1	12±2.1	4±3.3	11±1.2
20	49.5453	-66.5110	1406±8	2.7	22±2.2	38±41	2.1±0.04	8.6±9.2	4.8±10	3±2	26±42
21	49.5478	-66.5112	291±3	1.8	5.8±0.59	25±1.1	0.53±0.003	1.4±0.16	2.9±0.39	1.8±0.79	28±2.3
22	49.5425	-66.5099	232±3	1.9	4.5±0.45	11±1.1	1.8±0.04	9±1.4	12±2.7	3.8±2.9	9±1.4
23	49.5355	-66.5079	857±6	2.7	14±1.4	25±1.1	1.9±0.06	7.5±0.96	7.1±0.97	3.3±2.4	17±1.5
24	49.5177	-66.5057	2839±11	2.4	48±4.8	37±1.1	3.9±0.06	14±1.5	11±1.3	3.9±3	17±1.1
26	49.5467	-66.5111	248±2	2.7	3.9±0.39	18±1.1	0.73±0.007	2.9±0.35	3.7±0.59	2.3±1.3	21±2.2
27	49.5464	-66.5106	81±2	1.3	2±0.21	20±1.1	0.55±0.02	3.5±0.49	1.6±0.24	1.6±0.75	34±3.3

Table 8.3: Catalog of NGC 1313 clump properties

ID	RA (deg)	Dec (deg)	W_{CO} (K km s ⁻¹)	CO _{max} (K)	Mass ($\times 10^3 M_{\odot}$)	Radius (pc)	σ_v (km s ⁻¹)	α_{vir}	Σ ($M_{\odot} \text{ pc}^{-2}$)	$\log(P_e/k_B)$ (K cm ⁻³)	t_{ff} (Myr)
1	49.6572	-66.4927	5211±10	8	40±4	19±4.6	2.8±0.02	4.3±1.2	36±18	4.5±3.5	6.7±2.5
2	49.5194	-66.5046	5884±11	7.7	46±4.6	22±6	2.9±0.02	4.4±1.3	32±18	4.3±3.3	7.7±3.3
3	49.5235	-66.5068	7222±12	7.1	60±6	20±8	3.7±0.04	5.4±2.2	46±36	4.8±3.8	6.2±3.7
4	49.6700	-66.4934	4709±9	7	39±3.9	22±3.9	2.6±0.01	4.3±0.9	26±9.8	4.2±3.2	8.5±2.3
5	49.6580	-66.4929	3738±10	6.8	32±3.2	17±1.1	3.2±0.03	6.2±0.75	35±5.7	4.6±3.6	6.5±0.72
6	49.6568	-66.4929	5991±12	6.7	51±5.1	23±1.1	5.4±0.07	15±1.7	30±4.1	4.8±3.8	8.3±0.72
7	49.6148	-66.4786	5133±12	6.5	45±4.5	17±2.3	3.2±0.04	4.7±0.77	47±13	4.7±3.7	5.7±1.1
8	49.5622	-66.5039	1865±7	6.3	17±1.7	16±1.1	2.2±0.01	5.3±0.65	21±3.5	4±3.1	8.2±0.95
9	49.5833	-66.4787	2777±8	6.3	25±2.5	16±1.8	2.5±0.02	4.7±0.7	30±7.4	4.3±3.3	6.9±1.2
10	49.6193	-66.4787	1720±7	5.8	16±1.6	14±3.5	2.3±0.03	5.6±1.5	25±12	4.2±3.2	7.2±2.6
11	49.6624	-66.4882	3290±10	5.7	31±3.1	17±2	2.5±0.05	3.8±0.62	36±9.6	4.4±3.4	6.3±1.2
12	49.6584	-66.4925	2997±9	5.5	29±2.9	18±1.1	3.2±0.02	7.3±0.87	30±4.9	4.5±3.5	7.1±0.77
13	49.6562	-66.4936	2512±9	5.5	25±2.5	18±3.9	2.3±0.02	4.3±1	25±11	4.1±3.1	7.9±2.6
14	49.5140	-66.5035	3134±9	5.5	31±3.1	14±3.5	3.8±0.1	7.6±2.1	52±27	5±4.1	4.8±1.8
15	49.5192	-66.5068	2043±7	5.5	20±2	16±3	2.4±0.03	5.5±1.2	25±9.6	4.2±3.2	7.5±2.1
16	49.6751	-66.4930	2409±8	5.4	24±2.4	22±1.1	2.4±0.03	6±0.7	16±2.3	3.9±2.9	11±0.99
17	49.6708	-66.4934	5964±11	5.3	60±6	25±1.1	4.6±0.07	10±1.2	32±4.3	4.7±3.7	8.3±0.7
18	49.5205	-66.5055	1786±8	5.2	18±1.8	21±1.1	2.2±0.04	6.4±0.76	13±1.8	3.7±2.7	12±1.1
19	49.5827	-66.4785	1919±7	5	20±2	19±1.1	2.1±0.02	4.8±0.57	18±2.8	3.9±2.9	9.6±0.98
20	49.5200	-66.5068	1345±6	5	14±1.4	15±1.1	2±0.03	5±0.64	19±3.3	3.9±3	8.4±1
21	49.5251	-66.5065	1367±6	4.9	14±1.4	17±1.1	2.1±0.03	6±0.74	16±2.7	3.9±2.9	9.6±1.1
22	49.5126	-66.5041	1610±7	4.9	17±1.7	19±1.1	2.7±0.03	9.7±1.1	14±2.2	4±3	11±1.1
23	49.6210	-66.4794	1347±6	4.7	15±1.5	17±1.1	1.9±0.02	4.7±0.57	17±2.8	3.8±2.8	9.3±1
24	49.5173	-66.5038	2726±10	4.6	30±3	17±1.1	3.2±0.09	6.8±0.9	35±5.8	4.6±3.7	6.5±0.73
25	49.5226	-66.5062	2142±8	4.5	24±2.4	13±1.7	4.1±0.06	11±1.8	45±13	5±4.1	5±1

Table 8.4: Catalog of NGC 7793 dendrogram properties

ID	RA (deg)	Dec (deg)	W_{CO} (K km s ⁻¹)	CO _{max} (K)	Mass (×10 ³ M _⊙)	Radius (pc)	σ_v (km s ⁻¹)	α_{vir}	Σ (M _⊙ pc ⁻²)	$\log(P_e/k_B)$ (K cm ⁻³)	t_{ff} (Myr)
1	359.4799	-32.5892	729±5	1.3	15±1.5	25±25	1.7±0.03	5.3±5.3	7.8±15	3.2±2.2	17±25
2	359.4799	-32.5892	185±2	1.3	3.8±0.38	10±1.6	1±0.02	3.2±0.58	11±3.5	3.3±2.3	9.1±2.1
3	359.4799	-32.6049	635±5	1.2	14±1.4	29±35	2.8±0.07	18±22	5.4±13	3.4±2.5	22±39
4	359.4776	-32.5917	2234±7	3	26±2.7	22±1.1	2.6±0.05	6.4±0.77	18±2.6	4±3.1	10±0.92
5	359.4776	-32.5917	1863±6	3	22±2.2	22±1.1	2.6±0.05	7.8±0.91	15±2	3.9±2.9	11±1
6	359.4809	-32.5915	1585±7	1.5	30±3	28±32	2.3±0.08	5.9±6.6	12±27	3.6±2.7	14±24
7	359.4771	-32.5896	608±4	1.7	11±1.1	20±6.2	1.7±0.05	6.1±2.1	8.9±5.7	3.4±2.4	14±6.6
8	359.4762	-32.5879	756±5	1.9	12±1.2	16±2.2	2±0.06	5.9±1.1	16±4.8	3.9±2.9	9.3±2.1
9	359.4792	-32.6042	417±4	1.2	9.4±0.94	41±1.1	2.8±0.2	41±6.1	1.8±0.2	2.8±2	45±2.9
10	359.4794	-32.6046	148±2	1.1	3.5±0.35	13±10	0.41±0.08	0.72±0.64	6.5±10	2.2±1.8	13±15
11	359.4765	-32.6013	2165±7	3.9	22±2.2	20±17	1.9±0.02	3.9±3.4	17±30	3.8±2.8	10±13
12	359.4765	-32.6013	1667±5	3.9	17±1.7	19±16	1.8±0.02	4.6±3.8	14±23	3.7±2.7	11±14
13	359.4756	-32.5957	203±3	1.1	4.7±0.47	24±1.1	0.63±0.03	2.4±0.34	2.6±0.35	1.9±1	28±2.4
14	359.4786	-32.5921	230±3	1.4	4.5±0.45	21±1.1	1.2±0.03	8.2±1	3.2±0.46	2.6±1.7	24±2.2
15	359.4809	-32.5915	1056±6	1.5	20±2	24±15	2±0.07	5.8±3.6	11±13	3.5±2.6	14±13
16	359.4805	-32.5888	122±2	1.2	2.6±0.27	22±1.1	1±0.02	10±1.2	1.8±0.26	2.2±1.3	32±2.9
17	359.4757	-32.6012	88±1	1.2	1.9±0.19	12±1.1	0.49±0.005	1.8±0.24	4.3±0.89	2.2±1.2	16±2.3
18	359.4777	-32.5908	1833±7	2.4	25±2.5	29±29	2±0.01	5.4±5.4	9.7±19	3.4±2.4	16±24
19	359.4739	-32.5875	62±1	1.3	1.3±0.13	10±1.1	0.22±0.002	0.46±0.069	4±0.96	1.6±0.59	15±2.5
20	359.4775	-32.6046	1049±6	1.8	18±1.8	21±10	2.2±0.04	6.5±3.2	13±13	3.8±2.8	12±8.6
21	359.4774	-32.6016	284±3	1.3	5.8±0.59	12±9.3	1.2±0.02	3.5±2.8	13±21	3.5±2.5	8.8±10
22	359.4804	-32.5977	208±3	1.1	4.9±0.49	21±1.4	0.63±0.02	2±0.28	3.5±0.59	2.1±1.2	23±2.6
23	359.4760	-32.5979	1089±5	3.3	12±1.2	21±1.1	2±0.02	7.6±0.88	9.1±1.3	3.5±2.5	14±1.3
24	359.4777	-32.5908	620±4	2.4	8.5±0.85	15±5.1	1.2±0.008	3±1	12±8.3	3.3±2.3	10±5.3
25	359.4777	-32.5908	346±2	2.4	4.7±0.47	12±5.1	1±0.02	3.1±1.4	11±9.8	3.3±2.3	9.6±6.4

Table 8.5: Catalog of NGC 7793 clump properties

ID	RA (deg)	Dec (deg)	W_{CO} (K km s ⁻¹)	CO _{max} (K)	Mass (×10 ³ M _⊙)	Radius (pc)	σ_v (km s ⁻¹)	α_{vir}	Σ (M _⊙ pc ⁻²)	$\log(P_e/k_B)$ (K cm ⁻³)	t_{ff} (Myr)
1	359.4553	-32.5808	6263±10	7	42±4.2	24±15	2.1±0.005	3.1±1.9	22±27	3.9±2.9	9.8±9
2	359.4512	-32.5872	2352±6	6.6	16±1.6	15±1.1	2.5±0.03	6.4±0.81	24±4.2	4.3±3.3	7.3±0.89
3	359.4656	-32.6028	5839±9	6.4	41±4.1	20±2.7	2.6±0.04	3.9±0.67	32±9.3	4.3±3.3	7.4±1.5
4	359.4661	-32.6028	8442±10	6.4	60±6	36±1.1	3.3±0.02	7.6±0.79	14±1.7	3.9±2.9	15±0.99
5	359.4540	-32.5818	4094±8	6.4	29±2.9	19±8.1	2.4±0.02	4.4±2	26±23	4.2±3.2	7.9±5.1
6	359.4432	-32.5836	2453±7	6	18±1.8	17±1.1	2.9±0.03	9.2±1.1	19±3.1	4.2±3.3	8.8±0.93
7	359.4578	-32.5991	4701±9	6	34±3.4	30±1.1	2.1±0.02	4.4±0.47	12±1.5	3.5±2.5	14±1.1
8	359.4612	-32.5903	15170±14	5.9	1.1e+02±11	39±23	3.9±0.06	6.2±3.8	23±28	4.2±3.2	12±11
9	359.4612	-32.5910	9829±12	5.9	71±7.1	31±21	3.7±0.02	6.9±4.6	23±30	4.3±3.3	11±11
10	359.4533	-32.5979	1978±5	5.8	15±1.5	17±1.1	2±0.01	5.2±0.62	17±2.8	3.9±2.9	9.1±1
11	359.4642	-32.5907	3755±7	5.6	28±2.8	22±13	2.4±0.01	5.4±3.2	18±21	3.9±2.9	10±9.2
12	359.4569	-32.5905	1531±5	5.6	11±1.1	14±1.1	2.6±0.07	9.2±1.3	20±3.7	4.2±3.3	7.8±1
13	359.4447	-32.6030	2239±6	5.5	18±1.8	31±1.1	1.5±0.01	4.5±0.48	5.8±0.7	2.9±1.9	22±1.6
14	359.4563	-32.5904	3315±6	5.5	25±2.5	20±6.9	2.6±0.02	6.1±2.2	20±14	4.1±3.1	9.3±4.8
15	359.4609	-32.6000	4685±9	5.4	37±3.7	16±6.7	2.2±0.01	2.4±1.1	48±42	4.5±3.5	5.3±3.4
16	359.4618	-32.5801	5024±9	5.3	40±4	22±10	2.9±0.03	5.3±2.6	27±26	4.3±3.3	8.4±6
17	359.4605	-32.5754	1746±6	5.2	14±1.4	16±1.1	1.6±0.02	3.3±0.4	17±2.9	3.7±2.7	9±1
18	359.4569	-32.5905	963±4	5.2	7.5±0.75	12±4	1.6±0.05	4.6±1.6	16±10	3.8±2.8	8.3±4
19	359.4567	-32.5931	3330±8	5.1	26±2.6	20±8.5	2.2±0.04	4.4±1.9	21±18	4±3	9.2±5.8
20	359.4479	-32.5958	4401±9	5.1	36±3.6	25±6.3	2.5±0.05	4.9±1.3	18±9.1	3.9±2.9	11±4.2
21	359.4552	-32.5909	1896±6	5	15±1.5	16±1.1	2.2±0.02	6.2±0.76	18±3.1	4±3	8.7±0.98
22	359.4301	-32.5975	5314±10	5	46±4.6	28±1.1	2.9±0.02	5.8±0.63	19±2.4	4±3	11±0.87
23	359.4260	-32.5770	4700±9	5	42±4.2	34±32	1.8±0.02	3.1±2.9	12±22	3.3±2.3	16±23
24	359.4506	-32.5951	3167±7	5	26±2.6	29±1.1	2.1±0.02	5.7±0.62	9.7±1.2	3.4±2.4	16±1.2
25	359.4666	-32.5869	2156±6	4.9	18±1.8	19±13	1.9±0.02	4.5±3.2	16±23	3.8±2.8	10±11

A5 Data for Chapter 4: Molecular Ridge Structure Analysis

Tables of all data used in Chapter 4 are presented below. This includes dendrogram and clump CO structure properties for the Ridge (Tables 8.6 and 8.7) and 30 Dor (Tables 8.8 and 8.9), and dendrogram properties only for N159 (Table 8.10), N113 (Table 8.11), and CS(2-1) structure in the Ridge (Table 8.12). Where properties were not able to be fit or which were deconvolved to become not-a-number, no value is given. For brevity, only the first 25 entries of each table are shown (unless there are fewer than 25 entries). The full tables are available as supplementary materials at the University of Virginia Dataverse³ (Finn 2023).

³<https://doi.org/10.18130/V3/P3APTZ>

Table 8.6: Catalog of Molecular Ridge dendrogram properties

Clump	W_{CO} (K km s ⁻¹)	CO(2-1) _{max} (K)	Mass ($\times 10^3 M_{\odot}$)	Radius (pc)	σ_v (km s ⁻¹)	α_{vir}	Σ ($M_{\odot} \text{ pc}^{-2}$)
0	23610	2.2	2e+02±20	47±0.085	3.3±0.04	4.8±0.3	29±3
1	11490	2.2	99±9.9	28±0.052	2.4±0.03	3.2±0.2	39±3.9
2	340	0.46	2.9±0.29	7.1±0.045	1.1±0.07	5.7±0.55	19±1.9
3	10790	2.2	93±9.3	28±0.052	2.4±0.03	3.2±0.2	36±3.6
4	10670	2.2	92±9.2	28±0.052	2.4±0.03	3.3±0.21	36±3.6
5	47	0.36	0.41±0.041	—	0.52±0.05	—	—
6	183	0.46	1.6±0.16	2.4±0.036	1.1±0.07	3.4±0.33	88±9.2
7	24	0.27	0.2±0.02	—	0.44±0.06	—	—
8	42	0.43	0.36±0.036	—	0.56±0.04	—	—
9	10360	2.4	89±8.9	9.5±0.018	3±0.03	1.8±0.11	3.2e+02±32
10	10080	2.4	87±8.7	9.6±0.018	3±0.03	1.8±0.11	3e+02±30
11	706	0.69	6.1±0.61	3.6±0.026	1.1±0.04	1.3±0.1	1.5e+02±15
12	5549	2.2	48±4.8	14±0.027	2.2±0.02	2.9±0.18	73±7.3
13	5176	2.2	44±4.4	14±0.027	2.2±0.02	3±0.19	68±6.8
14	3709	2.2	32±3.2	14±0.027	2.3±0.02	4.3±0.27	49±4.9
15	451	0.69	3.9±0.39	3.1±0.026	0.99±0.04	1.5±0.12	1.3e+02±13
16	323	0.69	2.8±0.28	2.5±0.027	0.75±0.03	0.96±0.075	1.4e+02±14
17	3428	1.7	29±2.9	14±0.032	1.6±0.02	2.3±0.15	48±4.8
18	3066	1.7	26±2.6	14±0.031	1.5±0.02	2.3±0.15	45±4.5
19	3225	1.7	28±2.8	14±0.032	1.6±0.02	2.3±0.15	45±4.5
20	3106	2.2	27±2.7	13±0.024	2.5±0.03	5.7±0.36	54±5.4
21	1022	1.5	8.8±0.88	4.3±0.016	1±0.02	0.99±0.064	1.5e+02±15
22	93	0.52	0.8±0.08	0.58±0.094	0.46±0.03	0.29±0.04	7.6e+02±2.6e+02
23	40	0.57	0.34±0.034	—	0.18±0.02	—	—
24	27	0.27	0.23±0.023	—	0.99±0.1	—	—

Table 8.7: Catalog of Molecular Ridge clump properties

Clump	W_{CO} (K km s ⁻¹)	CO(2-1) _{max} (K)	Mass ($\times 10^3 M_{\odot}$)	Radius (pc)	σ_v (km s ⁻¹)	α_{vir}	Σ (M_{\odot} pc ⁻²)
1	1565	2.6	13±1.3	3±0	1.3±0	0.69±0.042	4.8e+02±48
2	2202	2.2	19±1.9	5.2±0	0.84±0	0.36±0.022	2.2e+02±22
3	710	2.2	6.1±0.61	1.8±0	0.8±0	0.35±0.022	6e+02±60
4	1972	2.1	17±1.7	4.6±0	1.3±0	0.79±0.049	2.6e+02±26
5	899	2.1	7.7±0.77	3±0	0.67±0	0.34±0.021	2.7e+02±27
6	2505	2.4	22±2.2	1.5±0	2±0	0.52±0.032	3e+03±3e+02
7	1309	2	11±1.1	4.3±0	0.83±0	0.49±0.03	2e+02±20
8	1135	1.9	9.8±0.98	4±0	1±0	0.83±0.051	1.9e+02±19
9	818	1.9	7±0.7	2.6±0	0.85±0	0.5±0.031	3.3e+02±33
10	989	1.9	8.5±0.85	3.8±0	0.79±0	0.52±0.032	1.9e+02±19
11	1398	1.9	12±1.2	3.8±0	1±0	0.6±0.037	2.7e+02±27
12	1048	1.9	9±0.9	2.1±0	1.6±0	1.1±0.07	6.8e+02±68
13	429	1.8	3.7±0.37	0.22±0	0.67±0	0.052±0.0032	—
14	1055	1.8	9.1±0.91	3.1±0	1.2±0	0.88±0.054	3e+02±30
15	932	1.8	8±0.8	3.3±0	1±0	0.84±0.052	2.3e+02±23
16	2351	4.3	20±2	2.7±0	0.93±0	0.22±0.014	8.6e+02±86
17	1027	1.7	8.8±0.88	2±0	1.2±0	0.64±0.039	6.7e+02±67
18	2236	1.7	19±1.9	3.2±0	2.2±0	1.5±0.095	5.9e+02±59
19	931	1.7	8±0.8	2.4±0	1.3±0	0.96±0.059	4.6e+02±46
20	812	1.6	7±0.7	3.3±0	1.1±0	1±0.062	2e+02±20
21	2502	1.7	22±2.2	4.4±0	1.7±0	1.1±0.065	3.6e+02±36
22	386	1.5	3.3±0.33	0.45±0	0.81±0	0.17±0.01	—
23	867	1.6	7.5±0.75	2.4±0	1.5±0	1.5±0.089	4.1e+02±41
24	675	1.7	5.8±0.58	3.6±0	0.65±0	0.49±0.03	1.4e+02±14
25	759	1.5	6.5±0.65	4.2±0	0.86±0	0.9±0.056	1.2e+02±12

Table 8.8: Catalog of 30 Dor dendrogram properties

Clump	W_{CO} (K km s ⁻¹)	CO(2-1) _{max} (K)	Mass (×10 ³ M _⊙)	Radius (pc)	σ_v (km s ⁻¹)	α_{vir}	Σ (M _⊙ pc ⁻²)
1	447	0.12	0.24±0.024	—	0.42±0.1	—	—
2	253	0.12	0.14±0.014	—	0.31±0.09	—	—
3	634	0.13	0.34±0.034	—	0.96±0.2	—	—
4	507	0.17	0.27±0.027	1.2±0.092	0.38±0.07	1.2±0.29	63±11
5	364500	2.1	2e+02±20	11±0.021	3.4±0.04	1.2±0.075	6.1e+02±61
6	363100	2.1	2e+02±20	11±0.021	3.4±0.04	1.2±0.075	6e+02±61
7	360000	2.1	1.9e+02±19	11±0.021	3.4±0.04	1.2±0.075	6e+02±60
8	359400	2.1	1.9e+02±19	11±0.021	3.4±0.04	1.2±0.075	6e+02±60
9	1587	0.29	0.86±0.086	—	0.89±0.09	—	—
10	97	0.081	0.052±0.0052	3.5±0.11	—	—	1.5±0.17
11	337300	2.1	1.8e+02±18	11±0.021	3.3±0.04	1.2±0.076	5.6e+02±56
12	9316	0.6	5±0.5	—	1.9±0.08	—	—
13	197	0.12	0.11±0.011	—	0.42±0.1	—	—
14	826	0.14	0.45±0.045	—	1.2±0.3	—	—
15	183	0.1	0.099±0.0099	—	—	—	—
16	178	0.11	0.096±0.0096	—	0.11±0.06	—	—
17	906	0.16	0.49±0.049	—	0.93±0.2	—	—
18	323400	2.1	1.8e+02±18	11±0.021	3.3±0.04	1.2±0.077	5.4e+02±54
19	322300	2.1	1.7e+02±17	11±0.021	3.3±0.04	1.2±0.077	5.4e+02±54
20	305400	2.1	1.7e+02±17	11±0.021	3.2±0.04	1.2±0.078	5.1e+02±51
21	304500	2.1	1.6e+02±16	11±0.021	3.2±0.04	1.2±0.078	5.1e+02±51
22	295600	2.1	1.6e+02±16	11±0.021	3.1±0.03	1.2±0.076	4.9e+02±49
23	292800	2.1	1.6e+02±16	11±0.021	3.1±0.03	1.2±0.076	4.9e+02±49
24	280700	2.1	1.5e+02±15	11±0.021	3±0.03	1.1±0.072	4.7e+02±47
25	204	0.1	0.11±0.011	—	0.21±0.08	—	—

Table 8.9: Catalog of 30 Dor clump properties

Clump	W_{CO} (K km s ⁻¹)	CO(2-1) _{max} (K)	Mass ($\times 10^3 M_{\odot}$)	Radius (pc)	σ_v (km s ⁻¹)	α_{vir}	Σ (M_{\odot} pc ⁻²)
1	70390	4	38±3.8	—	1.8±0	—	—
2	37730	2.1	20±2	2.2±0	1.2±0	0.3±0.018	1.5e+03±1.5e+02
3	30520	2.3	17±1.7	—	1±0	—	—
4	54820	1.8	30±3	2.9±0	1.9±0	0.67±0.041	1.2e+03±1.2e+02
5	22310	1.9	12±1.2	1.6±0	1.1±0	0.3±0.019	1.7e+03±1.7e+02
6	37470	1.7	20±2	2.1±0	1.7±0	0.54±0.033	1.6e+03±1.6e+02
7	33370	1.6	18±1.8	3.1±0	1.4±0	0.59±0.036	6.6e+02±66
8	33860	1.8	18±1.8	1.7±0	1.6±0	0.45±0.028	2e+03±2e+02
9	18220	1.5	9.9±0.99	1.7±0	1±0	0.34±0.021	1.2e+03±1.2e+02
10	26980	1.5	15±1.5	3.6±0	0.9±0	0.37±0.023	3.9e+02±39
11	38190	1.4	21±2.1	1.1±0	2.8±0	0.78±0.048	5.9e+03±5.9e+02
12	15570	1	8.4±0.84	1.2±0	1.5±0	0.59±0.036	2.2e+03±2.2e+02
13	8685	1.1	4.7±0.47	2.1±0	0.66±0	0.36±0.022	3.7e+02±37
14	13190	0.93	7.1±0.71	1.7±0	1.5±0	1±0.062	8.3e+02±83
15	17730	1.1	9.6±0.96	2.6±0	1.1±0	0.64±0.04	5e+02±50
16	9606	0.95	5.2±0.52	—	1.4±0	—	—
17	6583	0.81	3.6±0.36	0.65±0	0.82±0	0.23±0.014	2.9e+03±2.9e+02
18	6904	0.62	3.7±0.37	1.3±0	0.97±0	0.61±0.038	7.5e+02±75
19	14230	0.87	7.7±0.77	2.8±0	1±0	0.72±0.044	3.4e+02±34
20	6949	0.95	3.8±0.38	1.9±0	0.58±0	0.31±0.019	3.7e+02±37
21	4163	0.55	2.3±0.23	0.51±0	0.79±0	0.27±0.016	2.9e+03±2.9e+02
22	10170	0.72	5.5±0.55	—	1.8±0	—	—
23	3543	0.7	1.9±0.19	—	0.66±0	—	—
24	3592	0.81	1.9±0.19	—	0.65±0	—	—
25	2694	0.79	1.5±0.15	—	0.44±0	—	—

Table 8.10: Catalog of N159 dendrogram properties

Clump	W_{CO} (K km s ⁻¹)	$CO(2-1)_{\max}$ (K)	Mass ($\times 10^3 M_{\odot}$)	Radius (pc)	σ_v (km s ⁻¹)	α_{vir}	Σ ($M_{\odot} \text{ pc}^{-2}$)
0	14790	2.6	1.7e+02±17	4.6±0.01	2.7±0.02	0.37±0.023	2.6e+03±2.6e+02
1	23400	2.6	2.8e+02±28	13±0.022	2.9±0.03	0.75±0.047	5.1e+02±51
2	8349	2.1	99±9.9	9.5±0.019	2.1±0.02	0.83±0.053	3.5e+02±35
3	45	0.41	0.54±0.054	—	0.58±0.04	—	—
4	387	0.78	4.6±0.46	2±0.024	1.5±0.05	1.8±0.14	3.7e+02±38
5	4288	2.1	51±5.1	4.2±0.012	1.9±0.02	0.55±0.035	9.1e+02±91
6	184	0.92	2.2±0.22	—	0.51±0.02	—	—
7	2752	2.1	33±3.3	3.7±0.011	1.8±0.02	0.69±0.043	7.7e+02±77
8	324	1.1	3.8±0.38	1.2±0.025	0.88±0.02	0.47±0.032	8.1e+02±88
9	1880	2.1	22±2.2	3.3±0.011	1.6±0.02	0.72±0.046	6.3e+02±63
10	5541	2.6	65±6.5	4±0.01	2.2±0.02	0.54±0.034	1.3e+03±1.3e+02
11	79	0.81	0.93±0.093	—	0.54±0.02	—	—

Table 8.11: Catalog of N113 dendrogram properties

Clump	W_{CO} (K km s ⁻¹)	$CO(2-1)_{\max}$ (K)	Mass ($\times 10^3 M_{\odot}$)	Radius (pc)	σ_v (km s ⁻¹)	α_{vir}	Σ ($M_{\odot} \text{ pc}^{-2}$)
0	353500	3.2	1.3e+02±13	5.3±0.0098	2±0.01	0.3±0.019	1.4e+03±1.4e+02
1	338400	3.2	1.2e+02±12	5.3±0.0098	2±0.01	0.31±0.019	1.4e+03±1.4e+02
2	328100	3.2	1.2e+02±12	5.3±0.0098	1.9±0.01	0.32±0.02	1.3e+03±1.3e+02
3	325700	3.2	1.2e+02±12	5.3±0.0098	1.9±0.01	0.32±0.02	1.3e+03±1.3e+02
4	285400	3.2	1e+02±10	5.3±0.0097	1.9±0.01	0.33±0.02	1.2e+03±1.2e+02
5	274200	3.2	99±9.9	5.2±0.0097	1.8±0.01	0.33±0.021	1.1e+03±1.1e+02
6	217200	3.2	79±7.9	5.1±0.0095	1.8±0.01	0.38±0.024	9.7e+02±98
7	49320	3.2	18±1.8	1.8±0.0094	1.2±0.009	0.26±0.016	1.7e+03±1.7e+02
8	30960	3	11±1.1	—	1.1±0.009	—	—
9	747	0.33	0.27±0.027	—	0.33±0.04	—	—
10	6458	1.4	2.3±0.23	1.7±0.018	0.32±0.008	0.14±0.0096	2.5e+02±26
11	6235	1.2	2.3±0.23	—	0.5±0.01	—	—
12	3432	0.6	1.2±0.12	—	0.66±0.03	—	—
13	3661	1.1	1.3±0.13	—	0.45±0.01	—	—
14	754	0.39	0.27±0.027	—	0.15±0.03	—	—
15	645	0.28	0.23±0.023	—	0.45±0.05	—	—
16	2845	0.6	1±0.1	—	0.59±0.03	—	—

Table 8.12: Catalog of Molecular Ridge CS(2-1) dendrogram properties

Clump	W_{CS} (K km s ⁻¹)	CS(2-1) _{max} (K)	Radius (pc)	σ_v (km s ⁻¹)
0	16	0.13	—	0.89±0.2
1	1038	0.61	1.5±0.058	3±0.1
2	487	0.61	1.4±0.062	1.6±0.07
3	172	0.61	—	1.3±0.06
4	6	0.1	—	0.022±0.6
5	19	0.14	—	0.57±0.1
6	198	0.61	—	0.8±0.04
7	12	0.096	—	0.71±0.3
8	78	0.34	2±0.071	1.1±0.09
9	87	0.2	2.4±0.092	1.4±0.2
10	20	0.25	—	0.4±0.06
11	8	0.099	—	0.44±0.2
12	26	0.15	—	0.66±0.1
13	198	0.21	5.4±0.08	1.5±0.2
14	10	0.14	—	0.48±0.1
15	48	0.21	—	1.5±0.2
16	26	0.34	—	0.23±0.03
17	288	0.46	5.2±0.046	1.6±0.1
18	28	0.15	3.9±0.098	0.51±0.1
19	122	0.29	1.7±0.087	0.96±0.1
20	67	0.29	0.32±0.4	0.92±0.09
21	286	0.32	8.2±0.07	1.1±0.1
22	123	0.17	8.3±0.11	1±0.2
23	84	0.17	5.8±0.092	1.3±0.2
24	110	0.33	2.9±0.06	0.86±0.08

A6 Data for Chapter 5: RADEX Fitting and YSO Comparison

Tables of the data derived and used in Chapter 5 are presented below. This includes the integrated line fluxes of each of the identified CO clumps (Table 8.13), the derived clump properties from the RADEX fitting as well as their matches YSOs (Table 8.14), and the fitted properties of the YSOs (Table 8.15).

Table 8.13: Integrated Line Fluxes of Clumps

Clump	$^{12}\text{CO}(1-0)$	$^{12}\text{CO}(2-1)$	$^{13}\text{CO}(1-0)$	$^{13}\text{CO}(2-1)$	CS(2-1)
1	70.9±0.4	62.7±0.3	5.4±0.04	6.45±0.08	0.411±0.04
2	46.3±0.3	42.7±0.3	4.84±0.04	4.18±0.07	0.229±0.03
3	42.4±0.3	—	6.97±0.05	—	1.15±0.03
4	75.7±0.4	81.7±0.4	10.1±0.06	14.4±0.1	3.07±0.04
5	58.1±0.3	57.9±0.3	8.67±0.05	7.8±0.08	1.83±0.03
6	100±0.4	83.1±0.4	9.57±0.05	8.1±0.09	0.699±0.04
7	119±0.5	98.1±0.4	10.5±0.06	8.78±0.1	1.12±0.04
8	277±0.8	202±0.6	20.1±0.08	14.6±0.1	2.68±0.06
9	31.6±0.3	28.4±0.2	2.47±0.03	2.13±0.06	0.371±0.03
10	12.4±0.2	—	1.4±0.02	—	0.27±0.02
11	57.9±0.3	—	6.2±0.05	—	1.38±0.03
12	44.6±0.3	42.4±0.3	5.32±0.04	5.19±0.06	0.463±0.03
13	34.7±0.3	38.6±0.3	4.96±0.04	4.74±0.06	0.462±0.03
14	53.5±0.3	65.6±0.4	7.34±0.05	9.21±0.08	0.816±0.03
15	9.17±0.1	11.2±0.1	0.988±0.02	1.42±0.04	0.154±0.02
16	75.9±0.4	65.3±0.3	7.62±0.05	6.33±0.08	0.335±0.03
17	59.2±0.3	55.4±0.3	7.29±0.05	7.07±0.07	0.325±0.03
18	14.6±0.2	13.1±0.2	1.82±0.02	1.98±0.04	0.0939±0.02
19	77.6±0.4	72.8±0.4	8.09±0.05	7.89±0.09	0.416±0.04
20	8.75±0.1	9.12±0.1	1.03±0.02	0.788±0.03	0.0461±0.01
21	16.1±0.2	12.5±0.2	1.54±0.02	1.74±0.05	0.0953±0.02
22	78.8±0.4	65.7±0.3	6.37±0.04	5.23±0.08	0.317±0.03
23	151±0.6	130±0.5	15.1±0.07	15±0.1	1.34±0.04
24	96.2±0.5	99.1±0.5	11.2±0.06	12.4±0.09	1.26±0.03
25	79.6±0.4	72.2±0.4	9.61±0.06	9.74±0.08	0.898±0.03
26	100±0.5	93.6±0.4	13.3±0.07	13.5±0.1	1.47±0.04
27	26.6±0.2	26.4±0.2	2.43±0.03	2.83±0.05	0.269±0.02
28	33.9±0.3	31.6±0.2	3.8±0.03	3.58±0.06	0.534±0.02
29	9.18±0.1	9.45±0.1	0.907±0.02	1.17±0.04	0.321±0.02
30	29.8±0.2	30.7±0.2	2.29±0.03	2.38±0.06	0.646±0.03
31	16.8±0.2	18.4±0.2	2.09±0.03	1.8±0.05	0.24±0.02
32	5.83±0.1	4.79±0.1	0.403±0.02	0.341±0.03	0.21±0.01

Note: All line fluxes are integrated over the whole clump in units of $10^3 \text{ K km s}^{-1} \text{ arcsec}^2$. Clumps 3, 10, and 11 do not have corresponding APEX data. The uncertainty is a 10% error from the absolute flux calibration plus the rms error added in quadrature.

Table 8.14: Derived Clump Properties

Clump ^a	Mass ^{bc} ($10^3 M_{\odot}$)	η_{H_2} ^{bc} (10^3 cm^{-3})	T_{kin} ^{bc} (K)	σ_v^c (km/s)	σ_R^c (pc)	α_{vir}^d	Number of YSOs ^e	Total M YSOs ^e (M_{\odot})
2	$9.5^{+2.5}_{-0.62}$	$2.1^{+2}_{-0.75}$	17^{+15}_{-6}	2.3 ± 0.034	6.6 ± 3.7	7.9 ± 4.6	2	8.5 ± 1.2
4	$22^{+0.63}_{-0.54}$	$3.7^{+2.2}_{-0.81}$	$18^{+5.6}_{-5.1}$	1.8 ± 0.017	8 ± 4.5	2.7 ± 1.5	3	47 ± 4.9
5	$19^{+0.83}_{-0.61}$	$2^{+1.2}_{-0.53}$	$16^{+4.5}_{-4.5}$	1.9 ± 0.024	7 ± 2.6	3.1 ± 1.2	0	—
6	$19^{+1.8}_{-0.39}$	$1.6^{+0.94}_{-0.59}$	$23^{+13}_{-8.6}$	1.8 ± 0.014	7.4 ± 2.4	3 ± 0.98	0	—
7	$18^{+0.95}_{-0.5}$	$1.7^{+0.59}_{-0.26}$	$19^{+4.9}_{-3.3}$	1.5 ± 0.0076	8.9 ± 3.8	2.6 ± 1.1	1	6.5 ± 0.87
8	$36^{+4.5}_{-2.1}$	$0.65^{+0.46}_{-0.35}$	32^{+21}_{-10}	2.2 ± 0.0096	9.3 ± 2.2	2.7 ± 0.68	0	—
12	$10^{+0.42}_{-0.34}$	$3.8^{+2.6}_{-1.3}$	$18^{+5.6}_{-5.2}$	0.97 ± 0.0057	6.7 ± 0.6	1.4 ± 0.13	2	13 ± 1.5
13	$10^{+1.2}_{-0.83}$	$2.4^{+1.8}_{-0.88}$	$20^{+8.8}_{-6.9}$	1.2 ± 0.007	7.3 ± 1.3	2.2 ± 0.47	0	—
14	$15^{+0.35}_{-0.25}$	$3.9^{+2.2}_{-1.1}$	$20^{+6.6}_{-6}$	1.6 ± 0.012	7.8 ± 0.96	3 ± 0.37	5	52 ± 3.8
16	$16^{+2.1}_{-1.3}$	$1.3^{+0.77}_{-0.44}$	$23^{+18}_{-9.9}$	2 ± 0.035	6.7 ± 0.91	3.7 ± 0.66	0	—
17	$15^{+0.43}_{-0.23}$	$2.5^{+1.1}_{-0.52}$	$19^{+7.3}_{-5.9}$	1.3 ± 0.0087	8 ± 0.48	1.9 ± 0.12	2	5.9 ± 0.83
18	$3.6^{+0.22}_{-0.16}$	$3.2^{+3.6}_{-0.94}$	$13^{+4}_{-3.5}$	1.1 ± 0.029	4.8 ± 0.84	3.5 ± 0.66	1	12 ± 1.5
19	$14^{+0.73}_{-0.58}$	$2.7^{+2}_{-0.95}$	$17^{+5.6}_{-5}$	1.8 ± 0.025	10 ± 5	5.3 ± 2.6	0	—
22	$11^{+1.1}_{-0.4}$	$1.2^{+1.4}_{-0.79}$	$23^{+9}_{-9.2}$	1.8 ± 0.013	7.9 ± 1.6	5.1 ± 1.1	0	—
23	$30^{+2.1}_{-2.4}$	$1.7^{+0.88}_{-0.53}$	36^{+22}_{-16}	1.7 ± 0.0078	8.5 ± 2.5	1.7 ± 0.53	0	—
24	$22^{+1.2}_{-1.1}$	$2.6^{+1.2}_{-0.8}$	29^{+13}_{-10}	1.6 ± 0.0088	7.7 ± 1.5	2.1 ± 0.43	2	29 ± 3.1
25	$19^{+0.95}_{-0.89}$	$2.4^{+1}_{-0.63}$	$25^{+10}_{-8.2}$	1.2 ± 0.01	7.2 ± 2.5	1.2 ± 0.42	1	5 ± 1.7
26	$26^{+1.4}_{-0.89}$	$2.5^{+1.2}_{-0.8}$	$24^{+11}_{-8.2}$	1.4 ± 0.011	6.9 ± 2.2	1.2 ± 0.39	5	45 ± 4
27	$4.1^{+0.28}_{-0.22}$	$1.8^{+2}_{-0.68}$	17^{+5}_{-5}	0.97 ± 0.012	6.1 ± 1.1	3.1 ± 0.59	1	4.9 ± 0.65
28	$8.1^{+2.3}_{-1.2}$	$3^{+3.9}_{-1.2}$	21^{+23}_{-11}	2.1 ± 0.037	5.1 ± 0.28	6.2 ± 1.3	1	3.2 ± 1.1
31	$3.4^{+0.28}_{-0.21}$	$2.6^{+2.1}_{-0.75}$	$16^{+5.9}_{-4.8}$	1.1 ± 0.02	4.9 ± 0.43	3.7 ± 0.43	0	—

^aCO clump identifying numbers are shown in Figure 5.7. Clumps 3, 10, and 11 are not included because they do not have corresponding APEX data. Clumps 1, 20, 29, 30, and 32 are not included because more than 75% of the pixels had poor RADEX fits for η_{H_2} . Clumps 9, 15, and 21 are not included because the RADEX fits had unphysical variations between pixels.

^bResult of RADEX fitting.

^cCalculation described in §5.4.2.

^dCalculated with Equation 5.7.

^eIdentifying YSOs, matching them to associated CO clumps, and fitting YSO masses is described in §5.5.

Table 8.15: Fitted YSO Properties

Name	M_* (M_\odot)	$\log(\dot{M})$ (M_\odot/yr)	Clump Assignment
J84.636381-70.144787	4.9±0.8	-5.2±0.3	1
J84.677275-70.194884	4.8±1.0	-5.2±0.3	2
J84.663696-70.163174	3.7±0.5	-5.2±0.3	2
J84.722292-70.227647	4.9±0.6	-4.6±0.3	3
J84.739529-70.22909	15.4±2.0	-6.8±0.3	3
J84.815252-70.224064	9.2±2.4	-8.0±1.1	3
J84.746459-70.227471	8.6±1.2	-4.6±0.3	3
J84.829777-70.220668	11.5±1.6	-11.3±0.4	3
J84.879808-70.20452	21.8±3.9	-7.4±0.3	4
J84.879594-70.200559	20.5±2.7	-9.1±0.3	4
053925.03-701255.0	4.6±1.3	-6.1±0.5	4
J84.962153-70.133828	6.5±0.9	-4.6±0.3	7
J85.101423-70.133438	11.2±1.8	-8.6±0.4	10
J85.057077-70.165809	15.1±2.7	-10.1±0.7	11
J85.050246-70.168067	15.4±2.0	-11.6±0.7	11
054012.00-700916.0	15.3±2.1	-6.3±0.3	11
054037.80-700914.0	6.5±0.9	-8.7±0.5	12
J85.18818-70.154154	6.2±1.2	-8.0±0.8	12
J054036.65-701201.1	4.2±1.3	-8.1±1.4	14
J85.179372-70.186003	15.4±2.0	-7.9±0.3	14
J85.193443-70.189071	15.4±2.1	-6.8±0.3	14
J85.207422-70.169937	8.1±1.5	-4.6±0.3	14
J85.192755-70.17054	8.5±1.3	-4.6±0.3	14
J85.225346-70.235587	4.7±0.8	-5.2±0.3	17
054054.33-701318.8	1.2±0.1	-7.8±0.5	17
J85.317317-70.265032	11.5±1.5	-9.1±0.3	18
J85.276729-70.393765	20.5±2.7	-9.1±0.3	24
054113.61-702329.1	9.0±1.5	-7.8±0.5	24
J054047.85-702551.1	5.0±1.7	-8.0±1.5	25
J85.18708-70.468313	20.5±2.7	-6.8±0.3	26
J85.180541-70.480586	6.5±0.9	-4.6±0.3	26
054044.25-702824.7	6.9±2.0	-5.8±0.4	26
054043.94-702918.5	4.6±1.7	-7.9±1.6	26
054038.61-702800.5	6.6±1.0	-6.9±0.3	26
J85.143381-70.523952	4.9±0.6	-5.2±0.3	27
J85.133273-70.508695	3.2±1.1	-5.2±0.3	28
J054026.85-703202.9	2.1±0.3	-11.3±0.3	29

References

- Abd-El-Khalick, F. & Lederman, N. G. 2000, *International Journal of Science Education*, 22, 665, definitely use this one in discussing our lack of NOS result!!!
- Adamo, A., Hollyhead, K., Messa, M., Ryon, J. E., Bajaj, V., Runnholm, A., Aalto, S., Calzetti, D., Gallagher, J. S., Hayes, M. J., Kruijssen, J. M. D., König, S., Larsen, S. S., Melinder, J., Sabbi, E., Smith, L. J., & Östlin, G. 2020, *MNRAS*, 499, 3267
- Adamo, A., Kruijssen, J. M., Bastian, N., Silva-villa, E., & Ryon, J. 2015, *MNRAS*, 452, 246
- Adamo, A., Ryon, J. E., Messa, M., Kim, H., Grasha, K., Cook, D. O., Calzetti, D., Lee, J. C., Whitmore, B. C., Elmegreen, B. G., Ubeda, L., Smith, L. J., Bright, S. N., Runnholm, A., Andrews, J. E., Fumagalli, M., Gouliermis, D. A., Kahre, L., Nair, P., Thilker, D., Walterbos, R., Wofford, A., Aloisi, A., Ashworth, G., Brown, T. M., Chandar, R., Christian, C., Cignoni, M., Clayton, G. C., Dale, D. A., de Mink, S. E., Dobbs, C., Elmegreen, D. M., Evans, A. S., Gallagher, J. S., I., Grebel, E. K., Herrero, A., Hunter, D. A., Johnson, K. E., Kennicutt, R. C., Krumholz, M. R., Lennon, D., Levay, K., Martin, C., Nota, A., Östlin, G., Pellerin, A., Prieto, J., Regan, M. W., Sabbi, E., Sacchi, E., Schaerer, D., Schiminovich, D., Shabani, F., Tosi, M., Van Dyk, S. D., & Zackrisson, E. 2017, *ApJ*, 841, 131

- Adamo, A., Östlin, G., & Zackrisson, E. 2011, *MNRAS*, 417, 1904
- Andre, T., Whigham, M., Hendrickson, A., & Chambers, S. 1999, *Journal of Research in Science Teaching*, 36, 719
- Archer, L., Dewitt, J., & Osborne, J. 2015, *Science Education*, 99, 199
- Archer, L., Dewitt, J., Osborne, J., Dillon, J., Willis, B., & Wong, B. 2010, *Science Education*, 94, 617
- Archer, L., Moote, J., MacLeod, E., Francis, B., & DeWitt, J. 2020, *ASPIRES 2: Young people's science and career aspirations, age 10-19*, Tech. rep., UCL Institute of Education
- Aschbacher, P. R., Li, E., & Roth, E. J. 2010, *Journal of Research in Science Teaching*, 47, 564
- Ashman, K. M. & Zepf, S. E. 2001, *AJ*, 122, 1888
- Asplund, M., Grevesse, N., Sauval, A. J., & Scott, P. 2009, *ARA&A*, 47, 481
- Aydede, M. N. & Kesercioğlu, T. 2010, in *Procedia - Social and Behavioral Sciences*, Vol. 2, 3783–3786
- Baba, J., Morokuma-Matsui, K., & Saitoh, T. R. 2017, *MNRAS*, 464, 246
- Bacchini, C., Fraternali, F., Iorio, G., & Pezzulli, G. 2019, *A&A*, 622, A64
- Ballesteros-Paredes, J., Klessen, R. S., & Vázquez-Semadeni, E. 2003, *ApJ*, 592, 188
- Baram-Tsabari, A. & Yarden, A. 2011, *International Journal of Science and Mathematics Education*, 9, 523

- Barlow, R. 2004, *Asymmetric Errors*
- Barman, C. R., Ostlund, K. L., Gatto, C. C., & Halferty, M. 1997, in *AETS Conference Proceedings*, 688
- Besla, G., Kallivayalil, N., Hernquist, L., van der Marel, R. P., Cox, T. J., & Kereš, D. 2012, *MNRAS*, 421, 2109
- Bhattacharyya, S., Mead, T. P., & Nathaniel, R. 2011, *School Science and Mathematics*, 111, 345
- Bian, L., Leslie, S. J., & Cimpian, A. 2017, *Science*, 355, 389
- Bica, E., Claria, J. J., Dottori, H., Santos, J. F. C., J., & Piatti, A. E. 1996, *ApJS*, 102, 57
- Bigiel, F., Leroy, A., Walter, F., Brinks, E., de Blok, W. J. G., Madore, B., & Thornley, M. D. 2008, *AJ*, 136, 2846
- Bland-Hawthorn, J. & Gerhard, O. 2016, *ARA&A*, 54, 529
- Bolatto, A. D., Leroy, A. K., Rosolowsky, E., Walter, F., & Blitz, L. 2008, *ApJ*, 686, 948
- Bolatto, A. D., Wolfire, M., & Leroy, A. K. 2013, *ARA&A*, 51, 207
- Bonnor, W. B. 1956, *MNRAS*, 116, 351
- Bothwell, M. S., Kennicutt, R. C., & Lee, J. C. 2009, *MNRAS*, 400, 154
- Brand, J. & Wouterloot, J. G. A. 1995, *A&A*, 303, 851
- Bredderman, T. 1983, *Review of Educational Research*, 53, 499

- Bressan, A., Marigo, P., Girardi, L., Salasnich, B., Dal Cero, C., Rubele, S., & Nanni, A. 2012, MNRAS, 427, 127
- Brinchmann, J., Charlot, S., White, S. D., Tremonti, C., Kauffmann, G., Heckman, T., & Brinkmann, J. 2004, MNRAS, 351, 1151
- Brown, G. & Gnedin, O. Y. 2021, MNRAS, 508, 5935
- Cabanac, R. A., Vanzi, L., & Sauvage, M. 2005, ApJ, 631, 252
- Calzetti, D., Kennicutt, R. C., Engelbracht, C. W., Leitherer, C., Draine, B. T., Kewley, L., Moustakas, J., Sosey, M., Dale, D. A., Gordon, K. D., Helou, G. X., Hollenbach, D. J., Armus, L., Bendo, G., Bot, C., Buckalew, B., Jarrett, T., Li, A., Meyer, M., Murphy, E. J., Prescott, M., Regan, M. W., Rieke, G. H., Roussel, H., Sheth, K., Smith, J. D. T., Thornley, M. D., & Walter, F. 2007, ApJ, 666, 870
- Calzetti, D., Lee, J. C., Sabbi, E., Adamo, A., Smith, L. J., Andrews, J. E., Ubeda, L., Bright, S. N., Thilker, D., Aloisi, A., Brown, T. M., Chandar, R., Christian, C., Cignoni, M., Clayton, G. C., Silva, R. D., Mink, S. E. D., Dobbs, C., Elmegreen, B. G., Elmegreen, D. M., Evans, A. S., Fumagalli, M., Gallagher, J. S., Gouliermis, D. A., Grebel, E. K., Herrero, A., Hunter, D. A., Johnson, K. E., Kennicutt, R. C., Kim, H., Krumholz, M. R., Lennon, D., Levay, K., Martin, C., Nair, P., Nota, A., Östlin, G., Pellerin, A., Prieto, J., Regan, M. W., Ryon, J. E., Schaerer, D., Schiminovich, D., Tosi, M., Dyk, S. D. V., Walterbos, R., Whitmore, B. C., & Wofford, A. 2015, AJ, 149
- Carignan, C. & Puche, D. 1990, AJ, 100, 394
- Carli, L. L., Alawa, L., Lee, Y. A., Zhao, B., & Kim, E. 2016, Psychology of Women Quarterly, 40, 244

- Carlson, L. R., Sewilo, M., Meixner, M., Romita, K. A., & Lawton, B. 2012, *A&A*, 542, A66
- Castets, A., Duvert, G., Dutrey, A., Bally, J., Langer, W. D., & Wilson, R. W. 1990, *A&A*, 234, 469
- Ceci, S. J., Williams, W. M., & Barnett, S. M. 2009, *Psychological Bulletin*, 135, 218
- Chandrasekhar, S. 1967, *An introduction to the study of stellar structure* (Dover Publications, Inc.)
- Chen, C. H. R., Indebetouw, R., Chu, Y.-H., Gruendl, R. A., Testor, G., Heitsch, F., Seale, J. P., Meixner, M., & Sewilo, M. 2010, *ApJ*, 721, 1206
- Cheryan, S., Master, A., & Meltzoff, A. N. 2015, *Frontiers in Psychology*, 6
- Chevance, M., Kruijssen, J. M. D., Vazquez-Semadeni, E., Nakamura, F., Klessen, R., Ballesteros-Paredes, J., Inutsuka, S.-i., Adamo, A., & Hennebelle, P. 2020a, *Space Sci. Rev.*, 216, 50
- Chevance, M., Madden, S. C., Fischer, C., Vacca, W. D., Lebouteiller, V., Fadda, D., Galliano, F., Indebetouw, R., Kruijssen, J. M. D., Lee, M.-Y., Poglitsch, A., Polles, F. L., Cormier, D., Hony, S., Iserlohe, C., Krabbe, A., Meixner, M., Sabbi, E., & Zinnecker, H. 2020b, *MNRAS*, 494, 5279
- Choi, Y., Olsen, K. A. G., Besla, G., van der Marel, R. P., Zivick, P., Kallivayalil, N., & Nidever, D. L. 2022, *ApJ*, 927, 153
- Christensen, M. B. E. 2019, *Frontiers for Young Minds*, 7:92
- Chun, K. & Harris, E. 2011, *STEM Out-of-School Time Programs for Girls*, Tech. rep., Harvard Family Research Project

- Cignoni, M., Sabbi, E., van der Marel, R. P., Tosi, M., Zaritsky, D., Anderson, J., Lennon, D. J., Aloisi, A., de Marchi, G., Gouliermis, D. A., Grebel, E. K., Smith, L. J., & Zeidler, P. 2015, *ApJ*, 811, 76
- Cohen, R. S., Dame, T. M., Garay, G., Montani, J., Rubio, M., & Thaddeus, P. 1988, *ApJ*, 331, L95
- Colombo, D., Hughes, A., Schinnerer, E., Meidt, S. E., Leroy, A. K., Pety, J., Dobbs, C. L., García-Burillo, S., Dumas, G., Thompson, T. A., Schuster, K. F., & Kramer, C. 2014, *ApJ*, 784
- Conselice, C. J. 2006, *ApJ*, 638, 686
- Costa, A. H., Johnson, K. E., Indebetouw, R., Finn, M. K., Brogan, C. L., & Reines, A. 2021, *ApJ*, 918, 76
- Curran, F. C. & Kellogg, A. T. 2016, *Educational Researcher*, 45, 273
- Davies, R. D., Elliott, K. H., & Meaburn, J. 1976, *MmRAS*, 81, 89
- Davis. 2021, in prep
- de Vaucouleurs, G. 1963, *ApJ*, 137, 720
- DeWitt, J. & Archer, L. 2015, *International Journal of Science Education*, 37, 2170
- Dicaire, I., Carignan, C., Amram, P., Marcelin, M., Hlavacek-Larrondo, J., de Denus-Baillargeon, M. M., Daigle, O., & Hernandez, O. 2008, *AJ*, 135, 2038
- Dobashi, K., Bernard, J. P., Hughes, A., Paradis, D., Reach, W. T., & Kawamura, A. 2008, *A&A*, 484, 205

- Dobbs, C. L., Adamo, A., Few, C. G., Calzetti, D., Dale, D. A., Elmegreen, B. G., Evans, A. S., Gouliermis, D. A., Grasha, K., Grebel, E. K., Johnson, K. E., Kim, H., Lee, J. C., Messa, M., Ryon, J. E., Smith, L. J., Thilker, D., Ubeda, L., & Whitmore, B. 2017, MNRAS, 464, 3580
- Dobbs, C. L., Burkert, A., & Pringle, J. E. 2011, MNRAS, 413, 2935
- Dobbs, C. L., Pettitt, A. R., Corbelli, E., & Pringle, J. E. 2018, MNRAS, 478, 3793
- Dobbs, C. L. & Pringle, J. E. 2013, MNRAS, 432, 653
- Dobbs, C. L., Pringle, J. E., & Naylor, T. 2013, MNRASL, 437
- Dobbs, C. L., Rosolowsky, E., Pettitt, A. R., Braine, J., Corbelli, E., & Sun, J. 2019, MNRAS, 485, 4997
- Donovan Meyer, J., Koda, J., Momose, R., Mooney, T., Egusa, F., Carty, M., Kenicutt, R., Kuno, N., Rebolledo, D., Sawada, T., Scoville, N., & Wong, T. 2013, ApJ, 772
- Ebert, R. 1955, ZAp, 37, 217
- Elmegreen, B. G. 1989, ApJ, 338, 178
- Elmegreen, B. G. 2009, Astrophysics and Space Science, 324, 83
- Elmegreen, B. G. 2018, ApJ, 854, 16
- Elmegreen, B. G. & Efremov, Y. N. 1997, ApJ, 480, 235
- Elmegreen, B. G. & Falgarone, E. 1996, ApJ, 471, 816
- Elmegreen, B. G., Kim, S., & Staveley-Smith, L. 2001, ApJ, 548, 749

- Elmegreen, B. G. & Scalo, J. 2004, *ARA&A*, 42, 211
- Elmegreen, D. M. & Elmegreen, B. G. 1984, *ApJS*, 54, 127
- Elmegreen, D. M., Elmegreen, B. G., Adamo, A., Aloisi, A., Andrews, J., Annibali, F., Bright, S. N., Calzetti, D., Cignoni, M., Evans, A. S., Gallagher, John S., I., Gouliermis, D. A., Grebel, E. K., Hunter, D. A., Johnson, K., Kim, H., Lee, J., Sabbi, E., Smith, L. J., Thilker, D., Tosi, M., & Ubeda, L. 2014, *ApJ*, 787, L15
- Evans, Neal J., I. 1999, *ARA&A*, 37, 311
- Evans, Neal J., I., Dunham, M. M., Jørgensen, J. K., Enoch, M. L., Merín, B., van Dishoeck, E. F., Alcalá, J. M., Myers, P. C., Stapelfeldt, K. R., Huard, T. L., Allen, L. E., Harvey, P. M., van Kempen, T., Blake, G. A., Koerner, D. W., Mundy, L. G., Padgett, D. L., & Sargent, A. I. 2009, *ApJS*, 181, 321
- Faesi, C. M., Lada, C. J., & Forbrich, J. 2016, *ApJ*, 821, 125
- Falgarone, E., Phillips, T. G., & Walker, C. K. 1991, *ApJ*, 378, 186
- Fall, S. M. & Zhang, Q. 2001, *ApJ*, 561, 751
- Field, G. B., Blackman, E. G., & Keto, E. R. 2011, *MNRAS*, 416, 710
- Finn, M. 2023, Data for Environmental Conditions of the Extremes of Star Formation
- Finn, M. K., , & Team, D. S. B. K. 2020, in *Embracing the Future: Astronomy Teaching And Public Engagement ASP Conference Series*, ed. G. Schultz, J. Barnes, A. Fraknoi, & L. Shore, Vol. 531 (Astronomical Society of the Pacific)
- Finn, M. K., Indebetouw, R., Johnson, K. E., Costa, A. H., Chen, C.-H. R., Kawamura, A., Onishi, T., Ott, J., Sewiło, M., Tokuda, K., Wong, T., & Zahorecz, S. 2022, *AJ*, 164, 64

- Finn, M. K., Indebetouw, R., Johnson, K. E., Costa, A. H., Chen, C. H. R., Kawamura, A., Onishi, T., Ott, J., Tokuda, K., Wong, T., & Zahorecz, S. 2021, *ApJ*, 917, 106
- Finn, M. K., Johnson, K. E., Brogan, C. L., Wilson, C. D., Indebetouw, R., Harris, W. E., Kamenetzky, J., & Bemis, A. 2019, *ApJ*, 874, 120
- Finn, M. K., Mazzei, R., Drechsler, B., Telkamp, Z., Rao, M., Agrawal, P., & McAlister, A. 2023, *Journal of STEM Outreach*
- Fomalont, E., van Kempen, T., Kneissl, R., Marcelino, N., Barkats, D., Corder, S., Cortes, P., Hills, R., Lucas, R., Manning, A., & Peck, A. 2014, *The Messenger*, 155, 19
- Fry, R., Kennedy, B., & Funk, C. 2021, *STEM Jobs See Uneven Progress in Increasing Gender, Racial and Ethnic Diversity*, Tech. rep., Pew Research Center
- Fukui, Y., Harada, R., Tokuda, K., Morioka, Y., Onishi, T., Torii, K., Ohama, A., Hattori, Y., Nayak, O., Meixner, M., Sewiło, M., Indebetouw, R., Kawamura, A., Saigo, K., Yamamoto, H., Tachihara, K., Minamidani, T., Inoue, T., Madden, S., Galametz, M., Lebouteiller, V., Mizuno, N., & Chen, C. H. R. 2015, *ApJ*, 807, L4
- Fukui, Y., Kawamura, A., Minamidani, T., Mizuno, Y., Kanai, Y., Mizuno, N., Onishi, T., Yonekura, Y., Mizuno, A., Ogawa, H., & Rubio, M. 2008, *ApJS*, 178, 56
- Fukui, Y., Tokuda, K., Saigo, K., Harada, R., Tachihara, K., Tsuge, K., Inoue, T., Torii, K., Nishimura, A., Zahorecz, S., Nayak, O., Meixner, M., Minamidani, T., Kawamura, A., Mizuno, N., Indebetouw, R., Sewiło, M., Madden, S., Galametz, M., Lebouteiller, V., Chen, C. H. R., & Onishi, T. 2019, *ApJ*, 886, 14

- Fukui, Y., Torii, K., Hattori, Y., Nishimura, A., Ohama, A., Shimajiri, Y., Shima, K., Habe, A., Sano, H., Kohno, M., Yamamoto, H., Tachihara, K., & Onishi, T. 2018, *ApJ*, 859, 166
- Fukui, Y., Tsuge, K., Sano, H., Bekki, K., Yozin, C., Tachihara, K., & Inoue, T. 2017, *PASJ*, 69, L5
- Furuta, T., Kaneda, H., Kokusho, T., Ishihara, D., Nakajima, Y., Fukui, Y., & Tsuge, K. 2019, *PASJ*, 71, 95
- Furuta, T., Kaneda, H., Kokusho, T., Nakajima, Y., Fukui, Y., & Tsuge, K. 2021, *PASJ*, 73, 864
- Gao, Q., Wang, W., Liu, J.-F., & Yoachim, P. 2016, arXiv e-prints, arXiv:1602.07841
- Gao, Y. & Solomon, P. M. 2004, *ApJ*, 606, 271
- Gerner, T., Beuther, H., Semenov, D., Linz, H., Vasyunina, T., Bihr, S., Shirley, Y. L., & Henning, T. 2014, *A&A*, 563, A97
- Geyer, M. P. & Burkert, A. 2001, *MNRAS*, 323, 988
- Ginard, D., González-García, M., Fuente, A., Cernicharo, J., Alonso-Albi, T., Pilleri, P., Gerin, M., García-Burillo, S., Ossenkopf, V., Rizzo, J. R., Kramer, C., Goicoechea, J. R., Pety, J., Berné, O., & Joblin, C. 2012, *A&A*, 543, A27
- Ginsburg, A., Bally, J., Barnes, A., Bastian, N., Battersby, C., Beuther, H., Brogan, C., Contreras, Y., Corby, J., Darling, J., De Pree, C., Galván-Madrid, R., Garay, G., Henshaw, J., Hunter, T., Kruijssen, J. M. D., Longmore, S., Lu, X., Meng, F., Mills, E. A. C., Ott, J., Pineda, J. E., Sánchez-Monge, Á., Schilke, P., Schmiedeke, A., Walker, D., & Wilner, D. 2018, *ApJ*, 853, 171

- Gong, M., Ostriker, E. C., Kim, C.-G., & Kim, J.-G. 2020, *ApJ*, 903, 142
- Gooding, J. & Metz, B. 2011, *The Science Teacher*, 34
- Goodman, A. A., Barranco, J. A., Wilner, D. J., & Heyer, M. H. 1998, *ApJ*, 504, 223
- Grasha, K., Calzetti, D., Adamo, A., Kim, H., Elmegreen, B. G., Gouliermis, D. A., Dale, D. A., Fumagalli, M., Grebel, E. K., Johnson, K. E., Kahre, L., Kennicutt, R. C., Messa, M., Pellerin, A., Ryon, J. E., Smith, L. J., Shabani, F., Thilker, D., & Ubeda, L. 2017a, *ApJ*, 840, 113
- Grasha, K., Calzetti, D., Bittle, L., Johnson, K. E., Donovan Meyer, J., Kennicutt, R. C., Elmegreen, B. G., Adamo, A., Krumholz, M. R., Fumagalli, M., Grebel, E. K., Gouliermis, D. A., Cook, D. O., Gallagher, J. S., Aloisi, A., Dale, D. A., Linden, S., Sacchi, E., Thilker, D. A., Walterbos, R. A., Messa, M., Wofford, A., & Smith, L. J. 2018, *MNRAS*, 481, 1016
- Grasha, K., Chen, Q. H., Battisti, A. J., Acharyya, A., Ridolfo, S., Poehler, E., Mably, S., Verma, A. A., Hayward, K. L., Kharbanda, A., Poetrodjojo, H., Seibert, M., Rich, J. A., Madore, B. F., & Kewley, L. J. 2022, *ApJ*, 929, 118
- Grasha, K., Elmegreen, B. G., Calzetti, D., Adamo, A., Aloisi, A., Bright, S. N., Cook, D. O., Dale, D. A., Fumagalli, M., Gallagher, J. S., I., Gouliermis, D. A., Grebel, E. K., Kahre, L., Kim, H., Krumholz, M. R., Lee, J. C., Messa, M., Ryon, J. E., & Ubeda, L. 2017b, *ApJ*, 842, 25
- Grudić, M. Y., Hopkins, P. F., Faucher-Giguère, C.-A., Quataert, E., Murray, N., & Kereš, D. 2018, *MNRAS*, 475, 3511
- Gruendl, R. A. & Chu, Y.-H. 2009, *ApJS*, 184, 172

- Gunderson, E. A., Ramirez, G., Levine, S. C., & Beilock, S. L. 2012, *Sex Roles*, 66, 153
- Hannon, S., Lee, J. C., Whitmore, B. C., Chandar, R., Adamo, A., Mobasher, B., Aloisi, A., Calzetti, D., Cignoni, M., Cook, D. O., Dale, D., Deger, S., della Bruna, L., Elmegreen, D. M., Gouliermis, D. A., Grasha, K., Grebel, E. K., Herrero, A., Hunter, D. A., Johnson, K. E., Kennicutt, R., Kim, H., Sacchi, E., Smith, L., Thilker, D., Turner, J., Walterbos, R. A., & Wofford, A. 2019, *MNRAS*, 490, 4648
- Harris, W. E., Harris, G. L. H., & Alessi, M. 2013, *ApJ*, 772, 82
- Harris, W. E. & Pudritz, R. E. 1994, *ApJ*, 429, 177
- Haworth, T. J., Shima, K., Tasker, E. J., Fukui, Y., Torii, K., Dale, J. E., Takahira, K., & Habe, A. 2015, *MNRAS*, 454, 1634
- Hayes, C. R., Matthews, A. M., Song, Y., Linden, S. T., Wilson, R. F., Finn, M., Huang, X., Johnson, K. E., Mcalister, A. M., Prager, B., Seifert, R., Liss, S. E., Burkhardt, A. M., & Troup, N. 2020, *Physical Review Physics Education Research*, 16
- Heikkilä, A., Johansson, L. E. B., & Olofsson, H. 1999, *A&A*, 344, 817
- Henize, K. G. 1956, *ApJS*, 2, 315
- Hernandez, S., Winch, A., Larsen, S., James, B. L., & Jones, L. 2022, *AJ*, 164, 89
- Herrera, C. N., Boulanger, F., & Nesvadba, N. P. H. 2011, *A&A*, 534, A138
- Herrera, C. N., Boulanger, F., Nesvadba, N. P. H., & Falgarone, E. 2012, *A&A*, 538, L9

- Heyer, M. & Dame, T. M. 2015, *ARA&A*, 53, 583
- Heyer, M., Krawczyk, C., Duval, J., & Jackson, J. M. 2009, *ApJ*, 699, 1092
- Heyer, M. H., Carpenter, J. M., & Snell, R. L. 2001, *ApJ*, 551, 852
- Howard, C. S., Pudritz, R. E., & Harris, W. E. 2018, *Nature Astronomy*, 2, 725
- Hughes, A., Wong, T., Ott, J., Muller, E., Pineda, J. L., Mizuno, Y., Bernard, J. P., Paradis, D., Maddison, S., Reach, W. T., Staveley-Smith, L., Kawamura, A., Meixner, M., Kim, S., Onishi, T., Mizuno, N., & Fukui, Y. 2010, *MNRAS*, 406, 2065
- Hunt, L. K., García-Burillo, S., Casasola, V., Caselli, P., Combes, F., Henkel, C., Lundgren, A., Maiolino, R., Menten, K. M., Testi, L., & Weiss, A. 2015, *A&A*, 583, A114
- Hunter. 2023, *PASP*
- Indebetouw, R., Brogan, C., Chen, C. H. R., Leroy, A., Johnson, K., Muller, E., Madden, S., Cormier, D., Galliano, F., Hughes, A., Hunter, T., Kawamura, A., Kepley, A., Lebouteiller, V., Meixner, M., Oliveira, J. M., Onishi, T., & Vasyunina, T. 2013, *ApJ*, 774, 73
- Indebetouw, R., Whitney, B. A., Kawamura, A., Onishi, T., Meixner, M., Meade, M. R., Babler, B. L., Hora, J. L., Gordon, K., Engelbracht, C., Block, M., & Misselt, K. 2008, *AJ*, 136, 1442
- Indebetouw, R., Wong, T., Chen, C. H. R., Kepley, A., Lebouteiller, V., Madden, S., & Oliveira, J. M. 2020, *ApJ*, 888, 56
- Johnson, K. 2002, *Science*, 297, 776

- Johnson, K. E., Brogan, C. L., Indebetouw, R., Testi, L., Wilner, D. J., Reines, A. E., Chen, C. H. R., & Vanzi, L. 2018, *ApJ*, 853, 125
- Johnson, K. E., Hunt, L. K., & Reines, A. E. 2009, *AJ*, 137, 3788
- Johnson, K. E. & Kobulnicky, H. A. 2003, *ApJ*, 597, 923
- Johnson, K. E., Leroy, A. K., Indebetouw, R., Brogan, C. L., Whitmore, B. C., Hibbard, J., Sheth, K., & Evans, A. S. 2015, *ApJ*, 806, 35
- Johnson, L. C., Seth, A. C., Dalcanton, J. J., Beerman, L. C., Fouesneau, M., Lewis, A. R., Weisz, D. R., Williams, B. F., Bell, E. F., Dolphin, A. E., Larsen, S. S., Sandstrom, K., & Skillman, E. D. 2016, *ApJ*, 827, 33
- Johnson, L. C., Seth, A. C., Dalcanton, J. J., Beerman, L. C., Fouesneau, M., Weisz, D. R., Bell, T. A., Dolphin, A. E., Sandstrom, K., & Williams, B. F. 2017, *ApJ*, 839, 78
- Kacharov, N., Neumayer, N., Seth, A. C., Cappellari, M., McDermid, R., Walcher, C. J., & Böker, T. 2018, *MNRAS*, 480, 1973
- Karpudewan, M., Zain, A. N. M., & Chandrasegaran, A. 2017, *Overcoming students' misconceptions in science* (Springer)
- Kauffmann, J., Pillai, T., Zhang, Q., Menten, K. M., Goldsmith, P. F., Lu, X., & Guzmán, A. E. 2017, *A&A*, 603, A89
- Keller, C. 2001, *Journal of Social Psychology*, 141, 165
- Kennicutt, Robert C., J. 1998, *ApJ*, 498, 541
- Kennicutt, R. C. & Evans, N. J. 2012, *ARA&A*, 50, 531

- Khullar, S., Krumholz, M. R., Federrath, C., & Cunningham, A. J. 2019, MNRAS, 488, 1407
- Kim, J.-G., Kim, W.-T., & Ostriker, E. C. 2018, ApJ, 859, 68
- Kind, P. M. & Kind, V. 2007, Studies in Science Education, 43, 37
- Koda, J., Hirota, A., Egusa, F., Sakamoto, K., Sawada, T., Heyer, M., Baba, J., Boissier, S., Calzetti, D., Donovan Meyer, J., Elmegreen, B. G., Gil de Paz, A., Harada, N., Ho, L. C., Kobayashi, M. I. N., Kuno, N., Lee, A. M., Madore, B. F., Maeda, F., Martin, S., Muraoka, K., Nakanishi, K., Onodera, S., Pineda, J. L., Scoville, N., & Watanabe, Y. 2023, arXiv e-prints, arXiv:2303.12108
- Koda, J., Scoville, N., Hasegawa, T., Calzetti, D., Donovan Meyer, J., Egusa, F., Kennicutt, R., Kuno, N., Louie, M., Momose, R., Sawada, T., Sorai, K., & Umei, M. 2012, ApJ, 761
- Koda, J., Scoville, N., Sawada, T., Vigne, M. A. L., Vogel, S. N., Potts, A. E., Carpenter, J. M., Corder, S. A., Wright, M. C., White, S. M., Zauderer, B. A., Patience, J., Sargent, A. I., Bock, D. C., Hawkins, D., Hodges, M., Kembball, A., Lamb, J. W., Plambeck, R. L., Pound, M. W., Scott, S. L., Teuben, P., & Woody, D. P. 2009, ApJ, 700
- Koeppen, J. & Kegel, W. H. 1980, A&AS, 42, 59
- Koribalski, B. S., Staveley-Smith, L., Kilborn, V. A., Ryder, S. D., Kraan-Korteweg, R. C., Ryan-Weber, E. V., Ekers, R. D., Jerjen, H., Henning, P. A., Putman, M. E., Zwaan, M. A., Blok, W. J. G. D., Calabretta, M. R., Disney, M. J., Minchin, R. F., Bhathal, R., Boyce, P. J., Drinkwater, M. J., Freeman, K. C., Gibson, B. K., Green, A. J., Haynes, R. F., Juraszek, S., Kesteven, M. J., Knezek, P. M., Mader,

- S., Marquarding, M., Meyer, M., Mould, J. R., Oosterloo, T., O'brien, J., Price, R. M., Sadler, E. M., Schröder, A., Stewart, I. M., Stootman, F., Waugh, M., Warren, B. E., Webster, R. L., & Wright, A. E. 2004, *AJ*, 128, 16
- Koribalski, B. S., Wang, J., Kamphuis, P., Westmeier, T., Staveley-Smith, L., Oh, S. H., López-Sánchez, Á. R., Wong, O. I., Ott, J., de Blok, W. J. G., & Shao, L. 2018, *MNRAS*, 478, 1611
- Krahm, G., Finn, M. K., Indebetouw, R., Johnson, K. E., Kamenetzky, J., & Bemis, A. subm., *ApJ*
- Krishnamurthi, A. & Porro, I. 2008, in *EPO and a Changing World ASP Conference Series*, ed. C. Germany, M. Gibbs, & J. W. Moody, Vol. 389
- Kroupa, P. 2002, *Science*, 295, 82
- Kroupa, P., Aarseth, S., & Hurley, J. 2001, *MNRAS*, 321, 699
- Lada, C. J., Lombardi, M., & Alves, J. F. 2010, *ApJ*, 724, 687
- Lardo, C., Davies, B., Kudritzki, R. P., Gazak, J. Z., Evans, C. J., Patrick, L. R., Bergemann, M., & Plez, B. 2015, *ApJ*, 812, 160
- Larsen, S. S., Mora, M. D., Brodie, J. P., & Richtler, T. 2007, in *Stellar Populations as Building Blocks of Galaxies*, ed. A. Vazdekis & R. Peletier, Vol. 241, 435–439
- Larson, R. B. 1981, *MNRAS*, 194, 809
- Lazariv, T. & Lehmann, C. 2018, *Goodness-of-Fit Tests for Large Datasets*
- Lederman, N. G., Abd-El-Khalick, F., Bell, R. L., & Schwartz, R. S. 2002, *Journal of Research in Science Teaching*, 39, 497

Lee, J. C., Gil de Paz, A., Tremonti, C., Kennicutt, Robert C., J., Salim, S., Bothwell, M., Calzetti, D., Dalcanton, J., Dale, D., Engelbracht, C., Funes, S. J. J. G., Johnson, B., Sakai, S., Skillman, E., van Zee, L., Walter, F., & Weisz, D. 2009, ApJ, 706, 599

Leroy, A. K., Bolatto, A. D., Ostriker, E. C., Walter, F., Gorski, M., Ginsburg, A., Krieger, N., Levy, R. C., Meier, D. S., Mills, E., Ott, J., Rosolowsky, E., Thompson, T. A., Veilleux, S., & Zschaechner, L. K. 2018, ApJ, 869, 126

Leroy, A. K., Rosolowsky, E., Usero, A., Sandstrom, K., Schinnerer, E., Schrub, A., Bolatto, A. D., Sun, J., Barnes, A. T., Belfiore, F., Bigiel, F., den Brok, J. S., Cao, Y., Chiang, I.-D., Chevance, M., Dale, D. A., Eibensteiner, C., Faesi, C. M., Glover, S. C. O., Hughes, A., Jiménez Donaire, M. J., Klessen, R. S., Koch, E. W., Kruijssen, J. M. D., Liu, D., Meidt, S. E., Pan, H.-A., Pety, J., Puschignig, J., Querejeta, M., Saito, T., Sardone, A., Watkins, E. J., Weiss, A., & Williams, T. G. 2022, ApJ, 927, 149

Leroy, A. K., Schinnerer, E., Hughes, A., Rosolowsky, E., Pety, J., Schrub, A., Usero, A., Blanc, G. A., Chevance, M., Emsellem, E., Faesi, C. M., Herrera, C. N., Liu, D., Meidt, S. E., Querejeta, M., Saito, T., Sandstrom, K. M., Sun, J., Williams, T. G., Anand, G. S., Barnes, A. T., Behrens, E. A., Belfiore, F., Benincasa, S. M., Bešlić, I., Bigiel, F., Bolatto, A. D., den Brok, J. S., Cao, Y., Chandar, R., Chastenet, J., Chiang, I.-D., Congiu, E., Dale, D. A., Deger, S., Eibensteiner, C., Egorov, O. V., García-Rodríguez, A., Glover, S. C. O., Grasha, K., Henshaw, J. D., Ho, I.-T., Kepley, A. A., Kim, J., Klessen, R. S., Kreckel, K., Koch, E. W., Kruijssen, J. M. D., Larson, K. L., Lee, J. C., Lopez, L. A., Machado, J., Mayker, N., McElroy, R., Murphy, E. J., Ostriker, E. C., Pan, H.-A., Pessa, I., Puschignig, J., Razza,

- A., Sánchez-Blázquez, P., Santoro, F., Sardone, A., Scheuermann, F., Sliwa, K., Sormani, M. C., Stuber, S. K., Thilker, D. A., Turner, J. A., Utomo, D., Watkins, E. J., & Whitmore, B. 2021, *ApJS*, 257, 43
- Li, F., Wang, J., Gao, F., Liu, S., Zhang, Z.-Y., Li, S., Gong, Y., Li, J., & Shi, Y. 2021, *MNRAS*
- Long, M., Steinke, J., Applegate, B., Lapinski, M. K., Johnson, M. J., & Ghosh, S. 2010, *Science Communication*, 32, 356
- Longmore, S. N., Bally, J., Testi, L., Purcell, C. R., Walsh, A. J., Bressert, E., Pestalozzi, M., Molinari, S., Ott, J., Cortese, L., Battersby, C., Murray, N., Lee, E., Kruijssen, J. M. D., Schisano, E., & Elia, D. 2013, *MNRAS*, 429, 987
- Lucchini, S., D’Onghia, E., & Fox, A. J. 2021, *ApJ*, 921, L36
- Madau, P., Pozzetti, L., & Dickinson, M. 1998, *ApJ*, 498, 106
- Maddalena, R. J. & Thaddeus, P. 1985, *ApJ*, 294, 231
- Mangum, J. G. & Shirley, Y. L. 2015, *PASP*, 127, 266
- Matthews, A. M., Johnson, K. E., Whitmore, B. C., Brogan, C. L., Leroy, A. K., & Indebetouw, R. 2018, *ApJ*, 862, 147
- McCreedy, D. & Dierking, L. D. 2013, *Cascading influences: Long-term impacts of informal STEM experiences for girls*, Tech. rep., The Franklin Institute
- McLaughlin, D. E. & Fall, S. M. 2008, *ApJ*, 679, 1272
- McMullin, J. P., Waters, B., Schiebel, D., Young, W., & Golap, K. 2007, in *Astronomical Society of the Pacific Conference Series*, Vol. 376, *Astronomical Data Analysis Software and Systems XVI*, ed. R. A. Shaw, F. Hill, & D. J. Bell, 127

- Meidt, S. E., Hughes, A., Dobbs, C. L., Pety, J., Thompson, T. A., García-Burillo, S., Leroy, A. K., Schinnerer, E., Colombo, D., Querejeta, M., Kramer, C., Schuster, K. F., & Dumas, G. 2015, *ApJ*, 806
- Meidt, S. E., Schinnerer, E., García-Burillo, S., Hughes, A., Colombo, D., Pety, J., Dobbs, C. L., Schuster, K. F., Kramer, C., Leroy, A. K., Dumas, G., & Thompson, T. A. 2013, *ApJ*, 779
- Meixner, M., Gordon, K. D., Indebetouw, R., Hora, J. L., Whitney, B., Blum, R., Reach, W., Bernard, J.-P., Meade, M., Babler, B., Engelbracht, C. W., For, B.-Q., Misselt, K., Vijh, U., Leitherer, C., Cohen, M., Churchwell, E. B., Boulanger, F., Frogel, J. A., Fukui, Y., Gallagher, J., Gorjian, V., Harris, J., Kelly, D., Kawamura, A., Kim, S., Latter, W. B., Madden, S., Markwick-Kemper, C., Mizuno, A., Mizuno, N., Mould, J., Nota, A., Oey, M. S., Olsen, K., Onishi, T., Paladini, R., Panagia, N., Perez-Gonzalez, P., Shibai, H., Sato, S., Smith, L., Staveley-Smith, L., Tielens, A. G. G. M., Ueta, T., van Dyk, S., Volk, K., Werner, M., & Zaritsky, D. 2006, *AJ*, 132, 2268
- Meixner, M., Panuzzo, P., Roman-Duval, J., Engelbracht, C., Babler, B., Seale, J., Hony, S., Montiel, E., Sauvage, M., Gordon, K., Misselt, K., Okumura, K., Chaniel, P., Beck, T., Bernard, J. P., Bolatto, A., Bot, C., Boyer, M. L., Carlson, L. R., Clayton, G. C., Chen, C. H. R., Cormier, D., Fukui, Y., Galametz, M., Galliano, F., Hora, J. L., Hughes, A., Indebetouw, R., Israel, F. P., Kawamura, A., Kemper, F., Kim, S., Kwon, E., Lebouteiller, V., Li, A., Long, K. S., Madden, S. C., Matsuura, M., Muller, E., Oliveira, J. M., Onishi, T., Otsuka, M., Paradis, D., Poglitsch, A., Reach, W. T., Robitaille, T. P., Rubio, M., Sargent, B., Sewilo, M., Skibba, R.,

- Smith, L. J., Srinivasan, S., Tielens, A. G. G. M., van Loon, J. T., & Whitney, B. 2013, *AJ*, 146, 62
- Menon, S. H., Grasha, K., Elmegreen, B. G., Federrath, C., Krumholz, M. R., Calzetti, D., Sánchez, N., Linden, S. T., Adamo, A., Messa, M., Cook, D. O., Dale, D. A., Grebel, E. K., Fumagalli, M., Sabbi, E., Johnson, K. E., Smith, L. J., & Kennicutt, R. C. 2021, *MNRAS*, 507, 5542
- Messa, M., Adamo, A., Calzetti, D., Reina-Campos, M., Colombo, D., Schinnerer, E., Chandar, R., Dale, D. A., Gouliermis, D. A., Grasha, K., Grebel, E. K., Elmegreen, B. G., Fumagalli, M., Johnson, K. E., Kruijssen, J. M. D., Östlin, G., Shabani, F., Smith, L. J., & Whitmore, B. C. 2018, *MNRAS*, 477, 1683
- Messa, M., Calzetti, D., Adamo, A., Grasha, K., Johnson, K. E., Sabbi, E., Smith, L. J., Bajaj, V., Finn, M. K., & Lin, Z. 2021, *ApJ*, 909, 121
- Miller, A. E., Cioni, M.-R. L., de Grijs, R., Sun, N.-C., Bell, C. P. M., Choudhury, S., Ivanov, V. D., Marconi, M., Oliveira, J., Petr-Gotzens, M., Ripepi, V., & van Loon, J. T. 2022, *MNRAS*
- Miller, D. I., Nolla, K. M., Eagly, A. H., & Uttal, D. H. 2018, *Child Development*, 89, 1943
- Miville-Deschênes, M.-A., Murray, N., & Lee, E. J. 2017, *ApJ*, 834, 57
- Mizuno, N., Yamaguchi, R., Mizuno, A., Rubio, M., Abe, R., Saito, H., Onishi, T., Yonekura, Y., Yamaguchi, N., Ogawa, H., & Fukui, Y. 2001, *PASJ*, 53, 971
- Mondal, C., Subramaniam, A., George, K., Postma, J. E., Subramanian, S., & Barway, S. 2021, *ApJ*, 909, 203

- Muraoka, K., Takeda, M., Yanagitani, K., Kaneko, H., Nakanishi, K., Kuno, N., Sorai, K., Tosaki, T., & Kohno, K. 2016, PASJ, 68, 18
- Murphy, C. & Beggs, J. 2005, Primary science in the UK: a scoping study, Tech. rep., Wellcome Trust
- Mutch, S. J., Croton, D. J., & Poole, G. B. 2011, ApJ, 736, 84
- Narayanan, D., Krumholz, M., Ostriker, E. C., & Hernquist, L. 2011, MNRAS, 418, 664
- Nayak, O., Meixner, M., Fukui, Y., Tachihara, K., Onishi, T., Saigo, K., Tokuda, K., & Harada, R. 2018, ApJ, 854, 154
- Nayak, O., Meixner, M., Indebetouw, R., De Marchi, G., Koekemoer, A., Panagia, N., & Sabbi, E. 2016, ApJ, 831, 32
- Nguyen, N. K., Pettitt, A. R., Tasker, E. J., & Okamoto, T. 2018, MNRAS, 475, 27
- Nikolić, S., Garay, G., Rubio, M., & Johansson, L. E. B. 2007, A&A, 471, 561
- Nishimura, A., Tokuda, K., Kimura, K., Muraoka, K., Maezawa, H., Ogawa, H., Dobashi, K., Shimoikura, T., Mizuno, A., Fukui, Y., & Onishi, T. 2015, ApJS, 216, 18
- NSTA, N. S. T. A. 2000, The nature of science: NSTA Position Statement
- O'Connell, R. W., Gallagher, John S., I., & Hunter, D. A. 1994, ApJ, 433, 65
- Oey, M. S., Herrera, C. N., Silich, S., Reiter, M., James, B. L., Jaskot, A. E., & Micheva, G. 2017, ApJ, 849, L1

- Oka, T., Hasegawa, T., Sato, F., Tsuboi, M., Miyazaki, A., & Sugimoto, M. 2001, *ApJ*, 562, 348
- Orozco-Duarte, R., Wofford, A., Vidal-García, A., Bruzual, G., Charlot, S., Krumholz, M. R., Hannon, S., Lee, J., Wofford, T., Fumagalli, M., Dale, D., Messa, M., Grebel, E. K., Smith, L., Grasha, K., & Cook, D. 2022, *MNRAS*, 509, 522
- Padoan, P., Juvela, M., Bally, J., & Nordlund, Å. 2000, *ApJ*, 529, 259
- Peñaloza, C. H., Clark, P. C., Glover, S. C. O., Shetty, R., & Klessen, R. S. 2017, *MNRAS*, 465, 2277
- Pell, T. & Jarvis, T. 2001, *International Journal of Science Education*, 23, 847
- Pelupessy, F. I. & Portegies Zwart, S. 2012, *MNRAS*, 420, 1503
- Peters, W. L., Freeman, K. C., Forster, J. R., Manchester, R. N., & Ables, J. G. 1994, *MNRAS*, 269, 1025
- Pettitt, A. R., Dobbs, C. L., Baba, J., Colombo, D., Duarte-Cabral, A., Egusa, F., & Habe, A. 2020, *MNRAS*, 498, 1159
- Pettitt, A. R., Egusa, F., Dobbs, C. L., Tasker, E. J., Fujimoto, Y., & Habe, A. 2018, *MNRAS*, 480, 3356
- Pietrzyński, G., Graczyk, D., Gieren, W., Thompson, I. B., Pilecki, B., Udalski, A., Soszyński, I., Kozłowski, S., Konorski, P., Suchomska, K., Bono, G., Moroni, P. G. P., Villanova, S., Nardetto, N., Bresolin, F., Kudritzki, R. P., Storm, J., Gallenne, A., Smolec, R., Minniti, D., Kubiak, M., Szymański, M. K., Poleski, R., Wyrzykowski, Ł., Ulaczyk, K., Pietrukowicz, P., Górski, M., & Karczmarek, P. 2013, *Nature*, 495, 76

- Portegies Zwart, S. F., McMillan, S. L. W., & Gieles, M. 2010, *ARA&A*, 48, 431
- Previs, K. K. 2016, *Science Communication*, 38, 303
- Qing, G., Wang, W., Liu, J.-F., & Yoachim, P. 2015, *ApJ*, 799, 19
- Querejeta, M., Schinnerer, E., Meidt, S., Sun, J., Leroy, A. K., Emsellem, E., Klessen, R. S., Muñoz-Mateos, J. C., Salo, H., Laurikainen, E., Bešlić, I., Blanc, G. A., Chevance, M., Dale, D. A., Eibensteiner, C., Faesi, C., García-Rodríguez, A., Glover, S. C. O., Grasha, K., Henshaw, J., Herrera, C., Hughes, A., Kreckel, K., Kruijssen, J. M. D., Liu, D., Murphy, E. J., Pan, H. A., Pety, J., Razza, A., Rosolowsky, E., Saito, T., Schrubba, A., Usero, A., Watkins, E. J., & Williams, T. G. 2021, *A&A*, 656, A133
- Quinn, D. M. & Cooc, N. 2015, *Educational Researcher*, 44, 336
- Radburn-Smith, D. J., de Jong, R. S., Seth, A. C., Bailin, J., Bell, E. F., Brown, T. M., Bullock, J. S., Courteau, S., Dalcanton, J. J., Ferguson, H. C., Goudfrooij, P., Holfeltz, S., Holwerda, B. W., Purcell, C., Sick, J., Streich, D., Vlajic, M., & Zucker, D. B. 2011, *ApJS*, 195, 18
- Radburn-Smith, D. J., Roškar, R., Debattista, V. P., Dalcanton, J. J., Streich, D., de Jong, R. S., Vlajić, M., Holwerda, B. W., Purcell, C. W., Dolphin, A. E., & Zucker, D. B. 2012, *ApJ*, 753, 138
- Rahm, J., Gonsalves, A. J., & Lachaine, A. 2022, *Journal of the Learning Sciences*, 31, 199
- Rahner, D., Pellegrini, E. W., Glover, S. C. O., & Klessen, R. S. 2018, *MNRAS*, 473, L11

- Reines, A. E., Sivakoff, G. R., Johnson, K. E., & Brogan, C. L. 2011, *Nature*, 470, 66
- Rice, T. S., Goodman, A. A., Bergin, E. A., Beaumont, C., & Dame, T. M. 2016, *ApJ*, 822, 52
- Riedinger, K. & Taylor, A. 2016, “I Could See Myself as a Scientist”: The Potential of Out-of-School Time Programs to Influence Girls’ Identities in Science, Tech. rep., *Afterschool Matters*
- Robitaille, T. P. 2017, *A&A*, 600, A11
- Robitaille, T. P. & Whitney, B. A. 2010, *ApJ*, 710, L11
- Robitaille, T. P., Whitney, B. A., Indebetouw, R., & Wood, K. 2007, *ApJS*, 169, 328
- Rolleston, W. R. J., Trundle, C., & Dufton, P. L. 2002, *A&A*, 396, 53
- Rosolowsky, E., Hughes, A., Leroy, A. K., Sun, J., Querejeta, M., Schrubba, A., Usero, A., Herrera, C. N., Liu, D., Pety, J., Saito, T., Bešlić, I., Bigiel, F., Blanc, G., Chevance, M., Dale, D. A., Deger, S., Faesi, C. M., Glover, S. C. O., Henshaw, J. D., Klessen, R. S., Kruijssen, J. M. D., Larson, K., Lee, J., Meidt, S., Mok, A., Schinnerer, E., Thilker, D. A., & Williams, T. G. 2021, *MNRAS*, 502, 1218
- Rosolowsky, E. W., Pineda, J. E., Kauffmann, J., & Goodman, A. A. 2008, *ApJ*, 679, 1338
- Ryon, J. E., Gallagher, J. S., Smith, L. J., Adamo, A., Calzetti, D., Bright, S. N., Cignoni, M., Cook, D. O., Dale, D. A., Elmegreen, B. E., Fumagalli, M., Gouliermis, D. A., Grasha, K., Grebel, E. K., Kim, H., Messa, M., Thilker, D., & Ubeda, L. 2017, *ApJ*, 841, 92

Sabbi, E., Calzetti, D., Ubeda, L., Adamo, A., Cignoni, M., Thilker, D., Aloisi, A., Elmegreen, B. G., Elmegreen, D. M., Gouliermis, D. A., Grebel, E. K., Messa, M., Smith, L. J., Tosi, M., Dolphin, A., Andrews, J. E., Ashworth, G., Bright, S. N., Brown, T. M., Chandar, R., Christian, C., Clayton, G. C., Cook, D. O., Dale, D. A., de Mink, S. E., Dobbs, C., Evans, A. S., Fumagalli, M., Gallagher, J. S., I., Grasha, K., Herrero, A., Hunter, D. A., Johnson, K. E., Kahre, L., Kennicutt, R. C., Kim, H., Krumholz, M. R., Lee, J. C., Lennon, D., Martin, C., Nair, P., Nota, A., Östlin, G., Pellerin, A., Prieto, J., Regan, M. W., Ryon, J. E., Sacchi, E., Schaerer, D., Schiminovich, D., Shabani, F., Van Dyk, S. D., Walterbos, R., Whitmore, B. C., & Wofford, A. 2018, *ApJS*, 235, 23

Sabbi, E., Lennon, D. J., Anderson, J., Cignoni, M., van der Marel, R. P., Zaritsky, D., De Marchi, G., Panagia, N., Gouliermis, D. A., Grebel, E. K., Gallagher, J. S., I., Smith, L. J., Sana, H., Aloisi, A., Tosi, M., Evans, C. J., Arab, H., Boyer, M., de Mink, S. E., Gordon, K., Koekemoer, A. M., Larsen, S. S., Ryon, J. E., & Zeidler, P. 2016, *ApJS*, 222, 11

Sacchi, E., Cignoni, M., Aloisi, A., Tosi, M., Adamo, A., Dale, D. A., Elmegreen, B. G., Elmegreen, D. M., Calzetti, D., Gouliermis, D. A., Grasha, K., Smith, L. J., Wofford, A., Lee, J. C., Sabbi, E., & Ubeda, L. 2019, *ApJ*, 878, 1

Sakamoto, S. 1994, *PASP*, 106, 1112

Sánchez, N., Alfaro, E. J., & Pérez, E. 2007, *ApJ*, 656, 222

Sandage, A. & Brucato, R. 1979, *AJ*, 84, 472

Satterthwait, D. 2010, *Teaching Science*, 56

Schaefer, B. E. 2008, *AJ*, 135, 112

- Schinnerer, E., Meidt, S. E., Pety, J., Hughes, A., Colombo, D., García-Burillo, S., Schuster, K. F., Dumas, G., Dobbs, C. L., Leroy, A. K., Kramer, C., Thompson, T. A., & Regan, M. W. 2013, *ApJ*, 779
- Schirm, M. R. P., Wilson, C. D., Madden, S. C., & Clements, D. L. 2016, *ApJ*, 823, 87
- Schmidt, M. 1959, *ApJ*, 129, 243
- Schmiedeke, A., Schilke, P., Möller, T., Sánchez-Monge, Á., Bergin, E., Comito, C., Csengeri, T., Lis, D. C., Molinari, S., Qin, S. L., & Rolffs, R. 2016, *A&A*, 588, A143
- Schöier, F. L., van der Tak, F. F. S., van Dishoeck, E. F., & Black, J. H. 2005, *A&A*, 432, 369
- Schreiner, C. & Sjøberg, S. 2007, in *The Re-Emergence of Values in Science Education*, ed. D. Corrigan, J. Dillon, & R. Gunstone, 231–247
- Schruba, A., Leroy, A. K., Walter, F., Bigiel, F., Brinks, E., de Blok, W. J. G., Kramer, C., Rosolowsky, E., Sandstrom, K., Schuster, K., Usero, A., Weiss, A., & Wiesemeyer, H. 2012, *AJ*, 143, 138
- Schwartz, R. S., Lederman, N. G., & Crawford, B. A. 2004, *Science Education*, 88, 610
- Seale, J. P., Looney, L. W., Wong, T., Ott, J., Klein, U., & Pineda, J. L. 2012, *ApJ*, 751, 42
- Seale, J. P., Meixner, M., Sewiło, M., Babler, B., Engelbracht, C. W., Gordon, K., Hony, S., Misselt, K., Montiel, E., Okumura, K., Panuzzo, P., Roman-Duval, J.,

- Sauvage, M., Boyer, M. L., Chen, C. H. R., Indebetouw, R., Matsuura, M., Oliveira, J. M., Srinivasan, S., van Loon, J. T., Whitney, B., & Woods, P. M. 2014, *AJ*, 148, 124
- Sewiło, M., Indebetouw, R., Carlson, L. R., Whitney, B. A., Chen, C. H. R., Meixner, M., Robitaille, T., van Loon, J. T., Oliveira, J. M., Churchwell, E., Simon, J. D., Hony, S., Panuzzo, P., Sauvage, M., Roman-Duval, J., Gordon, K., Engelbracht, C., Misselt, K., Okumura, K., Beck, T., Hora, J., & Woods, P. M. 2010, *A&A*, 518, L73
- Shirley, Y. L. 2015, *PASP*, 127, 299
- Sidorin, V. 2017, *Quickclump: Identify clumps within a 3D FITS datacube*
- Silva-Villa, E., Adamo, A., & Bastian, N. 2013, *MNRASL*, 436
- Silva-Villa, E. & Larsen, S. S. 2012, *MNRAS*, 423, 213
- Skrutskie, M. F., Cutri, R. M., Stiening, R., Weinberg, M. D., Schneider, S., Carpenter, J. M., Beichman, C., Capps, R., Chester, T., Elias, J., Huchra, J., Liebert, J., Lonsdale, C., Monet, D. G., Price, S., Seitzer, P., Jarrett, T., Kirkpatrick, J. D., Gizis, J. E., Howard, E., Evans, T., Fowler, J., Fullmer, L., Hurt, R., Light, R., Kopan, E. L., Marsh, K. A., McCallon, H. L., Tam, R., Van Dyk, S., & Wheelock, S. 2006, *AJ*, 131, 1163
- Smith, R. C. & MCELS Team. 1998, *PASA*, 15, 163
- Soeharto, Csapó, B., Sarimanah, E., Dewi, F. I., & Sabri, T. 2019, *Jurnal Pendidikan IPA Indonesia*, 8, 247
- Solomon, P. M., Rivolo, A. R., Barrett, J., & Yahil, A. 1987, *ApJ*, 319, 730

- Sorai, K., Hasegawa, T., Booth, R. S., Rubio, M., Morino, J. I., Bronfman, L., Handa, T., Hayashi, M., Nyman, L. Å., Oka, T., Sakamoto, S., Seta, M., & Usuda, K. S. 2001, *ApJ*, 551, 794
- Stanghellini, L., Magrini, L., & Casasola, V. 2015, *ApJ*, 812
- Stein, M., Larrabee, T. G., & Barman, C. R. 2008, *Journal of Elementary Science Education*, 20, 1
- Steinke, J. 2005, *Science Communication*, 27, 27
- Steinke, J. & Tavarez, P. M. P. 2017, *International Journal of Gender, Science and Technology*, 9
- Sun, J., Leroy, A. K., Rosolowsky, E., Hughes, A., Schinnerer, E., Schrubba, A., Koch, E. W., Blanc, G. A., Chiang, I.-D., Groves, B., Liu, D., Meidt, S., Pan, H.-A., Pety, J., Querejeta, M., Saito, T., Sandstrom, K., Sardone, A., Usero, A., Utomo, D., Williams, T. G., Barnes, A. T., Benincasa, S. M., Bigiel, F., Bolatto, A. D., Boquien, M., Chevance, M., Dale, D. A., Deger, S., Emsellem, E., Glover, S. C. O., Grasha, K., Henshaw, J. D., Klessen, R. S., Kreckel, K., Kruijssen, J. M. D., Ostriker, E. C., & Thilker, D. A. 2022, *ApJ*, 164, 43
- Sun, J., Leroy, A. K., Schinnerer, E., Hughes, A., Rosolowsky, E., Querejeta, M., Schrubba, A., Liu, D., Saito, T., Herrera, C. N., Faesi, C., Usero, A., Pety, J., Kruijssen, J. M. D., Ostriker, E. C., Bigiel, F., Blanc, G. A., Bolatto, A. D., Boquien, M., Chevance, M., Dale, D. A., Deger, S., Emsellem, E., Glover, S. C. O., Grasha, K., Groves, B., Henshaw, J., Jimenez-Donaire, M. J., Kim, J. J., Klessen, R. S., Kreckel, K., Lee, J. C., Meidt, S., Sandstrom, K., Sardone, A. E., Utomo, D., & Williams, T. G. 2020, *ApJ*, 901, L8

- Sun, J., Leroy, A. K., Schrubba, A., Rosolowsky, E., Hughes, A., Kruijssen, J. M. D., Meidt, S., Schinnerer, E., Blanc, G. A., Bigiel, F., Bolatto, A. D., Chevance, M., Groves, B., Herrera, C. N., Hygate, A. P. S., Pety, J., Querejeta, M., Usero, A., & Utomo, D. 2018, *ApJ*, 860, 172
- Sun, N.-C., de Grijs, R., Cioni, M.-R. L., Rubele, S., Subramanian, S., van Loon, J. T., Bekki, K., Bell, C. P. M., Ivanov, V. D., Marconi, M., Muraveva, T., Oliveira, J. M., & Ripepi, V. 2018, *ApJ*, 858, 31
- Tikhonov, N. A. & Galazutdinova, O. A. 2016, *Astronomy Letters*, 42, 428
- Tobias, S. 1990, *They're Not Dumb, They're Different: Stalking the Second Tier*, Tech. rep., Research Corporation
- Tokuda, K., Fukui, Y., Harada, R., Saigo, K., Tachihara, K., Tsuge, K., Inoue, T., Torii, K., Nishimura, A., Zahorecz, S., Nayak, O., Meixner, M., Minamidani, T., Kawamura, A., Mizuno, N., Indebetouw, R., Sewiło, M., Madden, S., Galametz, M., Lebouteiller, V., Chen, C. H. R., & Onishi, T. 2019, *ApJ*, 886, 15
- Tokuda, K., Minami, T., Fukui, Y., Inoue, T., Nishioka, T., Tsuge, K., Zahorecz, S., Sano, H., Konishi, A., Rosie Chen, C. H., Sewiło, M., Madden, S. C., Nayak, O., Saigo, K., Nishimura, A., Tanaka, K. E. I., Sawada, T., Indebetouw, R., Tachihara, K., Kawamura, A., & Onishi, T. 2022, *ApJ*, 933, 20
- Trotta, R. 2008, *Contemporary Physics*, 49, 71
- Tsuge, K., Fukui, Y., Tachihara, K., Sano, H., Tokuda, K., Ueda, J., Iono, D., & Finn, M. K. 2021, *PASJ*, 73, S35
- Turner, J. A., Dale, D. A., Lee, J. C., Boquien, M., Chandar, R., Deger, S., Larson, K. L., Mok, A., Thilker, D. A., Ubeda, L., Whitmore, B. C., Belfiore, F., Bigiel,

- F., Blanc, G. A., Emsellem, E., Grasha, K., Groves, B., Klessen, R. S., Kreckel, K., Kruijssen, J. M. D., Leroy, A. K., Rosolowsky, E., Sanchez-Blazquez, P., Schinnerer, E., Schruba, A., Van Dyk, S. D., & Williams, T. G. 2021, *MNRAS*, 502, 1366
- Turner, J. A., Dale, D. A., Lilly, J., Boquien, M., Deger, S., Lee, J. C., Whitmore, B. C., Anand, G. S., Benincasa, S. M., Bigiel, F., Blanc, G. A., Chevance, M., Emsellem, E., Faesi, C. M., Glover, S. C. O., Grasha, K., Hughes, A., Klessen, R. S., Kreckel, K., Kruijssen, J. M. D., Leroy, A. K., Pan, H.-A., Rosolowsky, E., Schruba, A., & Williams, T. G. 2022, *MNRAS*, 516, 4612
- Turner, J. L., Consiglio, S. M., Beck, S. C., Goss, W. M., Ho, P. T. P., Meier, D. S., Silich, S., & Zhao, J.-H. 2017, *ApJ*, 846, 73
- Ulrich, R. K. 1976, *ApJ*, 210, 377
- van den Bergh, S., Morbey, C., & Pazder, J. 1991, *ApJ*, 375, 594
- van der Marel, R. P. & Kallivayalil, N. 2014, *ApJ*, 781, 121
- van der Tak, F. F. S., Black, J. H., Schöier, F. L., Jansen, D. J., & van Dishoeck, E. F. 2007, *A&A*, 468, 627
- van Griethuijsen, R. A., van Eijck, M. W., Haste, H., den Brok, P. J., Skinner, N. C., Mansour, N., Gencer, A. S., & BouJaoude, S. 2015, *Research in Science Education*, 45, 581
- Vandenberg, J., Rachmatullah, A., Lynch, C., Boyer, K. E., & Wiebe, E. 2021, *International Journal of Child-Computer Interaction*, 29
- Vincent-Ruz, P. & Schunn, C. D. 2018, *International Journal of STEM Education*, 5

- Virtanen, P., Gommers, R., Oliphant, T. E., Haberland, M., Reddy, T., Cournapeau, D., Burovski, E., Peterson, P., Weckesser, W., Bright, J., van der Walt, S. J., Brett, M., Wilson, J., Millman, K. J., Mayorov, N., Nelson, A. R. J., Jones, E., Kern, R., Larson, E., Carey, C. J., Polat, İ., Feng, Y., Moore, E. W., VanderPlas, J., Laxalde, D., Perktold, J., Cimrman, R., Henriksen, I., Quintero, E. A., Harris, C. R., Archibald, A. M., Ribeiro, A. H., Pedregosa, F., van Mulbregt, P., & SciPy 1.0 Contributors. 2020, *Nature Methods*, 17, 261
- Vlajić, M., Bland-Hawthorn, J., & Freeman, K. C. 2011, *ApJ*, 732, 7
- Vohl, D. 2017, Shwirl: Meaningful coloring of spectral cube data with volume rendering, *Astrophysics Source Code Library*, record ascl:1704.003
- Wainer, T. M., Johnson, L. C., Seth, A. C., Torresvillanueva, E. E., Dalcanton, J. J., Durbin, M. J., Dolphin, A., Weisz, D. R., Williams, B. F., & Phatter Collaboration. 2022, *ApJ*, 928, 15
- Walborn, N. R., Barbá, R. H., & Sewilo, M. M. 2013, *AJ*, 145, 98
- Walker, D. L., Longmore, S. N., Zhang, Q., Battersby, C., Keto, E., Kruijssen, J. M. D., Ginsburg, A., Lu, X., Henshaw, J. D., Kauffmann, J., Pillai, T., Mills, E. A. C., Walsh, A. J., Bally, J., Ho, L. C., Immer, K., & Johnston, K. G. 2018, *MNRAS*, 474, 2373
- Walsh, J. R. & Roy, J. R. 1997, *MNRAS*, 288, 726
- Wang, J., Zhang, Z., & Shi, Y. 2011, *MNRAS*, 416, L21
- Ward, J. L., Oliveira, J. M., van Loon, J. T., & Sewilo, M. 2016, *MNRAS*, 455, 2345
- Wei, L. H., Keto, E., & Ho, L. C. 2012, *ApJ*, 750, 136

- Whitmore, B. C. 2000, arXiv e-prints, astro
- Whitmore, B. C., Brogan, C., Chandar, R., Evans, A., Hibbard, J., Johnson, K., Leroy, A., Privon, G., Remijan, A., & Sheth, K. 2014, ApJ, 795, 156
- Whitmore, B. C., Chandar, R., Lee, J. C., Floyd, M., Deger, S., Lilly, J., Minsley, R., Thilker, D. A., Boquien, M., Dale, D. A., Henny, K., Scheuermann, F., Barnes, A. T., Bigiel, F., Emsellem, E., Glover, S., Grasha, K., Groves, B., Hannon, S., Klessen, R. S., Kreckel, K., Kruijssen, J. M. D., Larson, K. L., Leroy, A., Mok, A., Pan, H.-A., Pinna, F., Sánchez-Blázquez, P., Schinnerer, E., Sormani, M. C., Watkins, E., & Williams, T. 2023, MNRAS, 520, 63
- Whitmore, B. C., Chandar, R., Schweizer, F., Rothberg, B., Leitherer, C., Rieke, M., Rieke, G., Blair, W. P., Mengel, S., & Alonso-Herrero, A. 2010, AJ, 140, 75
- Whitney, B. A., Sewilo, M., Indebetouw, R., Robitaille, T. P., Meixner, M., Gordon, K., Meade, M. R., Babler, B. L., Harris, J., Hora, J. L., Bracker, S., Povich, M. S., Churchwell, E. B., Engelbracht, C. W., For, B. Q., Block, M., Misselt, K., Vijn, U., Leitherer, C., Kawamura, A., Blum, R. D., Cohen, M., Fukui, Y., Mizuno, A., Mizuno, N., Srinivasan, S., Tielens, A. G. G. M., Volk, K., Bernard, J. P., Boulanger, F., Frogel, J. A., Gallagher, J., Gorjian, V., Kelly, D., Latter, W. B., Madden, S., Kemper, F., Mould, J. R., Nota, A., Oey, M. S., Olsen, K. A., Onishi, T., Paladini, R., Panagia, N., Perez-Gonzalez, P., Reach, W., Shibai, H., Sato, S., Smith, L. J., Staveley-Smith, L., Ueta, T., Van Dyk, S., Werner, M., Wolff, M., & Zaritsky, D. 2008, AJ, 136, 18
- Williams, J. P., Blitz, L., & Stark, A. A. 1995, ApJ, 451, 252
- Williams, J. P., de Geus, E. J., & Blitz, L. 1994, ApJ, 428, 693

- Wilson, C. D., Petitpas, G. R., Iono, D., Baker, A. J., Peck, A. B., Krips, M., Warren, B., Golding, J., Atkinson, A., Armus, L., Cox, T. J., Ho, P., Juvela, M., Matsushita, S., Mihos, J. C., Pihlstrom, Y., & Yun, M. S. 2008, *ApJS*, 178, 189
- Wong, T., Hughes, A., Ott, J., Muller, E., Pineda, J. L., Bernard, J.-P., Chu, Y.-H., Fukui, Y., Gruendl, R. A., Henkel, C., Kawamura, A., Klein, U., Looney, L. W., Maddison, S., Mizuno, Y., Paradis, D., Seale, J., & Welty, D. E. 2011, *ApJS*, 197, 16
- Wong, T., Hughes, A., Tokuda, K., Indebetouw, R., Onishi, T., Bandurski, J. B., Chen, C. H. R., Fukui, Y., Glover, S. C. O., Klessen, R. S., Pineda, J. L., Roman-Duval, J., Sewilo, M., Wojciechowski, E., & Zahorecz, S. 2019, *ApJ*, 885, 50
- Wong, T., Oudshoorn, L., Sofovich, E., Green, A., Shah, C., Indebetouw, R., Meixner, M., Hacar, A., Nayak, O., Tokuda, K., Bolatto, A. D., Chevance, M., De Marchi, G., Fukui, Y., Hirschauer, A. S., Jameson, K. E., Kalari, V., Lebouteiller, V., Looney, L. W., Madden, S. C., Onishi, T., Roman-Duval, J., Rubio, M., & Tielens, A. G. G. M. 2022, *ApJ*, 932, 47
- Wünsch, R., Jáchym, P., Sidorin, V., Ehlerová, S., Palouš, J., Dale, J., Dawson, J. R., & Fukui, Y. 2012, *A&A*, 539, A116
- Yamaguchi, R., Mizuno, N., Mizuno, A., Rubio, M., Abe, R., Saito, H., Moriguchi, Y., Matsunaga, K., Onishi, T., Yonekura, Y., & Fukui, Y. 2001, *PASJ*, 53, 985
- Yang, B., Stancil, P. C., Balakrishnan, N., & Forrey, R. C. 2010, *ApJ*, 718, 1062
- Yu, S.-Y., Ho, L. C., & Wang, J. 2021, *ApJ*, 917, 88
- Zackrisson, E., Rydberg, C.-E., Schaerer, D., Östlin, G., & Tuli, M. 2011, *ApJ*, 740,

Zhang, Z.-Y., Gao, Y., Henkel, C., Zhao, Y., Wang, J., Menten, K. M., & Güsten, R.
2014, ApJ, 784, L31

Zhu, M., Seaquist, E. R., & Kuno, N. 2003, ApJ, 588, 243

Zivick, P., Kallivayalil, N., Besla, G., Sohn, S. T., van der Marel, R. P., del Pino, A.,
Linden, S. T., Fritz, T. K., & Anderson, J. 2019, ApJ, 874, 78